POLISH ACADEMY OF SCIENCES
INSTITUTE OF PHYSICS

Established in 1920 by
the Polish Physical Society

ACTA PHYSICA POLONICA

- General Physics
- Atomic and Molecular Physics
- Condensed Matter
- Optics and Quantum Optics
- Quantum Information
- Biophysics
- Applied Physics

A Special Segment of This Issue Contains Selected Papers from the 14th Symposium of Magnetic Measurements and Modelling SMMM'2023
Zakopane, October 16–18, 2023

RECOGNIZED BY THE EUROPEAN
PHYSICAL SOCIETY

Volume 146 — Number 1, Warsaw, July 2024

PL ISSN 0587-4246 ATPLB6 146 (1) 1–120 (2024)

Address of the Publisher:
Instytut Fizyki PAN
al. Lotników 32/46
02-668 Warszawa, Poland
e-mail: appol@ifpan.edu.pl

Printed in Poland:
Drukarnia HAJSTRA Sp. z o.o.
M. Langiewicza 28
05-825 Grodzisk Mazowiecki
drukarnia-hajstra.com
e-mail: hajstra.biuro@gmail.com

POLISH ACADEMY OF SCIENCES
INSTITUTE OF PHYSICS

Established in 1920 by
the Polish Physical Society

ACTA PHYSICA POLONICA

- General Physics
- Atomic and Molecular Physics
- Condensed Matter
- Optics and Quantum Optics
- Quantum Information
- Biophysics
- Applied Physics

A Special Segment of This Issue Contains Selected Papers from the 14th Symposium of Magnetic Measurements and Modelling SMMM'2023
Zakopane, October 16–18, 2023

RECOGNIZED BY THE EUROPEAN PHYSICAL SOCIETY

Volume 146 — Number 1, Warsaw, July 2024

PL ISSN 0587-4246 ATPLB6 146 (1) 1–76 (2024)

Selected papers presented at the 14th Symposium of Magnetic Measurements and Modelling SMMM'2023

Zakopane, Poland, October 16–18, 2023

Editors of the Proceedings:

Jan Szczygłowski
Mariusz Najgebauer

WARSAW

POLISH ACADEMY OF SCIENCES
INSTITUTE OF PHYSICS

The Symposium was organized by

- Polish Society of Theoretical and Applied Electrical Engineering, Częstochowa Branch

In cooperation with

- Faculty of Electrical Engineering, Częstochowa University of Technology
- Institute of Metrology and Biomedical Engineering, Faculty of Mechatronics, Warsaw University of Technology

Under the auspices of

- Committee of Metrology and Research Equipment, Polish Academy of Sciences
- Rector of Czestochowa University of Technology, prof. dr hab. inż. Norbert Sczygiol

Scientific Committee

Marcos F. de Campos	Fluminense Federal University, Brazil
Krzysztof Chwastek	Częstochowa University of Technology, Poland
Andrzej Demenko	Poznań University of Technology, Poland
Victorino Franco	University of Sevilla, Spain
Janusz Gajda	AGH University of Science and Technology, Poland
Piotr Gębara	Częstochowa University of Technology, Poland
Roman Gozdur	Lodz University of Technology, Poland
Kay Hameyer	RWTH Aachen University, Germany
Paweł Jabłoński	Częstochowa University of Technology, Poland
Krzysztof Kluszczyński	Cracow University of Technology, Poland
Peter Kollár	Pavol Jozef Šafárik University in Košice, Slovakia
Branko Koprivica	University of Kragujevac, Serbia
Pavol Kováč	Slovak Academy of Sciences, Slovakia
Łukasz Mielczarek	Brockhaus Measurements, Germany
Jia Yan	Law University of Seville, Spain
Marek Lis	Częstochowa University of Technology, Poland
Istvan Meszáros	Budapest University of Technology and Economics, Hungary
Yosef Pinhasi	Ariel University, Israel
Pavel Ripka	Czech Technical University in Prague, Czech Republic

Ryszard Sroka	AGH University of Science and Technology, Poland
Dorota Stachowiak	Poznań University of Technology, Poland
Peter Svec	Slovak Academy of Sciences, Slovakia
Roman Szewczyk	Warsaw University of Technology, Poland
Jan Sykulski	University of Southampton, United Kingdom
Sławomir Tumański	Warsaw University of Technology, Poland (retired Professor)
Manuel Vázquez	Institute of Material Science of Madrid, Spain (retired Professor)
RafałWojciechowski	Poznań University of Technology, Poland
Mirosław Wołoszyn	Gdańsk University of Technology, Poland
Asher Yahalom	Ariel University, Israel
Stan Żurek	Megger Ltd., United Kingdom

Organizing Committee

Jan Szczygłowski	*Chairman*
Mariusz Najgebauer	*Co-Chairman*
Damian Gzieł	
Adam Jakubas	
Ewa Łada-Tondyra	
Agnieszka Najgebauer	
Wojciech Pluta	

Preface

The proceedings volume contains selected papers presented during the 14th Symposium of Magnetic Measurements and Modelling "SMMM'2023", which took place in Zakopane (Poland), October 16–18, 2023. The Symposium was organized by the Częstochowa Branch of the Polish Society of Theoretical and Applied Electrical Engineering (PTETiS) in cooperation with the Faculty of Electrical Engineering of the Częstochowa University of Technology and the Institute of Metrology and Biomedical Engineering, Faculty of Mechatronics, Warsaw University of Technology.

The Symposium has emerged as a continuation of the Symposia of Magnetic Measurements held previously. The 14^{th} Symposium of Magnetic Measurements & Modelling provided an excellent opportunity for scientists and engineers dealing with magnetic measurements and modelling of magnetic properties to present and discuss the results of their research. The scope of the Symposium has been extended to include modelling of properties and applications of magnetic materials and covered the following topics: measurements of magnetic quantities, indirect measurements of physical quantities using magnetic measurements, measurement techniques in a high-frequency range, nondestructive evaluation of materials, modelling of magnetic properties, magnetocaloric and magnetomechanical effect, structure and properties of magnetic materials, sensors and actuators, magnetic circuits in electrical machines, mechatronics systems.

Over 30 people from domestic and foreign academic centres, research institutes and industry participated in the Symposium, including:

- Professor Marcos Flavio de Campos, UFF — Federal Fluminense University (Brasil);
- Professor Peter Kollár, Pavol Jozef Šafárik University in Košice (Slovakia);
- Professor Branko Koprivica, University of Kragujevac (Serbia);
- Łukasz Mierczak, PhD, Brockhaus Measurements (Germany);
- Professor Denisa Olekšáková, Technical University of Košice (Slovakia);
- Professor Zdenek Roubal, Brno University of Technology (Czech Republic).

During the Symposium, 7 sessions were organized and 28 presentations were presented. In the plenary session, two invited talks were given:

(1) Ł. Mierczak, "*Advanced measurement technologies for magnetic materials used in automotive applications*",

(2) M.F. de Campos, J.A. de Castro, "*Comparative view of coercivity mechanisms in soft and hard magnetic materials*".

The Organizing Committee would like to express its gratitude to all participants for the high-level presentation of their research, which concerned the scientific and engineering aspects of measurement and modelling the properties of soft magnetic materials.

Jan Szczygłowski
Mariusz Najgebauer
Editors of the Proceedings

Selected papers presented at the 14th Symposium of Magnetic Measurements and Modelling SMMM'2023

Two Approaches to Model Power Loss Under Increased Excitation Frequency

K. Chwastek[a,*], M. Najgebauer[a], B. Koprivica[b], S. Divac[b] and M. Rosić[b]

[a] *Częstochowa University of Technology, Faculty of Electrical Engineering, al. Armii Krajowej 17, 42-201 Częstochowa, Poland*
[b] *University of Kragujevac, Faculty of Technical Sciences Čačak, Svetog Save 65, 32000 Čačak, Serbia*

Doi: 10.12693/APhysPolA.146.9 *e-mail: krzysztof.chwastek@pcz.pl

This paper focuses on two models used for the determination of power loss components in steel samples under dynamic magnetizing conditions. The considered models differ in their approach as far as the possibility of distinguishing bulk and localized eddy currents is concerned. Two samples of non-oriented electrical steel differing in silicon weight contents are the subject of experiments. A comparison of the obtained results, as well as their discussion, is given in the paper.

topics: soft magnetic materials, core loss, loss separation, modeling

1. Introduction

The concept of loss separation in soft magnetic materials is considered an important problem for practitioners [1, 2]. The present paper is focused on two approaches to model power loss in chosen grades of electrical steel. For analysis, we have chosen non-oriented (dynamo) electrical steel with a thickness of 0.35 mm (grade M330-35A) as well as steel with silicon content increased up to 6.5% (grade JNEX, 0.1 mm thick, produced on commercial scale by the Japanese enterprise JFE Steel). The aim of the paper is to compare two possible approaches to the separation issue in terms of their predictive capabilities and accuracy. The first one relies on the so-called three-term separation scheme, which in the contemporary literature is usually ascribed to G. Bertotti [3]. The other one was proposed several years ago by one of the authors of the present paper [4].

As pointed out in a recent publication [5], non-oriented electrical steels are the most widespread soft magnetic material (SMM), accounting for around 80% of the total amount. They are commonly used as a core material in rotating electrical machines. According to [6], energy loss due to re-magnetization processes in electrical steels is estimated at a 5% level of the total produced energy worldwide. Therefore, a better understanding of energy dissipation processes in these SMMs may stimulate potential energy savings and reduction in environmental burden (greenhouse gas emission).

The range of produced non-oriented electrical steels includes several different types of steels, featuring miscellaneous silicon and aluminum content (the volumetric percentage of these two chemical elements is usually provided as a whole) and various sheet thicknesses. The volumetric silicon content in these materials is in the range of 1–3.7%, whereas for aluminum — 0.2–0.8%. Considering silicon content alone, it is expedient to introduce a distinction between low silicon steels (up to 2 wt% Si, used in household appliances), conventional steels (around 3.2 wt% Si), and high silicon alloys (around 6.5 wt% Si + Al).

Increase in silicon content in the alloy leads to significant changes in the material properties:

- the admixture of silicon significantly increases the resistivity of the material, which is equivalent to limiting its loss during re-magnetization by limiting loss associated with the flow of eddy currents;
- the saturation induction value and the magnetostriction coefficient are reduced. This effect is more noticeable for high silicon alloys;
- the coefficient of magneto-crystalline anisotropy is reduced, which results in an increase in sheet permeability;
- magnetic aging (deterioration of magnetic properties of cores over time) is inhibited by capturing carbon atoms;
- the strength and stiffness of the considered alloys increases.

Aluminum affects the alloy properties in a similar way to silicon, which explains why it is sometimes used as its partial replacement. Article [7] draws attention to the fact that increasing the percentage of silicon and aluminum in the alloy may have an adverse effect on the mechanical properties of the alloy and the values of saturation magnetization and thermal conductivity. These parameters are also important in many applications. From the point of view of a manufacturer of electrical machines, it is desirable that the steel has a low level of loss and high values of magnetic permeability and thermal conductivity. From the steelmaker's perspective, it is preferred to keep the silicon and aluminum content as low as possible in order to make workability simpler.

The development of technology for producing sheets with increased silicon content is one of the latest achievements in contemporary research on soft magnetic materials [8]. Research on this group of SMMs was initiated in the mid-eighties of the last century in Japan [9–11]. Tests on magnetic properties of high silicon alloys produced in laboratory conditions, most often by rapid solidification of molten metal, have also been carried out in the USA and China. Alloys with approximately 6.5 wt% Si feature unique magnetic properties, such as almost zero magnetostriction, the highest value of permeability, and the lowest core loss among all electrical steels that contain silicon. Japanese enterprise JFE Steel Corp. is the only commercial producer of microcrystalline high-silicon steel (the brand name is JNEX).

Figure 1 depicts a comparison of material core loss per unit weight (commonly referred to as core loss density), measured at 1 T and 10 kHz. From Fig. 1, it is clear that electrical steels with increased silicon content are highly competitive against other comparable materials. Iron-based amorphous alloy, i.e., Metglas, features lower core loss, however, it is more difficult to process (harder workability, material available commercially only as cylinder-shaped cores wound of thin ribbon).

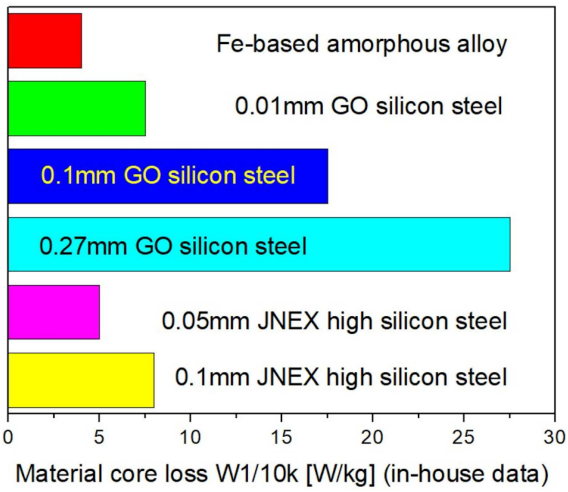

Fig. 1. Visual comparison of core loss for several alloys used in electrical engineering. Source: own work, based on JFE Steel Corp. promotional material.

2. Loss separation issue

One of the most controversial problems in magnetics is the proper description of energy dissipation in SMMs. According to the approach prevailing in contemporary literature, one can distinguish energy loss due to the hysteresis phenomenon and the flow of eddy currents in different time- and spatial scales. This approach is usually attributed to G. Bertotti, a representative of the so-called Torino school of magnetics [3], although the concept seems to be much older. Within Bertotti's framework, it is assumed that there exists a direct relationship between the macroscopic properties of an SMM subject to cyclic re-magnetization (power loss P, amplitude of flux density B_m, excitation frequency f) and the dynamics of the so-called magnetic objects (MOs) [12, 13]. The definition of MOs is, however, somewhat imprecise; in order to prove this we shall use a direct citation from the landmark paper [3]: "In particular, it has been shown that a single MO can be identified with a single Bloch wall in grain-oriented materials with large domains [20], whereas, in microcrystalline materials, the whole domain structure inside a single grain plays the role of a single MO [21], [22]."[†1]

An applied magnetic field with uniform spatial distribution tends to introduce a uniform distribution of magnetization within the sample cross-section. In a structurally homogeneous material, the equilibrium state is indeed achieved, and the loss related to the re-magnetization process is then given with the well-known expression for the so-called classical loss. The tendency to obtain a uniform distribution of magnetization is counteracted by structural inhomogeneities existing in the material, which are the sources of internal fields of magnetostatic origin, local coercive fields, and/or reaction fields related to eddy current flow. The internal fields feature highly inhomogeneous spatial distribution.

The "statistical" approach to the description of power loss within the SMM is based on an observation that domain wall movement during re-magnetization has a discontinuous character, which naturally leads to the concept that the

[†1] The reference numbers given in the quote come from work [3] — editorial note.

TABLE I

Fitting results for the M330-35A steel (Bertotti's formula).

B_m [T]		Parameter	Uncertainty	Residual SSQE	Adj. R-square
0.5	K_1	0.00485	8.33×10^{-5}	2.43×10^{-8}	0.99921
	K_2	1.65×10^{-5}	1.07×10^{-6}		
	K_3	1.19×10^{-4}	2.13×10^{-5}		
1.0	K_1	0.01499	1.34×10^{-4}	1.65×10^{-8}	0.99957
	K_2	7.58×10^{-5}	3.88×10^{-6}		
	K_3	2.56×10^{-4}	4.81×10^{-5}		
1.5	K_1	0.03705	7.98×10^{-4}	5.90×10^{-7}	0.99644
	K_2	1.78×10^{-4}	2.32×10^{-5}		
	K_3	2.70×10^{-4}	2.87×10^{-4}		

TABLE II

Fitting results for the M330-35A steel (two-term formula (2)).

B_m [T]		Parameter	Uncertainty	Residual SSQE	Adj. R-square
0.5	K_4	0.00549	4.10×10^{-5}	1.39×10^{-4}	0.99999
	K_5	2.14×10^{-5}	1.58×10^{-7}		
	α	2	–		
1.0	K_4	0.01596	7.66×10^{-5}	5.45×10^{-5}	0.99998
	K_5	9.16×10^{-5}	9.11×10^{-7}		
	α	2	–		
1.5	K_4	0.03796	1.07×10^{-4}	1.07×10^{-4}	0.99999
	K_5	1.96×10^{-4}	1.28×10^{-6}		
	α	2	–		

magnetization process might be described as a time–spatial stochastic process, which consists of random sequences of elementary magnetization changes, each of them corresponding to a sudden, localized jump of a segment of domain wall. Loss due to hysteresis is related to the dynamics of elementary jumps of single domain walls, which lead to the flow of significant, localized eddy currents even in the case when the average magnetization values change slowly. Dynamic loss, on the other hand, is the result of overlapping eddy current paths. If one assumes the time–spatial independence of jumps, one obtains the expression for classical loss. Taking into consideration the time- and spatial correlations between jump sequences leads to the introduction of an additional term, representing the so-called excess (anomalous) loss, into the energy balance equation.

Different morphologies of SMMs used in practice imply different mappings of "internal" quantities n (number of MOs) and H_{exc} (excess field). Article [14] includes a compilation of formulas useful for determining $n = n(H_{exc})$. In particular, the relationship used for NO steel with 3.2 wt% Si is $n = H_{exc}/V_0$, where V_0 is a phenomenological parameter related to microstructure. The value of this parameter should be constant, however, the dependence $V_0 = V_0(B_m)$ disclosed in [15] for the NO steel is an indirect proof of the existence of weak points in Bertotti's theory.

Paper [14] additionally provides a more complicated relationship for the dependence $n = n(H_{exc})$ in microcrystalline 6.5 wt% Si steel, however, no explanation for the specific choice of a second-order polynomial in the form $n = n_0 + \frac{H_{exc}}{V_0} + (\frac{H_{exc}}{V_0})^2$ is provided.

From the practitioner's perspective, Bertotti's theory reduces to the following relationship for total power loss (valid for the simplest "internal" relationship $n = H_{exc}/V_0$)

$$P = K_1 f + K_2 f^2 + K_3 f^{3/2}, \tag{1}$$

where K_1, K_2, and K_3 are coefficients, whose values depend on maximum flux density. Note that the values of exponents are fixed to "2" and "3/2" — they correspond to two limiting cases of weak and strong skin effect. The first term corresponds to the Steinmetz relationship [16], the second one is the relationship for "classical" eddy current loss [17], whereas the third one is interpreted as the excess (anomalous) loss due to eddy currents induced around moving domain walls.

In [4], it is argued that the distinction between macroscopic and microscopic eddy currents in SMMs is hardly possible, and thus loss separation into three terms is somewhat artificial. In order to overcome this deficiency, an alternative relationship was proposed

$$P = K_4 f + K_5 f^{\alpha}, \tag{2}$$

TABLE III

Fitting results for the JNEX steel (Bertotti's formula).

B_m [T]		Parameter	Uncertainty	Residual SSQE	Adj. R-square
0.4	K_1	0.0019	5.49×10^{-5}	6.18×10^{-9}	0.99317
	K_2	2.05×10^{-6}	5.00×10^{-7}		
	K_3	2.06×10^{-5}	1.17×10^{-5}		
0.8	K_1	0.00592	6.77×10^{-5}	9.39×10^{-9}	0.99929
	K_2	6.26×10^{-6}	6.16×10^{-7}		
	K_3	1.16×10^{-4}	1.44×10^{-5}		
1.2	K_1	0.01316	2.49×10^{-4}	7.37×10^{-8}	0.99827
	K_2	1.19×10^{-5}	2.79×10^{-6}		
	K_3	3.83×10^{-4}	5.82×10^{-5}		

TABLE IV

Fitting results for the JNEX steel (two-term formula (2)).

B_m [T]		Parameter	Uncertainty	Residual SSQE	Adj. R-square
0.4	K_4	0.00196	1.69×10^{-5}	6.16×10^{-9}	0.99432
	K_5	5.38×10^{-6}	1.54×10^{-7}		
	α	0.9	–		
0.8	K_4	0.00631	4.83×10^{-5}	5.02×10^{-8}	0.99682
	K_5	2.06×10^{-5}	4.39×10^{-7}		
	α	0.9	–		
1.2	K_4	0.01445	1.72×10^{-4}	4.62×10^{-7}	0.99133
	K_5	5.40×10^{-5}	2.06×10^{-6}		
	α	0.9	–		

where the fractional exponent α accounts for eddy currents dissipated in all time- and spatial scales in the sample. Two-term expression (2) was proposed by analogy to the Poynting theorem. Let us notice that K_4 should take comparable values to K_1 (this term is the Steinmetz formula, representing quasi-static loss due to hysteresis). Both (1) and (2) have the same number of degrees of freedom (three parameters), which facilitates their comparison.

3. Modeling examples

For the NO steel grade M330-35A, modeling was carried out for three values of magnetic flux density (0.5, 1.0, and 1.5 T), which are often provided in the catalogs of steel producers. The considered frequency range was 5–400 Hz for this steel. In order to facilitate fitting, the relationships (1) and (2) were transformed (measured values of power loss density were divided by excitation frequency), and thus energy dissipated per unit mass and per volume was determined. The determined values of coefficients along with their uncertainties and other measures of quality of fit (residual sum of squared errors (SSQE), adjusted R-square) are provided in Tables I and II. Measurements were carried out using a Single Sheet Tester device connected to a digital computer used for signal waveform control and data acquisition.

When fitting the $P = P(f)$ dependence using (2) for the examined steels, we tried to use the same value of exponent α regardless of excitation flux density. For the examined NO steel, it was found that the value which might be assumed for subsequent analysis was equal to $\alpha = 2$, thus the relationship (2) reduced itself to Bertotti's formula with the third term skipped. Therefore, there would be no need to introduce the concept of anomalous (or excess) loss in order to describe the energy dissipation process for this material. This conclusion is consistent with the observations by Brailsford [18]. Let us notice that despite the residual sums of squared errors, which are the measure for deviations of experimental data points from the predicted trends (curves obtained with (1) or (2)), are smaller for Bertotti's formula (1), the uncertainties in determined values of model parameters are considerably higher. The estimated values of K_4 are somewhat higher than their counterparts from (1), i.e., K_1.

Tables III and IV contain the fitting results for the microcrystalline steel with increased silicon content. Since the explanation for the necessity to use more complicated relationships for $n = n(H_{exc})$ (leading to the altered formula for total loss) was missing in [14], and, on the other hand, the producer of this SMM claims that this steel is isotropic, we used the same relationships (1) and (2) for fitting as in the previous case. We used data for three equidistant values of flux density, namely 0.4, 0.8, and 1.2 T, corresponding to three different regions

TABLE V

Loss separation for chosen data points (M330-35A).

	Measured	(1)	(2)
1 T, 50 Hz	1.03 $\frac{\mathrm{W}}{\mathrm{kg}}$	1.03 $\frac{\mathrm{W}}{\mathrm{kg}}$	1.03 $\frac{\mathrm{W}}{\mathrm{kg}}$
Dynamic [%]	25	27.2	22.3
Hysteresis [%]	75	72.8	77.7
1.5 T, 50 Hz	2.39 $\frac{\mathrm{W}}{\mathrm{kg}}$	2.39 $\frac{\mathrm{W}}{\mathrm{kg}}$	2.39 $\frac{\mathrm{W}}{\mathrm{kg}}$
Dynamic [%]	22.5	22.5	20.6
Hysteresis [%]	77.5	77.5	79.4

TABLE VI

Loss separation for chosen data points (JNEX).

	Measured	(1)	(2)
1.2 T, 50 Hz	0.816 $\frac{\mathrm{W}}{\mathrm{kg}}$	0.823 $\frac{\mathrm{W}}{\mathrm{kg}}$	0.814 $\frac{\mathrm{W}}{\mathrm{kg}}$
Dynamic [%]	13.3	20	11.2
Hysteresis [%]	86.7	80	88.8
0.8 T, 50 Hz	0.350 $\frac{\mathrm{W}}{\mathrm{kg}}$	0.353 $\frac{\mathrm{W}}{\mathrm{kg}}$	0.350 $\frac{\mathrm{W}}{\mathrm{kg}}$
Dynamic [%]	10.6	16.1	9.9
Hysteresis [%]	89.4	83.9	90.1
0.8 T, 400 Hz	4.285 $\frac{\mathrm{W}}{\mathrm{kg}}$	4.298 $\frac{\mathrm{W}}{\mathrm{kg}}$	4.331 $\frac{\mathrm{W}}{\mathrm{kg}}$
Dynamic [%]	39.6	44.9	41.7
Hysteresis [%]	60.4	55.1	58.3

on the magnetization curve. In this case, the value of exponent α was fixed at 0.9. The considered frequency range was 10–400 Hz for this grade. Magnetic measurements in this case were also carried out using a computerized Single Sheet Tester device.

The final verification of the usefulness of both considered formulas is their predictive ability for several chosen data points. We compared the results of the computations with the experimental results, where the loss separation was determined using the method of two frequencies [19]. The results are compiled in Tables V and VI. It can be stated that both relationships (1) and (2) yield quite comparable results as far as the values of total loss density are concerned. The second formula describes the loss separation components slightly better than Bertotti's formula for the microcrystalline JNEX steel, however, generally speaking, it can be stated that both considered relationships were found to be useful for practical computations.

4. Conclusions

Both two- and three-term formulas for power loss separation can be useful for the prediction of the quasi-static and dynamic component(s) of total power loss in the case of the examined non-oriented steel grades.

The quasi-static component is dominant at lower frequencies, in particular at power frequency. It can be noticed that its contribution to the total loss decreases with the increase in frequency. Therefore, special attention will be paid in future research to the more accurate calculation of the model parameter related to this loss component for a wider range of frequencies. Future work might also be focused on a comparison of dependencies $P_{\mathrm{model}} = P_{\mathrm{model}}(f)$ for nominally the same magnetic material but measured with different methods (Epstein frame, Single Sheet or Strip Tester) in order to analyze the effect of measurement technique on the values of model parameters and predictive capabilities of both considered power loss separation schemes.

Acknowledgments

This project was supported within the framework of the Program No. 020/RID/2018/19 "Regional Initiative of Excellence" granted by the Minister of Science and High Education in the years 2019–2023, the amount of funding PLN 12 000 000. From the project funds the costs of participation of the first author at the SMMM'2023 conference were covered.

References

[1] W.A. Pluta, *IEEE Trans. Magn.* **46**, 322 (2010).

[2] M. de Campos, *Mat. Sci. Forum* **869**, 596 (2016).

[3] G. Bertotti, *IEEE Trans. Magn.* **24**, 621 (1988).

[4] K. Chwastek, *Philos. Mag. Lett.* **90**, 809 (2010).

[5] K. Chwastek, *Sensors* **22**, 7873 (2022).

[6] A.J. Moses, P.I. Williams, O.A. Hoshtanar, *J. Magn. Magn. Mater.* **304**, 150 (2006).

[7] M.A. da Cunha, S. da Costa Paolinelli, *J. Magn. Magn. Mater.* **320**, 2485 (2008).

[8] G. Ouyang, X. Chen, Y. Liang, C. Macziewski, J. Cui, *J. Magn. Magn. Mater.* **481**, 234 (2019).

[9] Y. Takada, M. Abe, S. Masuda, J. Inagaki, *J. Appl. Phys.* **64**, 5367 (1988).

[10] Y. Tanaka, Y. Takada, M. Abe, S. Masuda, *J. Magn. Magn. Mater.* **83**, 275 (1990).

[11] H. Ninomiya, Y. Tanaka, A. Hiura, Y. Takada, *J. Appl. Phys.* **69**, 5358 (1991).

[12] G. Bertotti, *J. Appl. Phys.* **57**, 2110 (1985).

[13] G. Bertotti, *J. Appl. Phys.* **57**, 2118 (1985).

[14] J. Szczygłowski, *J. Electr. Eng.* **69**, 467 (2018).

[15] E. Barbisio, F. Fiorillo, C. Ragusa, *IEEE Trans. Magn.* **40**, 1810 (2004).

[16] C.P. Steinmetz, *Trans. AIEE* **9**, 1 (1892).

[17] C.D. Graham, Jr., *J. Appl. Phys.* **53**, 8276 (1982).

[18] F. Brailsford, *J. IEE Part II* **95**, 38 (1948).

[19] A. Chwaleba, M. Poniński, A. Siedlecki, *Metrologia elektryczna* WNT, 2014 (in polish).

Selected papers presented at the 14th Symposium of Magnetic Measurements and Modelling SMMM'2023

Investigations of Nernst Effect in Nickel Samples

Ł. Bernacki*, R. Gozdur and E. Raj

Department of Semiconductor and Optoelectronic Devices, Lodz University of Technology, Politechniki av. 10, 93-590 Lodz, Poland

Doi: 10.12693/APhysPolA.146.15 *e-mail: lukasz.bernacki@p.lodz.pl

Presented work concerns thermally activated 2D materials inducing an electric field in the presence of a magnetic field. The thermomagnetic Nernst effect combines these quantities, and several works reveal results that could be used for validation of the experimental setup before investigations of other structures with potential thermomagnetic effects. The paper shows experimental studies on the thermomagnetic Nernst effect observed in pure nickel samples. The scope of experimental studies covers relationships of the sensitivity of the Nernst coefficient to magnetic field ranging to 1 T and temperature gradient above room temperature. The obtained results were discussed in relation to the referenced works.

topics: direct current (DC), Nernst effect, thermomagnetic effect, nickel Nernst coefficient

1. Introduction

Currently, there is a trend towards sources of green energy exploitation and better energy conversion methods [1]. The article fits into these trends because it refers to the Nernst effect as the conversion of thermal energy into useful electrical energy.

The Nernst effect (NE) is a thermomagnetic phenomenon that combines thermal and electrical quantities and establishes a physical link for utilization as a direct energy converter between these two domains [2]. Thermomagnetic effects (e.g., magnetic hysteresis loop or eddy currents) are often excluded from research interest because of their dissipative and parasitic nature [3, 4]. Thermoelectric and thermomagnetic effects play a crucial role in linking thermal and electrical generators. The most popular type of thermoelectric generator is based on the Seebeck effect, which is mainly observed in semiconductors and provides good sensitivity in systems where thermoelectric generators act as sensors. The performance of these generators is still insufficient to make a breakthrough. Recent studies show that thermoelectric generators (TEGs) have the potential for further development and improvement.

A critical review of thermoelectric effects provided a breakthrough by highlighting the giant Nernst effect observed in URu_2Si_2 samples [5]. Several papers show significant values of the Nernst coefficient and achievable voltages, providing encouraging indications of materials in which the Seebeck effect is significantly higher. In paper [6], significant evidence is given that the thermal current and the electron current are compatible. Thus, in the Nernst effect, there can be a self-replication of the lift current due to the compatibility of the thermal and electron currents. In thermoelectric materials, the opposite phenomenon occurs, where the thermal current counteracts the electron current, and thus thermoelectric effects have a self-damping mechanism [7]. An interesting solution has also been presented in works [8, 9], where the authors show the combination of both thermoelectric and thermomagnetic generators [10]. The same situation occurs when observing the spin Seebeck effect (SSE), where the voltage due to SSE and the Nernst effect appear simultaneously. Very often the presented results on SSE are strongly distorted by the parasitic (NE) [3, 4]. Several papers show that NE can be used in direct energy conversion systems [11], but they do not represent a breakthrough.

There are several works showing that research is being carried out in the area of thermogenerators using the Nernst effect [3, 5]. The scientific papers do not confirm each other to determine the most promising direction for this technology. With this in mind, the authors of this paper wish to provide an overview of NE in the most commonly used nickel samples and will present a comparative analysis. The lack of convergence in the presented data leads us to attempt to revise the experimental results with our own experiment.

2. Overview of the Nernst effects

Three Nernst effects are distinguished in the scientific literature [12]. The first of these is the Nernst effect (NE). The NE is a thermomagnetic effect in which a temperature gradient in the presence of a magnetic field results in an electric field due to the deflection of diffusing electrons by the Lorentz force.

In metals, NE is the generation of a transverse electric field $\boldsymbol{E}_{\mathrm{NE}}$ when a perpendicular external magnetic field $\boldsymbol{B}_{ex}$ is applied to the sample and a temperature gradient ∇T is present in the plane of the sample (Fig. 1) [8, 9]. This means that the electric potential is attainable if the product of the field strength and the temperature gradient is non-zero and the field strength increases. The resulting electric field is expressed as the product of the magnetic field, the temperature gradient, and the Nernst coefficient Q_0 and is given by

$$\boldsymbol{E}_{\mathrm{NE}} = Q_0 \left(\boldsymbol{B}_{ex} \times \nabla T\right). \tag{1}$$

In ferromagnets, the observed electric field can contain two components that depend on the source of the magnetic field. The electric field is proportional to the external magnetic field whose origin is outside the sample. The second component is due to the intrinsic magnetization $\boldsymbol{M}$ of the residual field and is known as the anomalous Nernst effect (ANE) [13]. The resulting electric field can be expressed as

$$\boldsymbol{E} = \boldsymbol{E}_{\mathrm{NE}} + \boldsymbol{E}_{\mathrm{ANE}} = Q_0 \left(\boldsymbol{B}_{ex} \times \nabla T\right) + Q_S \left(\mu_0 \boldsymbol{M} \times \nabla T\right). \tag{2}$$

Another simplified approach is presented in paper [14], where the electric potential $\boldsymbol{E}$ is described as

$$\boldsymbol{E} = Q\, \boldsymbol{H}\, B\, \frac{\mathrm{d}t}{\mathrm{d}x}. \tag{3}$$

In this case, the dependence of the electric potential $\boldsymbol{E}$ is the result of the interactions between Nernst coefficient Q, the intensity of the magnetic field $\boldsymbol{H}$, the breadth of the specimen B, and the primary temperature gradient $\mathrm{d}t/\mathrm{d}x$. ANE is associated with high remanence materials. The obtained electric field values are usually very small, but they can be measured.

There is also the planar Nernst effect (PNE) [15], but it is not considered in this work.

Despite some significant work and the discovery of the giant Nernst effect, there has been no progress in the development of NE and related effects. On the other hand, there is no conclusive evidence that these effects are useless. TMEs are not popular because they do not represent a potential for large-scale energy conversion systems, but the continuing development of technology allows the use of micro-generation sources in ultra-low power devices where, in our opinion, these effects could find application as generation effects in energy converters.

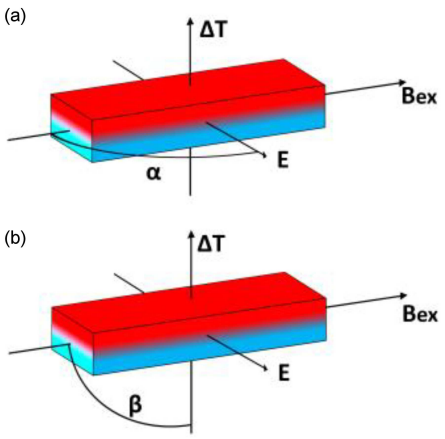

Fig. 1. The diagram of the electric potential $\boldsymbol{E}$, the intensity of the magnetic field $\boldsymbol{B}_{ex}$, and the temperature difference representing (a) the classical and anomalous Nernst effect and (b) the planar Nernst effect.

This study conducted experimental measurements of the Nernst effect (NE) in nickel and compared the results with those presented in existing publications. The current investigation extends the temperature range and enhances measurement accuracy, providing new insights into NE in nickel. While previous analyses focused on NE in pure elements, this study offers a more comprehensive understanding of the phenomenon. Papers [14, 16] provide selected measurement data and adjust a predictive curve for NE in nickel. This study aims to fill the data gap left by previous studies, which were extensive but lacked completeness and had a limited number of measurement points. Our research was carried out within the temperature range typical of human environments, and the results were compared with existing scientific data.

3. Preparation and measurements

The thermomagnetic Nernst effect was investigated in nickel samples under magnetic field excitation of 1 T in the temperature range of 263–232 K. Samples with overall dimensions $20 \times 4 \times 0.2$ mm^3 were tested in a transverse arrangement, i.e., in one in which the applied magnetic field vector was applied transversely to the temperature difference along the sample length, as shown in Fig. 1a [12]. Prior to comparative analysis, all necessary results and relevant coefficients had been normalized. Units of physical quantities were converted to be in agreement with the SI unit system.

The nanovoltmeter Agilent 34420A was used to measure the Nernst voltage. High accuracy and resolution are required as typical Nernst voltage values are in the order of a few μV [7]. The source of the

Summary of instrumentation accuracy. TABLE I

Device	Accuracy	Abs error
Lake Shore 475 DSP gaussmeter	0.05% RDG	0.3 mT
Agilent 34420A nanovoltmeter	50 ppm RDG + 20 ppm FSR	0.1 μV
Keithley DAQ6510 4-wire thermometer	0.06°C RDG	0.26°C
Omega PT100 sensor	0.2°C RDG	

constant and homogeneous external $\boldsymbol{B}_{ex}$ magnetic field is an electromagnet from Dexing Magnet, with field strengths ranging from a few mT to 2 T in the air. Lake Shore 475 DSP gaussmeter with HMMT-6J04-Vf test probe was used to measure the magnetic field applied under tests. The test bench holder consists of three pairs of voltage probes, allowing for the simultaneous measurement of up to three samples (e.g., reference samples and a tested sample). Samples under test were placed in a thermostatic chamber to ensure constant ambient temperature and the applied ΔT between two sides of the tested samples (Fig. 1). The temperature inside the chamber and ΔT were controlled using a high-performance, low-noise LTC1923 Analog Devices thermoelectric temperature controller. Temperatures were measured by means of Keithley DAQ6510 multimeter and Omega PT-100 sensors (accuracy class 1/3B). Instruments were autocalibrated, zero reference level was adjusted, and NPLC averaging was enabled. Instruments' accuracies were collected in Table I.

The process of measurement involves taking simultaneous readings from probes measuring Nernst voltages and the value of applied magnetic field strength on the surface of the test samples. At each measuring point, more than 100 measurements are taken, and the final result is the average of these measurements. The system repeatedly exposes the samples to an external magnetic field of up to 0.6 T with a fixed step throughout the cycle (Fig. 2).

4. Results and discussion

The relationships between the potential V_{NE} and biasing magnetic field $\boldsymbol{B}_{ex}$ are depicted in Fig. 3. Measurements were carried out in the steady state. The measurements were repeated a given number of times for each setup of magnetic field and temperature difference. The paper presents averaged results that demonstrate the comparable magnetization characteristics of nickel. Saturation occurs at around 50 mT, representing the maximum value achieved by the potential V_{NE}. The voltage peaks are observed at $\Delta T = 60$°C. Our findings are consistent with results published in other papers [14, 16].

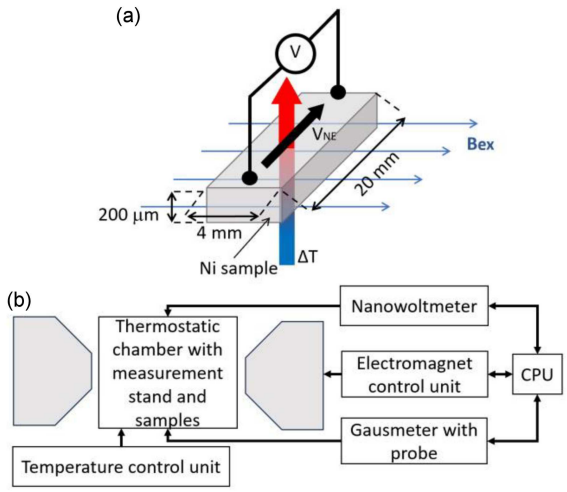

Fig. 2. The schematic diagram of (a) tested Ni sample and (b) thermostatic chamber with measurement setup.

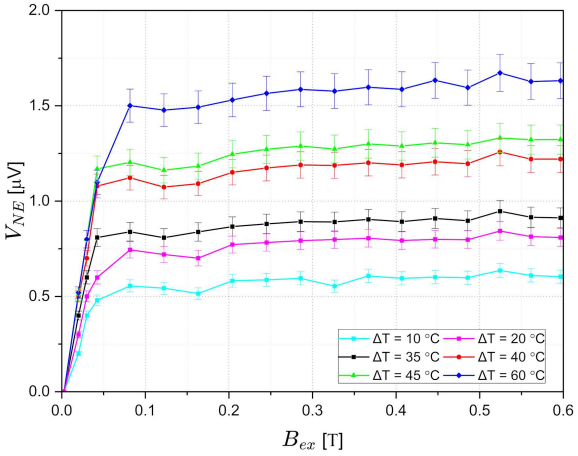

Fig. 3. The Nernst voltage as a function of the magnetic field at selected temperatures.

Figure 4a and 4b compares the obtained measurements with previously published findings [14, 16]. A.W. Smith examined two samples of pure nickel (black dashed line and blue dotted line) [16]. The red and the purple straight lines represent data obtained by the authors of the present study. The relationship between the resulting voltage V_{NE}, temperature differences ΔT, and external magnetic field strength $\boldsymbol{B}_{ex}$ are consistent with the predictions of the theory of the thermomagnetic Nernst effect in ferromagnetic materials [4]. These exhibit similar magnetization characteristics to that of nickel. Saturation transpires approximately at 40 mT, which marks the highest value attained by the voltage V_{NE}. The voltage reaches its peak at $\Delta T = 60$°C in this study, whereas A.W. Smith's research indicates that the maximum value occurs between 300–340°C, followed by a decline, which is normal and attributed to the Curie temperature. For nickel,

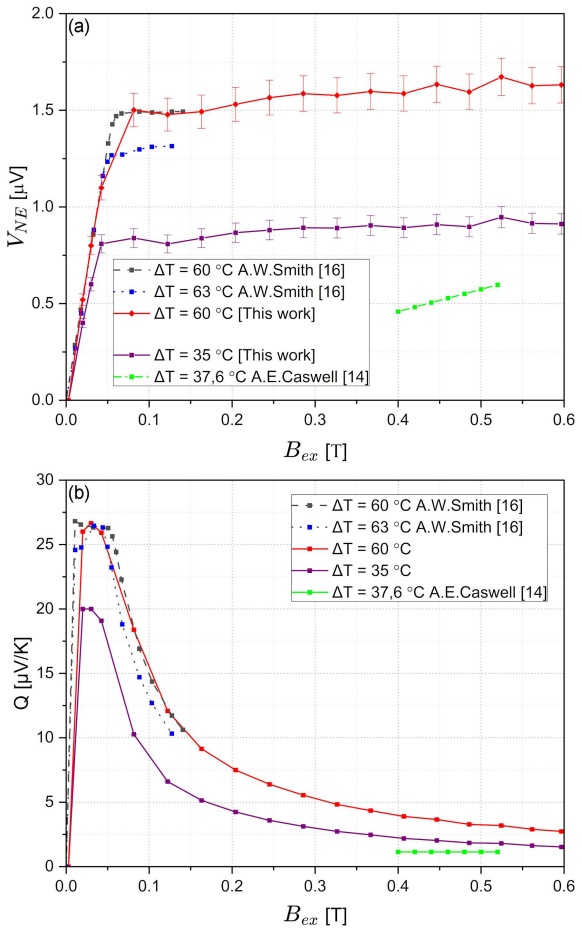

Fig. 4. The Nernst voltage as a function of the magnetic field at selected temperatures. (a) A comparison of data obtained in this work (red straight line) and data obtained by A.W. Smith [16] (black dashed and blue dotted line) and by A.E. Caswell [14] (dash-dotted green line). (b) The Nernst coefficient Q as a function of the magnetic field at temperature difference $\Delta T \sim 60$°C and $\Delta T \sim 35$°C.

the Curie temperature is about 350°C. A.E. Caswell presented data for a pure nickel sample, depicted as a green, dash-dotted line (Fig. 5).

The selected field-dependent Nernst coefficient Q for a $\Delta T \sim 60$°C is shown in Fig. 4b. The relationship in the steady state is comparable to those presented in work [16] for two different materials. An increase in temperature leads to a rise in the number of unpaired electrons, which in turn results in an increase in the material's magnetic moment. According to the Curie–Weiss law, magnetic susceptibility is proportional to the magnetic moment, and therefore, a temperature increase also causes an increase in magnetic susceptibility. At low magnetic fields, the atomic moments of Ni are chaotically oriented, leading to a linear increase in magnetic susceptibility. As the magnetic field rises, the atomic moments begin to align, resulting in a

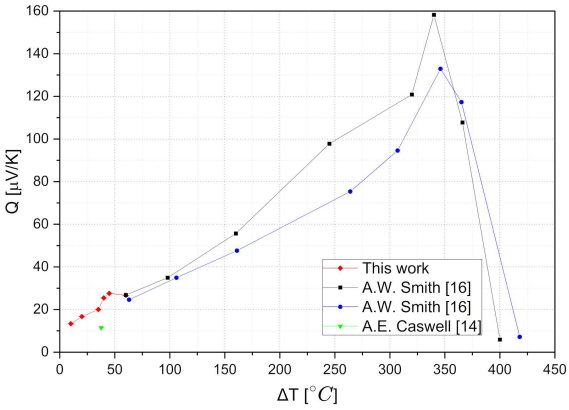

Fig. 5. A comparison of the Nernst coefficient Q as a function of temperature T obtained in this work (red rhombus) and data obtained by A.W. Smith [16] (blue circled and black squared line) and A.E. Caswell [14] (green triangulated line).

decrease in magnetic susceptibility. At sufficiently high fields, all atomic moments align, and the magnetic susceptibility reaches a saturation point [16]. The highest recorded value of Q was 26.6 μV/K at approximately 40 mT. This result was confirmed by Smith, who obtained a similar value of 26.8 μV/K under the same conditions. The difference between the two measurements was only 0.75%, which is within the permissible error of the applied nanovoltmeter.

The authors of previous studies [14, 16] have conducted measurements and fitted a curve to characterize the Nernst effect in this material. However, these investigations were not exhaustive and included only a limited number of measurement points. In contrast, our current study has undertaken comprehensive measurements across a temperature spectrum typically encountered in the human environment, which holds significant potential for thermoelectric generation applications. We observed that the maximum value of the Nernst coefficient, Q, which is 158 μV/K, was achieved at a temperature of 340 K.

5. Conclusions

The study has shown that the value of the Nernst voltage in the nickel samples is in agreement with the literature data. The investigations also show a strong dependence of the Nernst voltage on the magnetic properties of the substrates. The effect observed in nickel means that this type of substrate cannot be used in thermomagnetic generators. The experimental setup for studying the Nernst effect has been thoroughly verified, and the results are in agreement with other works. Experimental data allows for a more complete understanding of the

Nernst effect and its potential applications in energy conversion technologies. Moreover, the results may indicate a new area of application of devices using the Nernst effect as sensors.

References

[1] T.-Z. Ang, M. Salem, M. Kamarol, H. Shekhar, H.A. Nazari, N. Prabaharan, *Energy Strategy Rev.* **43**, 100939 (2022).

[2] T. Chuang, P. Su, P. Wu, S. Huang, *Phys. Rev. B.* **96**, 174406 (2017).

[3] K.I. Uchida, H. Adachi, T. Kikkawa, A. Kirihara, M. Ishida, S. Yorozu, S. Maekawa, E. Saitoh, *Proc. IEEE* **104**, 1946 (2016).

[4] H. Kannan, X. Fan, H. Celik, X. Han, J.Q. Xiao, *Sci. Rep.* **7**, 6175 (2017).

[5] R. Bel, H. Jin, K. Behnia, J. Flouquet, P. Lejay, *Phys. Rev. B* **70**, 220501(R) (2004).

[6] R. Karplus, J.M. Luttinger, *Phys. Rev.* **95**, 1154 (1954).

[7] K. Behnia, H. Aubin, *Reports Prog. Phys.* **79**, 046502 (2016).

[8] Y. Sakuraba, *Scr. Mater.* **111**, 29 (2016).

[9] S.W. Angrist, *J. Heat Transf.* **85**, 41 (1963).

[10] A. Ziabari, M. Zebarjadi, D. Vashaee, A. Shakouri, *Rep. Prog. Phys.* **79**, 095901 (2016).

[11] M. Mizuguchi, S. Nakatsuji, *Sci. Technol. Adv. Mater.* **20**, 262 (2019).

[12] E.H. Sondheimer, *Proc. R. Soc. Lond. A* **193**, 484 (1948).

[13] M. Mizuguchi, S. Nakatsuji, *Sci. Technol. Adv. Mater.* **20**, 262 (2019).

[14] A.E. Caswell, *Phys. Rev.* **20**, 280 (1922).

[15] Y. Pu, E. Johnston-Halperin, D.D. Awschalom, J. Shi, *Phys. Rev. Lett.* **97**, 036601 (2006).

[16] A.W. Smith, *Phys. Rev.* **33**, 295 (1911).

Selected papers presented at the 14th Symposium of Magnetic Measurements and Modelling SMMM'2023

Cumulative Distribution Functions as Hysteresis Models

M.F. de Campos* and J.A. de Castro

Federal Fluminense University (UFF), Av. dos Trabalhadores 420 Volta Redonda RJ, 27255-125 Brazil

Doi: 10.12693/APhysPolA.146.20 *e-mail: marcosflavio@id.uff.br

The cumulative distribution functions can be used as the basis for hysteresis models. Here it is described how, using only 3 parameters, including one representing the shape, hysteresis curves can be constructed using symmetric distribution functions. The model is useful in the interpretation of magnetic Barkhausen noise data. The model also has a clear physical meaning because it represents the distribution of coercivity inside the sample. An isotropic Stoner–Wohlfarth hysteresis was partially modelled by a three-parameter cumulative distribution function of Gaussian hysteresis for the 1st and 3rd quadrants. Asymmetric distributions will provide better hysteresis adjustment, but these are four-parameter models.

topics: hysteresis, magnetic Barkhausen noise (MBN), Stoner–Wohlfarth, cumulative distribution function (CDF)

1. Introduction

Hysteresis modelling has been the subject of many recent studies [1–7] because it allows, among other things, a better understanding of the processes related to the reversal of magnetization. The main idea of this study is to use a function representing the shape of hysteresis. Cumulative distribution functions (CDF) are a very reasonable choice for describing the hysteresis form, as discussed in this paper.

The inspiration for using the cumulative distribution function comes from several sources, especially from the Benitez model [8] for the magnetic Barkhausen noise (MBN). This model [8] assumes that the envelope of the MBN signal can be divided into two Gaussians and has previously been applied to study the grain size effect [9]. The physical basis for the Benitez model [8] is that MBN can be interpreted as a differential $\mathrm{d}B/\mathrm{d}t$ [10]; see, for example, the paper by H.J. Williams, W. Shockley, and C. Kittel [11].

In the case of a soft magnetic material, even in a quasi-static condition with a frequency near zero, several different processes take place inside the hysteresis [12]: (i) irreversible rotation of domains, (ii) irreversible domain wall displacement, (iii) creation and annihilation of domain walls, (iv) elimination of "90° closure domains", associated with magnetostrictive effects. Thus, it is difficult to cover all these different processes within a single model. Besides, the fact that soft magnetic materials have 3 easy axes (iron) or 4 easy axes (nickel) makes it very difficult to evaluate the magnetization processes, also due to the difficulty of evaluating the demagnetizing field [13, 14].

The sigmoidal shape of the hysteresis is due to magnetocrystalline anisotropy. Otherwise, the hysteresis would be an ellipsoid, as assumed, for example, in the superellipse model [15]. Cumulative distribution functions well reflect the sigmoidal shape, such as the error function, which is used to study atomic diffusion processes [16].

One of the objectives here is to find a model with a small number of parameters. For example, the Jiles–Atherton (JA) model has 5 adjusting parameters, as described in the Sablik–Jiles model for plastic deformation [17]. However, even with 5 parameters, the JA model was not able to fit or obtain the experimental hystereses, which were modified due to the plastic deformation in electrical steels [18]. The reason is simple, namely the JA model imposes a Langevin function as the "skeleton" of the curve. However, this is an unrealistic assumption. Thus, the JA model can be considered a purely phenomenological model. In other words, the JA model only gives a geometric description of hysteresis. Therefore, other functions can be considered as those representing the "hysteresis skeleton". One of such functions is the Gaussian distribution [19].

The Stoner–Wohlfarth (SW) model has been successful in describing the complete hysteresis of 2:17 type SmCo magnets [20, 21], and the reason is that the only reversal process in that case is coherent rotation. Thus, as a starting point, the Gaussian CDF

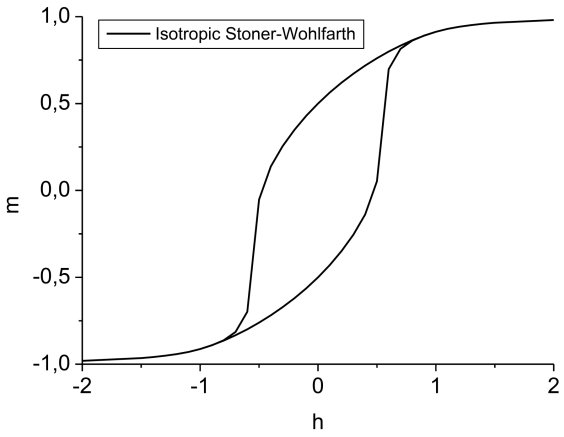

Fig. 1. Isotropic Stoner–Wohlfarth model.

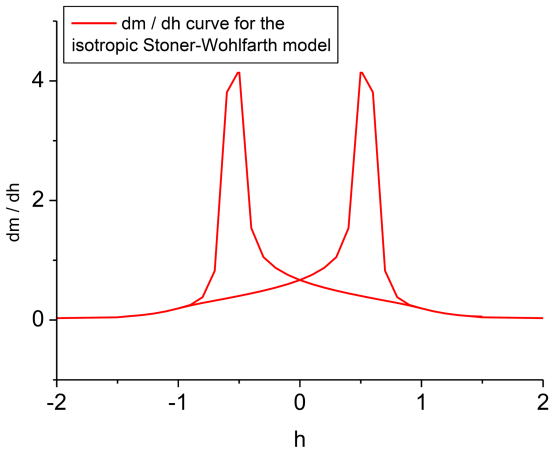

Fig. 2. The $\mathrm{d}m/\mathrm{d}h$ curve for the isotropic Stoner–Wohlfarth model.

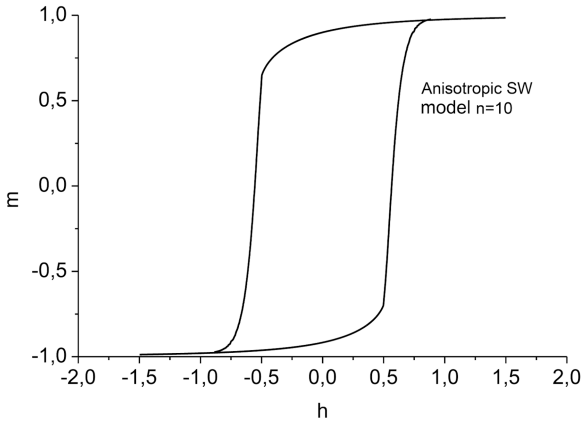

Fig. 3. Textured Stoner–Wohlfarth model; n=10.

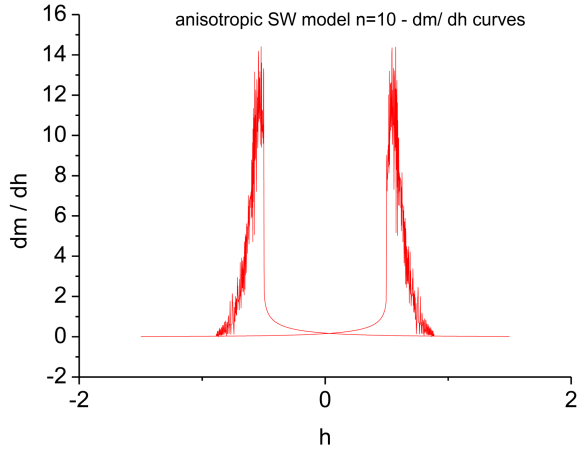

Fig. 4. The $\mathrm{d}m/\mathrm{d}h$ curve for textured isotropic Stoner–Wohlfarth model; $n = 10$.

model will be compared with isotropic SW hysteresis. The derivative of any hysteresis is a distribution function, and it represents portions of the sample with reversal of magnetization promoted by a given applied field.

2. Isotropic and anisotropic Stoner–Wohlfarth model and its derivative

The isotropic Stoner–Wohlfarth (SW) model [22, 23] is a case where there are only 3 parameters; 2 are the scale parameters related to the abscise and ordinate, and the shape of the hysteresis is due to texture — isotropic in the case of Fig. 1. It is observed, even for this very simple case, that the $\mathrm{d}M/\mathrm{d}H$ curves only could be represented by an asymmetrical distribution (see Fig. 2).

In other words, the distributions obtained with the $\mathrm{d}M/\mathrm{d}H$ curves define the shape of the hysteresis. Then, by observing the derivative of experimental hysteresis, a compatible distribution can be chosen, and thus, the hysteresis can be better modelled. In this paper, M is the magnetization, and H is the applied field, while m is the reduced magnetization $m = M/M_s$, and h is the reduced field $h = H/H_A$, where H_A is the anisotropy field, and M_s is the saturation magnetization. The Stoner–Wohlfarth model uses dimensionless parameters m and h.

Figures 3 and 4 show the hysteresis calculated with $n = 10$ and its derivative, respectively. As aforementioned, this is a 3-parameter model, with the texture given by $n = 10$ and $M_r/M_s = 0.917$, because $M_r/M_s = n + 1/n + 2$. In the case of the isotropic SW model, $f(\alpha) = 1$ [22]. For the anisotropic SW model, the magnetization $m(h)$ needs to be altered according to the distribution, i.e.,

$$m_{\parallel} = \frac{\int_0^{2\pi} \mathrm{d}\alpha \; f(\alpha)\cos(\alpha-\varphi)\sin(\alpha)}{\int_0^{2\pi} \mathrm{d}\alpha \; f(\alpha)\sin(\alpha)}. \qquad (1)$$

Here, in Figs. 3 and 4, n=10 [23] was used with the distribution given by

$$f(\alpha) = \cos^n(\alpha). \tag{2}$$

The conclusion from both Figs. 2 and 4 is that the distributions $\mathrm{d}M/\mathrm{d}H$ obtained from SW hysteresis are asymmetrical. Thus, it is quite possible that the Gaussian function is not the best option for representing the hysteresis in Figs. 1 and 3 because Gaussian instead has a symmetrical distribution.

As a title of curiosity, a "perfect square" hysteresis would be obtained with $n = \infty$. By making $\mathrm{d}M/\mathrm{d}H$, then for $n = \infty$ instead of the distribution, the line would appear at the point $h = 1$. Thus, by increasing n, the squareness of the hysteresis increases, as well as the sharpness of the corresponding distribution. Thus, by differentiating the hysteresis curve, it is possible to establish methods for determining the squareness, which is a relevant parameter in some applications [24].

3. Cumulative distribution function: Gaussian case

The integral of a distribution function is its cumulative distribution function (CDF), here denoted by Φ,

$$\Phi = \int \mathrm{d}x\ \mathrm{e}^{-x^2}. \tag{3}$$

The most commonly used distribution is the "normal" or Gaussian distribution. But there are many others, such as Cauchy–Lorentz, which is also symmetrical. In the case of the Gaussian distribution (3), there is a solution for the infinite integration interval given by

$$\Phi = \int_{-\infty}^{\infty} \mathrm{d}x\ \mathrm{e}^{-x^2} = \sqrt{\pi} \tag{4}$$

— a famous result first obtained by Laplace. Note that (3) can be solved numerically by means of a Taylor series expansion.

Then, if the integral is to be equal to unity or 100% by definition, it is necessary to divide it by $\sqrt{\pi}$. If a constant a multiplies x^2, as in the following expression

$$\Phi = \int_{-\infty}^{\infty} \mathrm{d}x\ \mathrm{e}^{-ax^2} = \sqrt{\frac{\pi}{a}}, \tag{5}$$

then for obtaining the normalization $\int \mathrm{d}x\ f(x) = 1$, it is necessary to divide the integral (5) by $\sqrt{\pi/a}$. As a consequence, the error function is defined as

$$\mathrm{erf}(x) = \frac{2}{\sqrt{\pi}} \int_0^x \mathrm{d}t\ \mathrm{e}^{-t^2}. \tag{6}$$

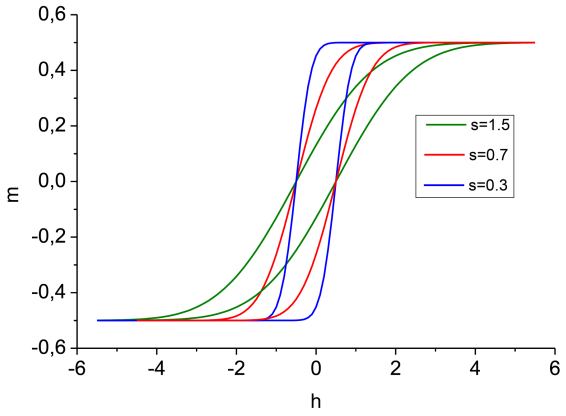

Fig. 5. Effect of parameter s on the hysteresis curve of the CDF Gaussian hysteresis model. All curves used the same scale parameter p = 0.5. Thus, all hysteresis have the same H_c.

Therefore, the cumulative distribution of a Gaussian is given by the error function (erf), as follows

$$y = \frac{1}{2}\,\mathrm{erf}\left(\frac{x}{\sqrt{2}}\right). \tag{7}$$

Cumulative distribution functions can be used as hysteresis models, especially if the applied field allows for proximity of sample saturation and, thus, the hysteresis has a sigmoidal shape. In the case of applied fields distant from saturation, the hysteresis has an ellipsoid shape, and then the sigmoidal hysteresis models are not valid. Thus, the CDF model may not be suitable for describing minor loops. When plotted on the graph, (7) has a sigmoidal shape. For (7), the center of hysteresis at $(0, 0)$ is obtained for $y_1 = y_2 = y - 0.5$, and $x_1 = x - 0.5$ and $x_2 = x + 0.5$.

The standard deviation s of the Gaussian function can be taken into account, as seen in

$$y = \frac{1}{2}\,\mathrm{erf}\left(\frac{x}{s\sqrt{2}}\right). \tag{8}$$

Also, the shift parameter p promotes an alteration in the hysteresis shape, and it is defined as $x_p = x + p$ and $x_p = x - p$, as seen in (8). Coercivity is related to the parameter p, whereas permeability is associated with the parameter s. For example, increasing s has the effect of reducing permeability, as observed in Fig. 5. The effect of the p parameter on hysteresis is depicted in Fig. 6. This is only a 3-parameter model (in contrast with the JA 5-parameter hysteresis). A mean-field parameter, as in the SW–CLC[†1] model [20], can also be included if necessary, increasing the number of parameters to 4. It should be noted that in this model, for the same p, the coercivity is the same, as can be observed in Figs. 5 and 6.

[†1] CLC — Callen–Liu–Cullen

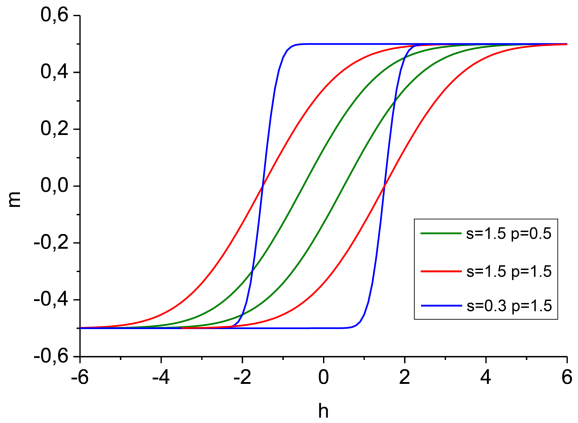

Fig. 6. Effect of parameter p on the hysteresis shape of the CDF Gaussian hysteresis model. It should be noted that, for same p, same coercivity.

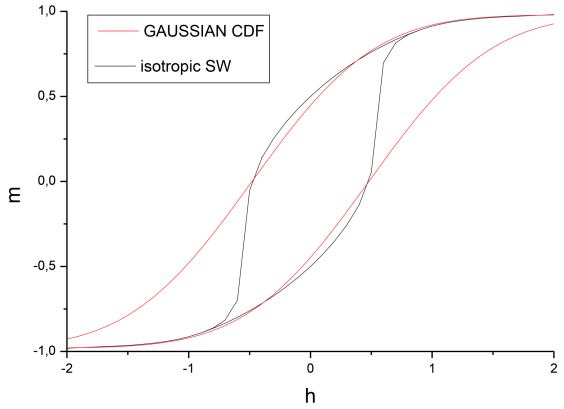

Fig. 7. SW isotropic hysteresis compared with the CDF Gaussian hysteresis model. Model parameters: $s = 0.79$, $\Psi = 1.96$, and $p = 0.48$.

In the CDF Gaussian hysteresis model, the scale parameter of the abscise is p, whereas the shape parameter is s. Thus, a third parameter related to the ordinate — Ψ — is defined in

$$y = \Psi \frac{1}{2} \operatorname{erf}\left(\frac{x}{s\sqrt{2}}\right). \tag{9}$$

The model is useful for application in the analysis of Barkhausen magnetic noise data. Any other probability function, such as, for example, Voigt or Lorentzian, can also be used as the basis for similar hysteresis models. The physical interpretation of the parameter p is that it represents the coercive field. The model, therefore, has a clear physical meaning, namely, it gives the distribution of the coercive force inside the sample, which may concern different regions (groups of grains) or individual grains.

Another possibility for a symmetrical distribution is the raised cosine distribution [25], i.e.,

$$y = \frac{1}{2S_c}\left[1 + \cos\left(\frac{x}{S_c}\pi\right)\right], \tag{10}$$

and the respective CDF distribution given as

$$\Phi = \frac{1}{2}\left[1 + \frac{x}{S_c} + \frac{1}{\pi}\sin\left(\frac{x}{S_c}\pi\right)\right]. \tag{11}$$

Here, S_c denotes the hysteresis shape parameter for the raised cosine distribution. The Laplace distribution [26] is also a possibility, i.e.,

$$y = \frac{1}{2S_L}\exp\left(-\frac{|x|}{S_L}\right), \tag{12}$$

$$\Phi = \frac{1}{2}\exp\left(\frac{x}{S_L}\right) \quad \text{for} \quad x \le 0, \tag{13}$$

$$\Phi = 1 - \frac{1}{2}\exp\left(-\frac{x}{S_L}\right) \quad \text{for} \quad x \le 0. \tag{14}$$

It should be noted that the CDF of the Laplace distribution is different for $x < 0$ and for $x > 0$ (see (13) and (14)). For the Laplace distribution, S_L is the shape parameter. Both the raised cosine distribution and the Laplace distribution are easy to integrate and do not present a very complicated CDF.

4. Models comparison

In Fig. 7, the comparison of the CDF Gaussian hysteresis model with the isotropic SW hysteresis is presented. The fitting parameters are $s = 0.79$ and $\Psi = 1.96$. The parameter p was set to 0.48, because in the SW isotropic model, the coercivity is 0.48. In Fig. 7, it is noted that the adjustment is only partial. However, by making the p parameter flexible, it was possible to model the 1st and 3rd quadrants of the SW isotropic curve, as seen in Fig. 8.

5. Additional comments

The comparison of the two models in Fig. 7 shows the limitation of the CDF Gaussian hysteresis model. However, a reasonable fitting was presented in Fig. 8 for the 1st and 3rd quadrants of the hysteresis.

Modelling a hysteresis is a very laborious process that involves trial and error to see if a given distribution can fit the experimental data. Instead of fitting the hysteresis, fitting the derivative $\mathrm{d}M/\mathrm{d}H$ can be a more rapid method for finding the hysteresis parameters.

Other functions can be considered. Unfortunately, asymmetrical distribution functions have at least 2 shape parameters, and this increases the number of parameters to four. Even so, this is better than the JA model with 5 parameters.

Alternative possibilities for the symmetric Gaussian distribution are skewed distributions. Especially the asymmetric Laplace distribution [27]

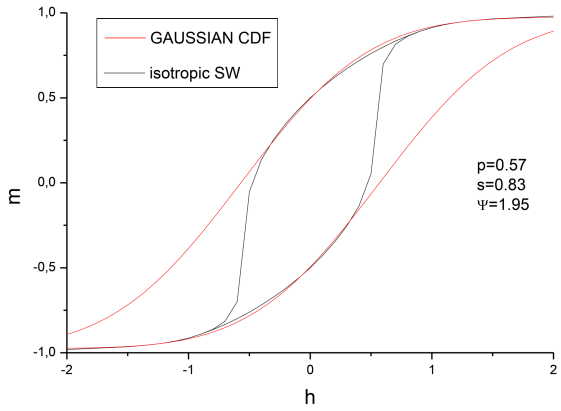

Fig. 8. SW isotropic hysteresis compared with the CDF Gaussian hysteresis model. Model parameters: $s = 0.83$, $\Psi = 1.95$, and $p = 0.57$.

could solve the problem of modelling hysteresis. Another possibility is the Weibull distribution [28]. The Gamma distribution is also an alternative [29].

The Gamma function was established by Euler after studying the Wallis formula for π. This gave its name to a family of integrals, i.e., the Wallis integrals, which are solved using the Gamma function [30].

6. Conclusions

The cumulative distribution functions (CDFs) can be used as the basis for hysteresis models. Here it is described how, using only two additional constant parameters, a sigmoidal hysteresis curve can be constructed. The model is useful in the interpretation of magnetic Barkhausen noise data. The model also has a clear physical meaning because it represents the distribution of the coercive field inside the sample. The model is first presented for a Gaussian distribution function, but it can be easily extended to Voigt, Lorentzian, or any other distribution.

An isotropic Stoner–Wohlfarth hysteresis was partially modelled by a three-parameter CDF Gaussian hysteresis, but only in the 1st and 3rd quadrants. Asymmetric distributions will provide better hysteresis adjustment, but these are 4-parameter models.

Acknowledgments

The authors thank Fundação de Amparo à Pesquisa do Estado do Rio de Janeiro) (FAPERJ) and Conselho Nacional de Desenvolvimento Científico e Tecnológico (CNPq).

References

[1] K. Chwastek, M. Najgebauer, P. Jabłoński, T. Szczegielniak, D. Kusiak, B. Koprivica, M. Rosić, S. Divac, *Appl. Sci.* **13**, 9134 (2023).

[2] S. Gryś, M. Najgebauer, *Measurement* **174**, 108962 (2021).

[3] K. Chwastek, P. Gębara, A. Przybył, R. Gozdur, A.P.S. Baghel, B.S. Ram, *Appl. Sci.* **13**, 12009 (2023).

[4] A. Przybył, P. Gębara, R. Gozdur, K. Chwastek, *Energies* **15**, 7951 (2022).

[5] M.B. de Souza Dias, F.J.G. Landgraf, K. Chwastek, *Energies* **15**, 1128 (2022).

[6] K. Chwastek, *Solid State Phenomena* **220–221**, 652 (2015).

[7] P. Jabłoński, M. Najgebauer, M. Bereźnicki, *Energies* **15**, 2869 (2022).

[8] J.A. Pérez-Benítez, J. Capó-Sánchez, J. Anglada-Rivera, L.R. Padovese, *J. Magn. Magn. Mater.* **288**, 433 (2005).

[9] M.F. de Campos, F.R.F. da Silva, J.F.C. Lins, E.F. Monlevade, M.A. Campos, J. Perez-Benitez, H. Goldenstein, L.R. Padovese, *IEEE Trans. Magn.* **49**, 1305 (2013).

[10] L.F.T. Costa, G. Gerhardt, F. Missell, M.F. De Campos, *Acta Phys. Pol. A* **136**, 740 (2019).

[11] H.J. Williams, W. Shockley, C. Kittel, *Phys. Rev.* **80**, 1090 (1950).

[12] S. Real Janasi, V.A. Lázaro-Colán, F.J.G. Landgraf, M.F. de Campos, *Mater. Sci. Forum* **775–776**, 404 (2014).

[13] M.F. de Campos, F.J.G. Landgraf, A.P. Tschiptschin, *J. Magn. Magn. Mater.* **226–230**, 1536 (2001).

[14] H. Lawton, K.H. Stewart, *Proc. R. Soc. London A* **193**, 72 (1984).

[15] F.A. Sampaio da Silva, D. Rodrigues, G.V. Concílio, J.A. de Castro, M.F. de Campos, *Mater. Sci. Forum* **899**, 554 (2017).

[16] P.G. Shewmon, *Transformations in Metals* Indo American Books, 2007.

[17] M.J. Sablik, D.C. Jiles, *IEEE Trans. Magn.* **29**, 2113 (1993).

[18] M.F. de Campos, M.J. Sablik, F.J.G. Landgraf, T.K. Hirsch, R. Machado, R. Magnabosco, C.J. Gutierrez, A. Bandyopadhyay, *J. Magn. Magn. Mater.* **320**, e377 (2008).

[19] M.F. de Campos, *Adv. Mater. Sci.* **20**, 16 (2020).

[20] M.F. de Campos S.A. Romero, F.J.G. Landgraf, F.P. Missell *J. Phys. Conf. Ser.* **303**, 012049 (2011).

[21] S.A. Romero, M.F. de Campos, J.A. de Castro, A.J. Moreira, F.J.G. Landgraf, *J. Alloys Compd.* **551**, 312 (2013).

[22] M.F. de Campos, S.A. Romero, L.M. da Silva, J.A. de Castro, "Shape Anisotropy and Magnetic Texture Determination in Anisotropic and Isotropic Alnico Magnets" *JOM* (2024).

[23] M.F. de Campos, S.A. Romero, J.A. de Castro, *J. Magn. Magn. Mater.* **564**, 170119 (2022).

[24] G.A. Paterson, X. Zhao, M. Jackson, D. Heslop, *Geochem. Geophys. Geosyst.* **19**, 1925 (2018).

[25] M. Ahsanullah, M. Shakil, B.M. Golam Kibria, *J. Pure Appl. Anal.* **5**, 63 (2019).

[26] S. Kotz, T.J. Kozubowski, K. Podgórski, *The Laplace Distribution and Generalizations*, Birkhäuser, Basel, 2001.

[27] Y.M. Amer, *Am. J. Appl. Math. Stat.* **6**, 239 (2018).

[28] A.W. Bydałek, R. Stępnik, P. Migas, *JOM* **76**, 548 (2024).

[29] M.V. Jambunathan, *Ann. Math. Stat.* **25**, 401 (1954).

[30] P. Sebah, X. Gourdon, "Introduction to the Gamma Function", 2002.

Selected papers presented at the 14th Symposium of Magnetic Measurements and Modelling SMMM'2023

Are There Any Alternatives for Rare-Earth Permanent Magnets?

M.F. de Campos*

Federal Fluminense University (UFF), Av. dos Trabalhadores 420 Volta Redonda RJ, 27255-125 Brazil

Doi: 10.12693/APhysPolA.146.26 *e-mail: marcosflavio@id.uff.br

Iron-based rare-earth permanent magnets are in high demand due to a large number of their applications, including electric cars and cell phones. Alternatives to rare-earth permanent magnets are discussed. Hard ferrites appear to be the simplest option for the replacement of rare-earth magnets due to their easy processing and low cost. The possibilities of replacing NdPrFeB magnets are discussed on the basis of the Bethe–Slater curve. Instead of developing alternatives to rare-earth magnets, research should focus on cheap production of Nd and Pr.

topics: permanent magnets, ferrite magnets, rare-earth magnets, Bethe–Slater curve

1. Introduction

Rare-earth permanent magnets are essential in many applications, for example, motors of electric cars [1], which may use 1–2 kg of NdFeB-type magnets per vehicle. These magnets are described by the stoichiometric formula $RE_2Fe_{14}B$, where RE (rare-earth) element is neodymium or praseodymium, and terbium or dysprosium can be added to increase the operation temperature. NdFeB magnets are also extensively used in loudspeakers of cell phones and in hard-disk motors [2]. The large number of applications has led to a large increase in demand, which has driven up the price of rare-earth elements Nd, Pr, Dy, and Tb.

Reports by the U.S. government [3] and the European Union [4, 5] indicate that electric vehicles and off-shore wind turbines can significantly increase the demand for rare-earth permanent magnets in the forthcoming years.

The present study discusses possible alternatives to rare-earth magnets of the REFeB family. Possible ferromagnetic compounds are discussed on the basis of the Bethe–Slater curve. From this analysis, RE–Fe alloys with nitrogen or Mn-based alloys with aluminum or bismuth appear to be good candidates. However, phase instability problems preclude large-scale commercial utilization of SmFeN or MnAl compounds.

SmCo-based magnets use cobalt, which is in high demand due to a large number of applications, such as batteries in electric cars. Therefore, cobalt-based magnets are not an option for replacement of NdFeB magnets due to the high price of cobalt.

The most clear alternatives for NdFeB are barium and strontium ferrite magnets, which have the formula $BaFe_{12}O_{19}$ or $SrFe_{12}O_{19}$. These magnets are oxides and have very simple processing. Whereas ferrite magnets are in the range of 3–7 US$/kg [6, 7], NdFeB magnets are at 50 US$/kg or more. Thus, although the maximum energy product of ferrite magnets is 10% of NdFeB, ferrite magnets are an option when there is no volume limitation. As ferrites are oxides, they have low resistivity and can be an interesting option in rotating machines.

Ores containing Pr and Nd, for example, monazite, are very abundant around the world. Thus, Nd and Pr can become cheap thanks to better technologies for concentrating rare-earth elements from ore, as well as improving rare-earth oxide separation methods [8, 9] for magnet manufacture.

2. Rare-earth elements

Rare-earth elements are not particularly rare, but they were first identified in an ore from Ytterby (Sweden) [10], which was considered rare at that time. Earth was the name given to the calcinated residues in the late XVIII century. Rare-earth elements are not very common in Europe, but as a phosphate monazite $REPO_4$, they are found in many parts of the world [11], for example, on the shores of Brazil and the United States [12] as monazite sand. Some rare-earth minerals, such as monazite and xenotime, have also a significant amount of thorium and uranium. Uranium has applications

TABLE I

Rare-earth proportion in some possible mining sites in Brazil compared with the Mountain Pass Mine in California, USA.

	CBMM Araxa (Minas Gerais) monazite	Morro do Ferro Poços de Caldas (Minas Gerais) monazite	Serra Verde (Goiás) ionic clay	Pitinga (Amazonas) xenotime	Caldeira Poços de Caldas (Minas Gerais) ionic clay	Mountain Pass (California, USA) bastnaesite
La_2O_3	30.6	26.6	32.1	0.5	46.8	33.79
CeO_2	44.1	48.7	4.2	5.0	18.3	49.59
Pr_6O_{11}	4.6	5.0	5.9	0.7	6.5	4.12
Nd_2O_3	15.3	13.7	19.3	2.2	17.9	11.16
Sm_2O_3	1.58	1.5	3.3	1.9	2.0	0.85
Eu_2O_3	0.38	0.4	0.2	0.2	0.5	0.105
Gd_2O_3	1.28	0.9	3.2	4.0	1.4	0.21
Tb_4O_7	0.12	0.1	0.5	1.0	0.2	0.016
Dy_2O_3	0.42	0.5	3.2	8.7	0.8	0.034
Ho_2O_3	0.06	0.1	0.7	2.1	0.1	0.004
Er_2O_3	0.15	0.2	2.0	5.4	0.3	0.006
Tm_2O_3	0.01	–	0.3	0.9	0	0.002
Yb_2O_3	0.06	0.2	1.8	6.2	0.3	0.002
Lu_2O_3	0.01	0.02	0.3	0.4	0	< 0.01
Y_2O_3	1.29	2.0	23.0	60.8	4.7	< 0.13

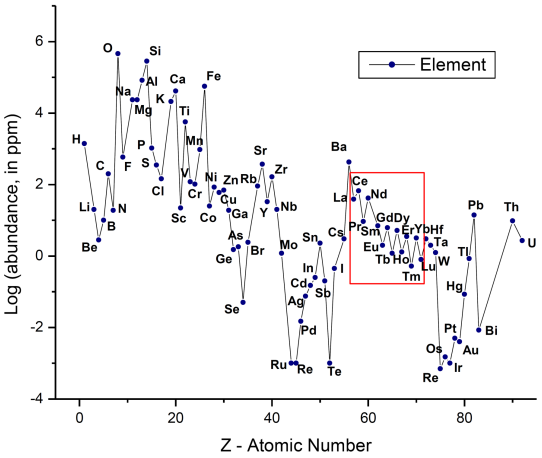

Fig. 1. Abundance of elements in the crust of Earth. In the red box — a lanthanide series. Elements with odd atomic numbers are less abundant, which confirms the Oddo–Harkinks rule.

in nuclear plants, but thorium has virtually no applications, and thorium disposal is usually a significant and expensive problem.

Figure 1 was constructed from data provided by Lide [13]. Light rare earths (Ce, La, Pr, and Nd) are abundant, but heavy rare-earth elements such as Tb, Ho, and Eu are scarce. This is reflected in the ores, as can be seen in Table I. The data in Table I was presented in a previous study [14], and now it is updated with data from the Caldeira project in Poços de Caldas (Minas Gerais, Brazil) [15]. For comparison, data from the Mountain Pass mine near Las Vegas in the United States [16] is also included. After the bankruptcy of the Mountain Pass mine in 2015 [17], many rare-earth mining projects

TABLE II

Polarization of saturation, anisotropy field, and Curie temperature of 2:14:1 compounds.

	J_s [T]	$\mu_0 H_A$ [T]	T_C [°C]	Ratio $\mu_0 H_A / J_s$
Y	1.41	2.0	298	1.4
Ce	1.17	2.6	150	2.2
Pr	1.56	8.7	296	5.6
Nd	1.6	7.7	312	4.8
Gd	0.89	2.5	387	2.8
Tb	0.70	22	347	31.4
Dy	0.71	15	325	21,1
Ho	0.81	7.5	300	9.3

in Brazil were either postponed or canceled. Many projects have been announced in Brazil recently, i.e., in 2023, aiming at the extraction of rare-earth elements from the ionics clays. Deposits containing ionic clays have gained much attention recently [18], and one of the reasons is the larger amount of heavy rare-earth elements, as can be seen in Table I. In contrast, the Mountain Pass bastnaesite mine has only traces of dysprosium and terbium (see Table I). It can also be observed in Table I that most of the ores contain Pr and Nd in an approximate proportion of 1:3, confirming the Oddo–Harkins rule [19]. Nd and Pr are not usually separated in the production of a magnet, and this alloy is commercially available under the name didymium. The separation of neodymium and praseodymium is a very difficult task due to the chemical similarities between these elements [20–24].

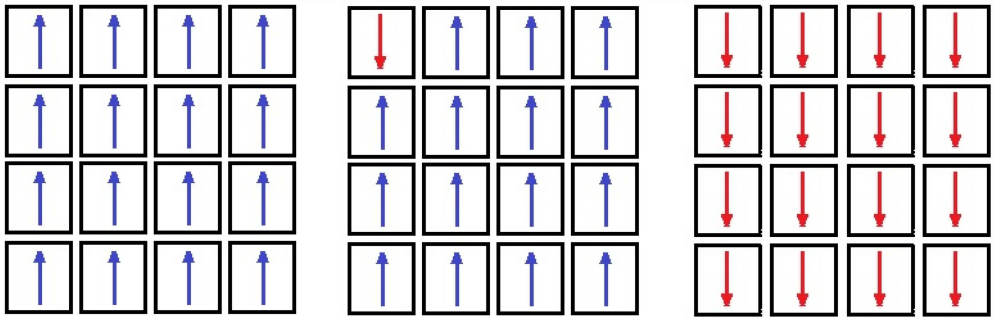

Fig. 2. Chain effect. Reversal of magnetization in a given grain provokes a chain or cascade effect, with the inversion of the magnetization in the neighbor grains. A high ratio $\mu_0 H_A/J_s$ avoids the chain effect.

TABLE III

Chemical composition of some magnets found in motors of electric vehicles, according to S. Munro [35].

	Tesla Model 3 magnet	"standard automotive magnet"
Dy	1.19	3.47
Nd	23.01	19.90
Pr	7.70	6.67
Sm	1.42	0.86
Fe	57.38	62.51
Co	1.72	1.79
Cu	2.11	1.10
Al	0.96	1.37
O	4.50	2.33

Table II was compiled on the basis of several sources [25–30]. The three most relevant intrinsic properties are T_C — Curie temperature, J_s — polarization of saturation, H_A — anisotropy field, and M_s — magnetization of saturation. Dy, Ho, and Gd are commercially available as ferroalloys, and the only explanation for this is that they are used as alloying elements in NdPrFeB magnets. Alloying iron reduces the melting temperature, making it easier to obtain Fe–Dy, Fe–Gd, and Fe–Ho rather than the pure metals Dy, Ho, and Gd. Dysprosium and terbium are essential for increasing the operation temperature in NdPrFeB magnets. Holmium is a cheap alternative to dysprosium. Gd increases the Curie temperature, as can be seen in Table II, but it significantly reduces the anisotropy field, and thus, the Gd addition is used in the cheaper grades. The addition of cerium has some significant problems as it reduces both T_C and H_A, i.e., Ce reduces the operation temperature and coercivity. Also, because Ce has a lower magnetization of saturation, it "dilutes" the magnetic moment, and this implies a larger volume of the magnet. In conclusion, cerium-based magnets cannot compete with barium or strontium magnets because they would be very expensive given the similar properties of ferrites at room temperature.

TABLE IV

Magnet mass per motor of electric vehicle.

Vehicle	Magnet mass [kg]
Honda Accord M	0.755
Honda Accord G	1.24
Nissan Leaf	1.895
Toyota Prius 2010	0.768
Toyota Prius 2004	1.232
Lexus LS 600h	1.349
Toyota Camry	0.928
Toyota Prius 2017	0.544
BMW i3 2016	2
Tesla Model 3	1.783
Jaguar I-PACE	1.85
Volkswagen ID.3	2.5
Chevrolet Volt	1.57

The non-written rule is that the anisotropy field should be well above saturation to avoid a chain effect. For example, the ratio $\mu_0 H_A/J_s$ for $Nd_2Fe_{14}B$ is 4.8 (see Table II). It is very difficult to find phases with such high ratios. One of them are the $BaFe_{12}O_{19}$ ferrites, with $H_A = 16$ kOe [31] and $M_s = 4.8$ kG [32], where such ratio is 3.3 and also $T_C = 450$°C. In addition to the chain effect [33] exemplified in Fig. 2, grain size is another very relevant variable. The grain should be the size of a single domain. Thus, melt-spinning is a common practice used for hard magnetic materials to obtain nanocrystalline magnets. Another possibility is shape anisotropy [34], which allows the use of even very soft phases as hard magnetic materials.

Munro [35] mentioned the chemical composition of magnets used in electric vehicles. It is observed in Table III that such a magnet has a 1:3 Pr/Nd proportion and contains some dysprosium (and not Ho, Gd, or Ce). Table IV is an update of the table of a previously presented study [36]. Table IV shows that the electric vehicle industry has a clear preference for motors with magnets in the rotor. This saves energy and increases motor efficiency,

resulting in increased autonomy of the electric car. However, high-efficiency motors without magnets are possible, as in the old Tesla Model S and Audi e-tron [37]. General Motors Company (GM) tried a motor with ferrite in the 2015 Chevrolet Volt [38], but gave preference for NdFeB-type in later versions[†1]. Motors with ferrite-based rotors are less efficient than those with NdFeB-based rotors [39, 40].

In many designs, the magnets are inserted in the rotor following a "double V" topology [41], which allows for a reduction of the cogging torque [42], a typical problem at low speeds. Tesla made a significant innovation with the carbon-wrapped rotor [43], enabling the elimination of the radial and tangential iron ribs of the rotor, thus avoiding problems of magnetic flux leakage [44, 45]. These high-efficiency designs in general request NdFeB-type magnets, using 0.5–2.5 kg of magnets per motor, as can be seen in Table IV.

Also, wind turbines request NdFeB-type magnets, especially for giant off-shore turbines [46, 47]. Thus, the question is about the possibility of replacing rare-earth magnets with other types of magnets. Although some elements are truly scarce, such as terbium and dysprosium, light rare-earth elements such as Nd and Pr are very common, and monazite, for example, is a very common ore, found in almost the entire world. Thus, research should be directed towards cheaper production methods for Nd and Pr, as well as avoiding Tb and Dy, and this can be obtained with better designs that allow lower operation temperatures.

3. Alternatives for rare-earth permanent magnets

Before discussing possible phases, it is worth adding that a relevant hint can be given by the Stoner–Wohlfarth (SW) model [48]. The energy E is here

$$E = -HM_s\cos(\theta-\alpha) + K_1\sin^2(\theta), \tag{1}$$

where K_1 is the magnetocrystalline anisotropy. The angle between the external field H and the crystal easy axis is α. The angle between M_s and the easy axis is θ. By making $\mathrm{d}E/\mathrm{d}\theta = 0$ and $\mathrm{d}^2E/\mathrm{d}\theta^2 = 0$, the critical field h_c for irreversible rotation is obtained as

$$h_c = \frac{(1-t^2+t^4)^{1/2}}{1+t^2}, \tag{2}$$

and it is a function of t, where t relates to α by [49]

$$t = (\tan(\alpha))^{1/3}. \tag{3}$$

[†1]Chevrolet gave similar names for different vehicles; Chevrolet Volt is a hybrid, whereas Bolt is a full battery car.

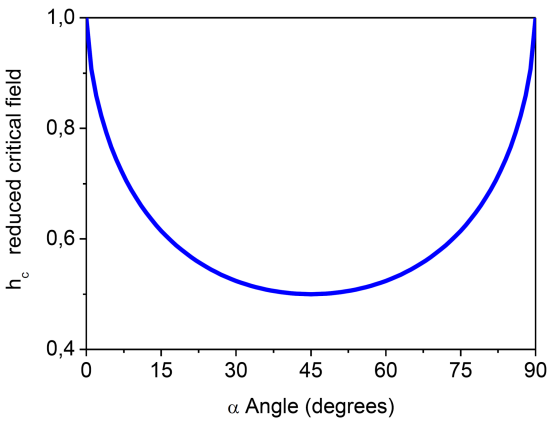

Fig. 3. Reduced field h_c as a function of angle α. According to the Stoner–Wohlfarth (SW) model, there are regions of reversible and irreversible rotation. For $-0.5 \le h_c \le 0.5$, there is always reversible rotation.

TABLE V

Polarization of saturation and anisotropy field for hard ferrites, Mn-based compounds, and nitrogen-related compounds.

	Reference	J_s [T]	$\mu_0 H_A$ [T]	Ratio $\mu_0 H_A/J_s$
MnAl	[50]	0.62	4.0	6.4
MnBi	[50]	0.78	3.7	4.7
$BaFe_{12}O_{19}$	[50, 51]	0.48	1.6	3.4
$SrFe_{12}O_{19}$	[50, 51]	0.46	1.95	4.3
α''-$Fe_{16}N_2$	[52]	2.68	1.7	0.6
$Sm_2Fe_{17}N_3$	[53]	1.54	14	9.1

According to Fig. 3, a useful criterion is that the suitable phases for permanent magnets should fulfill $\mu_0 H_A/J_s > 2$ to avoid the chain effect. This limits considerably the possible candidate phases.

Table V was constructed mainly based on data from Luborsky [50], and the anisotropy values for Ba and Sr ferrites were recently determined [51] to be very close to the values reported by Luborsky [50]. Also, data for nitrogen compounds α''-$Fe_{16}N_2$ [52] and $Sm_2Fe_{17}N_3$ [53] are also included in Table V. It is observed in Table V that the manganese compounds MnAl and MnBi are appearing as possibilities for replacing hard ferrites. Thus, among other possible candidates to replace NdFeB and ferrites, the main other families are [54] $Fe_{16}N_2$, MnAl and MnBi, and $Sm_2Fe_{17}N_x$ magnets, because a high anisotropy field is an essential condition. Again, it is worth recalling the criterion $\mu_0 H_A/J_s > 2$, and this criterion is satisfied by $Sm_2Fe_{17}N_x$, MnBi, and MnAl. The permanent magnet market in 2022 [55] shown in Table VI, in addition to ferrites and NdFeB, only mentions Alnico and SmCo.

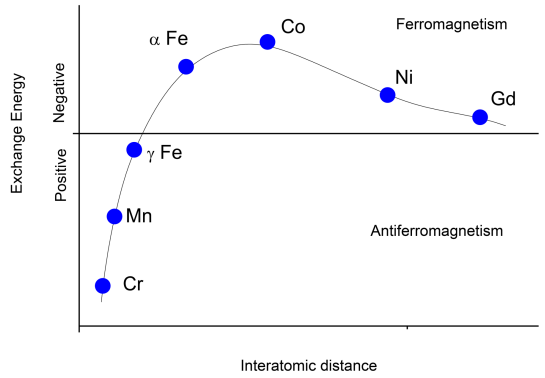

Fig. 4. The Bethe–Slater curve. Scheme based on Hosford [58].

TABLE VI

Percentage of the 23 US$ billion world permanent magnet market in 2022 [55].

Type of magnet	% of the market
sintered NdFeB	58%
bonded NdFeB	6%
sintered ferrite	26%
flexible ferrite	4%
injection molded ferrite	3%
SmCo	1%
Alnico	1%
others	1%

According to data in Table VI, only NdFeB and ferrites are disputing the market. The reason is simple, namely ferrite is very cheap, and other materials can not compete in terms of cost. Alnico has some niche applications, essentially sensors, and SmCo 2:17 has some high-temperature applications. $SmCo_5$ has been almost completely replaced by SmCo 2:17, i.e., SmCoFeCuZr. The fluctuation of cobalt price also precludes a larger usage of Co-based magnets such as SmCo 2:17, $SmCo_5$, and Alnico. In $SmCo_5$ magnets, 2/3 of the weight is cobalt. As can be seen in Table VI, Alnico is the only commercial magnet with a coercivity mechanism due to shape anisotropy [56, 57].

Figure 4 is based on the Hosford version [58] of the Bethe–Slater curve. It is semi-empirical, but it is still used for the interpretation of experimental results [59]. The Bethe–Slater curve is considered to be able to explain why stainless steels are not ferromagnetic. For example, the interatomic distance in FCC iron is smaller: for BCC iron — PF = 0.68, for FCC iron — PF = 0.74, where PF = packing factor. It follows that stainless steel 304 with 18% Cr and 8% Ni is not ferromagnetic.

Essentially, it is suggested in Fig. 4 that increasing the separation between Fe atoms and between Mn atoms can make them ferromagnetic. In manganese-based alloys, this is achieved by alloying Mn with large atoms: Bi, Al, and Ga. For iron-based alloys, this is achieved by using interstitial elements, such as boron or nitrogen. Thus, all suggestions by the Bether-Slater curve were already exploited experimentally. Heusler alloys are ferromagnetic, but their alloying elements were diamagnetic or paramagnetic, as can be seen in the classical Cu_2MnAl composition [60]. The Bether–Slater curve also suggests rare-earth compounds, as can be noted from the presence of gadolinium in Fig. 4.

However, to be permanent magnet, the candidate phase needs to have high magnetocrystalline anisotropy in addition to ferromagnetism itself. Besides, the phase diagram is decisive, and so metastable phases are usually not suitable for commercial application due to lack of reproducibility.

The commercial production of Mn-based alloys has several problems: corrosion [61], metastable phases [62], and difficult processing. In 1980, MnAlC was commercially available from Matsushita, but its properties were hardly comparable with Alnico magnets and had the drawback of expensive processing [63]. The recoil curves presented by Abdelnour et al. [63] are similar to others found in SmCo 2:17 magnets [64], SmCoCu [65], and barium ferrites [31] — and this implies that all of them are the single domain size. This characteristic is essential and explains why many studies employ melt-spinning. The reason is obtaining single-domain particle size because this is a condition that allows to maximize the coercivity.

Approximately 60 years ago, the Phillips Company did intense research to develop commercial MnAl and MnBi magnets [62], reporting for MnAl coercivity up to 6 kOe. However, in MnAl alloys, the magnetic phase is metastable, and manganese alloys oxidize easily, making the production of magnets very difficult.

Lodex was a material that used the principle of shape anisotropy [32]. It was commercially available but had a coercivity of only $\sim$ 1 kOe [66]. Daido Steel has a bonded magnet made with melt-spun $Sm_2Fe_{17}Nx$ alloy in the catalog. A typical problem in nitrogen-based alloys is the lack of reproducibility. The nitrogen expands the lattice. To reduce internal stresses, the nitrogen atoms are expelled. Thus, phase instability is a significant issue in nitrogen magnetic alloys.

As almost all the possibilities given by the Bethe–Slater curve [67–69] were already tested, replacing NdFeB or barium and strontium ferrites is indeed a very difficult task.

4. Conclusions

It is difficult to find permanent magnetic materials that can compete with ferrites (cost) or NdFeB (performance). SmCo and Alnico still have

some niche applications. These are the principal 4 families of commercial permanent magnets. The other main candidates are or were commercially available.

Lodex and MnAlC were manufactured commercially. SmFeN is also manufactured commercially. However, these alternatives have problems competing with traditional materials: Alnico, SmCo, and especially ferrites and NdFeB. For a rare-earth free phase to be able to compete with ferrites, it is necessary that it has at least 50% higher H_A and 50% M_s than Sr and Ba ferrites. Except for MnBi and MnAl, such materials do not exist.

The Bether–Slater curve provides suggestions for phases that can be used as permanent magnets. But these suggestions were also exhausted.

Instead of researching new materials to replace NdPrFeB magnets, research should focus on cheap production of Nd and Pr. There are immense deposits of monazite in the world, containing significant amounts of Nd and Pr. Terbium and dysprosium, on the other hand, will always be scarce and expensive.

The ratio $\mu_0 H_A/J_s$ is suggested as a tool to evaluate the possibility of a given phase to be a candidate for a permanent magnet. The criterion is $\mu_0 H_A/J_s > 2$ to avoid the chain or cascade effect.

Acknowledgments

The author thanks Fundação de Amparo à Pesquisa do Estado do Rio de Janeiro) (FAPERJ) and Conselho Nacional de Desenvolvimento Científico e Tecnológico (CNPq).

References

[1] G. Zorpette, "What Is Tesla's Mystery Magnet?" *IEEE Spectrum* (2023).

[2] X. Lim "Global Initiative Mines Retired Hard Disk Drives for Materials and Magnets" *IEEE Spectrum* (2019).

[3] B.J. Smith, M.E. Riddle, M.R. Earlam, C. Iloeje, D. Diamond, *Rare Earth Permanent Magnets: Supply Chain Deep Dive Assessment*, U.S. Department of Energy, 2022.

[4] P. Alves Dias, S. Bobba, S. Carrara, B. Plazzotta, *The Role of Rare Earth Elements in Wind Energy and Electric Mobility*, EUR 30488 EN, Publications Office of the European Union, Luxembourg 2020, JRC122671.

[5] S. Carrara, S. Bobba, D. Blagoeva et al., *Supply Chain Analysis and Material Demand Forecast in Strategic Technologies and Sectors in the EU – A Foresight Study*, Publications Office of the European Union, Luxembourg 2023, JRC132889.

[6] M.F. de Campos, D. Rodrigues, J.A. de Castro, *Mater. Sci. Forum* **912**, 106 (2018).

[7] J. McKenzie, "Powering the Green Economy: The Guest for Magnets without Rare Earths", Physics World, 2023.

[8] S.V.S.H. Pathapati, M.L. Free, P.K. Sarswat, *Processes* **11**, 2070 (2023).

[9] M. Traore, A. Gong, Y. Wang et al., *J. Rare Earths* **41**, 182 (2023).

[10] C.K. Jørgensen, in: *Handbook on the Physics and Chemistry of Rare Earths*, Vol. 11, 1988, Ch. 75, p. 197.

[11] S.-L. Liu, H.-R. Fan, X. Liu, J. Meng, A.R. Butcher, L. Yann, K.-F. Yang, X.-C. Li, *Ore Geol. Rev.* **157**, 105428 (2023).

[12] J. Merle, *Monazite deposits of the southeastern Atlantic States*, USGS, 1953.

[13] D.R. Lide, *CRC Handbook of Chemistry and Physics*, 90th ed. CRC Press/Taylor and Francis, Boca Raton (FL) 2010.

[14] M.F. de Campos, in: *Proc. of the 25th Int. Workshop on Rare Earth Permanent Magnets and Advanced Magnetic Materials and Their Applications (REPM 2018)*, Beijing 2018, A0400-01.

[15] M. de Carvalho, *Projeto Caldeira — Desenvolvendo o Depósito de ETR de Maior Teor no Mundo*, 2013.

[16] S.B. Castor, *Can. Mineral.* **46**, 779 (2008).

[17] SEC Technical Report Summary, Pre-Feasibility Study Mountain Pass Mine, San Bernardino County (CA), SRK Consulting, 2022.

[18] P. Hellman, *Rare Earths Assessment of Ionic Adsorbed Deposits*, 2023.

[19] J.Y. Galarza, J. Meléndez, A. Karakas, M. Asplund, D. Lorenzo-Oliveira, *Mon. Not. R. Astron. Soc. Lett.* **502**, L104 (2021).

[20] X. Guangxian, X. Jimei *New Frontiers in Rare Earth Science and Applications: Proceedings of the International Conference on Rare Earth Development and Applications, Beijing, 1985.* Academic Press Inc, 1985.

[21] X. Wang, K. Huang, W. Cao, P. Sun, N. Sui, W. Song, H. Liu, *J. Rare Earths* **38**, 203 (2020).

[22] V.V. Belova, *Theor. Found. Chem. Eng.* **51**, 599 (2017).

[23] S. Gao, *Inorg. Chem. Front.* **8**, 10 (2021).

[24] J. Lucas, P. Lucas, T. Le Mercier, A. Rollat, W.G. Davenport, *Rare Earths: Science, Technology, Production and Use*, Elsevier, 2014.

[25] Z. Chen, Y.K. Lim, D. Brown, *IEEE Trans. Magn.* **51**, 2102104 (2015).

[26] J.F. Herbst, M.S. Meyer, F.E. Pinkerton, *J. Appl. Phys.* **111**, 07A718 (2012).

[27] B. Zhou, Y. Liu, S. Li, W. Fan, X. Liao, J. He, H. Yu, Z. Liu, *J. Rare Earths* **41**, 1058 (2023).

[28] S. Hirosawa, Y. Matsuura, H. Yamamoto, S. Fujimura, M. Sagawa, H. Yamauchi, *J. Appl. Phys.* **59**, 873 (1986).

[29] J.F. Herbst, *Rev. Mod. Phys.* **63**, 819 (1991).

[30] E.A. Périgo, I. Titov, R. Weber, D. Honecker, E.P. Gilbert, M.F. de Campos, A. Michels, *J. Alloys Compd.* **677**, 139 (2016).

[31] M.F. de Campos, F.A. Sampaio da Silva, S.A. Romero, J.A. de Castro, in: *14th Int. Symp. on Linear Drivers for Industry Applications (LDIA)*, 2023.

[32] B.D. Cullity, C.D. Graham Jr., *Introduction to Magnetic Materials*, 2nd ed., Wiley, Hoboken (NJ) 2009.

[33] M.F. de Campos, J.A. de Castro *J. Rare Earths* **37**, 1015 (2019).

[34] M.F.de Campos, *Mater. Sci. Forum* **869**, 591 (2016).

[35] S. Munro, *Comparing 10 Leading EV Motors* (free webcast), 2020.

[36] M.F. de Campos, J.A. de Castro, in: 2019-Sustainable Industrial Processing Summit, Vol. 13, 2019, p. 103.

[37] R. Thomas, H. Husson, L. Garbuio, L. Gerbaud, in: 17th Int. Conf. on Electrical Machines, Drives and Power Systems (ELMA), Sofia 2021.

[38] S. Jurkovic, K. Rahman, B. Bae, N. Patel, P. Savagian, in: *2015 IEEE Energy Conversion Congress and Exposition (ECCE)*, IEEE, 2015.

[39] Q. Ma, A. El Refaie, B. Lequesne, *IEEE Trans. Ind. Appl.* **56**, 1452 (2020).

[40] J. Frevert, in: KMT 2022; 13. GMM/ETG-Symposium, Linz, 2022.

[41] J.R. Hendershot, Electric Traction Machine Choices for Hybrid & Electric Vehicles, Florida International University, 2014.

[42] E. Dalla, Low Cogging Torque, "High Torque Density Traction Motor", US Patent 2020/0127508 A1, 2020.

[43] L.E. Olsen, D. Nelson, K. Laskaris, H. Ge, E. Filip, C. Vega, P. Pellerey, V. Papanikolaou, "Permanent Magnet Motor with Wrapping", World Patent WO2021225902A1, 2021.

[44] J. Binder, M. Silvagni, S. Ferrari, B. Deusinger, A. Tonoli, G. Pellegrino, in: *2023 IEEE Workshop on Electrical Machines Design, Control and Diagnosis (WEMDCD)*, 2023.

[45] M. Clauer, A. Binder, *Elektrotech. Inftech.* **140**, 302 (2023).

[46] A. Bensalah, G. Barakat, Y. Amara, *Energies* **15**, 6700 (2022).

[47] G.E. Barter, L. Sethuraman, P. Bortolotti, J. Keller, D.A. Torrey, *Appl. Energy* **344**, 121272 (2023).

[48] E.C. Stoner, E.P. Wohlfarth, *IEEE Trans. Magn.* **27**, 3475 (1991).

[49] M.F de Campos, J.A de Castro, *Acta Phys. Pol. A* **136**, 737 (2019).

[50] F.E. Luborsky, *J. Appl. Phys.* **37**, 1091 (1966).

[51] M.F. de Campos, S.A. Romero, D. Rodrigues, *Mater. Sci. Forum* **881**, 128 (2016).

[52] M. Mehedi, Ph.D. Thesis, University of Minnesota, Twin Cities, 2018.

[53] D. Liang, W. Yang, X. Wang et al., *AIP Adv.* **13**, 025104 (2023).

[54] J. Cui, M. Kramer, L. Zhou, F. Liu, A. Gabay, G. Hadjipanayis, B. Balasubramanian, D. Sellmyer, *Acta Mater.* **158**, 118 (2018).

[55] J. Ormerod, A. Karati, A.P.S. Baghel, D. Prodius, I.C. Nlebedim, *Sustainability* **15**, 14901 (2023).

[56] E.P. Wohlfarth, *Adv. Phys.* **8**, 87 (1959).

[57] E.C. Stoner, *Rep. Prog. Phys.* **13**, 83 (1950).

[58] W. Hosford, *Physical Metallurgy*, 2nd ed., CRC Press, 2010.

[59] A. Perrin, S. McCall, M. McElfresh, D.E. Laughlin, M.E. McHenry, *J. Phase Equilib. Diffus.* **42**, 617 (2021).

[60] S. Tavares, K. Yang, M.A. Meyers, *Prog. Mater. Sci.* **132**, 101017 (2023).

[61] C. Zhou, M. Pan, *Int. J. Electrochem. Sci.* **14**, 10387 (2019).

[62] A.J.J. Koch, P. Hokkeling, M.G. von der Steeg, K.J. de Vos, *J. Appl. Phys.* **31**, S75 (1960).

[63] Z. Abdelnour, H. Mildrum, K. Strnat, *IEEE Trans. Magn.* **17**, 2651 (1981).

[64] S.A. Romero, D. Rodrigues Jr., T. Germano, R. Cohen, J.A. de Castro, M.F. de Campos, *Appl. Nanosci.* **13**, 6353 (2023).

[65] S.A. Romero, A.J. Moreira, F.F.G. Landgraf, M.F. de Campos, *J. Magn. Magn. Mater.* **514**, 167147 (2020).

[66] S. Constantinides, "Manufacture of Modern Permanent Magnet Materials", 2014.

[67] V. Chaudhary, R. Ramanujan, *Sci. Rep.* **6**, 35156 (2016).

[68] E. Burzo, *Rom. Rep. Phys.* **63**, Supplement, 1316 (2011).

[69] J. Kitagawa, K. Sakaguchi, T. Hara, F. Hirano, N. Shirakawa, M. Tsubota, *Metals* **10**, 1644 (2020).

Selected papers presented at the 14th Symposium of Magnetic Measurements and Modelling SMMM'2023

The Concept of Heat and the Hysteresis Loop: The Evolution of the Losses Models

M.F. de Campos*

Federal Fluminense University (UFF), Av. dos Trabalhadores 420, Volta Redonda RJ, 27255-125 Brazil

Doi: 10.12693/APhysPolA.146.34 *e-mail: marcosflavio@id.uff.br

The origin of iron losses in ferromagnetic materials is commented on, starting with the definition of heat. The different possible dissipative mechanisms inside a hysteresis curve, which originate heat, as well as its relationship to the magnetic Barkhausen noise, are discussed in detail. The loss separation model is better explained by using the concept of heat, especially to understand losses when eddy currents are small (at very low frequencies).

topics: losses, hysteresis, heat, dissipative processes

1. Introduction

Since the time of Fourier [1], heat has been discussed mathematically. The laws derived by Kirchhoff and Fick are analogous to Fourier's law of heat transmission. Nowadays, heat is described essentially as "jumping atoms." In other words, heat is explained as kinetic energy. Increasing temperature manifests itself in an increasing "jumping frequency" of atoms.

Atoms were a controversial subject in the XIX century. It was only in the XX century, after the study of the Brownian movement by Einstein, Smoluchowski, and Perrin, that the concept of atoms was widely accepted. This also influenced the way heat was defined. As the definitions of heat in the XIX century avoided mentioning the controversial atoms, the concept of heat in the XIX century was not very well formulated.

Here, the evolution of loss models over time is discussed, starting with the earlier XIX-century models of Heaviside [2] and J.J. Thomson [3]. As the area of the hysteresis loop is heat, the concept of atoms is important to understand the different dissipative processes that may happen inside the hysteresis cycle, as well as the loss separation. Epstein — the inventor of the Epstein frame — used loss separation as early as 1907 [4]. Anomalous losses were discussed already in the 1930s by Legg, under the name "residual" instead of "anomalous" [5]. The name "residual losses" persists to this day for soft ferrites. Another relevant development is Prigogine's principle of minimum energy production. Thus, domain walls can be understood as "dissipative structures" according to Prigogine's theory [6]. As defined by Prigogine, self-organization is possible without violating the 2nd law of thermodynamics. Domain walls are thus interpreted as structures with self-organization.

In the present study, the different possible dissipative mechanisms inside a hysteresis curve (i.e., heat) are discussed in detail, as well as its relationship with the magnetic Barkhausen noise (MBN), including the mathematical relationship between MBN and hysteresis.

2. The concept of heat

The area of the hysteresis loop is heat. Therefore, a good knowledge of what heat is is relevant for understanding losses. Here, the concept of heat will be briefly reviewed, with special attention paid to historic developments.

The discussion about heat has a long history. It can be traced back to Empedocles of Agrigento, who correctly concluded the existence of air and vacuum [7]. However, the definitions of Empedocles about water, fire, and earth were incorrect. Only after Lavoisier [8], it becomes clear that water is H_2O [9], and that fire is the result of combustion, a reaction involving oxygen. And about the earth? It seems that everything else was described by Empedocles as "earth."

Evidently, in the Empedocles theory, atoms are missing. Atoms were a controversial subject even at the start of the XX century. The concept of atoms by Demokritos was essentially mathematical: When solving an integral $f(x) = \int \mathrm{d}x$, $\mathrm{d}x$ can not be

zero. Thus, dx should be "non-divisible" or "a-tom." This was important for the Archimedes exhaustion method, and the modern version of it is named a Riemann sum [10].

One of the most difficult concepts in science is energy [11]. Energy is never absolute, it always needs a reference. Energy always is a variation, ΔE. Thus, energy is not positive or negative. Instead of writing $E = m\,g\,d$ (m is the mass, g is the gravity acceleration, d is the height), it is more accurate to express $\Delta E = mg\,\Delta d$.

The XX century started with two equations [12], i.e.,

$$E = k_{\mathrm{B}}T, \tag{1}$$

$$E = hf, \tag{2}$$

where T is the temperature, k_{B} is the Boltzmann constant, f is the frequency, and h is the Planck constant. The Boltzmann constant first appeared in the paper by Planck [13, 14]. In two simple expressions, i.e., (1) and (2), one makes use of the Planck constant, and another makes use of the Boltzmann constant.

In (1), what is implicit is the concept of atoms. According to (1), the temperature corresponds to the energy. Atoms, however, were a subject of intense discussion in the early XX century [15], and Mach used to ask "did you see one?" Much later, Binnig saw atoms [16].

As aforementioned, atoms were a very controversial subject throughout the XIX century. It was only in the XX century, after the study of the Brownian movement by Einstein, Smoluchowski, and Perrin, that the concept of atoms was widely accepted. This fact turned out to have an impact on the definition of heat. As the definitions of heat in the XIX century avoided mentioning controversial atoms, the concept of heat was not perfectly formulated. For example, Maxwell's 1872 definition of heat [17] is obsolete because Maxwell avoided controversial atoms at that time [18]. On the other hand, (1) translates heat into "jumping atoms" (or oscillating atoms). Maxwell equations were used long before atom theory was accepted, for example by Heaviside to understand losses and the skin effect [19, 20].

From chemistry, the idea of an isomer indirectly suggests the existence of atoms [21]. Maybe the first indirect evidence of atoms is in the Fourier equation for heat. Fourier is cited by Fick [22], which also cites Ohm [23]. Fourier profoundly influenced physicists of the XX century, including Maxwell [24] and Lord Kelvin [25]. Therefore, Ohm applied the Fourier heat equation [23] to the diffusion of electricity in a conductor.

The Fick 1st law is given by

$$J = -D\frac{\partial C}{\partial x} \tag{3}$$

for the one-dimensional case. Here, J is the flux, D is the diffusion coefficient, and C is the concentration; (3) is for the steady state.

The 2nd Fick law given by

$$\frac{\partial C}{\partial t} = \frac{\partial}{\partial x}\left(D\frac{\partial C}{\partial x}\right) \tag{4}$$

is valid when there is a variation of the concentration C with time. If D is independent of concentration, (4) becomes

$$\frac{\partial C}{\partial t} = D\frac{\partial^2 C}{\partial x^2}. \tag{5}$$

The diffusion coefficient D is given by

$$D = D_0 \exp\left(-\frac{Q}{RT}\right), \tag{6}$$

where D_0 is the pre-exponential factor [26], Q is the enthalpy variation, R_{gas} is the gas constant, and T is temperature. There is a relationship between R_{gas} and k_{B}, given by $R_{\mathrm{gas}} = k_{\mathrm{B}}N_{\mathrm{A}}$ (where N_{A} is Avogadro's number). Thus, the energy barrier given by (1) appears in (6). The same mathematics for solving heat problems can be used for solving the problems of atom diffusion in solids [27].

One of the last anti-atomists, Ostwald, surrendered to atom theory in 1908 [28]. Ostwald is famous in materials science due to the "Ostwald Ripening" — the phenomenon responsible for precipitation hardening in aluminum alloys [29], a method still used today for strengthening the wings of airplanes [30]. Ostwald was the 1909 Nobel Prize laureate in chemistry for catalysis [31], even with a lack of perception of the actual origin of this phenomenon.

Possibly the most relevant fact here are the dates on which the papers were published: Einstein, 1905 [32]; Smoluchowski, 1906 [33]; Perrin, 1910 [34]. This means that atoms were still debatable in 1908 [35]. Thus, other areas of science, such as for example electrical engineering, neglected the controversial atoms, especially until 1910.

Existence of atoms means the non-continuity of matter. Matter can not be treated as a continuum if atoms do exist. Besides, a complete revolution will occur in 1914 [36], with the X-ray diffraction and a series of implications. Then, the crystalline structure could be determined, and the atoms could be approximated by a sphere (an ellipsoid, in fact) to determine the crystalline structures. This is named the "rigid sphere model" in which atoms are treated as macroscopic spheres [37].

Then, after 1914, it becomes clear that "jumping atoms" store energy or temperature in the crystalline structure, as given in (1). The higher the jumping frequency, the higher the temperature. Nevertheless, heating as the Joule effect $P = RI^2$ was described much earlier, in 1840 (here P is power, I is current, and R is resistance) [38].

Noise is sound. Sound is vibration. Thus, this discussion is also useful for understanding MBN — the magnetic Barkhausen noise [39]. The noise indicates dissipative processes, namely "jumping atoms" (or oscillating atoms). In the analysis of MBN by

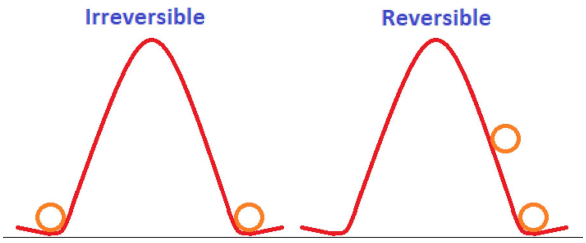

Fig. 1. Ball-hill model for reversible and irreversible processes.

Stoner [40], there is no relationship between the hysteresis curve and MBN [41]. Noise of transformers [42] is an analogous phenomenon, indicating that the loss of energy produces sound. As aforementioned, noise is sound and sound is vibration.

As an example of the similarity between the Fourier heat equation and electromagnetism, Lord Kelvin's theory (1854) for the "telegraph equation" was developed [25] in analogy with the Fourier heat diffusion law. This is shown by

$$\frac{\partial^2 V}{\partial x^2} = R\,C_p \frac{\partial V}{\partial t}. \tag{7}$$

Here, V is the voltage, and C_p is the capacitance. Heaviside introduced the electromagnetic inductance term [43]; then (7) becomes

$$\frac{\partial^2 V}{\partial x^2} = R\,C_p \frac{\partial V}{\partial t} + L\,C_p \frac{\partial^2 V}{\partial t^2}, \tag{8}$$

with L as the inductance. Materials scientists, in contrast with electrical engineers, are typically interested in concentration variation with time, as in (5), which remains in modern use. Thus, equation (7), although very similar to (5), was written differently. Nevertheless, the modern version of (7) is (8), with the Heaviside inductance term.

3. Quasi-static losses

It is important to start by separating between irreversible and reversible processes. There are both types of domain wall movement: reversible and irreversible. Also, there is domain rotation, both reversible and irreversible. Losses happen in irreversible processes.

Figure 1 uses the ball-hill analogy to illustrate the reversible/irreversible process. If the ball goes to the other side of the hill, then the process is irreversible. Figure 2 illustrates reversibility/irreversibility using potential gravitational energy [44]. In Fig. 2, if a block goes from (a) to (b) and then back to (a), then the process is reversible. However, if the block goes from (a) to (b) and then to (c), the process is irreversible. Chen [45] also uses the ball-hill model to describe the irreversible movement of the domain wall.

Among the dissipative processes happening once in each hysteresis cycle, resulting in the hysteresis losses component P_h, the following can be listed [46]:

(i) Irreversible rotation of domains,
(ii) Irreversible domain wall displacement,
(iii) Creation and annihilation of domain walls,
(iv) Elimination of "90° closure domains" associated with magnetostrictive effects.

Microeddy currents surrounding domain walls could generate losses when a domain wall moves between different pinning sites [47]. To avoid this effect, Stewart [48] made the domain wall move very slowly in a very low-frequency experiment. Even so, losses did not become zero. The explanation was given by Shockley in the discussion at the end of the article [48]: "there will be certainly irreversible energy losses due to the fracture of Néel spikes." Therefore, Shockley, in 1951, was already indicating another dissipative mechanism, not only heating by the Joule effect according to the basic formula $P = RI^2$ [49]. Therefore, the suggestion by Becker [50], and especially by Graham [51], that the only cause for losses are microeddys [51] has no experimental basis. Besides, the noise is evidence of the dissipative process. Sound means vibration. Thus, "jumping atoms" (or oscillating atoms) are behind the occurrence of transformer noise [52, 53].

4. History of loss separation

Every theory needs to be experimentally tested. This was Lavoisier's way of ruling out the old theory of phlogiston [54]. Also, calculations by Heaviside appeared in order to explain experimental observations [55]. According to Russell (1904) [56], the eddy current loss problem was first solved by Heaviside (1884) for wires [2] and later by J.J. Thomson for sheets (1892) [3]. In 1904, the classic loss expression

$$P_{cl} = \frac{\pi^2\, f^2\, e^2\, B_{\max}^2}{6\rho} \tag{9}$$

could be found in textbooks such as that of Russell [56]. Here, B is the induction, f is the frequency, e is the thickness, and ρ is the resistivity. Graham [51] could not find the original source of (9). The separation between the eddy losses and the hysteresis losses P_h is mentioned not only in the 1904 book of Russell [56] but also by Morris (1906) [57] and Epstein (1907) [4]. Thus, at the beginning of the XX century, loss separation was commonplace.

The exact origin of the so-called "anomalous loss component" (P_a) is less known. Instead of "anomalous losses," Legg in 1936 [5] uses the term "residual losses" and finds it by the difference $P_t - P_h - P_{cl}$, identical to today's definition of anomalous losses. Therefore,

$$P_a = P_t - P_h - P_{cl}. \tag{10}$$

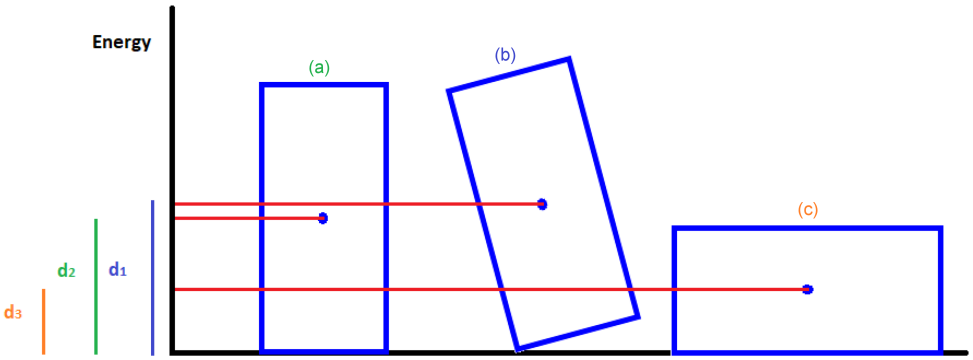

Fig. 2. Illustration of a reversible and irreversible process. The points at the center of the blocks denote the center of gravity. It should be noted that $d_1 > d_2 > d_3$ and that all heights d are defined for the same point of reference. (a) Metastable equilibrium, $E = mg\,d_2$. (b) Unstable equilibrium, $E = mg\,d_1$. (c) Stable equilibrium, $E = mg\,d_3$.

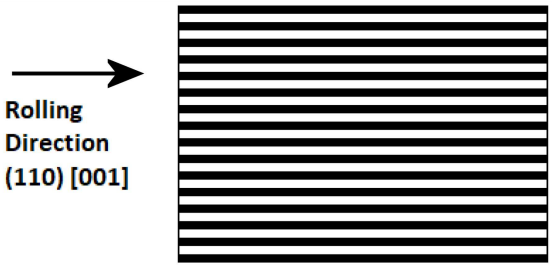

Fig. 3. Typical domain wall structure in GO steels, displaying the 180° domain walls.

The name "residual losses" remains in use for MnZn ferrites [58–62]. In (10), P_t is the total losses, and P_h is the quasi-static losses, given by

$$P_h = f \oint \mathrm{d}H\ B. \tag{11}$$

Actually, (9) neglects the skin effect, which can be significant at high frequencies or large thicknesses [63]. The "almost undecipherable papers" of Heaviside [55] are among the first to address the skin effect [43]. Equation (9) was deduced for constant permeability, which is an assumption far from reality.

Based on the Pry and Bean model [64], the anomalous losses can be expressed by [65]

$$P_a = \frac{k}{n\,\rho}\sqrt{G_s}\,f^{3/2}\,e^2\,B_{\max}^2, \tag{12}$$

and so $P_a \propto x/e$, where x is the distance between the domain walls; n is the number of domain walls, $n \propto 1/x$; and $c = k/n$ (n is dimensionless) [65], where k is experimental constant.

The dependence of anomalous losses as a function of frequency as $f^{3/2}$ is explained by Haller–Kramer [66, 67] and Sakaki [68], especially by observing the domain wall structures as a function of frequency [69]. Thus, (12) is similar to (9) except for frequency. The theoretical paper of Haller and Kramer [67] does not mention loss separation anywhere, but, in fact, makes use of loss separation by mixing energies due to eddy-current dissipation and domain nucleation–annihilation dissipation. The dependence of P_a with the square of the thickness has been observed experimentally [70, 71]. Equation (12) was confirmed experimentally for a series of alloys with different resistivities by Hong et al. [72].

In heavily deformed electrical steels, it was found that the anomalous losses were near zero [73], but the reported numbers were slightly negative, as noted in [74]. After that, one of the authors of the 2012 study [73] — F.J.G. Landgraf — examined those steel sheets with a micrometer and discovered that the thickness values used in the calculations of the 2012 paper [73] were slightly overestimated. After this correction was done, the anomalous losses were found to be zero! This result is in remarkable agreement with (12): If $G\,s$ is small then P_a, is near zero; or if n is high, then P_a is also near zero.

Of fundamental relevance to the loss separation model is the experimental observation that magnetic aging only affects the hysteresis losses (P_h) but not the other part, related to P_a. Thus, $P_t = P_p + P_a + P_h$, but the part $P_p + P_a$ is a constant under magnetic aging [49]. In 2006 [49], we were unaware that this experimental observation was reported by Epstein in 1907 [4] and by Beckley and Thompson in 1970 [75]. This result, namely that magnetic aging only affects hysteresis losses P_h, has been confirmed in several other studies [76, 77].

Loss separation in grain-oriented electrical steels has led to complex results [78], especially when considering the transverse direction [79]. For typical non-oriented electrical steels, a slight improvement of texture decreases both the hysteresis losses P_h and the anomalous losses components P_a. The complex results of Pluta [78] can be understood by the analysis of the domain wall structure in the grain-oriented (GO) electrical steels, see Fig. 3, which only displays

Quantitative effect of several variables on three loss components. TABLE I

Variable	Classical eddy	Hysteresis	Anomalous	References
induction (B)	$B_{\max}^2$	$B_{\max}^{1.6-2.0}$	$B_{\max}^{1.5-2.0}$	still debatable
frequency (f)	f^2	f	$f^{3/2}$	[66], [67], [68]
resistivity (ρ)	$1/\rho$	–	$1/\rho$	[70]
thickness (e)	e^2		e^2	[70], [71]
grain size (G_s)	–	$1/G_s$	$\sqrt{G_s}$	[69]

Qualitative effect of several factors on three loss components. TABLE II

Increase or improvement	Eddy current	Hysteresis	Anomalous	References
Si or Al content [%]	decreases	decreases	decreases	[72]
better texture	–	decreases	decreases	[78], [79]
number of domain walls (n)	–	increases	decreases	[64]
plastic deformation (rolling)	–	increases	decreases	[73]
applied stress (compression)	–	increases	increases	[80], [82], [83], [84]
number of inclusions	–	increases	(no effect)	[4], [49],[75], [76], [77]

the 180° domain walls. Obviously, nucleation of domains at 90° is required before any of the 90° domain wall movement, as discussed previously [79]. The domain wall displacement at 90° of the rolling direction is very difficult because, according to the Kondorsky law, the H field change or the domain wall displacement is given by $H \sim 1/\cos(\theta)$, and this gives an infinite field for $\theta = 90°$. This entails the need to form domains at 90° by rotation [79], which results in a very strange "stepped" hysteresis shape [80, 81].

The effect of stress — either compressive or tensile — depends on the magnetostrictive characteristics of the material. For grain-oriented electrical steel, compressive stress in general increases losses [80, 82], and this trend is also commonly observed for non-oriented electrical steels [83, 84]. There is a relevant observation: If the number of domain walls increases, then the pinning effect of domain walls at the surface can increase hysteresis losses [85], especially for very thin sheets.

Tables I and II summarize the predictions of the loss separation model given by (9)–(12). Since the model was presented in 2006 [69], it has resisted many experimental tests. However, the induction dependence for each P_h or P_a term is still a subject of debate and deserves to be investigated in future studies.

Electric vehicles have provoked an increasing demand for steels with better properties, high resistivity, and small thickness [86–89], and the loss separation model can be useful for improving these materials. The steel sheet thickness of the Tesla Model 3 is 0.25 mm [90]. It is difficult to improve the mechanical properties of such thin sheets. Then, a possible option for increasing both resistivity and mechanical properties is solid solution strengthening, and high manganese steels provide such a possibility [91].

5. Conclusions

Analogies between Fourier's heat law, Fick's diffusion law, and Ohm's law are discussed, with emphasis on historical developments. The concept of heat became clear after Boltzmann's ideas were accepted, but this only happened in the XX century.

This paper gives an overview of how the concept of heat evolved with time and why it is relevant for understanding the loss separation model. As "jumping atoms" (or oscillating atoms) are associated with heat, it becomes easier to understand the dependence of the hysteresis losses term P_h on the frequency f. The loss separation model was discussed in detail, emphasizing the practical applications.

Acknowledgments

The author thanks Fundação de Amparo à Pesquisa do Estado do Rio de Janeiro) (FAPERJ) and Conselho Nacional de Desenvolvimento Científico e Tecnológico (CNPq).

References

[1] J.B.F. Fourier, *The Analytical Theory of Heat*, trans. A. Freeman, Cambridge University Press, 2009 (1st ed. 1822).

[2] O. Heaviside, *The Electrician*, 1884, p. 583.

[3] J.J. Thomson, *The Electrician*, 1892, p. 599.

[4] J. Epstein, *J. Inst. Electr. Eng.* **38**, 28 (1907).

[5] V.E. Legg, *The Bell Syst. Tech. J.* **15**, 39 (1936).

[6] G. Nicolis, I. Prigogine, *Self-Organization in Non-Equilibrium System* John Wiley & Sons, 1977.

[7] P. Ball, *The Elements: A Visual History of Their Discovery*, University of Chicago Press, 2021.

[8] H. Guerlac, *Hist. Stud. Phys. Sci.* **7**, 193 (1976).

[9] P. Needham, *Int. Stud. Philos. Sci.* **16**, 205 (2002).

[10] R.B. Guenther, J.W. Lee, *Aspects of Integration: Novel Approaches to the Riemann and Lebesgue Integrals*, CRC Press, Chapman & Hall, 2023.

[11] J. Coopersmith, *Energy, the Subtle Concept: The Discovery of Feynman's Blocks from Leibniz to Einstein*, Oxford University Press, 2015.

[12] M. Planck, *Ann. Phys.* **309**, 553 (1901).

[13] M. Planck, *Eight Lectures on Theoretical Physics Delivered at Columbia University in 1909*, New York Columbia University Press, 1915.

[14] M. Planck, *Nobel Lectures — Physics 1901–1921*, Elsevier Publishing Company, Amsterdam 1967.

[15] C.A. Gearhart, *Boltzmann's Atom: The Great Debate that Launched a Revolution in Physics*, David Lindley Free Press, New York 2001.

[16] G. Binnig, H. Rohrer, *Rev. Mod. Phys.* **59**, 615 (1987).

[17] J.C. Maxwell, *Theory of Heat*, 1872.

[18] C. Charalampous, *Perspect. Sci.* **29**, 189 (2021).

[19] G.S. Smith, *Eur. J. Phys.* **35**, 025002 (2014).

[20] B.J. Hunt, *The Maxwellians*, Cornell University Press, 1994.

[21] S. Esteban, *J. Chem. Educ.* **85**, 1201 (2008).

[22] A. Fick, *Phil. Mag.* **10**, 30 (1855).

[23] G.S. Ohm, The Galvanic Circuit Investigated Mathematically, 1st English trans. from 1st ed., William Francis, New York 1827.

[24] T.N. Narasimhan, *Rev. Geophys.* **37**, 151 (1999).

[25] W. Thomson, *Philos. Mag.* **7**, 502 (1854).

[26] M.F. de Campos, *Mater. Sci. Forum* **727–728**, 163 (2012).

[27] J. Crank, *The Mathematics of Diffusion*, 2nd ed., Oxford University Press, New York 1975.

[28] W. Ostwald, *Outlines of General Chemistry*, trans. T.W. White, Macmillan and co., London 1912.

[29] B.A. Pletcher, K.-G. Wang, M. E. Glicksman, *Int. J. Mater. Res.* **103**, 1289 (2012).

[30] E. Hornbogen, *J. Light Metals* **1**, 127 (2001).

[31] G. Ertl, *Angew. Chem. Int. Ed.* **48**, 6600 (2009).

[32] A. Einstein, *Ann. Phys.* **322**, 549 (1905) (in German).

[33] M. von Smoluchowski, *Ann. Phys.* **326**, 756 (1906) (in German).

[34] J. Perrin, *J. Phys. Theor. Appl.* **9**, 5 (1910).

[35] J. Renn, *Ann. Phys.* **14**, Supplement, 23 (2005).

[36] B.W. Lawrence, *Proc. R. Soc. Lond. A* **89**, 468 (1914).

[37] S. Ono, H. Satomi, J. Yuhara, *Comput. Mater. Sci.* **218**, 111959 (2023).

[38] R. de Andrade Martins, *Notes Rec.* **76**, 117 (2022).

[39] H. Barkhausen, *Phys. Z.* **20**, 401 (1919).

[40] E.C. Stoner, *Rev. Mod. Phys.* **25**, 2 (1953).

[41] L.F.T. Costa, G.J.L. Gerhardt, F.P. Missell, M.F. de Campos, *Acta Phys. Pol. A* **136**, 740 (2019).

[42] C.-H. Hsu, Y.-M. Huang, M.-F. Hsieh, C.-M. Fu, S. Adireddy, D.B. Chrisey, *AIP Adv.* **7**, 056681 (2017).

[43] C. Donaghy-Spargo, *Philos. Trans. R. Soc. A* **376**, 20170457 (2018).

[44] J.W. Cahn, in: *The Selected Works of John W. Cahn*, Eds. W.C. Carter, W.C. Johnson, Wiley 1998.

[45] C.W. Chen, *Magnetism and Metallurgy of Soft Magnetic Materials*, 1977, p. 129.

[46] S.R. Janasi, V.A. Lázaro-Colán, F.J.G. Landgraf, M.F. de Campos, *Mater. Sci. Forum* **775–776**, 404 (2014).

[47] K.H. Stewart, *Proc. Phys. Soc. A* **63**, 761 (1950).

[48] K.H. Stewart, *J. Phys. Radium* **12**, 325 (1951).

[49] M.F. de Campos, M. Emura, F.J.G. Landgraf, *J. Magn. Magn. Mater.* **304**, e593 (2006).

[50] J.J. Becker, *J. Appl. Phys.* **34**, 1327 (1963).

[51] C.D. Graham, *J. Appl. Phys.* **53**, 8276 (1982).

[52] T. Tanzer, H. Pregartner, R. Labinsky, M. Witlatschil, A. Muetze, K. Krischan, in: *2017 IEEE Int. Electric Machines and Drives Conf. (IEMDC)*, 2017.

[53] S. Taguchi, *Trans. ISIJ* **17**, 604 (1977).

[54] J.R. Partington, D. McKie, *Ann. Sci.* **4**, 113 (1939).

[55] I. Yavetz, *From Obscurity to Enigma: The Work of Oliver Heaviside 1872–1889*, 1995.

[56] A. Russell, *A Treatise on the Theory of Alternating Currents*, Vol. 1, 1st Ed. Cambridge University Press, 1904.

[57] D.K. Morris, G.A. Lister, *J. Inst. Electr. Eng.* **37**, 264 (1906).

[58] S.H. Chen, S.C. Chang, C.Y. Tsay, K.S. Liu, I.N. Lin, *J. Eur. Ceram. Soc.* **21**, 1931 (2001).

[59] O. Inoue, N. Matsutani, K. Kugimiya, *IEEE Trans. Magn.* **29**, 3532 (1993).

[60] H. Kobiki, A. Fujita, S. Gotoh, *J. Phys. IV Proc.* **7**, C1-103 (1997).

[61] W.H. Jeong, Y.H. Han, B.M. Song, *J. Appl. Phys.* **91**, 7619 (2002).

[62] A. Fujita, H. Kobiki, S. Gotoh, *J. Magn. Soc. Jpn.* **22**, Supplement, S1 (1998).

[63] P. Jabłoński, M. Najgebauer, M. Bereźnicki, *Energies* **15**, 2869 (2022).

[64] R.H. Pry, C.P. Bean, *J. Appl. Phys.* **29**, 532 (1958).

[65] M.F. de Campos, *Acta Phys. Pol. A* **136**, 705 (2019).

[66] T.R. Haller, J.J. Kramer, *J. Appl. Phys.* **41**, 1034 (1970).

[67] T.R. Haller, J.J. Kramer, *J. Appl. Phys.* **41**, 1036 (1970).

[68] Y. Sakaki, *IEEE Trans. Magn.* **16**, 569 (1980).

[69] M.F. de Campos, J.C Teixeira, F.J.G. Landgraf, *J. Magn. Magn. Mater.* **301**, 94 (2006).

[70] E.T. Stephenson, *J. Appl. Phys.* **57**, 4226 (1985).

[71] M.A. Trindade, M.F. de Campos, F.J.G. Landgraf, N.B. de Lima, A. Almeida, *Mater. Sci. Forum* **930**, 466 (2018).

[72] J. Hong, H. Choi, S. Lee, J.K. Kim, Y.M. Koo, *J. Magn. Magn. Mater.* **439**, 343 (2017).

[73] D.L. Rodrigues, J.R.F. Silveira, G.J.L. Gerhardt, F.P. Missell, F.J.G. Landgraf, R. Machado, M.F. de Campos, *IEEE Trans. Magn.* **48**, 1425 (2012).

[74] S.E. Zirka, Y.I. Moroz, S. Steentjes, K. Hameyer, K. Chwastek, S. Zurek, *J. Magn. Magn. Mater.* **394**, 229 (2015).

[75] P. Beckley, J.E. Thompson, *Proc. IEEE* **117**, 2194 (1970).

[76] K.M. Marra, F.J.G. Landgraf, V.T. Buono, *J. Magn. Magn. Mater.* **320**, e631 (2008).

[77] A.A. de Almeida, F.J.G. Landgraf, *Mater. Res.* **22**, e20180506 (2019).

[78] W.A. Pluta, *J. Magn. Magn. Mater.* **499**, 166270 (2020).

[79] M.F. de Campos, M.A. Campos, F.J.G. Landgraf, L.R. Padovese, *J. Phys. Conf. Ser.* **303**, 012020 (2011).

[80] F. Brailsford, Z.H.M. Abu-Eid, *Proc. Inst. Electr. Eng.* **110**, 751 (1963).

[81] F. Brailsford, *Physical Principles of Magnetism*, Van Nostrand, London 1966.

[82] D. Brown, C. Holt, J.E. Thompson, *Proc. Inst. Electr. Eng.* **112**, 183 (1965).

[83] K. Ali, K. Atallah, D. Howe, in: *Int. Workshop on Rare-Earth Magnets and Their Applications 14*, São Paulo 1996, World Scientific, Singapore 1996, p. 632.

[84] A. Baghel, J. Blumenfeld, L. Santandrea, G. Krebs, L. Daniel, *Electr. Eng.* **101**, 845 (2019).

[85] N. Morito, M. Komatsubara, Y. Shimizu, *History and Recent Development of Grain Oriented Electrical Steel. at Kawasaki Steel*, Kawasaki Steel Technical Report No. 39, 1998, p. 3.

[86] M. Najgebauer, J. Szczyglowski, A. Kaplon, in: *2015 Selected Problems of Electrical Engineering and Electronics (WZEE), Kielce (Poland)*, IEEE, 2015.

[87] G. Ouyang, X. Chen, Y. Liang, C. Macziewski, J. Cui, *J. Magn. Magn. Mater.* **481**, 234 (2019).

[88] N. Leuning, M. Jaeger, B. Schauerte et al., *Materials* **14**, 6588 (2021).

[89] Y. Du, R. O'Malley, M.F. Buchely, *Appl. Sci.* **13**, 6097 (2023).

[90] C.-L. Lin, H.-M. Dai, C.-H. Chao, S. Wei, C.-F. Yang, *Sensors Mater.* **35**, 4131 (2023).

[91] M.F de Campos, *Przegląd Elektrotechniczny* **2019**, 7 (2019).

Selected papers presented at the 14th Symposium of Magnetic Measurements and Modelling SMMM'2023

Simulation of Thermomagnetic Properties of MnCoGe Alloy

P. Gębara[a,*], R. Gozdur[b] and K. Chwastek[c]

[a]*Department of Physics, Częstochowa University of Technology, Armii Krajowej 19, 42-200 Częstochowa, Poland*
[b]*Department of Semiconductor and Optoelectronic Devices, Łódź University of Technology, Stefanowskiego 18/22, 90-924 Łódź, Poland*
[c]*Department of Electrical Power Engineering, Częstochowa University of Technology, Armii Krajowej 17, 42-200 Częstochowa, Poland*

Doi: 10.12693/APhysPolA.146.41 *e-mail: piotr.gebara@pcz.pl

In this paper, phenomenological modeling and experimental studies were conducted to predict the magnetocaloric properties of the MnCoGe alloy. The temperature dependence of magnetization was measured and calculated using a simple phenomenological model. A good correlation between simulated and experimentally determined data was observed. The phenomenological model allowed us to reveal theoretical values of the magnetic entropy change, full width at half maximum of ΔS_M vs T curve, and relative cooling power.

topics: magnetocaloric materials, magnetic entropy change, relative cooling power

1. Introduction

Since the early nineties of the twentieth century, the issues of nature protection, in particular the problems related to ozone layer depletion, have been treated seriously. High pollution caused by freon compounds destroyed a significant part of this protective part of Earth's atmosphere. The Montreal Protocol, established in 1993, forbade the use of the aforementioned compounds in sprays and domestic cooling devices. Freon was also used as an active element in refrigerators. The efficiency of the cooling process based on the compression/decompression of freon gas is about 45%.

A more efficient cooling technique is magnetic refrigeration based on the magnetocaloric effect [1]. The temperature change in magnetic material at adiabatic conditions is realized by the variations of the external magnetic field. An example of the magnetocaloric material with a Curie temperature close to room temperature is pure Gd [2, 3]. Its disadvantage is that it is relatively expensive.

A significant increase in the number of papers on the topic has been observed after the discovery of a giant magnetocaloric effect in the $Gd_5Ge_2Si_2$ alloy by Pecharsky and Gschneider [4]. For many years, a lot of different materials have been studied, such as the manganites [5], the $La(Fe,Si)_{13}$-type alloys [6–8], or Heusler alloys [9].

Another interesting group of magnetocaloric materials are equiatomic alloys of MM'X-type (where M, M' are transition metals and X — metaloid) [10–13]. The good magnetocaloric properties of these alloys are due to the formation of low-temperature orthorhombic TiNiSi-type (space group $Pnma$) and high-temperature hexagonal Ni_2Ti (space group $P6_3/mmc$). Modifications of chemical composition of the MnCoGe alloy induce changes in structural and magnetocaloric properties. Hamad in [14] proposed a phenomenological model to predict the thermomagnetic properties. The experimental studies of the MnCoGe alloy were carried out by one of the authors of the present paper in [15].

The aim of the present work is to verify the usefulness of the Hamad model applied to experimental data of MnCoGe alloy.

2. Experimental techniques

The MnCoGe alloy sample was prepared by arc-melting of the high purity (min. 3 N) constituent elements under low pressure of protective gas Ar. In order to ensure the homogeneity of the sample, the ingot was remelted several times. Phase constitution was studied by Bruker D8 Advance diffractometer with Cu K_α radiation, and the analysis results were shown previously

in [15]. Thermomagnetic properties were studied using Quantum Design PPMS (VSM option) in a magnetic field of up to 5 T and a wide range of temperatures and magnetic fields. The accuracy of measurements was 0.001 emu. The Maxwell relation was used to calculate the magnetic entropy change [4]

$$\Delta S_M(T,\Delta H) = \mu_0 \int_0^H \mathrm{d}H \left(\frac{\partial M(T,H)}{\partial T}\right)_H, \qquad (1)$$

where μ_0, H, M, and T are the magnetic permeability of vacuum, strength of the magnetic field, magnetization, and temperature, respectively.

The RCP values were calculated taking into account temperature dependences of magnetic entropy change using the following equation [16]

$$RCP = -\Delta S_{\max M}\ \delta T_{\mathrm{FWHM}}, \qquad (2)$$

where RCP is relative cooling power, δT_{FWHM} is the full width at half maximum of magnetic entropy change peak.

3. Phenomenological model by Hamad

The phenomenological model proposed by Hamad in [15] allows one to predict magnetization variations upon temperature in accordance with the following equation

$$M = \frac{(M_i + M_f)}{2} \tanh\Big(A\,(T_{\mathrm{C}} - T)\Big) + B\,T + C, \qquad (3)$$

where T_{C}, M_i, and M_f are the Curie temperature, and the initial and final value of magnetization at ferromagnetic–paramagnetic transition, respectively. The values of parameters required by the model were obtained from an experimental M vs T curve, which is shown in Fig. 1 together with marked selected points. These points were used for modeling the coefficients A, B, and C given with the following formulas

$$A = \frac{2\,(B - S_{\mathrm{C}})}{M_i - M_f}, \qquad (4)$$

$$B = \frac{\mathrm{d}M}{\mathrm{d}T}, \qquad (5)$$

$$C = \frac{M_i - M_f}{2} - B\,T_{\mathrm{C}}, \qquad (6)$$

$$S_{\mathrm{C}} = \frac{\mathrm{d}M}{\mathrm{d}T} \qquad \text{at} \qquad T = T_{\mathrm{C}}. \qquad (7)$$

The theoretical formula that describes the variation of magnetic entropy upon temperature is based on relationships (1) and (3) and is rewritten in the following form

$$\Delta S_M = \left[-A\frac{(M_i - M_f)}{2}\,\mathrm{sech}^2\big(A(T_{\mathrm{C}} - T)\big) + B\right] H_{\max}. \qquad (8)$$

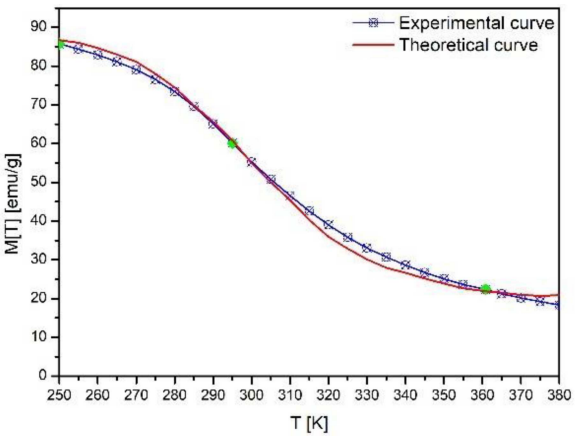

Fig. 1. Experimental and theoretical M vs T curves revealed for the MnCoGe alloy (under the change in magnetic field ~ 5 T).

A careful analysis of equation (8) revealed that the value of magnetic entropy change is strongly related to magnetization sensitivity $\mathrm{d}M/\mathrm{d}T$ at Curie temperature. High magnetic entropy change is dependent on high magnetic moment and the value of the first derivative of magnetization with respect to temperature at Curie point. The maximum value of magnetic entropy change may be written as

$$\Delta S_M = \left(-A\,\frac{(M_i - M_f)}{2} + B\right) H_{\max}. \qquad (9)$$

Prediction of the magnetic entropy change and its maximum value is extremely important and determines the usefulness of a given magnetocaloric material. Apart from maximum magnetic entropy change, the working temperature range is a significant parameter for magnetocaloric materials. In practice, the full width at half maximum (FWHM) of the $\Delta S_M(T)$ curve is the figure of merit. The full width at half maximum of magnetic entropy change is determined from the following equation

$$\delta T_{\mathrm{FWHM}} = \frac{2}{A}\cosh^{-1}\left(\sqrt{\frac{2A\,(M_i - M_f)}{A\,(M_i - M_f) + 2B}}\right). \qquad (10)$$

Taking into account relationships (2), (9), and (10), the relative cooling power can be written in the following form:

$$RCP = \left(M_i - M_f - 2\frac{B}{A}\right) H_{\max} \times \cosh^{-1}\left(\sqrt{\frac{2A\,(M_i - M_f)}{A\,(M_i - M_f) + 2B}}\right). \qquad (11)$$

Relationships (9), (10), and (11) allowed us to calculate magnetocaloric properties and compare them with experimental values. All of them are collected in Table I.

As it is shown in Fig. 1, the modeled temperature dependence of magnetization corresponds very well to the measured curve. The temperature

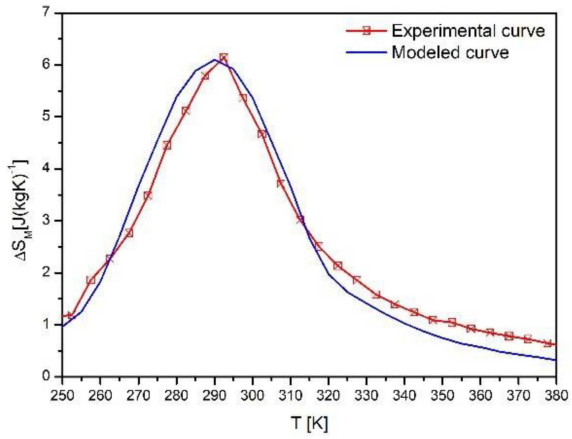

Fig. 2. Experimental and modeled magnetic entropy change for the as-cast MnCoGe alloy.

TABLE I

Experimental and theoretically modeled magnetocaloric properties of the MnCoGe alloy under the change in external magnetic field ~ 5 T.

	ΔS_M [J/(kg K)]	δT_{FWHM} [K]	RCP [J/kg]
Exp. value	6.17	36	222
Theor. value	6.09	43	262

dependence of magnetic entropy change obtained from experimental data and simulated using the phenomenological model were plotted in Fig. 2. Practically, both dependences overlap. The measured and the modeled values are comparable over the whole studied range. The phenomenological model delivered significantly higher values of δT_{FWHM} and, hence, relative cooling power. Modeled maximum entropy change decreased by 1%, while RCP and δT_{FWHM} increased by 18 and 19%, respectively.

Hamad's phenomenological model is a simple technique for the prediction of temperature dependences of magnetization or magnetic entropy change. The modeled values are reliable and comparable with measured results.

4. Conclusions

The evolution of magnetization due to the temperature changes for the MnCoGe alloy under the change in external magnetic field $\sim$ 5 T was modeled. The phenomenological model allowed us to predict the magnetocaloric properties of the MnCoGe alloy, such as magnetic entropy change, relative cooling power, and full width at half maximum. The magnetocaloric effect (MCE) was experimentally predicted indirectly by a calculation of magnetic entropy change based on magnetic isotherms. The produced alloy revealed relatively acceptable magnetocaloric properties and could be applied as an active element in magnetic cooling devices. Values of magnetic entropy change and relative cooling power delivered during modeling are reliable and reasonable. Moreover, they correspond well to their counterparts from experimental investigation.

Acknowledgments

P.G. would like to thank Professor Jan Świerczek, Head of the Department of Physics, Częstochowa University of Technology, for financial support.

References

[1] A.M. Tishin, Y.I. Spichkin, *The magnetocaloric effect and its applications*, CRC Press, New York 2003.

[2] V.K. Pecharsky, K.A. Gschneidner Jr., *J. Magn. Magn. Mater.* **200**, 44 (1999).

[3] A. Diaz-Garcia, J.Y. Law, P. Gębara, V. Franco, *JOM* **72**, 2845 (2020).

[4] V.K. Pecharsky, K.A. Gschneidner Jr., *Phys. Rev. Lett.* **78**, 4494 (1997).

[5] R. M'nassri, W. Cheikhrouhou-Koubaa, N. Chniba Boudjada, A. Cheikhrouhou, *J. Appl. Phys.* **113**, 073905 (2013).

[6] A. Fujita, Y. Akamatsu, K. Fukamichi, *J. Appl. Phys.* **85**, 4756 (1999).

[7] X.B. Liu, D.H. Ryan, Z. Altounian, *J. Magn. Magn. Mater.* **270**, 305 (2004).

[8] P. Gębara, J. Kovac,*J. Magn. Magn. Mater.* **454**, 298 (2018).

[9] A. He, V. Svitlyk, Y. Mozharivskyj, *Inorg. Chem.* **56**, 2827 (2017).

[10] K. Kutynia, P. Gębara, *Materials* **14**, 3129 (2021).

[11] K. Kutynia, A. Przybył, P. Gębara, *Materials* **16**, 5394 (2023).

[12] S.K. Pal, C. Frommen, S. Kumar, B.C. Hauback, H. Fjellvag, T.G. Woodcock, K. Nielsch, G. Helgesen, *J. Alloys Compd.* **775**, 22 (2019).

[13] X. Si, K. Zhou, R. Zhang, X. Ma, Z. Zhang, Y. Liu, *Mater. Res. Express* **5**, 126104 (2018).

[14] M.A. Hamad, *Phase Transitions* **85**, 106 (2012).

[15] P. Gębara, Z. Śniadecki, *J. Alloys Compd.* **796**, 153 (2019).

[16] K.A. Gschneidner Jr., V.K. Pecharsky, *Annu. Rev. Mater. Sci.* **30**, 387 (2000).

Selected papers presented at the 14th Symposium of Magnetic Measurements and Modelling SMMM'2023

Analysis of GRUCAD Model Behavior for Anhysteretic Curve Given by the Brillouin Function

R. Jastrzębski* and K. Chwastek

Faculty of Electrical Engineering, Częstochowa University of Technology, al. Armii Krajowej 17, 42-201 Częstochowa, Poland

Doi: 10.12693/APhysPolA.146.44 *e-mail: radoslaw.jastrzebski@pcz.pl

The paper focuses on an extension of the GRUCAD hysteresis model. The extension relies on the replacement of the Langevin function with a more general Brillouin function in an equation describing the anhysteretic curve. The proposed approach allows one to obtain better fitting capabilities for anisotropic soft magnetic materials, as demonstrated by the example of hysteresis curves of grain-oriented electrical steel.

topics: electrical steel, modeling, hysteresis curve, anhysteretic curve

1. Introduction

Taking into account that any magnetic hysteresis model is merely an approximation of real-life phenomena, it can be stated that an important stage in hysteresis modeling is the analysis of the qualitative behavior of models with different improvements.

Improvements can be understood as modifications of model equations, extensions aimed at correcting model behavior, or considerations of physical phenomena, such as the effect of excitation frequency, mechanical stress anisotropy, or temperature, which previously were not taken into account.

An exemplary modification may rely on the use of different elementary functions appearing in model equations. It is expected that model performance would be improved for different scenarios, and moreover, new knowledge on underlying physical principles would be gained. In the present paper, we consider an extension to the GRUCAD model [1], which uses a more general description of the anhysteretic curve in comparison to the original approach. The GRUCAD model is a recent low-dimensional description consistent with the laws of irreversible thermodynamics.

2. Model description

The description advanced by Jiles and Atherton [2] has attracted a lot of attention in the scientific community in the last thirty years. This formalism is still very attractive to scientists and engineers alike. In the present paper, we focus on the GRUCAD model, which is a modification of the Jiles–Atherton (JA) approach proposed by the Brazilian GRUCAD [1, 3]. The most important advantage of GRUCAD model is that it addresses a number of problems encountered in the original description, as pointed out in [4, 5]. The crucial difference between the original JA formalism and the GRUCAD model is that the latter description uses offsetting (shifting) from the anhysteretic curve along the H axis, not along the M axis. This feature allows one to obtain quasi-static minor hysteresis loops without fragments with negative differential susceptibility, and moreover, it is correct from the perspective of energy balance relationships. As a reminder, the anhysteretic curve describes the state of global equilibrium in the thermodynamic sense.

The GRUCAD description has yet another important feature, namely it is formulated as a B-input model — this feature facilitates the interpretation of results. Magnetic measurements carried out in accordance with international standards are carried out for a controlled polarization rate (in practice, for soft magnetic materials, the difference between polarization and flux density may be neglected). Thus, the model reflects real-life measurement conditions.

Previously, the behavior of the GRUCAD model was analyzed in some papers co-authored by the authors of the present contribution, mentioning, e.g., its application in describing hysteresis curves in a permalloy core [6], soft magnetic composites [7, 8], magnetocaloric LaFeCoSi alloys [9]. An extension aimed at consideration of the effect of excitation frequency was attempted for a nanocrystalline sample in [10], whereas paper [11] focused on model behavior in the case of DC-biased magnetization.

The set of equations used so far was

$$H_{\mathrm{an}} = \frac{B}{\mu_0} - M_s \left[\coth(\lambda) - \frac{1}{\lambda}\right], \tag{1}$$

$$\lambda = \frac{H_{\mathrm{an}}\,(1-\alpha) + B(\frac{\alpha}{\mu_0})}{a}, \tag{2}$$

$$\frac{\mathrm{d}H_{\mathrm{h}}}{\mathrm{d}B} = \frac{H_{\mathrm{HS}}\left[\coth(\lambda_H) - 1/\lambda_H\right] - H_{\mathrm{h}}}{\gamma\delta}, \tag{3}$$

$$\lambda_H = \frac{H_{\mathrm{h}} + \delta H_{\mathrm{HS}}}{a}, \tag{4}$$

$$H = H_{\mathrm{an}} + H_{\mathrm{h}}, \tag{5}$$

where α, a, γ, H_{HS}, and M_s were model parameters; $\delta = \pm 1$ was used to distinguish the ascending and descending loop branches; λ and λ_H were auxiliary variables; $H_{\mathrm{an}} = H_{\mathrm{an}}(B)$ was the anhysteretic field strength, and $H_{\mathrm{h}} = H_{\mathrm{h}}(B)$ denoted the irreversible field strength, related to hysteresis; μ_0 was permeability of free space; and B was magnetic flux density, which was the input variable in the model.

3. Comparison of different anhysteretic equations

In the preceding section, expressions (1) and (2) were used as a complete description of the anhysteretic curve. It can be easily noticed that (1) availed of the Langevin function.

The aim of the present paper is to introduce in that place a more general function, namely the Brillouin function

$$B_J(\lambda) = \frac{2J+1}{2J}\coth\left(\frac{2J+1}{2J}\lambda\right) - \frac{1}{2J}\coth\left(\frac{1}{2J}\lambda\right), \tag{6}$$

in which an additional parameter J appears. In solid-state physics, it is interpreted as an angular momentum quantum number. It takes either positive integer or half-integer values. Two limiting values are 0.5 (then the Brillouin function reduces to hyperbolic tangent) and ∞ (in practical computation $J \to 25$, then the Brillouin function approaches the Langevin function).

Exemplary shapes of curves reproduced with the Brillouin function in reduced units for different values of J parameter are depicted in Fig. 1. Additionally, in this figure, the dependence $y = \tanh(x/3)$ is shown. This dependence may be used instead of the Langevin function for smaller values of its argument, and the advantage of this function is that it can be inverted analytically.

The extension considered in this paper bears some resemblance to the approaches described in [12, 13]. The aforementioned papers considered that the proper choice of angular momentum quantum number J in the formula for the anhysteretic curve in the modified JA description might shed some light on the anisotropy class of the analyzed soft magnetic material. The present paper applied the same concept to another model, which, in our opinion, is a much better choice for people dealing with hysteresis modeling.

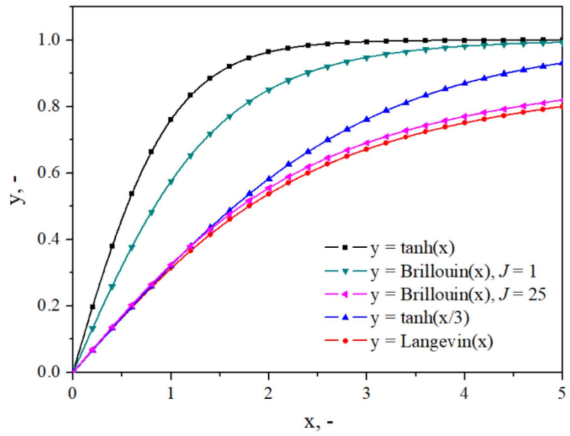

Fig. 1. The functions $L(x)$, $\tanh(x/3)$, and $B_J(x)$ for $J = 1.0$ and $J = 25$.

Replacing the Langevin function with the Brillouin function in (1) is the only modification applied to model equations in this paper. The concept is to vary the value of parameter J and to find such a set of model parameters that yields the best match to the measured hysteresis curve.

4. Modeling

In the present paper, we focus on modeling properties of samples made of two kinds of electrical steel, differing in morphology and magnetic properties. The rationale for our choice is that electrical steels are the most dominant group of soft magnetic materials worldwide (around 80% are non-oriented (NO) electrical steels, used as core materials for rotating machines, and around 16% are grain-oriented (GO) steels, whose application target are magnetic circuits of power and distributions transformers).

We consider two representative samples from each group, namely the grade M330-35A (NO steel, 0.35 mm thick) and the grade ET120-27 (GO steel, 0.27 mm thick).

Figures 2 and 3 depict modeling results for the non-oriented steel. Two extreme cases of the J value are considered for brevity. From the inspection of these figures, it is noticeable that the choice of $J = 25$ in the Brillouin function allows us to reproduce the shape of hysteresis slightly more accurately, in particular in the so-called knee region.

Figures 4 and 5 refer to grain-oriented electrical steel ET120-27, which exhibits a substantial anisotropy. The measurements were carried out along the rolling direction.

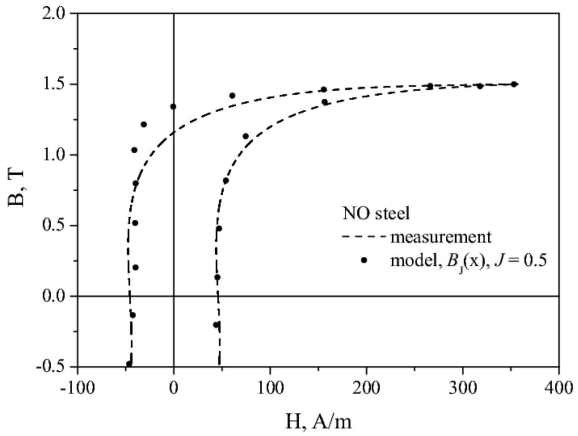

Fig. 2. The measured and the modeled hysteresis loop for the NO sample. The anhysteretic curve is given as $B_J(x)$, $J = 0.5$.

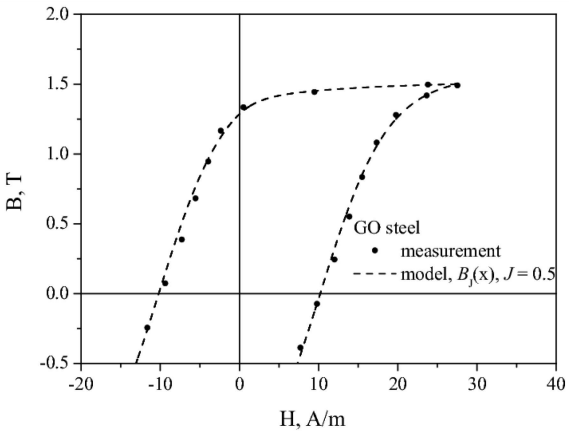

Fig. 4. The measured and the modeled hysteresis loop for the GO sample. The anhysteretic curve is given as $B_J(x)$, $J = 0.5$.

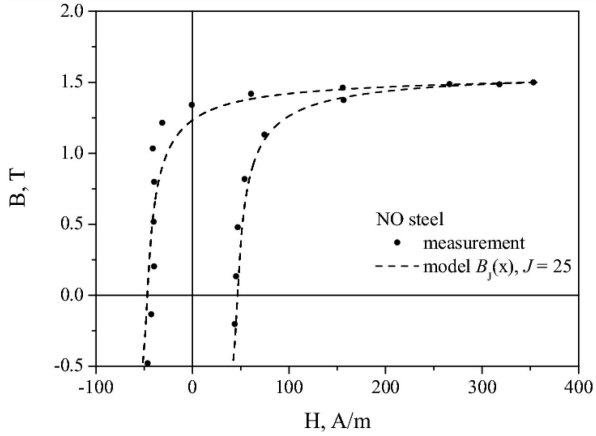

Fig. 3. The measured and the modeled hysteresis loop for the NO sample. The anhysteretic curve is given as $B_J(x)$, $J = 25$.

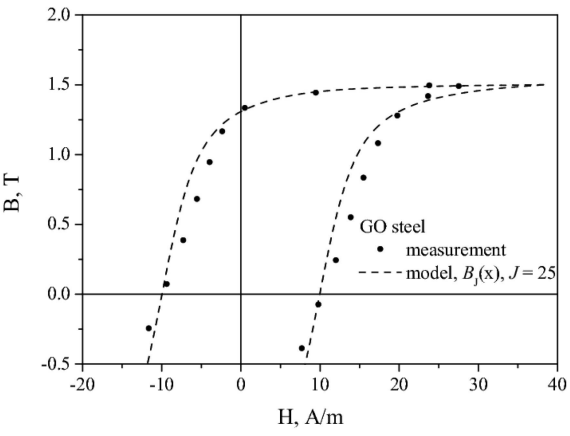

Fig. 5. The measured and the modeled hysteresis loop for the GO sample. The anhysteretic curve is given as $B_J(x)$, $J = 25$.

TABLE I

Values and percentage errors in chosen characteristic points for the non-oriented steel.

	H_c [A/m]	B_r [T]	$\lvert\Delta H_c\rvert$	$\lvert\Delta B_r\rvert$	$\lvert\Delta E\rvert$
Meas.	43.9	1.36			
$B(x)$ $J = 0.5$	45.8	1.15	4.3%	15.4%	7.5%
$B(x)$ $J = 5$	45.8	1.21	4.3%	10.9%	7.3%
$B(x)$ $J = 10$	43.1	1.11	1.9%	18.7%	27%
$B(x)$ $J = 15$	44.9	1.23	2.2%	9.7%	11%
$B(x)$ $J = 25$	44.3	1.23	2.8%	9.3%	10%
$L(x)$	45.3	1.25	3.1%	8.1%	8.4%

TABLE II

Values and percentage errors in chosen characteristic points for the grain-oriented steel.

	H_c [A/m]	B_r [T]	$\lvert\Delta H_c\rvert$	$\lvert\Delta B_r\rvert$	$\lvert\Delta E\rvert$
Meas.	10.00	1.30			
$B(x)$ $J = 0.5$	10.25	1.29	2.5%	1%	0.6%
$B(x)$ $J = 5$	9.85	1.37	1.5%	5%	2.6%
$B(x)$ $J = 10$	10.14	1.31	1.4%	1%	5.3%
$B(x)$ $J = 15$	10.02	1.30	0.2%	0%	3.7%
$B(x)$ $J = 25$	9.96	1.31	0.4%	1%	0.2%
$L(x)$	10.50	1.32	5.0%	2%	1.1%

Tables I and II contain information on measured and modeled values of coercive field strength and remanence induction for several selected values of J parameter. The last column (ΔE) refers to the relative difference between measured and modeled loop areas. Recalling that the hysteresis loop area is directly related to re-magnetization loss (the latter quantity may be computed from the loop area), the value of this parameter is an indirect measure of the modeling accuracy.

From the analysis of errors in the tables, it follows that, particularly for the GO steel, the modeling errors were dependent on the choice of J value. Despite the fact that the values in the table might suggest that the choice $J = 25$ is superior to $J = 0.5$, from a visual comparison of the modeled curves in Figs. 4 and 5, it follows that, in fact, the modeled curve for $J = 0.5$ describes the experimental data more accurately. Therefore, the choice $J = 0.5$ (the case of strong anisotropy) is preferred. Our model extension has proven to be useful.

5. Conclusions

In the paper, an extension to the GRUCAD hysteresis model was proposed. The essential concept was to modify one of the model equations. The Brillouin function was introduced in place of the Langevin function. This approach allowed us to make the description more flexible, enabling the consideration of different anisotropy classes of soft magnetic materials, which can be taken into account in the analysis by a proper choice of J parameter. The Langevin function is a limiting case of the Brillouin function obtained for $J \to \infty$.

The usefulness of the proposed model extension was verified using data for a strongly anisotropic material, namely grain-oriented electrical steel.

Future work will focus on additional verification of the proposed descriptions for other soft magnetic materials.

Acknowledgments

This project was supported within the framework of the Program No. 020/RID/2018/19 "Regional Initiative of Excellence" granted by the Minister of Science and High Education in the years 2019–2023, the amount of funding PLN 12 000 000. From the project funds the costs of participation of the first author at the SMMM'2023 conference were covered.

References

[1] P.I. Koltermann, L.A. Righi, J.P.A. Bastos, R. Carlson, N. Sadowski, N.J. Batistela, *Physica B* **275**, 233 (2000).

[2] L.A. Righi, N. Sadowski, R. Carlson, J.P.A. Bastos, N.J. Batistela, *IEEE Trans. Magn.* **37**, 3353 (2001).

[3] D.C. Jiles, D.L. Atherton, *J. Magn. Magn. Mater.* **61**, 48 (1986).

[4] S.E. Zirka, Y.I. Moroz, R. G. Harrison, K. Chwastek, *J. Appl. Phys.* **112**, 043916 (2012).

[5] R. Jastrzębski, K. Chwastek, *ITM Web of Conf.* **15**, 03003 (2017).

[6] R. Jastrzębski, K. Chwastek, I. Biondić, K. Miličević, *Acta Phys. Pol. A* **131**, 1228 (2017).

[7] R. Jastrzębski, A. Jakubas, K. Chwastek, *J. Electr. Eng.* **69**, 385 (2018).

[8] A. Jakubas, M. Najgebauer, R. Jastrzębski, *Przegląd Elektrotechniczny* **1**, 75 (2022).

[9] R. Gozdur, P. Gębara, K. Chwastek, *Open Phys.* **16**, 266 (2018).

[10] R. Jastrzębski, K. Chwastek, in: *2017 Progress in Applied Electrical Engineering (PAEE)*, IEEExplore, 2017.

[11] R. Jastrzębski, A. Jakubas, K. Chwastek, *Int. J. Appl. Electromagn. Mech.* **61**, S151 (2019).

[12] K. Chwastek, *J. Phys. D Appl. Phys.* **43**, 015005 (2010).

[13] K. Chwastek, J. Szczygłowski, *Arch. Electr. Eng.* **60**, 49 (2011).

Selected papers presented at the 14th Symposium of Magnetic Measurements and Modelling SMMM'2023

Modeling the Anhysteretic Magnetization Curve of Anisotropic Soft Magnetic Materials

R. Szewczyk*

Warsaw University of Technology, Faculty of Mechatronics, Institute of Metrology and Biomedical Engineering, św. A. Boboli 8, 02-525 Warsaw, Poland

Doi: 10.12693/APhysPolA.146.48 *e-mail: roman.szewczyk@pw.edu.pl

The paper presents the results of validating the model of anhysteretic magnetization curve of anisotropic soft magnetic materials utilizing the Boltzmann distribution of magnetic domain directions. It was confirmed that the editorial mistake in the original paper presenting the concept of anisotropic anhysteretic magnetization curve was reproduced in subsequent publications. Validation presented in the paper covers an anhysteretic magnetization curve model for magnetic materials with axial anisotropy and anisotropic grain-oriented electrical steels. However, the proposed correction of the model of the anisotropic anhysteretic magnetization curve can be extended to other types of anisotropy.

topics: magnetization curve, magnetic materials modeling, magnetic anisotropy, anhysteretic magnetization

1. Introduction

The concept of an anhysteretic magnetization curve [1] is very useful for modeling the magnetic hysteresis loops of soft magnetic materials. It is widely used in developing physical models of the magnetization process [2] and for practical applications, e.g., in gyrator–capacitor models of inductive components implemented with SPICE software [3]. Moreover, the recently presented measuring procedure enables accurate experimental determination of the anhysteretic magnetization curve of cores made of soft magnetic materials [4]. For these reasons, developing efficient and accurate models of the anhysteretic magnetization curve of both isotropic and anisotropic soft magnetic materials is crucial for theoretical analyses and practical applications.

2. Model of the anhysteretic magnetization curve of anisotropic materials

The commonly used model of the anhysteretic magnetization curve of isotropic materials utilizes the concept presented by D.C. Jiles and D. Atherton [1] in 1984. In this model, atomic magnetic moments in the description of paramagnetic materials were substituted by domain magnetic moments to describe the magnetic behavior of ferromagnetic material [2]. In this case, the Boltzmann distribution of domain magnetic moments leads to the model of an anhysteretic magnetization curve described by the Langevin function [2]

$$M_{\mathrm{ah}}(H) = M_s \left[\coth\left(\frac{H_e}{a}\right) - \frac{a}{H_e} \right], \tag{1}$$

where M_s is saturation magnetization, $H_e = H + \alpha M$, H is a magnetizing field, α is quantifying the interdomain coupling, M is the total magnetization of the material, and a is given as

$$a = \frac{N\, k_{\mathrm{B}} T}{\mu_0\, M_s}, \tag{2}$$

where N is the number of domains in unit cubic volume, k_{B} is Boltzmann constant, T is temperature, and μ_0 is magnetic constant.

In successive model development presented by Ramesh et al. in 1997 [5], the anisotropy in Maxwell–Boltzmann distribution was considered, leading to the following equation

$$M_{\mathrm{ah}}(H) = M_s \frac{\int_0^{\pi} \mathrm{d}\theta\ \mathrm{e}^{E(1)+E(2)} \sin(\theta)\cos(\theta)}{\int_0^{\pi} \mathrm{d}\theta\ \mathrm{e}^{E(1)+E(2)} \sin(\theta)}, \tag{3}$$

where energies $E(1)$ and $E(2)$ were determined for axial anisotropy as [5]

$$E(1) = \frac{H_e}{a}\cos(\theta) - \frac{K_{\mathrm{an}}}{\mu_0 M_s a}\sin^2(\psi-\theta), \tag{4}$$

$$E(2) = \frac{H_e}{a}\cos(\theta) - \frac{K_{\mathrm{an}}}{\mu_0 M_s a}\sin^2(\psi-\theta). \tag{5}$$

For anisotropic grain-oriented electrical steels, $E(1)$ and $E(2)$ were determined as [6]

$$E\,(1) = \frac{H_e}{a}\cos(\theta) - \frac{K_{\rm an}}{\mu_0 M_s a}\left[\cos^2(\psi-\theta)\sin^2(\psi-\theta) + \frac{\sin^4(\psi-\theta)}{4}\right], \tag{6}$$

$$E\,(2) = \frac{H_e}{a}\cos(\theta) - \frac{K_{\rm an}}{\mu_0 M_s a}\left[\cos^2(\psi+\theta)\sin^2(\psi+\theta) + \frac{\sin^4(\psi+\theta)}{4}\right], \tag{7}$$

where $K_{\rm an}$ is the dominant part of anisotropy energy density. It should be highlighted that the editorial mistake in the original publication presented by Ramesh et al. [5] in 1997 was reproduced in subsequent publications [6]. It can be easily determined that (3) can not be reduced to the Langevin equation for average magnetic anisotropy density equal to zero. Detailed analysis of the original publication indicates that the proper form of (3) should be [7]

$$M_{\rm ah}\,(H) = M_s\,\frac{\int\limits_0^{\pi} {\rm d}\theta\ {\rm e}^{\frac{E(1)+E(2)}{2}}\sin(\theta)\cos(\theta)}{\int\limits_0^{\pi} {\rm d}\theta\ {\rm e}^{\frac{(E(1)+E(2))}{2}}\sin(\theta)}. \tag{8}$$

After the above correction, (8) can be used to model the anhysteretic magnetization of materials with axial and grain-oriented types of anisotropy.

3. Validation of the model

The results of experimental measurements, presented previously in the literature [8], were used to validate the model. The influence of axial anisotropy, both parallel and perpendicular to the magnetization axis, was presented by G. Herzer [9]. The magnetic hysteresis loops of FINEMET $Fe_{73.5}Cu_1Nb_3Si_{13.5}B_9$ nanocrystalline alloy were measured after annealing in the magnetic field. As a result, the soft magnetic alloy with parallel anisotropy $K_{||}$ and two alloys with perpendicular anisotropy and values roughly estimated at $K_{1\perp} = 6$ J/m^3 and $K_{2\perp} = 20$ J/m^3 respectively, were produced [9]. Magnetic hysteresis of produced ring-shaped samples with axial anisotropy was measured in quasistatic conditions with a hysteresigraph system at room temperature [9].

The influence of grain-oriented anisotropy on the magnetic hysteresis loop of 0.30 mm-thick lamination of high-permeability grain-oriented electrical steel (with 3% silicon content) was presented by F. Fiorillo et al. [10]. Measurements were carried out at the Epstein frame according to the technical standard [11]. The anisotropy of grain-oriented electric steel was estimated at $K_{\rm GO} = 100$ J/m^3.

TABLE I

The parameters of the anhysteretic magnetization curve of soft magnetic material with parallel and perpendicular axial anisotropy.

Parameter	Parallel	Perpend. 1	Perpend. 2
M_s [A/m]	9.985×10^5		
α	10^{-6}		
$K_{\rm an}$ [J/m^3]	380.7	6.147	9.952
a [A/m]	0.653	0.452	7.754

TABLE II

The parameters of the anhysteretic magnetization curve of soft magnetic material with grain-oriented anisotropy in rolling (RD) and transverse (TD) direction.

Parameter	RD	TD
M_s [A/m]	1.435×10^6	1.077×10^6
α	6.179×10^{-6}	
$K_{\rm an}$ [J/m^3]	22.42	
a [A/m]	22.415	24.056

The identification of the parameters of the anhysteretic loop was carried out during the optimization process. For the modeling, two assumptions were taken:

1. the anhysteretic curve is located inside the magnetic hysteresis loop B–H of electric steel;
2. magnetic hysteresis is relatively small in the case of high-permeability grain-oriented electrical steel (with 3% of silicon content) measured by F. Fiorillo et al. [10].

A target function F for the optimization was the sum of squared differences between the model and experimental results,

$$F = \sum_{i=1}^{n}\left[B_{\rm an\ model}(H_i) - B_{\rm meas}(H_i)\right]^2, \tag{9}$$

where $B_{\rm an\ model}(H_i)$ was the result of modeling and $B_{\rm meas}(H_i)$ was the result of measurements — both for the value of magnetizing field equal to H_i. The values of flux density of the anhysteretic curve $B_{\rm an\ model}(H_i)$ were calculated for given values of magnetizing field H_i both during the increasing and decreasing of the magnetizing field H.

The differential evolution optimization algorithm [12] was used in the model parameters identification process. The differential evolution algorithm is robust on local minima and enables an efficient identification process. Calculations were performed with the Octave software [13]. For the calculations of integrals in (8), the Gauss–Kronrod quadrature method [14] was utilized.

The results of modeling of anhysteretic magnetization curves for soft magnetic materials with both axial and grain-oriented anisotropy are presented

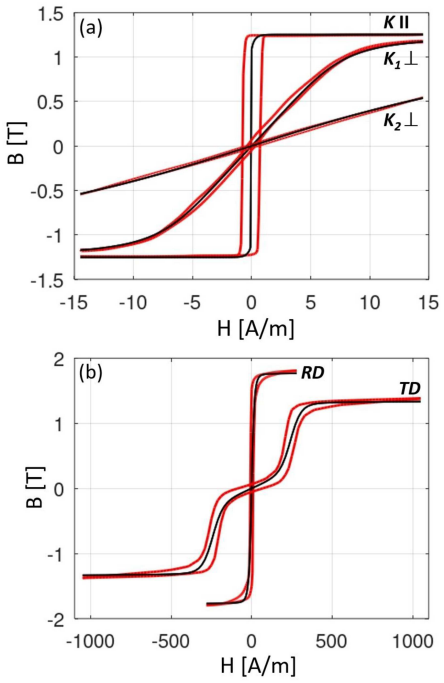

Fig. 1. Results of modeling of anhysteretic magnetization curves of soft magnetic materials: (a) with axial anisotropy, perpendicular $K_{\perp}$ and parallel $K_{||}$ to the magnetizing field H, (b) with grain-oriented anisotropy K_{GO} in the rolling direction (RD) and transverse (TD) direction. Results of modeling — black line, results of $B(H)$ loops measurements — red line.

in Fig. 1, whereas the model parameters of the anhysteretic curves are presented in Tables I and II for the above types of anisotropy, respectively.

The presented results clearly indicated that the model proposed by (4)–(8) very well reproduces the character of the anhysteretic magnetization curve of soft magnetic materials for both axial and grain-oriented anisotropy. This fact is especially important for the grain-oriented electric steel magnetized in the transverse direction, with its sophisticated shape of anhysteretic magnetization curve.

It should also be highlighted that the presented model enables accurate calculation of axial average anisotropy energy density K_{an} for perpendicular axial anisotropy. This good agreement is confirmed by the equation presented by G. Buttino [15]

$$K_{\mathrm{an}} = \frac{B_s^2}{2\mu_0\mu_r}. \tag{10}$$

On the other hand, it was observed that the calculated saturation magnetization M_s for electric steel is different in the rolling direction (RD) than in the transverse direction (TD). This phenomenon can be explained by the fact that in an anhysteretic curve model, saturation magnetization $M_s$should be considered technical saturation, not physical saturation [16].

4. Conclusions

The modeling results confirm that the corrected Maxwell–Boltzmann distribution-based model very well reproduces the character of a hysteretic curve for magnetic materials with axial and grain-oriented anisotropies. This good agreement was confirmed on the basis of experimental results presented previously in the literature.

However, a detailed analysis of achieved model parameters indicates that the physical background of the proposed model of the anhysteretic magnetization curve of anisotropic soft magnetic materials needs development and explanation. This explanation is especially necessary in the area of saturation magnetization of grain-oriented electrical steels with rolling direction and transverse direction anisotropy, as well as in the case of materials with axial anisotropy parallel to the magnetizing field direction.

References

[1] D.C. Jiles, D.L. Atherton, *J. Appl. Phys.* **55**, 2115 (1984).

[2] D.C. Jiles, D.L. Atherton, *J. Magn. Magn. Mater.* **61**, 48 (1986).

[3] R. Szewczyk, M. Nowicki, O. Petruk et al., *J. Magn. Magn. Mater.* **555**, 169376 (2022).

[4] M. Nowicki, *Materials* **11**, 2021 (2018).

[5] A. Ramesh, D.C. Jiles, Y. Bi., *J. Appl. Phys.* **81**, 5585 (1997).

[6] A.P. Baghel, S.V. Kulkarni, *J. Appl. Phys.* **113**, 043908 (2013).

[7] R. Szewczyk, *Materials* **7**, 5109 (2014).

[8] W. Mazgaj, M. Sierzega, Z. Szular, *Energies* **14**, 4110 (2021).

[9] G. Herzer, in: *Handbook of Magnetic Materials*, Elsevier, 1997.

[10] F. Fiorillo, L. Dupré, C. Appino, A.M. Rietto, *IEEE Trans. Magn.* **38**, 1467 (2002).

[11] IEC 60404-2:2008 International Standard, 2018.

[12] R. Storn, K. Price, *J. Glob. Optim.* **11**, 341 (1997).

[13] GNU Octave.

[14] D. Laurie, *Math. Comput.* **66**, 1133 (1997).

[15] G. Buttino, M. Poppi, *J. Magn. Magn. Mater.* **170**, 211 (1997).

[16] R. Szewczyk, *J. Phys. D Appl. Phys.* **40**, 4109 (2007).

Selected papers presented at the 14th Symposium of Magnetic Measurements and Modelling SMMM'2023

Designing an Improved Method to Determine the Anhysteretic Curve in Soft Magnetic Materials via the Jiles–Atherton Model

Z. Roubal* and V. Smejkal

Department of Theoretical and Experimental Electrical Engineering, Brno University of Technology, Technická 12, 612 00 Brno, Czech Republic

Doi: 10.12693/APhysPolA.146.51 *e-mail: roubalz@vutbr.cz

The article discusses a novel procedure for measuring the anhysteretic curve in soft magnetic materials. This curve frequently finds use in diverse applications, such as the Jiles–Atherton hysteresis model. The actual method is characterized in detail, including sample calculations for materials exhibiting various hysteresis loop shapes (ferrites, grain-oriented steel, and nanocrystalline material). To illustrate the benefits of the proposed approach, the authors compare the measurement-based and the simulated curves, the latter being obtained through an optimal interleaving of the model.

topics: anhysteretic curve, Jiles–Atherton hysteresis model, magnetic measurement.

1. Introduction

Hysteresis loop modeling embodies an important task in the analysis of various electrical circuits containing ferromagnetic cores. The applications include, for example, the transient behavior of classic power transformers and the research of switching power supplies. Several descriptions of hysteresis loops are available, including the Preisach mathematical model [1, 2] or the Jiles–Atherton (J-A) formalism [3], often implemented in SPICE-like simulation software. The parameter determination procedure of the Jiles–Atherton model presented in [3] may diverge in some cases. Thus, in a previously published experimental project [4], some modifications of the classic Jiles–Atherton model were analyzed using the least squares method in order to yield an improved hysteresis loop of the nanocrystalline material VITROPERM 500F. Here, the anhysteretic magnetization curve was obtained as an average of the upper and lower parts of the limiting hysteresis loop and was therefore not measured. The differences between the measured loop and that simulated via the Jiles–Atherton model were compared. The problem with the Jiles–Atherton model in approximating the VITROPERM 500F material rests in the rapid transition to saturation, dissimilar from the gradual transition of the Langevin equation [4]. Other sources use different initial approximations of the Jiles–Atherton model's parameters [5–9]. An overview of the state of the art is proposed in [10].

2. Tools for the magnetic curve measurements

The setup shown in Fig. 1 allowed us to characterize the primary magnetization curve, the quasi-static and dynamic hysteresis loop group, and the anhysteretic curve. The original set of instruments [11] was modified by using a more effective analog-to-digital (A/D) sampling device and a voltage-to-current (V/I) converter to deliver high-quality demagnetization of the sample and to measure the anhysteretic curve reliably; in small thorium samples, an automatically zeroed buffer amplifier is applicable [12]. A Siglent SDG2042X DDS generator with the true form technology was utilized to generate the required waveform, providing a sufficient resolution (14-bit) to expose the demagnetization waveform. The generator then excited a V/I converter, developed previously at the Department of Theoretical and Experimental Electrical Engineering (DTEEE) to facilitate magnetic measurements. In the converter, an OPA541 operational amplifier (OA) with a precision-sensing resistor in a Howland circuit is integrated. The requirements comprised a grounded output, stability of the zero converter (a prerequisite for compensation), and high output resistance. The stability at inductive loads was ensured. Generally, the sample can be a toroid or an Epstein frame. The current excites the magnetizing winding N_1 and is sensed at the shunt R_B. An electronic fluxmeter is connected

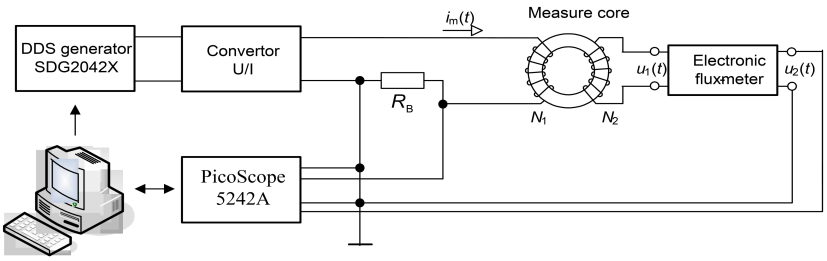

Fig. 1. The measuring setup.

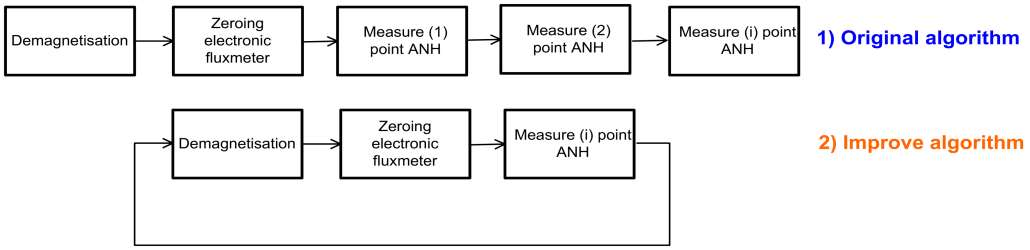

Fig. 2. The conventional and the improved algorithms.

to the secondary measuring winding N_2. The signals are converted into digital form using a 12-bit PicoScope 5242A oscilloscope. In quasi-hysteresis loop measurements, a 30 Hz low-pass filter is set to suppress the 50 Hz mains interference and other spurious effects from, for example, the switching power supply. The data are transferred via a USB[†1] interface to a PC[†2], where the processing is performed in MATLAB.

The measuring configuration is applicable up to a frequency of 5 kHz. At higher frequencies, a voltage amplifier appears to be more advantageous than a V/I converter, providing a harmonic excitation waveform of the magnetic flux density B. Then, measurements up to 100 kHz are feasible with a passive integrator.

3. Improving the algorithm to measure the anhysteretic curve

The various algorithms to measure the anhysteretic curve described in [13] are very demanding in terms of the stability of the zero of the electronic fluxmeter. Multiple measurement variants are possible, assuming three or two windings. When a quasi-static hysteresis loop requiring a processing time of 40 s is measured, we can execute a program-based correction of the measured data if the curve is closed [11]. The stored zero correction is also usable in measuring the initial magnetization curve. This option cannot be employed in an anhysteretic curve or, for example, where the total measurement time corresponds to 30 min and/or the samples are very small (an electronic fluxmeter range of less than 3 mWb) — such a procedure would render the results generally inapplicable.

Thus, in contrast to the original version of the point-by-point sequential measurement, demagnetizing the measured sample and zeroing the electronic fluxmeter took place between each measurement point (Fig. 2). As a result, the requirements for the stability of the electronic fluxmeter zero resemble those that relate to measuring the initial magnetization curve. The signal waveform to enable a single point measurement of the anhysteresis curve is described within

$$i_1(t) = I_{\max}\, \mathrm{e}^{-tA} \sin(2\pi f t) + I_{\mathrm{DC}} \left(1 - \mathrm{e}^{-\frac{t}{\tau}}\right), \tag{1}$$

where $I_{\max}$ is the maximum amplitude of the demagnetization signal, A denotes the amplitude decay constant, f refers to the frequency, I_{DC} represents the setpoint of the anhysteretic curve, and τ is the time constant of the setpoint. Regarding the experimentally preset values to ensure an optimum demagnetization of the sample, the waveform is shown in Fig. 3.

In the selected samples (including the oriented steel Sonaperm, Trafoker S, NiZn ferrite Amidon 43, and nanocrystalline material VITROPERM 500F), the measuring signal parameters read $I_{\max} = 0.6$ A, $A = 0.06$, $f = 1$ Hz, $\tau = 1$ s.

[†1] USB — Universal Serial Bus
[†2] PC — personal computer

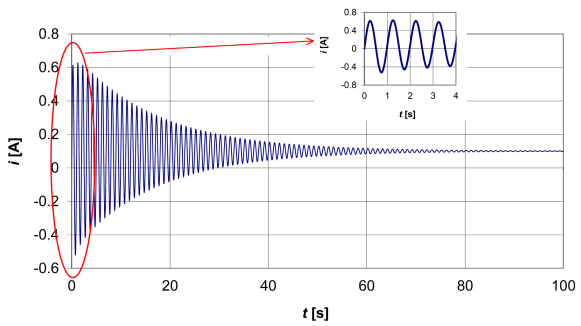

Fig. 3. The measured magnetization signal.

Further, I_{DC} equals zero at demagnetization but then gradually increases until the material is saturated.

In addition to the fluxmeter zero stability issues, we encountered problems with the V/I converter offset in materials having a nearly orthogonal hysteresis loop (Trafoker S). The favorable design, however, allowed the offset converter V/I to exhibit an offset below 20 μA.

The setup also includes a thermocouple to measure the temperature of the sample, similar to the scenario described in [14].

4. The Jiles–Atherton (J-A) hysteresis loop model

The initial equation to characterize this model is one that exposes the behavior in the magnetic material at the domain level. More concretely, the equation embodies a differential description that changes the output according to the varying direction of the input variable, namely the magnetic field strength. The total magnetization M is then given by

$$M = M_{irr} + M_{rev}, \tag{2}$$

where M_{irr} is the irreversible and M_{rev} the reversible magnetization. When the magnetization changes, irreversible shifts occur; these are defined by

$$\frac{\mathrm{d}M_{irr}}{\mathrm{d}H} = \frac{M_{an} - M_{irr}}{k\delta - \alpha\,(M_{an} - M_{irr})}. \tag{3}$$

In (3), M_{an} and M_{irr} denote the lossless (anhysteretic) and the irreversible magnetization, respectively; k is the parameter determining the curve broadening (i.e., the hysteresis losses); δ represents the sign parameter; and α represents the molecular field parameter [3]. The sign function δ follows the change in the direction of the magnetic field strength and is thus specified via

$$\delta = \begin{cases} +1, & \text{for} \quad \frac{\mathrm{d}H}{\mathrm{d}t} > 0, \\ -1, & \text{for} \quad \frac{\mathrm{d}H}{\mathrm{d}t} < 0. \end{cases} \tag{4}$$

Lossless magnetization is an ideal process where no disturbances in the crystal lattice (causing the losses) occur during the magnetization; its actual progress is thus determined by the displacement of the domain walls and the rotation of the spontaneous magnetization of the domains in the direction of the external field. This dependence is most often given by the Langevin function

$$M_{an} = M_{sat}\left[\coth\left(\frac{H_{ef}}{a}\right) - \frac{a}{H_{ef}}\right] = M_{sat}\left[\coth\left(\frac{H+\alpha M}{a}\right) - \frac{a}{H+\alpha M}\right], \tag{5}$$

where M_s is the saturation magnetization (a characteristic of each material, temperature-dependent), a [A/m] denotes the temperature-dependent shape parameter, and H_{ef} stands for the total magnetic field strength; this strength is obtained from the sum of the external field H and the internal (Weiss) field, which is $-\alpha$ times the magnetization M. The parameter α takes on values of the order of approximately 10^{-3} to 10^{-7}. As proposed in [5], (5) was derived for paramagnetic materials and thus does not always approximate the waveform exactly. Then, in some cases, other dependencies are used, such as the Brillouin function given by

$$M_{an} = M_{sat}\cdot\left[\frac{2J+1}{2J}\cosh\left(\frac{2J+1}{2J}\,\frac{H_{ef}}{a}\right) - \frac{1}{2J}\cosh\left(\frac{1}{2J}\,\frac{H_{ef}}{a}\right)\right], \tag{6}$$

where J [-] is the quantum number, a quantity that takes discrete values from 0.5 to ∞ [15], and α [A/m] has a meaning different from that in (5). In general, such a function can be any monotonic increasing function passing through zero and limiting to $\mp M_s$ for H_{ef} going to $\mp\infty$. If the waveform is measured, the obtained values can be applied.

The last part of (2) is reversible magnetization, expressed in the model as the difference between the lossless and the irreversible magnetization, which is attenuated [2], i.e.,

$$M_{rev} = c\,(M_{an} - M_{irr}), \tag{7}$$

where the parameter c belongs to the interval $0 < c < 1$. The resulting formula, which shows the magnetization change with the magnetic field strength variation, is formed by a derivative of (1), an addition to (2), and a derivative of (3); therefore,

$$\frac{\mathrm{d}M}{\mathrm{d}H} = \frac{\mathrm{d}M_{irr}}{\mathrm{d}H} + \frac{\mathrm{d}M_{rev}}{\mathrm{d}H} = \frac{\mathrm{d}M_{irr}}{\mathrm{d}H} + c\left(\frac{\mathrm{d}M_{an}}{\mathrm{d}H} - \frac{\mathrm{d}M_{irr}}{\mathrm{d}H}\right) = (1-c)\,\frac{M_{an}-M_{irr}}{k\delta - \alpha\,(M_{an}-M_{irr})} + c\,\frac{\mathrm{d}M_{an}}{\mathrm{d}H}. \tag{8}$$

The magnetization waveform M corresponding to the input waveform of the magnetic field strength H is then computed similarly to the procedure

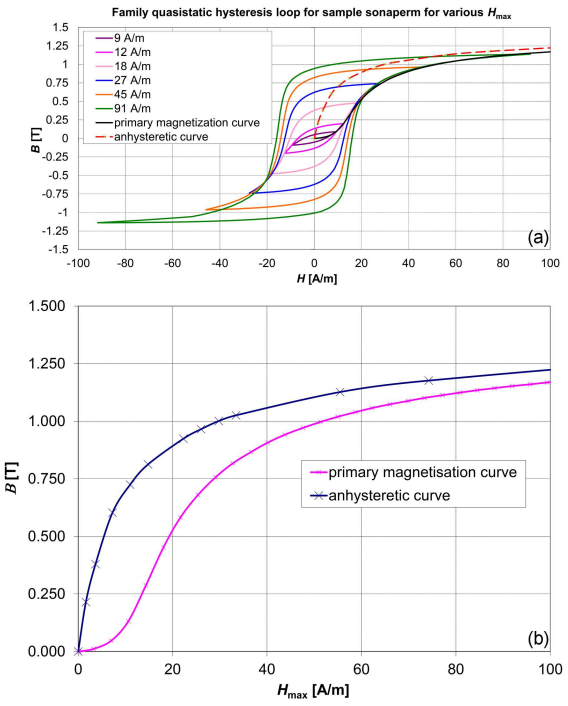

Fig. 4. The measuring hysteresis loop group, initial magnetization curve (a), and anhysteretic curve for the Sonaperm material (b).

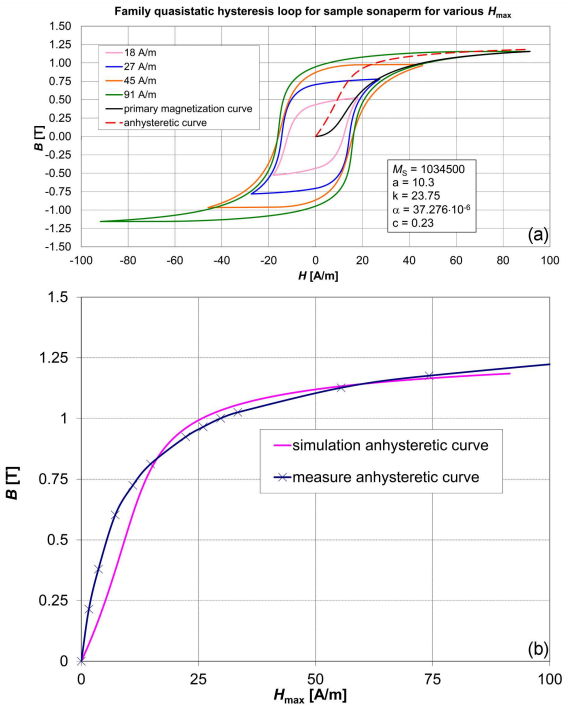

Fig. 5. The simulation hysteresis loop, initial magnetization curve (a), and anhysteretic curve for the Sonaperm material (b).

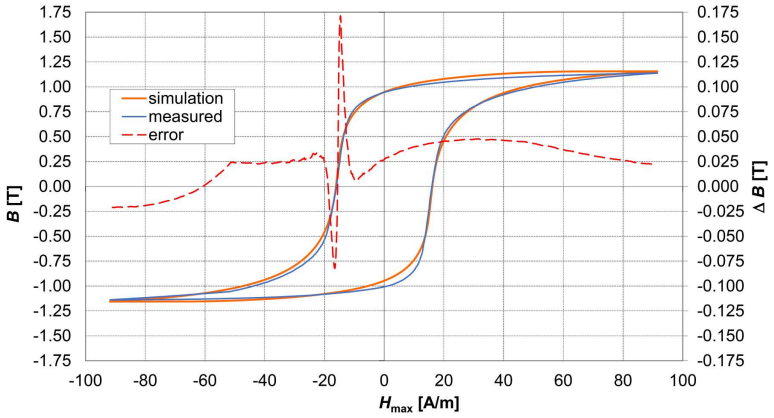

Fig. 6. Comparison of measured and simulated limiting hysteresis loop for the Sonaperm material. The error is calculated for the upper part of the hysteresis loop.

described in [4]: First, the lossless magnetization value is determined, according to options such as that from (5). Next, the change of the irreversible magnetization is established (3). Now, the reversible magnetization (7) is calculated, allowing us to express the resulting magnetization change according to (8). However, the previous values have already been entered, which means that the calculation can be carried out directly. The disadvantage is that an iterative method needs to be employed in the calculation, because the calculated value determined from the derivative of the magnetization and its preceding values appears in the result. During the procedure, we have to check whether the reversible magnetization (2) is smaller than the lossless magnetization in the first quadrant and, similarly, in the third quadrant when the magnetization field strength decreases from the top of the curve.

If the condition is not applied, the magnetization increases where the magnetic field intensity is reduced from the top of the loop, a process that does not correspond to the actual behavior of the magnetic material. In view of the above details, it can be concluded that obtaining the model parameters is not a simple task. It is possible to use the

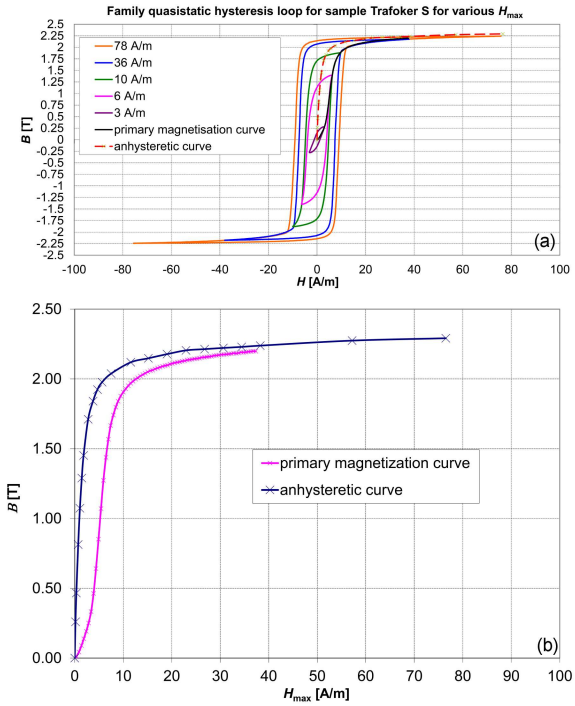

Fig. 7. The measuring hysteresis loop group, initial magnetization curve (a), and anhysteretic curve for the Trafoker S material (b).

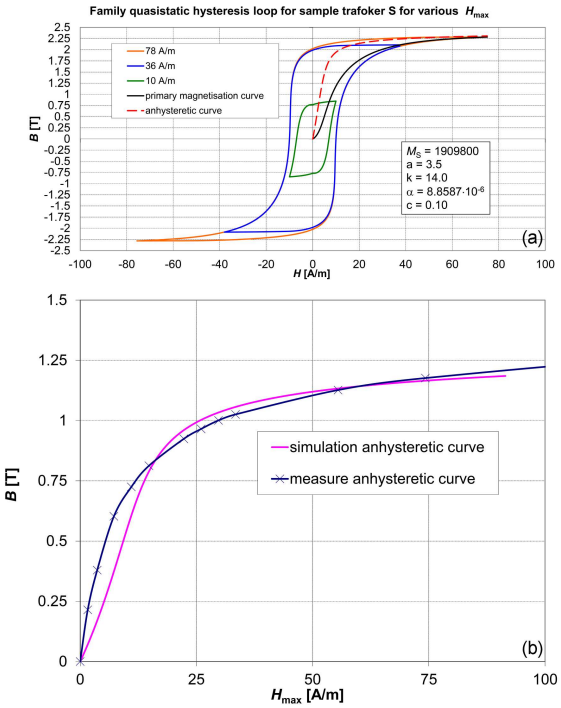

Fig. 8. The simulation hysteresis loop, initial magnetization curve (a), and anhysteretic curve for the Trafoker S material (b).

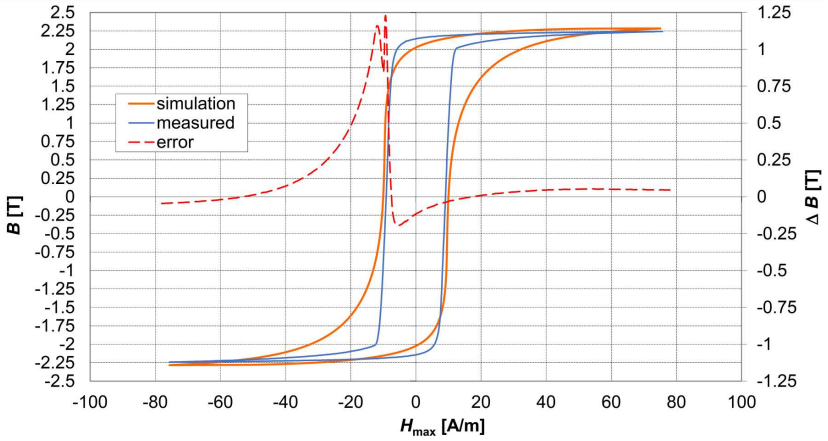

Fig. 9. Comparison of measured and simulated limiting hysteresis loop for the Trafoker S material. The error is calculated for the upper part of the hysteresis loop.

estimation of initial model values from [3] and [6] and then perform their parametric tuning using the least squares method for the best curve fitting.

5. The measured anhysteretic curve as compared with the model

All of the quasi-static hysteresis loops were measured for a period of 40 s, when the influence of eddy currents can be ignored. The excitation signal H was harmonic. A sample of an older oriented Sonaperm tail was used to verify the agreement of the anhysteretic curve measured via a modified algorithm and optimized for the best fit of the hysteresis loop group and the primary magnetization curve (Fig. 4). Such a scenario was employed due to the transition to saturation being more gradual than that of the modern oriented sheets. The toroidal sample had an outer diameter of 110 mm, an inner diameter of 70 mm, and a height of 20 mm. The magnetizing and the measuring winding, N_1 and N_2, had 100 and 50 turns, respectively.

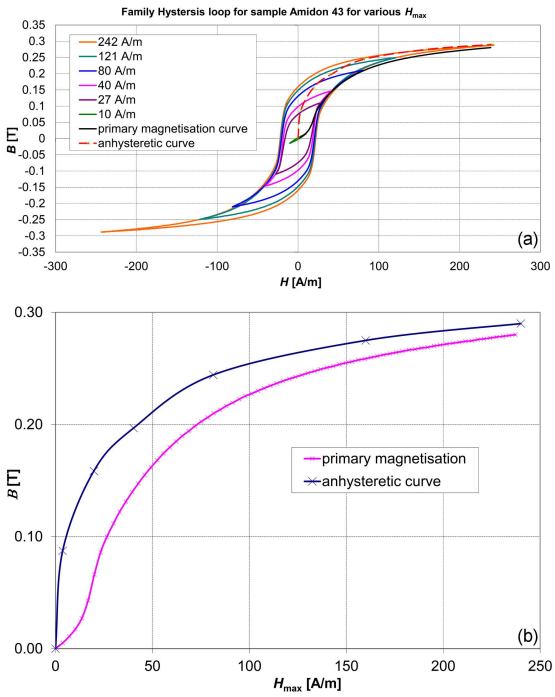

Fig. 10. The hysteresis loop group, initial magnetization curve (a), and anhysteretic curve for the MnZn ferrite material Amidon 43 (b).

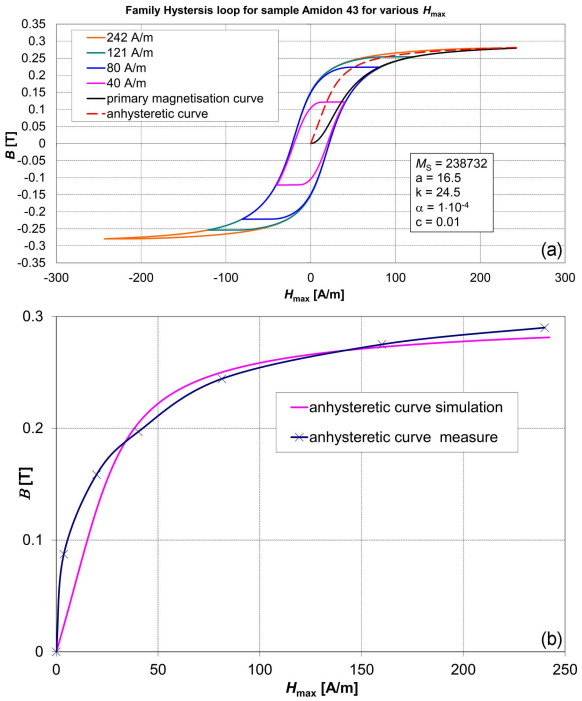

Fig. 11. The simulation hysteresis loop, initial magnetization curve (a), and anhysteretic curve for the ferrite material Amidon 43 (b).

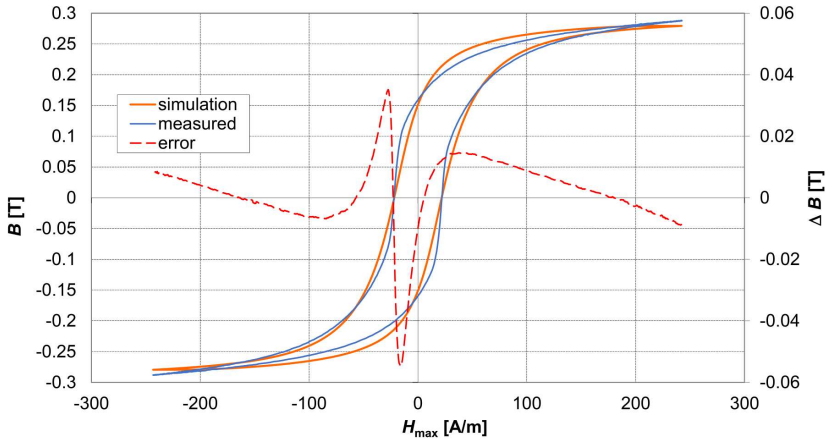

Fig. 12. Comparison of measured and simulated limiting hysteresis loop for the ferrite material Amidon 43.

The optimal parameters of the Jiles–Atherton model were determined in MATLAB by means of the least squares method (Fig. 5). The procedure indicated good agreement with the Langevin function and satisfactory progression of the optimized anhysteretic curve; the largest differences were found in low values of $H_{\max}$ (Fig. 6).

Subsequently, a calculation was performed for the more modern HI-B oriented silicon steel Trafoker S, showing that the J-A model with the Langevin function is practically unable to express the shape of the rectangular hysteresis loop (Figs. 7–9). Using a measured anhysteretic loop did not yield a better approximation. The toroidal sample had an outer diameter of 150 mm, an inner diameter of 110 mm, and a height of 30 mm. The magnetizing winding N_1 and the measuring winding N_2 had 150 and 100 turns, respectively.

The NiZn ferrite Amidon 43 possesses a hysteresis loop with a specific shape (Fig. 10). The initial permeability region is well characterized, but the sharp sides of the hysteresis loop are not visualized at all in the result (Figs. 11 and 12). Again, the measured anhysteretic loop appears to be steeper at the lower values of H.

The Jiles–Atherton model's parameters related to the individual materials. TABLE I

Material	M_s [A/m]	a [A/m]	α ($\times 10^{-6}$)	k [A/m]	c [–]
Sonamperm	1034500	10.3	37.276	23.75	0.23
Trafoker S	1909800	3.5	8.8587	14.0	0.10
Amidon 45	238732	16.5	100	24.5	0.01
Vitroperm 500F	–	–	1	0.75	0.01

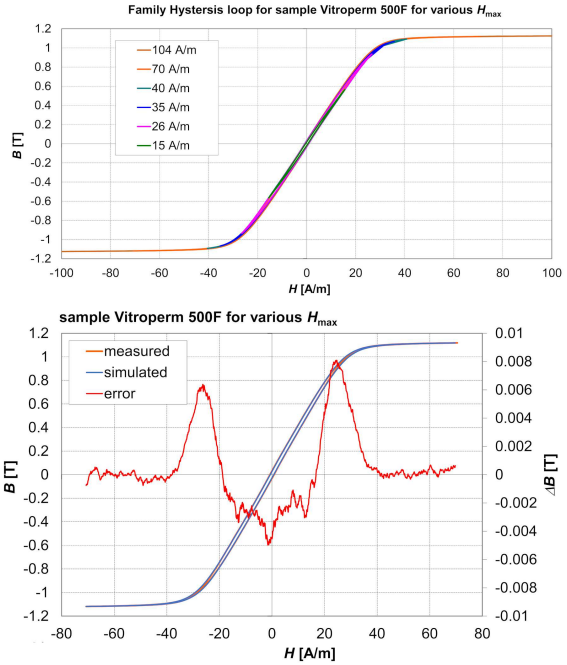

Fig. 13. The measuring hysteresis loop group for Vitroperm 500F (a) and the simulation relating to the measuring anhysteretic curve (b).

The toroidal sample had an outer diameter of 73.7 mm, an inner diameter of 38.9 mm, and a height of 12.7 mm. The magnetizing winding N_1 and the measuring winding N_2 had 135 and 44 turns, respectively.

The Vitroperm 500F nanocrystalline material exhibits a specific shape of the hysteresis loop, is very narrow, and saturates quickly (Fig. 13). Here, the measured anhysteretic loop should be ideally employed in the model to deliver a very small deviation between the measured and the simulated hysteresis loops. The toroidal sample showed an outer diameter of 30 mm, an inner diameter of 20 mm, and a height of 10 mm. The magnetizing winding N_1 had 8 turns, and the measuring winding N_2 had 200 turns.

6. Conclusions

The article presents an algorithm to measure an anhysteretic loop, outlining the typical hysteresis loop shapes (a smooth transition to saturation in the Sonaperm material, sharp transition and right-angled hysteresis loop in Trafoker S, spherical shape in Amidon 43, and a narrow hysteresis loop and sharp transition to saturation in Vitroperm 500F). The characteristics of the materials involved in the project are compared in terms of their characteristics and capabilities (Table I). By extension, the authors discuss the possible limits of the J-A hysteresis loop model. Generally, in strongly anisotropic materials such as Vitroperm 500F, the Langevin function is unsuitable, as it was derived for isotropic materials. Future research is planned to verify our description, modifying the characterization of the anhysteretic curve in accordance with the guidelines proposed in [16]. The procedures exposed herein involved an anhysteretic curve in the form of a table, ensuring the best approximation for the Vitroperm 500F material. The approximation error for the limiting hysteresis loop was below 0.8%.

References

[1] J. Eichler, M. Novák, M. Košek, *Acta Phys. Pol. A* **136**, 713 (2019).

[2] M. Novák, *Acta Phys. Pol. A* **136**, 731 (2019).

[3] D. Jiles, J. Thoelke, M. Devine, *IEEE Trans. Magn.* **28**, 27 (1992).

[4] Z. Roubal, V. Smejkal, in: *2013 9th Int. Conf. on Measurement*, 2013, p. 127.

[5] M. Novák, Ph.D. thesis, Technical University of Liberec, Liberec (Czech Republic) 2003.

[6] D. Lederer, H. Igarashi, A. Kost, T. Honma, *IEEE Trans. Magn.* **35**, 1211 (1999).

[7] K. Hergli, H. Marouani, M. Zidi, *Phys. B Cond. Matter* **549**, 74 (2018).

[8] K. Chwastek, J. Szczyglowski, *Math. Comput. Simulat.* **71**, 206 (2006).

[9] G. Xue, H. Bai, T. Li, Z. Ren, X. Liu, C. Lu, *Mathematics* **10**, 4431 (2022).

[10] R. Szewczyk, *AIP Conf. Proc.* **2131**, 020045 (2019).

[11] Z. Roubal, P. Marcon, M. Čáp, in: *Proc. 9th Int. Conf. 2012 ELEKTRO*, 2012, p. 460.

[12] T. Hejtmánek, Z. Roubal, in: *2021 13th Int. Conf. on Measurement*, 2021, p. 228.

[13] M. Nowicki, *Materials* **11**, 2021 (2018).

[14] T. Charubin, M. Urbański, M. Nowicki, in: *Recent Advances in Systems, Control and Information Technology: Proc. of the Int. Conf. SCIT 2016*, 2016, p. 593.

[15] K. Chwastek, *J. Physics D Appl. Phys.* **43**, 015005 (2009).

[16] R. Szewczyk, *Materials* **7**, 5109 (2014).

Selected papers presented at the 14th Symposium of Magnetic Measurements and Modelling SMMM'2023

Experimental Verification of the Method for Calculating Losses in DC/DC Converter Cores Based on Sinusoidal Excitations

D. Gziel[a,*], M. Najgebauer[a] and Ł. Mierczak[b]

[a] *Częstochowa University of Technology, Faculty of Electrical Engineering, Armii Krajowej 17, 42-200 Częstochowa, Poland*
[b] *Brockhaus Polska, Szparagowa 65, 42-280 Częstochowa, Poland*

Doi: 10.12693/APhysPolA.146.59 *e-mail: damian.gziel@pcz.pl

In this paper, the method for calculating losses in magnetic cores operating in a DC/DC power converter is experimentally verified for selected samples. The chosen method of calculating magnetic losses based on loss measurements under sinusoidal excitation is described, and the measurement process is discussed. The results of power loss measurements with a direct current bias for three different magnetic core materials, e.g., ferrite, nickel–iron–molybdenum alloy powder, and nanocrystalline, are presented. A quantitative determination of the deviations for the tested method is proposed, including the frequency dependence of the deviation distribution.

topics: magnetic core losses, power electronics, DC/DC converter, Steinmetz equations

1. Introduction

The key components of power electronic converters are magnetic cores. Their miniaturization is achieved by increasing the switching frequency, which results in higher losses in the magnetic core [1]. The value of these losses depends primarily on the type of core material [2]. The operation of the DC/DC power electronic converter causes the magnetic core of the inductor to operate under non-sinusoidal excitation conditions. In the analyzed case, the magnetic flux density has a triangular waveform, which, in addition to the frequency and amplitude, is characterized by the presence of a direct current (DC) component B_{DC}. The occurrence of the DC part of magnetic flux density B is related to the flow of unidirectional current through the inductor's windings, which causes the core to be magnetized with the DC component of the magnetic field strength H_{DC}. In the case of some magnetic materials, DC pre-magnetization has a significant impact on the loss level and cannot be neglected [3, 4]. The commonly used Steinmetz equation, as well as its modifications, e.g., those described in [5], do not allow one to take into account the influence of the constant component of the magnetic field strength on losses. The method based on the Steinmetz pre-magnetization graph (SPG) proposed in [3] requires many measurements in the converter operating conditions and adjustment of the coefficients for the improved generalized Steinmetz equation (IGSE) to the results obtained for subsequent H_{DC} values. Therefore, there is a need to develop, verify, and improve methods for estimating power losses of magnetic cores operating under such conditions. The article presents the results of experimental verification of the method for calculating losses in magnetic cores operating in a DC/DC converter based on sinusoidal losses for magnetic cores other than those in the original studies [6, 7].

2. Method description

The approach analyzed in this article was presented in [6] and [7]. This method uses sinusoidal losses with equivalent frequency to model losses with non-sinusoidal excitations. The equation for the energy density lost during one complete magnetization cycle with sinusoidal excitation was also analyzed [6]

$$Q_V = \frac{P_V(\tau)}{f} = C_m f^{x(f)-1} B^{y(f)} (c_{t_2}\tau^2 - c_{t_1}\tau + c_t), \tag{1}$$

where C_m, x, y are parameters characterizing the magnetic material; τ — core operating temperature, f — core magnetization frequency; P_V — power losses related to the core volume; c_{t_2}, c_{t_1}, c_t — coefficients of the polynomial taking into account the influence of temperature. This formula is based on the Steinmetz equation, however, it is expressed for energy losses and supplemented

with a polynomial taking into account the influence of temperature. The energy losses depend on the derivative of the magnetic flux density $\mathrm{d}B/\mathrm{d}t$. Assuming that $\dot{B} = \mathrm{d}B/\mathrm{d}t$, the arbitrary shape of the magnetic flux density can be represented using a linear-segmental description containing a weighting factor. This approach may also be useful in cases other than a DC/DC converter. The formula for the equivalent frequency of a sinusoidal signal in [7] takes the form

$$f_{\mathrm{eq(sin)}} = \frac{2}{\pi^2} \sum_{k=1}^{K} \left(\frac{B_k - B_{k-1}}{B_{\max} - B_{\min}} \right)^2 \frac{1}{t_k - t_{k-1}}, \qquad (2)$$

where K — the number of consecutive k-th segments of the linear-segmental magnetic flux density course. For a rectangular voltage waveform magnetizing the inductor core operating in a DC/DC converter, the magnetic flux density waveform in the core is triangular. If this waveform is symmetrical, then the frequency of the equivalent sinusoidal waveform can be expressed as [6]

$$f_{\mathrm{eq(sin)}} = \frac{8}{\pi^2} f_{\mathrm{rect}}, \qquad (3)$$

where f_{rect} is the frequency of the magnetic flux density waveform (excited by a rectangular voltage waveform) in the inductor core operating in a DC/DC converter. In [7], the authors proposed to include the equivalent frequency into the IGSE [8], obtaining a formula expressing the energy loss. Thereby, when the converter operates with a duty cycle of $D = 0.5$, which corresponds to a symmetrical triangular course of magnetic flux density, the equation for the energy lost in the core is simplified to the following form [7]

$$Q_{\mathrm{rect}} = Q_{\mathrm{eq(sin)}} \left(\Delta B_{\mathrm{rect}}, H_{\mathrm{DC}}, f_{\mathrm{eq(sin)}} \right), \qquad (4)$$

where ΔB is peak-to-peak magnetic flux density in the core; Q_{rect} and $Q_{\mathrm{eq(sin)}}$ — energy lost in the magnetic core under rectangular and sinusoidal excitation, respectively. As follows from (4), the energy lost in the core of the inductor operating in a DC/DC converter can be determined on the basis of sinusoidal losses for the equivalent frequency while maintaining the same value of the constant component of the magnetic field strength H_{DC} and the peak-to-peak magnetic flux density in the core, ΔB. Hence, to determine the losses corresponding to the operating conditions of the DC/DC converter, necessary measurements must be carried out.

3. Measurement process

The measurements results presented in [6, 7] confirmed the usefulness of the equivalent frequency method in loss modeling, however, the results obtained only concerned cores made of ferrite material 3C85 (Philips) [7] and iron powder material SK-08KSTB (TOHO ZINC) [6]. For this reason, the aim of this research is to verify the applicability of (4) in the loss calculation for magnetic cores made of other materials. It was assumed that the method verification would be carried out for the duty cycle $D = 0.5$, which corresponds to the symmetrical, triangular shape of the magnetic flux density waveform in a core. Three magnetic cores made of different materials were selected for testing, as presented in Table I (see also [9–11]).

TABLE I

Magnetic cores selected for measurements (A_L — inductance coefficient value for the number of turns $N = 1$) [9–11].

Core material	Core model name	A_L [nH]
N87 (ferrite core)	B64290L0038X087	900
MP (nickel, iron, molybdenum alloy powder material)	MP-065205-2	123
VITROPERM 500F (nanocrystalline core)	T60004-L2063-W627-52	18000

Inductors with powder or ferrite cores are often found in DC/DC converters. If a ferrite core is used, a core with a discrete air gap should be used to enable the inductor to operate at a higher DC. In the case of powder material, the material structure ensures the so-called distributed air gap in the core. In this research, all tested samples were without discrete air gaps to avoid the additional fringing effect associated with these core types [12, 13]. This phenomenon introduces unnecessary complications related to the loss measurements [14, 15], which is not desirable for the verification of the analyzed method. The nanocrystalline material VITROPERM 500F is generally used in the area of electromagnetic compatibility (EMC) applications (e.g., common mode chokes [11]). However, it was included in the research due to its different internal structure compared to the other samples. In order to verify the correctness of the analyzed method, measurements were carried out first in the operating conditions of a DC/DC converter and then with sinusoidal excitation at the equivalent frequency $f_{\mathrm{eq(sin)}}$ in accordance with the assumptions resulting from (4), i.e., with the same H_{DC} and ΔB values. The Brockhaus MPG 200 measurement system was used to measure the magnetic losses of selected cores. The system accuracy is $\leq 0.2\%$ and concerns the measurement of power losses under sinusoidal excitation conditions. In order to obtain core operating conditions corresponding to operation in a DC/DC converter, the "Free Curves" option was used to generate a custom waveform shape of the magnetic flux density by the measuring device. The accuracy of the measurement system for this option is $\leq 1.5\%$. The base clock accuracy of the data acquisition card in the measurement system

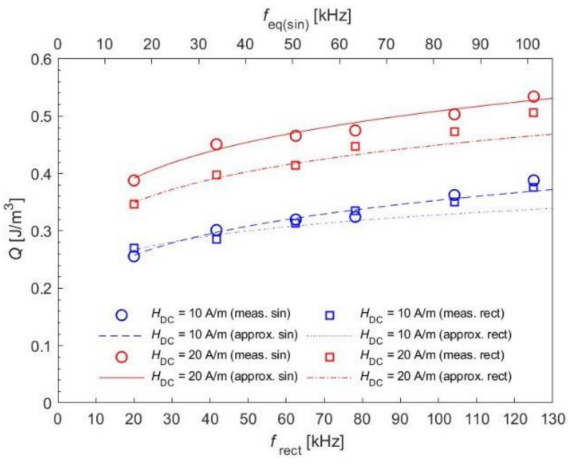

Fig. 1. Energy core losses versus frequency at $\Delta B = 0.1$ T.

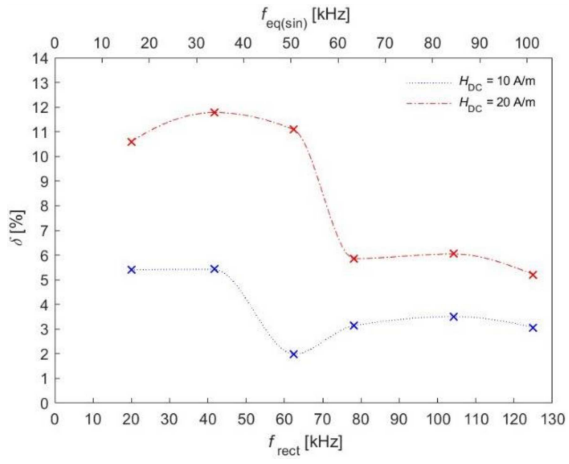

Fig. 2. Method deviation for N87 ferrite core at $\Delta B = 0.1$ T.

is ±0.01%. An additional limitation during measurements is the maximum number of points from which the measurement system can generate a custom waveform. For the maximum frequency of the triangular signal during measurements (rectangular voltage waveform), the f_{rect} frequency is 125 kHz, and this waveform is generated from only 20 points. At the lowest excitation frequency, $f_{\mathrm{rect}} = 10$ kHz, the waveform is generated from 100 points. The results are presented in the form of energy losses Q (per one complete sinewave cycle) related to the core volume, as presented in [6]. Since the accuracy of the measurement system is better with sinusoidal excitations, the energy loss measured for such excitations was taken as a reference point. Due to the fact that formula (3) can be transformed to determine the frequency in the conditions of a DC/DC converter based on the frequency of sinusoidal excitation, the following formula was proposed to assess the accuracy of the analyzed method

$$\delta_{\%} = \frac{\left|Q_{\mathrm{rect}} - Q_{\mathrm{eq(sin)}}\right|}{Q_{\mathrm{eq(sin)}}} \cdot 100\%. \tag{5}$$

4. Results and discussion

Energy losses measured in core operating under conditions corresponding to a DC/DC converter (values indicated by the square marker) and under sinusoidal excitation conditions (at the equivalent frequency and maintaining the same H_{DC} and ΔB values — indicated by the round marker) are presented in the figures below. The curves (solid or dashed) presented in the figures approximate the results based on a power function. Measurements were carried out for two different values of the DC component of the magnetic field strength. In the figures, the lower horizontal axis indicates the frequency of the rectangular voltage excitation, while

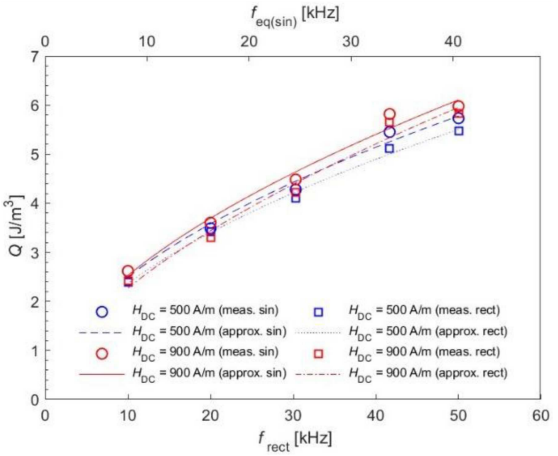

Fig. 3. Energy core losses versus frequency at ΔB = 0.2 T (MP-065205-2 powder core).

the upper horizontal axis indicates the corresponding value of the equivalent frequency of the sinusoidal excitation. The vertical axis indicates the energy lost according to the approach presented in [7].

Figures 1 and 2 present the energy loss measurements and the method deviation for ferrite core N87.

As expected, the measured energy losses increased with magnetization frequency. Moreover, the energy loss level was also noticeably dependent on the value of the DC component of magnetic field strength. In the case of the N87 ferrite core, the method provided an acceptable convergence of the measured and calculated values of core losses (Fig. 2). It should also be noted that in the case of the ferrite core, the approximation deviations were about two times higher for the larger DC component of $H_{\mathrm{DC}} = 20$ A/m.

The results obtained for the MP powder core are depicted in Figs. 3 and 4. Generally, the increase in energy losses in the function of frequency

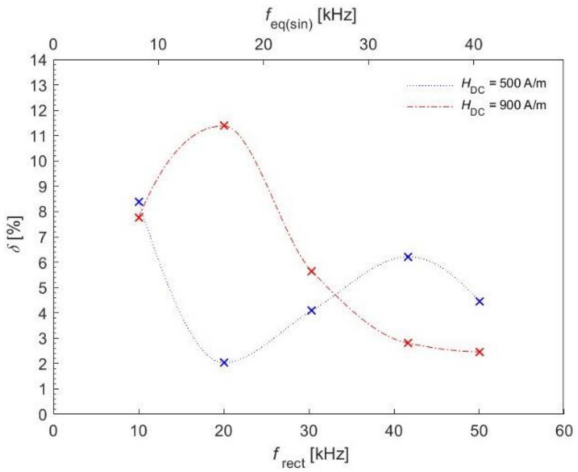

Fig. 4. Method deviation for MP-065205-2 powder core at $\Delta B = 0.2$ T.

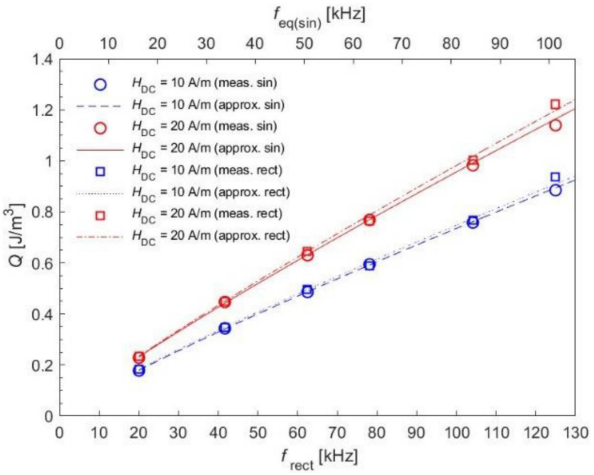

Fig. 5. Energy core losses versus frequency at $\Delta B = 0.2$ T (VITROPERM 500F nanocrystalline core).

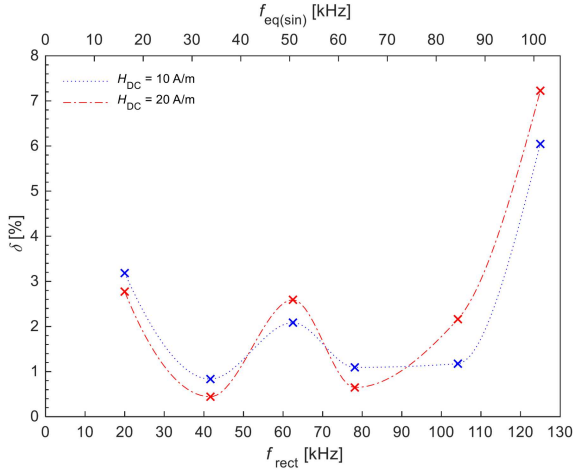

Fig. 6. Method deviation for VITROPERM 500F nanocrystalline core at $\Delta B = 0.2$ T.

is more dynamic than in the case of the N87 ferrite core. On the contrary to the ferrite core, only a very small increase in energy loss depending on the H_{DC} value was observed. This is a favorable feature of the MP powder core, especially for applications in DC/DC converters, because the losses are almost independent of the converter load current for a specific operating frequency. Due to the limitations of our measurement system, this core was measured in a lower frequency range (up to 50 kHz). As shown in Fig. 4, the method deviation does not exceed 12%.

Finally, Figs. 5 and 6 present the results for the last core made of VITROPERM 500F nanocrystalline material. Similarly to the other measured cores, energy losses strongly depended on the core magnetization frequency. For the nanocrystalline core, energy losses determined by the verified method provided small deviations in almost the entire frequency range, and the obtained deviation values indicated a weak dependence on the H_{DC} values.

5. Conclusions

In this paper, the method of estimating losses of inductor cores operating in the conditions of a DC/DC converter was presented. The analyzed method, based on losses measured at sinusoidal excitations, was verified for three different types of core material. Energy loss values provided by magnetic core manufacturers are usually determined for sinusoidal excitation conditions. Additionally, these losses are not obtained from measurements under DC bias conditions. For this reason, core losses cannot be easily estimated based directly on (3)–(4) without additional measurements. The verified method for loss estimation provided satisfactory results for the core made of nanocrystalline alloy. The maximum deviation of the loss estimation did not exceed 8%, and in a wide frequency range up to 110 kHz, the deviation was lower than 3.2%. For the constant component $H_{DC} = 10$ A/m, the method gave similar deviation values for both the nanocrystalline and ferrite cores. Slightly larger deviations (for $H_{DC} = 10$ A/m) occur for the powder core. However, for a higher value of the H_{DC} component, the method deviation in the case of the ferrite core increased noticeably in contrast to the nanocrystalline core. Due to the limitations of the measurement system, the frequency range for the MP powder core was limited (from 10 to 50 kHz). It is worth noting that in the original paper [7], the method for loss calculation was verified for another powder core (SK-08KSTB) for a frequency range limited to approximately 20 to 50 kHz. The results presented in this paper for the MP powder core are within acceptable limits appropriate for practical application.

Concluding, the analyzed method provided satisfactory results for calculating losses in the case of a symmetric triangular waveform of magnetic flux density in nanocrystalline (VITROPERM 500F) and ferrite (N87) inductor cores operating in DC/DC converters and acceptable results for nickel–iron–molybdenum alloy powder material (MP) in limited frequency range. Verification of the correctness of the analyzed method for other magnetic materials in extended frequency ranges, magnetic flux density, and duty cycle will be the subject of further research that would allow us to determine the limits of its applicability.

Acknowledgments

The project was financed under the program of the Polish Minister of Science and Higher Education under the name "Regional Initiative of Excellence" in the years 2019–2023, project number 020/RID/2018/19, the amount of financing PLN 12 000 000.

References

[1] D. Reusch, J. Strydom, J. Glaser, in: *2015 IEEE Energy Conversion Congress and Exposition (ECCE), Montreal*, IEEE, 2015 p. 381.

[2] D. Rodriguez-Sotelo, M. A. Rodriguez-Licea, A. G. Soriano-Sanchez, A. Espinosa-Calderon, F. J. Perez-Pinal, *IEEE Access* **8**, 56238 (2020).

[3] J. Mühlethaler, J. Biela, J.W. Kolar, A. Ecklebe, *IEEE Trans. Power Electron.* **27**, 953 (2012).

[4] A. Brockmeyer, in: *Proc. of Applied Power Electronics Conf. (APEC '96), San Jose*, IEEE, 1996, p. 454.

[5] D. Gzieł, M. Najgebauer, *Przegląd Elektrotechniczny* **96**, 238 (2020).

[6] M. Albach, T. Duerbaum, A. Brockmeyer, in: *PESC Record. 27th Annual IEEE Power Electronics Specialists Conf., Baveno (Italy)*, IEEE, 1996 p. 1463.

[7] H. Matsumori, T. Shimizu, T. Kosaka, N. Matsui, *AIP Adv.* **10**, 045001 (2020).

[8] K. Venkatachalam, C. R. Sullivan, T. Abdallah, H. Tacca, in: *2002 IEEE Workshop on Computers in Power Electronics, 2002. Proc., Mayaguez (PR)*, IEEE, 2002, p. 36.

[9] TDK, Ferrites and Accessories, 2023.

[10] Micrometals, MP-065205-2, 2021.

[11] Vacuumschmelze, Nanocrystalline Vitroperm EMC Products, 2021.

[12] A. Ayachit, M.K. Kazimierczuk, *IET Circuits Devices Syst.* **11**, 209 (2017).

[13] D. Gzieł, A. Jąderko, *Przegląd Elektrotechniczny* **99**, 292 (2023).

[14] A. Ayachit, M.K. Kazimierczuk, *IEEE Magn. Lett.* **7**, 1 (2016).

[15] Y. Miwa, T. Shimizu, K. Takano, H. Ishii, *IEEJ J. Ind. Appl.* **8**, 57 (2019).

Selected papers presented at the 14th Symposium of Magnetic Measurements and Modelling SMMM'2023

Comparison of Rayleigh Model and Steinmetz Law in Evaluation of Hysteresis Losses in Low Magnetizing Fields

M. Kachniarz*

Warsaw University of Technology, Institute of Metrology and Biomedical Engineering, A. Boboli 8, 02-525 Warszawa, Poland

Doi: 10.12693/APhysPolA.146.64 *e-mail: maciej.kachniarz@pw.edu.pl

The purpose of the following paper is to compare the applicability of Rayleigh hysteresis model and Steinmetz law in the evaluation of power losses of selected soft magnetic materials under the influence of low magnetizing fields. Both approximations are relatively simple in terms of computational complexity, thus they seem to be appropriate for technical applications that do not require extensive knowledge of the physical properties of the material. The selected soft magnetic materials, i.e., steels and ferrites, in the form of toroidal cores, were investigated in low magnetizing fields with a computer-controlled hysteresisgraph system. Both considered models were applied to the obtained power loss characteristics. The quality of the description provided by each model was compared in terms of root-mean-square deviation and determination coefficient R^2, which allowed us to choose the more suitable approximation.

topics: root-mean-square deviation, power loss, Rayleigh model, Steinmetz law

1. Introduction

Measurement and evaluation of power losses of inductive components seem to be crucial in terms of energy saving and reducing CO_2 emission in modern industry. About 285 TWh is lost annually in distribution transformers of power grids only [1], not taking into account losses of inductive components massively widespread in electronic devices.

Modeling of power losses in medium and high magnetizing fields is relatively complex. It can be performed utilizing elaborated physical models of magnetic hysteresis, like the Preisach model or the Jiles–Atherton model [2], by numerical integration of the computed hysteresis loop. However, it seems ineffective in engineering practice where simplicity of calculation is an important factor. Also, physical models dedicated to hysteresis losses, like the Pry and Bean model [3–5] or the Bertotti model [6–9], are not easily applicable, as they require knowledge of multiple microstructural parameters of the material. Moreover, these models are based either on special functions, like the modified Bessel function of the first kind in the Pry and Bean model, or on the time derivative of the magnetic flux density, which is computable only for basic waveform shapes (sinusoidal, triangular). For technical applications, models based on elementary functions and not necessarily involving microstructural parameters seem to be more suitable. Fortunately, in the case of low magnetizing fields of the so-called Rayleigh region, there is a possibility of utilizing such a model, as power losses can be approximated with the Rayleigh hysteresis model or Steinmetz law. Both are relatively simple mathematical approximations, based on second-order polynomial and power function, respectively, so they meet the established requirement of low computational complexity.

In the paper, the effectiveness of both approximations is compared on the set of measurement data including low-field power losses of four soft magnetic materials, i.e., two Ni–Zn ferrites and two structural steels. The quality of the approximation is expressed by means of normalized root-mean-square deviation (NRMSD) between the model and measurement data and determination coefficient R^2.

2. Investigated power loss models

The subject of investigation are two power loss models applicable for low magnetizing field regions. Both are simple mathematical approximations, convenient for technical applications.

The low magnetizing field region (Rayleigh region) is an initial part of the magnetization curve, where the macroscopic magnetization process is mostly governed by elastic deflections and translations of the domain walls, which give rise to the reversible and irreversible components of

magnetization, respectively [10]. Therefore, magnetic hysteresis occurs in this region, however, the hysteresis loop exhibits a peculiar shape, sometimes referred to as a lenticular loop [11, 12] or Rayleigh loop [13, 14]. The shape results from both branches of the loop being symmetrical second-order curves, whose intersection points are vertices of the loop. The commutation curve, composed of these vertices, follows the second-order equation known as Rayleigh law of magnetization [10, 13–15], i.e.,

$$B(H) = \mu_0 \left(\mu_i H + \nu_R H^2\right), \tag{1}$$

where B is magnetic flux density, H — magnetizing field, μ_i — initial relative magnetic permeability, ν_R — so-called Rayleigh coefficient, and $\mu_0 = 4\pi \times 10^{-7}$ H/m — magnetic permeability of free space. The linear term refers to a reversible component of magnetization, while the quadratic term describes an irreversible component giving rise to the magnetic hysteresis.

The Rayleigh hysteresis model was first introduced by Lord Rayleigh in 1887 [16]. The basis of the model is the assumption of linear dependence of relative magnetic permeability μ on the magnetizing field H [10, 13]

$$\mu(H) = \mu_i + \nu_R H, \tag{2}$$

which underlies the law of magnetization (1). Moreover, Rayleigh came to the realization that the lenticular hysteresis loop observed in the weak magnetizing field could be also described with the second-order equation, which for descending (upper) branch takes the form [10, 13, 14]

$$B_{\searrow}(H) = \mu_0 \left[\left(\mu_i + \nu_R H_m\right) H + \frac{\nu_R}{2}\left(H_m^2 - H^2\right)\right], \tag{3}$$

and for ascending (lower) branch

$$B_{\nearrow}(H) = \mu_0 \left[\left(\mu_i + \nu_R H_m\right) H - \frac{\nu_R}{2}\left(H_m^2 - H^2\right)\right], \tag{4}$$

where H_m is the amplitude of the magnetizing field. Later, on the basis of (3) and (4), equations describing specific parameters of the hysteresis loop were formulated, including coercive field, magnetic remanence, and energy loss density in the magnetization cycle. Due to the hysteresis loop being described by continuous functions that can be integrated, it is possible to provide an analytical formula for power loss. Total energy loss density corresponds to the surface area of the hysteresis loop [7, 10]

$$w_H = \int_{-B_m}^{B_m} \mathrm{d}B \; H(B), \tag{5}$$

with B_m being the maximum value of magnetic flux density. Note that (5) originates from the calculation of loop area A_H, so geometrically it is a product of the double integral over the surface limited by the $B_{\searrow}(H)$ and $B_{\nearrow}(H)$ functions. The form of total energy loss given by (5), most often provided in the literature, is obtained by changing the order of integration. However, in the Rayleigh region, the straight dependence between magnetic flux density and magnetizing field is known, as $B_{\searrow}(H)$ and $B_{\nearrow}(H)$ are given by (3) and (4), respectively. Therefore, the natural order of integration is more suitable. As the domain of integration can be considered as area A_H limited by magnetizing field extrema H_m and $-H_m$ and branches of the hysteresis loop $B_{\searrow}(H)$ and $B_{\nearrow}(H)$, (5) can be expressed by means of the double integral over the area A_H enclosed by hysteresis loop

$$w_H = \iint_{A_H} \mathrm{d}H \, \mathrm{d}B = \int_{-H_m}^{H_m} \mathrm{d}H \int_{B_{\nearrow}(H)}^{B_{\searrow}(H)} \mathrm{d}B = \int_{-H_m}^{H_m} \mathrm{d}H \, \Big(B_{\searrow}(H) - B_{\nearrow}(H)\Big). \tag{6}$$

After substitution, one can obtain

$$w_H = \int_{-H_m}^{H_m} \mathrm{d}H \; \mu_0 \Big(\mu_i H + \nu_R H_m H + \frac{\nu_R}{2} H_m^2 - \frac{\nu_R}{2} H^2 - \mu_i H - \nu_R H_m H + \frac{\nu_R}{2} H_m^2 - \frac{\nu_R}{2} H^2\Big), \tag{7}$$

which leads to

$$w_H = \mu_0 \alpha_R \int_{-H_m}^{H_m} \mathrm{d}H \; \left(H_m^2 - H^2\right) = \mu_0 \nu_R \left(H_m^2 \, 2H_m - \frac{2H_m^3}{3}\right) = \mu_0 \nu_R \left(2H_m^3 - \frac{2}{3} H_m^3\right). \tag{8}$$

This finally results in the expression of dependence between energy loss density w_H and magnetizing field amplitude H_m in the Rayleigh region [7, 13]

$$w_H\left(H_m\right) = \frac{4}{3} \mu_0 \nu_R \, H_m^3. \tag{9}$$

Therefore, the expression for power loss during dynamic magnetization in a low magnetizing field region takes the form

$$P_H\left(H_m\right) = f V_e \, \frac{4}{3} \mu_0 \nu_R \, H_m^3, \tag{10}$$

where f is the magnetizing field frequency, and V_e — effective volume of the magnetic material.

The Steinmetz law, in its basic form, was originally introduced in 1890 [17]. The dependence of the energy loss density on the maximum magnetic flux density takes the form of a simple power function [17, 18]

$$w_H(B_m) = \alpha B_m^{\eta}. \tag{11}$$

Exponent η is called the Steinmetz exponent (originally reported to be 1.6 [17]), and α is a proportionality factor. Thus, the power loss can be expressed as

$$P_H(B_m) = f V_e \alpha B_m^{\eta}. \tag{12}$$

TABLE I

Main magnetic properties of the investigated soft magnetic materials: $Ni_{0.36}Zn_{0.64}Fe_2O_4$ (A), $Ni_{0.36}Zn_{0.67}Fe_{1.97}O_4$ (B), X30Cr13 (C), and 13CrMo4-5 (D).

Material	A	B	C	D
B_m [T]	0.325	0.260	1.280	1.590
H_c [A/m]	45	95	785	670
B_r [T]	0.120	0.087	0.940	1.245
μ_i [−]	600	250	100	80
V_e [cm^3]	21.04	22.44	2.52	2.52

On the basis of the original Steinmetz law, numerous modifications were developed to better adapt it to the nonlinear character of the magnetization process [19]. A further extension of the power-function-based approximation are models based on the Widom scaling procedure [20, 21]. However, in the case of a low magnetizing field, the magnetic flux density waveform is relatively less distorted from the shape of the magnetizing waveform. Therefore, the nonlinearity of the magnetization process is less meaningful, and expression (12), based on the original Steinmetz equation, might be utilized for power loss approximation.

3. Investigated materials and measurement methodology

Four soft magnetic materials were selected for the experiment. Two of them were ferromagnetic ceramic materials (ferrites) of chemical composition $Ni_{0.36}Zn_{0.64}Fe_2O_4$ and $Ni_{0.36}Zn_{0.67}Fe_{1.97}O_4$, utilized for magnetic cores of wideband transformers and inductive coils. The other two were structural alloy steels X30Cr13 and 13CrMo4-5, used in the power industry. The main magnetic properties of the materials are summarized in Table I. In the case of ferrites, the presented data are provided according to the specification of the manufacturer — POLFER S.A. Maximum magnetic flux density B_m, coercive field H_c, and magnetic remanence B_r provided for steels were previously measured in the saturation region ($H_m = 5$ kA/m). Initial magnetic permeability μ_i of steels was previously determined for the frame-shaped samples used in magnetoelastic investigation [22, 23].

Investigated materials were formed into toroidal cores, providing a closed magnetic circuit within the sample in order to reduce the demagnetizing field [7]. Each sample was characterized by the effective volume V_e, calculated on the basis of geometrical dimensions of the sample.

The measurements were performed with a digitally controlled hysteresisgraph system. Dynamic magnetic characteristics of all four materials were investigated with the linearly changing magnetizing field (triangle waveform). The magnetizing field frequency for ferrites was 1.0 Hz, while for steels, it was 0.1 Hz. Such low frequencies allowed to significantly reduce the eddy current losses [24], especially in the case of steels. Thus, equation (5), in this case, describes the pure magnetic hysteresis losses.

For each material, a family of several hysteresis loops was measured with increasing values of the magnetizing field amplitude H_m. The limits of H_m corresponding to the Rayleigh region for investigated materials were established according to the values previously presented in paper [25]. Among other parameters, measured loops were characterized by the power loss P_H, which allowed us to obtain the characteristics of P_H as a function of maximum magnetic flux density B_m. All measurements were performed in standard laboratory conditions.

4. Results and discussion

On the basis of experimental results, the characteristics of power loss P_H were determined for the investigated materials. In order to provide a clear reference for both models, the dependence of P_H on maximum magnetic flux density B_m is presented.

The Rayleigh model coefficients of investigated materials were already determined in the previous research [25]. As can be seen in (12), only the Rayleigh coefficient ν_R affects the modeled value of power loss P_H. Coefficients of the Steinmetz law (10) were determined by means of linear regression. Applying natural logarithm to both sides of (12) leads to the expression

$$\ln(P_H) = \ln(fV_e\alpha) + \eta \ln(B_m)\,, \tag{13}$$

thus reducing the problem to linear dependence $y = b + ax$. Linear regression provides directly the value of $\eta = a$, while α is given as

$$\alpha = \frac{e^b}{fV_e}. \tag{14}$$

The determined values of coefficients are presented in Table II. The values of Steinmetz exponent η significantly exceed the original value of 1.6. However, it has to be noted that the presented results were obtained with a non-sinusoidal magnetic flux density waveform. This may lead to the increased exponent η, as well as to a more rapid failure of the model in approximation of power losses with B_m increasing further outside the Rayleigh region, where the nonlinearity of the magnetization process is getting more significant.

Model curves calculated with designated coefficients were applied to the experimental results and are presented in Figs. 1–4. The lower values of power loss for steels result from a much lower effective volume V_e of the steel cores used in the experiment (Table I).

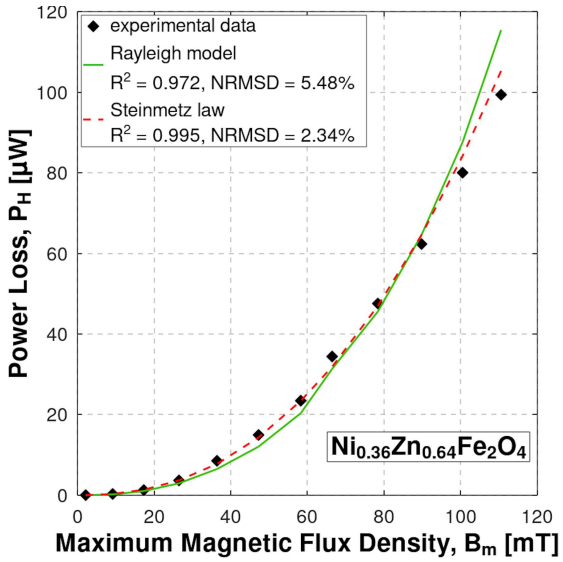

Fig. 1. Results of measurement and modeling of power loss P_H with Rayleigh model and Steinmetz law for $Ni_{0.36}Zn_{0.64}Fe_2O_4$ ferrite.

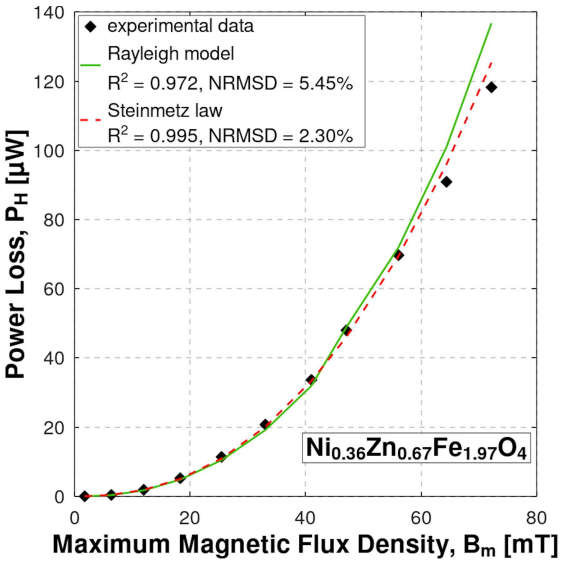

Fig. 2. Results of measurement and modeling of power loss P_H with Rayleigh model and Steinmetz law for $Ni_{0.36}Zn_{0.67}Fe_{1.97}O_4$ ferrite.

TABLE II

Determined values of coefficients of Rayleigh model [25] and Steinmetz law for investigated materials: $Ni_{0.36}Zn_{0.64}Fe_2O_4$ (A), $Ni_{0.36}Zn_{0.67}Fe_{1.97}O_4$ (B), X30Cr13 (C), and 13CrMo4-5 (D).

Material	Rayleigh model		Steinmetz law	
	μ_i [–]	ν_R [m/A]	α [–]	η [–]
A	644	10.45	881.63	2.35
B	285	1.90	2634.63	2.34
C	69	0.16	23456.43	2.69
D	64	0.79	5336.49	2.41

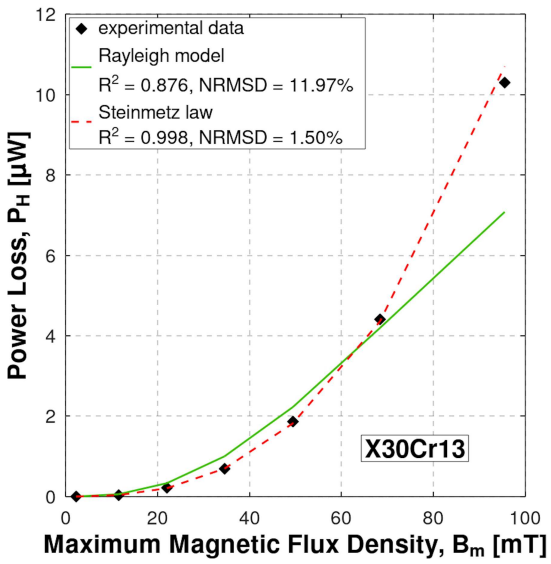

Fig. 3. Results of measurement and modeling of power loss P_H with Rayleigh model and Steinmetz law for X30Cr13 steel.

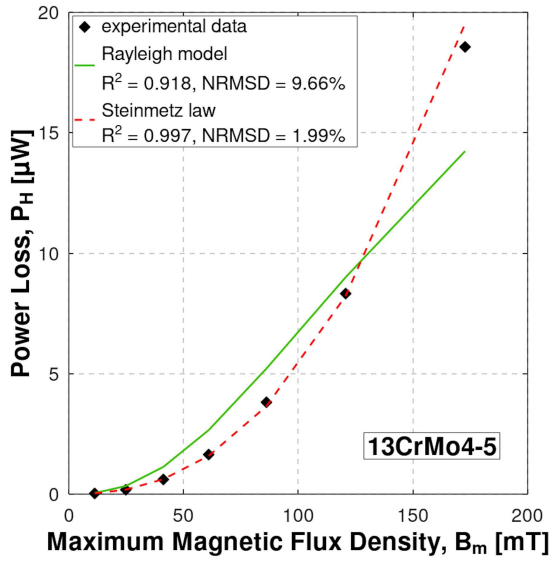

Fig. 4. Results of measurement and modeling of power loss P_H with Rayleigh model and Steinmetz law for 13CrMo4-5 steel.

In the case of Ni–Zn ferrites (Figs. 1 and 2), both models seem to approximate measured power losses relatively well. The Steinmetz law is slightly more consistent with experimental data. For steels (Figs. 3 and 4), the situation is more diversified. The Rayleigh model provides a significantly worse approximation, especially for points near the end of the measurement range. However, as it was previously presented in [25], the transition from the lenticular loop to the sigmoidal loop of investigated steels is much more rapid than in the case of ferrites and takes place in the fields much below the coercive field of the material. This results in a less accurate approximation of magnetic parameters, including

TABLE III

Statistical metrics of Rayleigh model and Steinmetz law for investigated materials: $Ni_{0.36}Zn_{0.64}Fe_2O_4$ (A), $Ni_{0.36}Zn_{0.67}Fe_{1.97}O_4$ (B), X30Cr13 (C), and 13CrMo4-5 (D).

Material	Rayleigh model		Steinmetz law	
	R^2 [–]	NRMSD [%]	R^2 [–]	NRMSD [%]
A	0.972	5.48	0.995	2.34
B	0.972	5.45	0.995	2.30
C	0.876	11.97	0.998	1.50
D	0.918	9.66	0.997	1.99

power loss, for the fields near the Rayleigh region limit. On the other hand, the Steinmetz law was proven to be valid also for the fields beyond the Rayleigh region, so the decrease in approximation quality near the region limit does not occur.

The quality of approximation for both models was evaluated with two statistical metrics. The determination coefficient R^2 was calculated according to the following formula [26]

$$R^2 = 1 - \frac{\sum_{i=1}^{n}\left(P_{Hi}-\hat{P}_{Hi}\right)^2}{\sum_{i=1}^{n}\left(P_{Hi}-\frac{1}{n}\sum_{i=1}^{n}P_{Hi}\right)^2}, \tag{15}$$

where P_{Hi} is the experimental value, $\hat{P}_{Hi}$ — value estimated by the model, and n — number of measurement points. Root-mean-square deviation (RMSD) normalized by the range of measured values — NRMSD — is expressed as [26]

$$\mathrm{NRMSD} = \frac{1}{\Delta P_{Hi}}\sqrt{\frac{1}{n}\sum_{i=1}^{n}\left(P_{Hi}-\hat{P}_{Hi}\right)^2}, \tag{16}$$

where ΔP_{Hi} is the range of measured values of P_{Hi}. The metrics characterizing both models were calculated for each investigated material. The resulting values are summarized in Table III.

The presented results indicate that for all investigated materials, the Steinmetz law provides better approximation in terms of both R^2 and NRMSD. Again, the difference is especially significant for steels. Values of NRMSD for Steinmetz law are in this case five to eight times lower than for the Rayleigh model. However, both models allow us to relatively well estimate the power loss P_H with R^2 over 0.9 (except for the Rayleigh model for X30Cr13 steel). The advantage of Steinmetz law results partially from the direct fitting of the model curve to the experimental data, while coefficients of the Rayleigh model are determined on the basis of fitting the Rayleigh law of magnetization (1) to the commutation curve. Such indirect determination of model coefficients might negatively influence the quality of approximation.

5. Conclusions

The experimental data presented in the paper allowed us to compare the power loss approximation capability in low magnetizing fields of two simple mathematical models: the Rayleigh model of hysteresis and Steinmetz law. Both models were applied to the set of experimental data obtained for two different kinds of soft magnetic materials: ferrimagnetic Ni–Zn ferrites and ferromagnetic structural steels.

The modeling results indicate that both models approximate the power loss in the Rayleigh region with satisfying quality. For ferrites, the determination coefficient R^2 is relatively high, slightly preferring Steinmetz law. In the case of steels, the difference in the quality of description is more prominent, and the statistical metrics of the Rayleigh model are significantly worse than those of Steinmetz law. The reason is probably a more rapid transformation of the hysteresis loop shape with increasing field amplitude, which does not follow the Rayleigh description well, but is in good agreement with the Steinmetz equation developed for a wider range of magnetizing fields, including high permeability region.

Despite the fact that both investigated models can be considered satisfyingly accurate in the estimation of power losses of soft magnetic materials in low magnetizing fields, further investigation is still required to validate the models for a higher range of magnetizing field frequency. Also, the investigation of modified versions of Steinmetz law seems to be interesting and may lead to further improvement of the approximation quality.

References

[1] R. Hasegawa, D. Azuma, *J. Magn. Magn. Mater.* **320**, 2451 (2008).

[2] F. Liorzou, B. Phelps, D.L. Atherton, *IEEE Trans. Magn.* **36**, 418 (2000).

[3] R.H. Pry, C.P. Bean, *J. Appl. Phys.* **29**, 532 (1958).

[4] T. Matsuo, M. Shimasaki, *IEEE Trans. Magn.* **42**, 919 (2006).

[5] K. Chwastek, A.P.S. Baghel, P. Borowik, B.S. Ram, S.V. Kulkarni, in: *2016 Progress in Applied Electrical Engineering (PAEE), Koscielisko-Zakopane*, IEEE, 2026.

[6] G. Bertotti, *IEEE Trans. Magn.* **24**, 621 (1988).

[7] G. Bertotti, *Hysteresis in Magnetism for Physicists, Materials Scientists, and Engineers*, Acad. Press, San Diego 1998.

[8] B. Koprivica, K. Chwastek, *Acta Phys. Pol. A* **136**, 709 (2019).

[9] J. Szczygłowski, P. Kopciuszewski, K. Chwastek, M. Najgebauer, W. Wilczyński, *Arch. Electr. Eng.* **60**, 59 (2011).

[10] B.D. Cullity, C.D. Graham, *Introduction to Magnetic Materials*, John Wiley & Sons, New York 2009.

[11] W.B. Ellwood, *Physics* **6**, 215 (1935).

[12] Yu.N. Starodubtsev, V.A. Kataev, K.O. Bessonova, V.S. Tsepelev, *J. Magn. Magn. Mater.* **479**, 19 (2019).

[13] D.C. Jiles, *Introduction to Magnetism and Magnetic Materials*, Chapman & Hall, London 1998.

[14] Yu.F. Ponomarev, *Phys. Met. Metallogr.* **104**, 469 (2007).

[15] J. Kováč, B. Kunca, L. Novák, *J. Magn. Magn. Mater.* **502**, 166555 (2020).

[16] Lord Rayleigh, *Philos. Mag.* **23**, 225 (1887).

[17] C.P. Steinmetz, *Trans. AIEE* **IX**, 1 (1892).

[18] F.J.G. Landgraf, M. Emura, M.F. de Campos, *J. Magn. Magn. Mater.* **320**, e531 (2008).

[19] D. Gzieł, M. Najgebauer, *Przegląd Elektrotechniczny* **97**, 238 (2020).

[20] M. Najgebauer, *Acta Phys. Pol. A* **131**, 1225 (2017).

[21] M. Najgebauer, in: *2019 Progress in Applied Electrical Engineering (PAEE), Koscielisko-Zakopane*, IEEE, 2019.

[22] M. Kachniarz, R. Szewczyk, *J. Electr. Eng.* **66**, 82 (2015).

[23] M. Kachniarz, K. Kołakowska J. Salach, R. Szewczyk, P. Nowak *Acta Phys. Pol. A* **133**, 660 (2018).

[24] P. Jabłoński, M. Najgebauer, M. Bereźnicki, *Energies* **15**, 2869 (2022).

[25] M. Kachniarz, R. Szewczyk, *Acta Phys. Pol. A* **131**, 1244 (2017).

[26] G. James, D. Witten, T. Hastie, R. Tibshirani, *An Introduction to Statistical Learning*, Springer, New York 2013.

Selected papers presented at the 14th Symposium of Magnetic Measurements and Modelling SMMM'2023

Structure and Magnetic Properties of the Magnetocaloric MnCoGe Modified by W

K. Kutynia, A. Przybył and P. Gębara*

Department of Physics, Częstochowa University of Technology, Armii Krajowej 19, 42-200 Częstochowa, Poland

Doi: 10.12693/APhysPolA.146.70 *e-mail: piotr.gebara@pcz.pl

The investigation of the nonmagnetic W-substitution effect on the structure and magnetocaloric properties of the MnCoGe alloy was conducted. The analysis of phase composition revealed the coexistence of a hexagonal Ni_2In-type phase and an orthorhombic TiNiSi-type phase. A detailed analysis of XRD patterns supported by Rietveld analysis showed changes in the lattice constants and the content of recognized phases, which depended on the W content in the alloy. A monotonic decrease in the Curie temperature with an increase in W content in the alloy composition was noticed. The values of ΔS_M measured for the variation of the external magnetic field ~ 5 T were equal to 5.30, 4.16, 2.32, and 3.01 for $Mn_{0.97}W_{0.03}CoGe$, $Mn_{0.95}W_{0.05}CoGe$, $Mn_{0.93}W_{0.07}CoGe$, and $Mn_{0.9}W_{0.1}CoGe$ alloy, respectively. The analysis of n vs T curves recovered for the tested alloys was characteristic of second-order phase transition.

topics: magnetocaloric effect, MM'X alloys, X-ray diffraction (XRD)

1. Introduction

Magnetic cooling is a phenomenon based on the magnetocaloric effect (MCE) and is a more environmentally friendly method of lowering temperature than conventional cooling techniques. This phenomenon has been known to mankind for over a hundred years, but we are still looking for ideal magnetocaloric materials that can be used commercially. The magnetocaloric effect is described as an adiabatic temperature change (ΔT_{ad}) or an isothermal change in magnetic entropy (ΔS_M). This phenomenon was discovered in 1881 by Warburg [1] and described in more detail independently by Debye in 1926 [2] and Giaugue in 1927 [3], but only thanks to research conducted by Pecharsky and Gschneidner Jr. in 1997 [4], the number of publications related to the topic of magnetocaloric materials increased exponentially. Currently, alloys are sought that are relatively cheap but also have the desired properties (large change in magnetic entropy ΔS_M and appropriate Curie temperature T_C).

At present, many scientists are focusing on MnCoGe alloys belonging to the group of MM'X alloys (where M or M' is a transition metal and X — a metalloid), which are characterized by excellent magnetocaloric properties. MM'X alloys crystallize in two phases: a high-temperature hexagonal phase of the Ni_2In-type (space group $P6_3/mmc$) and a low-temperature orthorhombic phase of the TiNiSi-type (P_{nma}) [5]. The magnetic moments of MM'X alloys are strongly related to the crystal structure because they cause magnetic transitions to be associated with discontinuous changes in the crystal symmetry as well as lattice parameters. Thanks to this feature, these alloys can exhibit gigantic MCE around the occurring first-order magnetostructural phase transitions [6].

Our previous articles based on MnCoGe alloys were based on partial substitution of Zr [7] and Pd [8] dopants. These changes improved the value of the magnetic entropy change and also increased the Curie temperature. Taking into account the research results described in [9], we decided to investigate the influence of the W dopant on the structure and magnetocaloric properties of $Mn_{1-x}W_xCoGe$ (where $x = 0.03$, 0.05, 0.07, and 0.1).

2. Sample preparation and experimental details

The ingot samples were prepared by arc-melting of high-purity constituent elements under low pressure of Ar. Compositions were established as follows: $Mn_{0.97}W_{0.03}CoGe$, $Mn_{0.95}W_{0.05}CoGe$, $Mn_{0.93}W_{0.07}CoGe$, and $Mn_{0.9}W_{0.1}CoGe$. Samples were remelted ten times in order to ensure their homogeneity. The structural study was based on X-ray diffraction and was carried out using a Bruker D8 ADVANCE diffractometer with Cu K_α radiation. Qualitative and quantity analysis was supported by

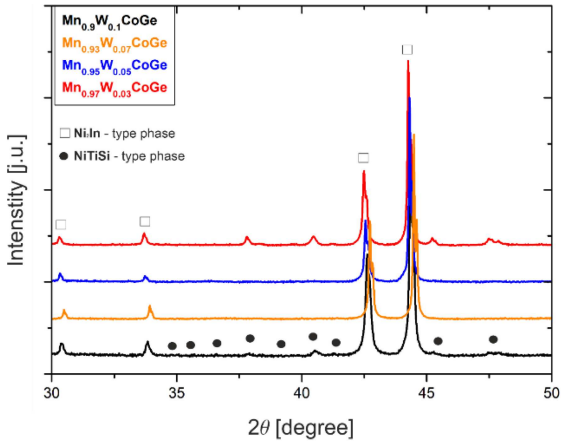

Fig. 1. The X-ray diffraction patterns collected at room temperature for samples of produced alloys.

Bruker EVA 4.0 software and PowderCell 2.4 package for the Rietveld refinement [10]. The magnetic properties (i.e., the Curie temperature and magnetic isotherms) were investigated using the Quantum Design Physical Properties Measuring System (PPMS) Model 6000, working over a wide range of magnetic fields and temperatures. In order to check structural transformation, the differential scanning calorimetry (DSC) curves were collected using a differential scanning calorimeter NETZSCH 214 Polyma (Selb, Germany) with a heating and cooling rate of 10 K/min. The microstructural observations were registered using scanning electron microscopy (SEM) JEOL 6610LV equipped with energy dispersive X-ray spectrometer (EDS).

3. Results and discussion

Figure 1 shows the XRD patterns of all tested $Mn_{1-x}W_xCoGe$ samples (where $x = 0.03$, 0.05, 0.07, and 0.1). The analysis revealed two different phases in the studied series of samples: dominant hexagonal Ni_2In phase and minor orthorhombic NiTiSi phase. During the analysis, reflexes corresponding to the orthorhombic NiTiSi-type phase were clearly visible for samples with $x = 0.03$ and 0.1. In the case of samples with $x = 0.05$ and 0.07, traces of this phase were detected. Moreover, the highest content of volume fraction of the NiTiSi-type phase with a minor Ni_2In-type phase for the $Mn_{0.9}W_{0.1}CoGe$ alloy was detected.

The calculations of the lattice constant for the recognized phases showed its monotonic rise with an increase in W in each sample. Such an effect is related to the different ionic radius of W ($r_W = 1.41$ Å) compared to a much lower Mn radius ($r_{Mn} = 1.18$ Å). In the work of Bażela et al. [11], the orthorhombic cell was treated as a distorted hexagonal cell, therefore in the case of the W atom, it affects the distortion of the cell and also favors the crystallization of the hexagonal Ni_2In-type phase, which is not desirable, taking into account magnetocaloric properties. A detailed examination of X-ray diffractograms excluded contamination with additional phases. The conclusions from the quantitative and qualitative analysis were supported by the Rietveld improvements, and the results are presented in Table I.

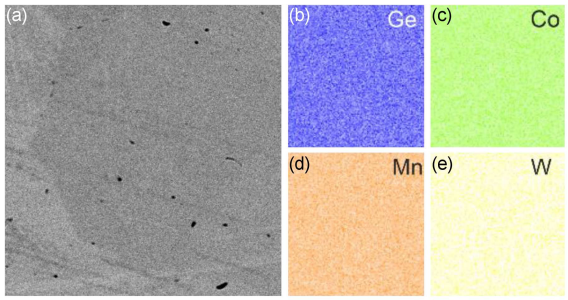

Fig. 2. The SEM micrograph (a) and corresponding EDS maps of the $Mn_{0.95}W_{0.05}CoGe$ alloy sample (b–e).

TABLE I

Data delivered by the Rietveld analysis for the investigated $Mn_{1-x}W_xCoGe$ alloy samples.

Alloy	Recognized phases	Lattice constant [Å] ±0.001	Volume fraction [%]
$Mn_{0.97}W_{0.03}CoGe$	hex Ni_2In-type	$a = 4.071$ $c = 5.284$	83
	ort NiTiSi-type	$a = 5.933$ $b = 3.819$ $c = 7.049$	17
$Mn_{0.95}W_{0.05}CoGe$	hex Ni_2In-type	$a = 4.073$ $c = 5.287$	93
	ort NiTiSi-type	$a = 5.937$ $b = 3.821$ $c = 7.051$	7
$Mn_{0.93}W_{0.07}CoGe$	hex Ni_2In-type	$a = 4.075$ $c = 5.286$	94
	ort NiTiSi-type	$a = 5.939$ $b = 3.824$ $c = 7.053$	6
$Mn_{0.9}W_{0.1}CoGe$	hex Ni_2In-type	$a = 4.079$ $c = 5.292$	92
	ort NiTiSi-type	$a = 5.943$ $b = 3.828$ $c = 7.061$	8

The microstructure of the samples was observed using the SEM technique. Fragment of the microstructure of the $Mn_{0.95}W_{0.05}CoGe$ sample is shown in Fig. 2a. The EDS maps collected for the tested sample microstructure show a uniform distribution of the components (Fig. 2b –e), which was expected based on previous studies presented in [8]. The concentration of nominal composition, i.e.,

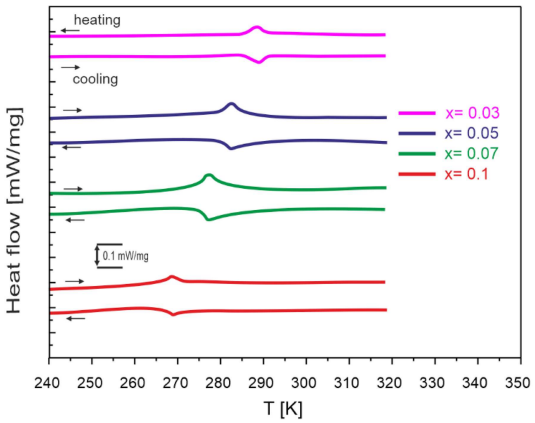

Fig. 3. The DSC curves and temperature dependences of magnetization (field cooling regime at $\Delta(\mu_0 H) = 0.1$ T).

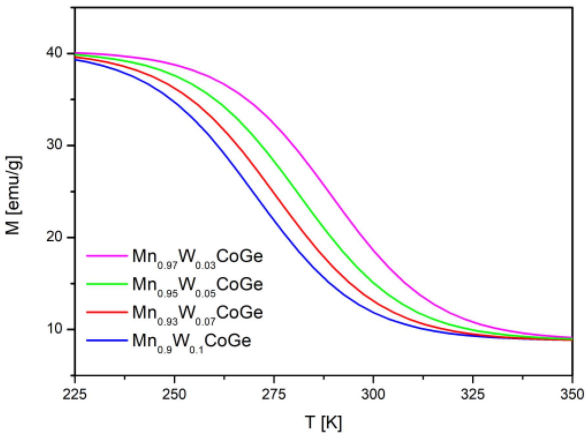

Fig. 4. The temperature dependences of magnetization collected under the external magnetic field of 0.1 T for all studied samples.

Mn — 31.67 at.%, W — 0.02 at.%, Co — 33.33 at.%, and Ge — 33.33 at.%, corresponds well with the values obtained by EDS measurement, i.e., Mn — 31.52 ± 0.22 at.%, W — 0.95 ± 0.18 at.%, Co — 33.2 ± 0.25 at.%, and Ge — 34.33 ± 0.36 at.%, respectively.

The DSC measurements performed for W-doped MnCoGe alloys are summarized in Fig. 3. DSC tests were performed to confirm the results of XRD analysis and to determine the temperatures of structural and magnetic transitions. Endothermic and exothermic peaks are present in all tested samples. The lambda-type peaks were detected for all studied samples in the vicinity of 282 K and 277 K for $Mn_{0.95}W_{0.05}CoGe$ and $Mn_{0.93}W_{0.07}CoGe$ alloy, respectively. The presence of lambda peaks in DSC curves suggests an occurrence of second-order phase transition in investigated specimens.

In order to reveal the Curie point of produced samples, the temperature dependences of magnetization were collected in a magnetic field of 0.1 T (in field cooling regime for the whole series (Fig. 4)). The Curie temperature was revealed by calculations of the first derivative of the M vs T dependences measured for all samples. The estimated values of the T_C were 284 ± 1, 276 ± 1, 270 ± 1, 265±1 K for $Mn_{0.97}W_{0.03}CoGe$, $Mn_{0.95}W_{0.05}CoGe$, $Mn_{0.93}W_{0.07}CoGe$, and $Mn_{0.9}W_{0.1}CoGe$, respectively. A gradual decrease in T_C was observed, which may be due to the reduction of the magnetic moment Mn by the addition of W. As it was mentioned above, the atomic radius of W is larger than Mn. It causes an increase in interatomic distances between Mn–Mn, Mn–Co, and Co–Co, which induces the weakening of exchange interactions and a decrease in the Curie temperature. Moreover, thermal hysteresis was not observed in all studied samples, which is also a confirmation of the occurrence of second-order phase transition in the produced materials [12].

The magnetocaloric effect is determined using indirect methods by calculating the change in magnetic entropy ΔS_M. These studies are based on magnetic isotherms measured over a wide range of temperatures. Maxwell's relations were used to calculate the change in magnetic entropy ΔS_M [13]

$$\Delta S_M(T, \Delta H) = \mu_0 \int_0^H \mathrm{d}H \left(\frac{\partial M(T,H)}{\partial T}\right)_H, \qquad (1)$$

where μ_0 is magnetic permeability, H is the magnetic field strength, M is the magnetization, and T is the temperature. The above equation (1) was implemented in Mathematica using the algorithm below [14]

$$\Delta S_M \frac{(T_i + T_{i+1})}{2} \approx \frac{1}{T_{i+1} - T_i} \left[\int_0^{B_{\max}} \mathrm{d}B\ M(T_{i+1}, B) - \int_0^{B_{\max}} \mathrm{d}B\ M(T_i, B) \right], \qquad (2)$$

where B is the magnetic field induction to the relation $B = \mu_0 H$.

The calculated temperature dependences of magnetic entropy change for all samples are presented in Fig. 5. The highest ΔS_M values calculated for a magnetic field change of ∼ 5 T were 5.30, 4.16, 3.23, and 3.01 J/(kg K) for $Mn_{0.97}W_{0.03}CoGe$, $Mn_{0.95}W_{0.05}CoGe$, $Mn_{0.93}W_{0.07}CoGe$, and $Mn_{0.9}W_{0.1}CoGe$, respectively. Similarly to our previous work on the selective substitution of Mn by Zr [7] and Pd [8], the change in magnetic entropy was the largest for the Zr and Pd dopant content of $x = 0.05$. An increase in the content of the W addition causes a decrease in the value of the magnetic entropy change, which confirmed the results of measuring the Curie temperature. Moreover, a successive significant broadening of the ΔS_M peak with an increase in W content was

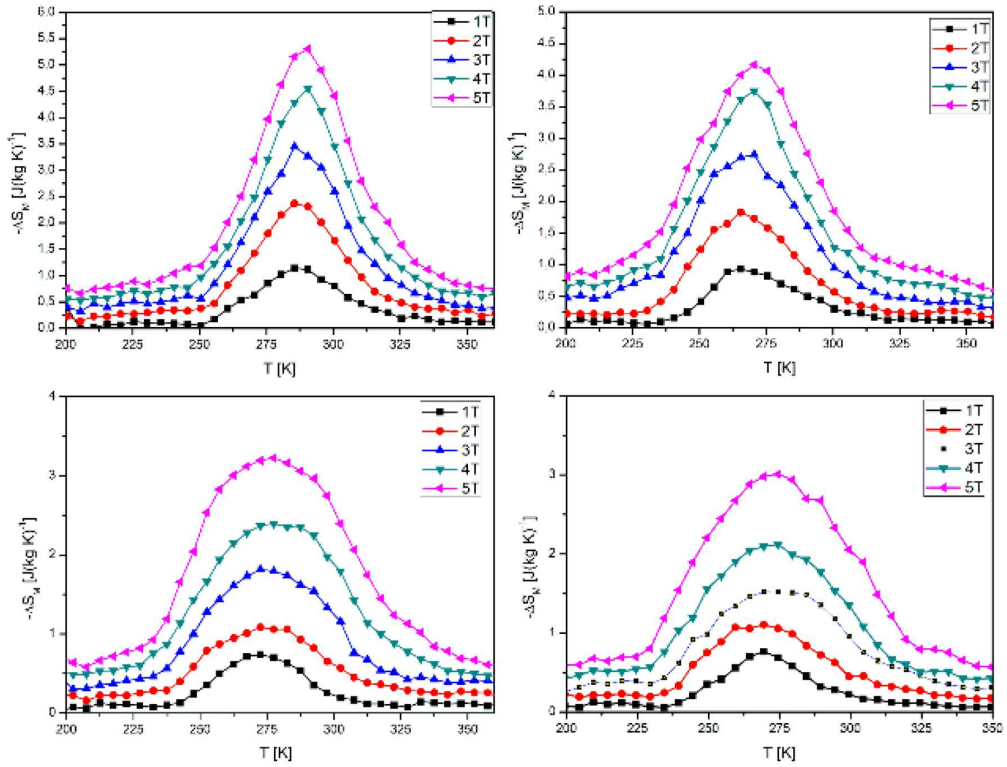

Fig. 5. The ΔS_M vs T curves revealed for $Mn_{0.97}W_{0.03}CoGe$ (a), $Mn_{0.95}W_{0.05}CoGe$ (b), $Mn_{0.93}W_{0.07}CoGe$ (c), and $Mn_{0.9}W_{0.1}CoGe$ (d) alloys.

noticed. Present results are much lower than those revealed for pure gadolinium, which is treated as a fundamental magnetocaloric material [15]. Such good properties of Gd are caused by the highest magnetic moment and the highest effective exchange coupling around room temperature [16]. Moreover, the results are also lower than those for MnCoGe modified by Fe or In addition, which is manifested by the fact that the ΔS_M value reached even 10.6 or 52 J/(kg K), respectively. The Curie temperature is comparable to those delivered in [17, 18].

Taking into account practical applications of MM'X alloys in domestic devices, the refrigeration capacity (RC) was calculated. The RC value was determined based on ΔS_M vs T curves using the following equation [19]

$$\mathrm{RC}\left(\delta T, H_{\max}\right) = \int_{T_{cold}}^{T_{hot}} \mathrm{d}T \; \Delta S_M\left(T, H_{\max}\right), \qquad (3)$$

where RC is the refrigerant capacity, $\delta T = T_{hot} - T_{cold}$ is the temperature range of the thermodynamic cycle (δT corresponds to the full width at half maximum of magnetic entropy change peak), and $H_{\max}$ is the maximum value of the external magnetic field.

Calculations of the RC parameter revealed almost the same values for each produced alloy from the series. It is related to a systematic increase in full width at half maximum with a rise in W content, despite a decrease in maximum magnetic entropy change. The values of the change in magnetic entropy ΔS_M and the refrigeration capacity RC are summarized in Table II.

A relatively simple and fast method to study order phase transition was proposed by Law et al. in [20]. This technique uses a phenomenological field dependence of the magnetic entropy change, which could be written by following relation [20]

$$\Delta S_M = C\left(B_{\max}\right)^n, \qquad (4)$$

where C is a constant depending on temperature and n is the exponent related to the magnetic state of the sample. Calculation of the exponent n by modifying (4) in the form proposed in [21] is as follows

$$\ln\left(\Delta S_M\right) = \ln(C) + n\ln\left(B_{\max}\right). \qquad (5)$$

As shown in [22], the exponent n depends on the magnetic state of the material. If we assume that the tested material obeys the Curie–Weiss law, the exponent n should be $n = 1$ in the ferromagnetic state (below T_{C}) and $n = 2$ in the paramagnetic state (above T_{C}). Its value at T_{C} is strongly related to critical exponents and could be written in the following form

$$n = 1 + \frac{1}{\delta\left(1 - \frac{1}{\beta}\right)}, \qquad (6)$$

where β and δ are critical exponents.

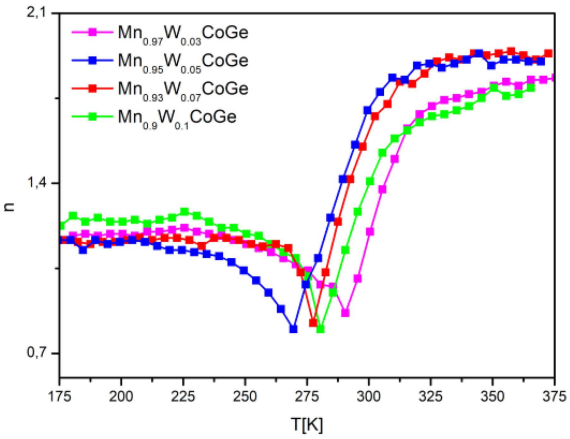

Fig. 6. Temperature dependence of the exponent n calculated for all tested (Mn,W)CoGe samples.

TABLE II

The magnetic entropy change ΔS_M and refrigeration capacity RC for the $Mn_{0.97}W_{0.03}CoGe$, $Mn_{0.95}W_{0.05}CoGe$, $Mn_{0.93}W_{0.07}CoGe$, and $Mn_{0.9}W_{0.1}CoGe$ alloys.

Sample	Magnetic field change $\Delta(\mu_0 H)$ [T]	Magnetic entropy change ΔS_M [J/(kg K)]	Refrigeration capacity RC [J/kg]
$Mn_{0.97}W_{0.03}CoGe$	1	1.14	32
	2	2.37	56
	3	3.45	74
	4	4.56	102
	5	5.30	134
$Mn_{0.95}W_{0.05}CoGe$	1	0.93	34
	2	1.83	58
	3	2.74	78
	4	3.75	104
	5	4.16	132
$Mn_{0.93}W_{0.07}CoGe$	1	0.74	33
	2	1.08	60
	3	1.82	76
	4	2.39	106
	5	3.23	135
$Mn_{0.9}W_{0.1}CoGe$	1	0.76	32
	2	1.11	64
	3	1.51	82
	4	2.12	108
	5	3.01	142

The n vs T curves for all tested samples are collected in Fig. 6. The shape of the n vs T curves constructed for the tested alloys with the addition of W is characteristic of the second type phase transition. A characteristic hump is observed near the Curie point value, which is typical for structural transformations similar to the results described in [23, 24]. The values of the exponent n revealed at the Curie point are 0.86, 0.79, 0.82, 0.79 for $Mn_{0.97}W_{0.03}CoGe$, $Mn_{0.95}W_{0.05}CoGe$, $Mn_{0.93}W_{0.07}CoGe$, and $Mn_{0.9}W_{0.1}CoGe$, respectively. These values are similar, which suggests that the values of critical exponents are close to others.

4. Conclusions

The research carried out in this work focused on the influence of partial substitution of Mn by W on the structure and thermomagnetic properties, as well as phase transitions of the tested MnCoGe alloys. XRD studies revealed the presence of two phases in all tested samples — an orthorhombic phase of the TiNiSi-type and a hexagonal phase of the Ni_2In-type with various W dopant contents. The detailed analysis of the X-ray diffraction pattern assisted by the Rietveld refinements did not reveal any structural transformation. The increase in the content of the addition of W at the expense of Mn in the tested alloys resulted in a decrease in the Curie temperature. A gradual decrease in magnetic entropy change with a rise of W in alloy composition was detected. The symmetrical shape of the temperature dependences of magnetic entropy change suggested second-order phase transition, which was confirmed by an analysis of n vs T curves constructed for the tested alloys. A course of all n vs T curves was independent of W content and characteristic of the second-order phase transition.

References

[1] E. Warburg, *Ann. Phys.* **13**, 141 (1881).

[2] P. Debye, *Ann. Phys.* **81**, 1154 (1926).

[3] W.F. Giauque, *J. Am. Chem. Soc.* **49**, 1864 (1927).

[4] V.K. Pecharsky, K.A. Gschneidner, Jr, *Phys. Rev. Lett.* **78**, 4494 (1997).

[5] G.J. Li, E.K. Liu, H.G. Zhang, Y.J. Zhang, J.L. Chen, W.H. Wang, H.W. Zhang, G.H. Wu, S.Y. Yu, *J. Magn. Magn. Mater.* **332**, 146 (2013).

[6] S. Lin, O. Tegus, E. Brück, W. Dagula, T. Gortenmulder, K. Buschow, *IEEE Trans. Magn.* **42**, 3776 (2006).

[7] K. Kutynia, P. Gębara, *Materials* **14**, 3129 (2021).

[8] K. Kutynia, A. Przybył, P. Gębara, *Materials* **16**, 539 (2023).

[9] P. Gębara, K. Kutynia, *Acta Phys. Pol. A* **135**, 298 (2019).

[10] W. Kraus, G. Nolze, *Powder Differ* **13**, 256 (1998).

[11] W. Bażela, A. Szytuła, J. Todorović, Z. Tomkowicz, A. Zięba, *Phys. Status Solidi A* **38**, 721 (1976).

[12] V.K. Pecharsky, K.A. Gschneider, Jr., *J. Appl. Phys.* **86**, 565 (1999).

[13] J. Świerczek, *J. Magn. Magn. Mater.* **322**, 2696 (2010).

[14] M.E. Wood, W.H. Potter, *Cryogenics* **25**, 667 (1985).

[15] A.M. Tishin, Y.I. Spichkin, *The Magnetocaloric Effect and its Application*, Institute of Physics Series in Condensed Matter Physics, 2003.

[16] S.K. Tripathy, K.G. Suresh, A.K. Nigam, *J. Magn. Magn. Mater.* **306**, 24 (2006).

[17] R.R. Wu, L.F. Bao, F.X. Hu et al., *Sci. Rep.* **5**, 18027 (2015).

[18] P. Gębara, M. Hasiak, *Materials* **14**, 185 (2021).

[19] A.O. Pecharsky, K.A. Gschneidner, V.K. Pecharsky, *J. Appl. Phys.* **93**, 4722 (2003).

[20] J.Y. Law, V. Franco, L.M. Moreno-Ramírez, A. Conde, D.Y. Karpenkov, I. Radulov, K.P. Skokov, O. Gutfleisch, *Nat. Commun.* **9**, 2680 (2018).

[21] V. Franco, A. Conde, V. Provenzano, R. Shull, *J. Magn. Magn. Mater.* **322**, 218 (2010).

[22] J. Świerczek, *Phys. Status Solidi A* **211**, 1567 (2014).

[23] K. Morrison, K.G. Sandeman, L.F. Cohen, C.P. Sasso, V. Basso, A. Barcza, M. Katter, J.D. Moore, K.P. Skokov, O. Gutfleisch, *Int. J. Refrig.* **35**, 1528 (2012).

[24] G.J. Li, E.K. Liu, H.G. Zhang, Y.J. Zhang, J.L. Chen, W.H. Wang, H.W. Zhang, G.H. Wu, S.Y. Yu, *J. Magn. Magn. Mater.* **332**, 146 (2013).

POLISH ACADEMY OF SCIENCES
INSTITUTE OF PHYSICS

Established in 1920 by
the Polish Physical Society

ACTA PHYSICA POLONICA

- General Physics
- Atomic and Molecular Physics
- Condensed Matter
- Optics and Quantum Optics
- Quantum Information
- Biophysics
- Applied Physics

RECOGNIZED BY THE EUROPEAN PHYSICAL SOCIETY

Volume 146 — Number 1, Warsaw, July 2024

PL ISSN 0587-4246 ATPLB6 146 (1) 77–120 (2024)

Comparative X-ray Diffraction Study of Two Liquid Crystalline Compounds with Chiral Centers Based on (S)-(+)-2-Octanol and (S)-(+)-3-Octanol

A. Deptuch[a,*], A. Lelito[b], B. Sęk[c] and M. Urbańska[d]

[a]*Institute of Nuclear Physics, Polish Academy of Sciences, Radzikowskiego 152, PL-31342 Kraków, Poland*
[b]*Faculty of Materials Engineering and Physics, Cracow University of Technology, Podchorążych 1, PL-30084 Kraków, Poland*
[c]*Faculty of Physics and Applied Computer Science, AGH University of Kraków, Reymonta 19, PL-30059 Kraków, Poland*
[d]*Institute of Chemistry, Military University of Technology, Kaliskiego 2, PL-00908 Warsaw, Poland*

Received: 11.03.2024 & Accepted: 23.04.2024

Doi: 10.12693/APhysPolA.146.79 *e-mail: aleksandra.deptuch@ifj.edu.pl

The structure of the antiferroelectric smectic C_A^* phase is investigated for two liquid crystals with almost identical molecular structures, except for chiral centers. The X-ray diffraction results determined the crystal unit cell parameters, smectic layer spacing, average distance within layers, and correlation length of the short-range positional order. The coefficients of thermal expansion are determined for the crystal phases. The molecular modeling with the semi-empirical PM7 method and density functional theory calculations with the def2TZVPP basis set and B3LYP-D3(BJ) functional are applied to determine the tilt angle of molecules from the experimental smectic layer spacing. The most probable conformations are then selected based on a comparison with the tilt angle measured by the electro–optic method, known from the previous results. In the most suitable molecular models, the chiral chain makes an approximately 90° angle with the molecular core, and some fragments in the fluorinated part of the achiral terminal chain are in the *gauche* conformation.

topics: X-ray diffraction, smectic liquid crystals, layer spacing, tilt angle

1. Introduction

The smectic phases are liquid crystalline (LC) phases characterized by the lamellar order. The lamellar order is quasi-long-range for the simplest smectic phases, and the positional order within the smectic layers is only short-range. In the smectic A (SmA) phase, the average tilt angle Θ of molecules relative to the layer normal is zero, while in the smectic C (SmC) phase, $\Theta \neq 0$. There are a few types of the SmC phase, including the synclinic, default SmC, and anticlinic SmC_A phases. In the latter, the tilt angle has an opposite sign in neighboring layers. The SmC^* and SmC_A^* phases, where * means that they are formed of chiral molecules, can show, respectively, the ferro- and antiferroelectric properties in certain conditions, corresponding to bistable and tristable switching under the influence of the electric field [1–3]. Particularly interesting are the LC compounds forming the SmC_A^* phase with a high tilt angle close to 45°, where the chevron defect in the LC alignment does not cause light leakage in the dark state of a display [4, 5].

The smectic layer spacing d, which can be obtained using the X-ray diffraction (XRD) method, is correlated with the tilt angle Θ. Determining the tilt angle from the XRD results and calculating molecular size using molecular modeling is not straightforward because the shapes of mesogenic molecules often deviate from the ideal rod. Consequently, there is a difference between the tilt of the molecular core (corresponding to the genuine tilt angle Θ measured by the electro-optic method) and the overall tilt of a molecule (referred to as the steric tilt angle) [6–8]. The formula for the tilt angle, which results from these considerations, is as follows

$$\Theta = \arccos(d/L) + \delta\Theta, \tag{1}$$

where L is the molecular length, and $\delta\Theta$ is the shape parameter. For a rod-like molecule, $\delta\Theta = 0$, while for non-linear molecules, this parameter can even

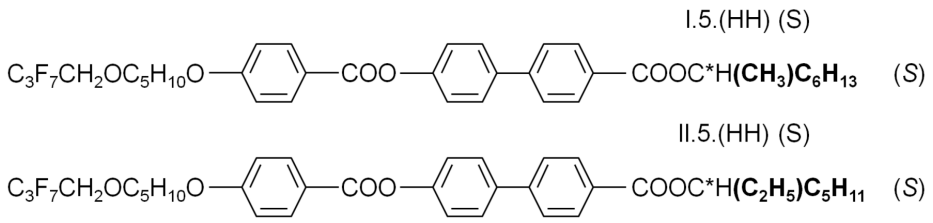

Fig. 1. Molecular formulas of I.5.(HH) (S) and II.5.(HH) (S).

exceed 20° [8]. It is necessary to test several molecular conformations to find the one that enables the best reproduction of the tilt angle measured by the electro-optic method [6–8]. In our previous papers and in the literature, various conformations are taken into account, including the more extended hockey-stick conformations [8–10] and more bent (C-shaped, zig–zag) ones [8, 10–12]. Knowledge of the most likely conformations can facilitate, e.g., the interpretation of the infrared (IR) spectra, the analysis of which usually involves the density functional theory (DFT) calculations of the intra-molecular vibrations [10, 11].

This work presents a comparative study of two chiral LC compounds. These compounds are (S)-4'-(1-methylheptylcarbonyl)biphenyl-4-yl 4-[5-(2,2,3,3,4,4,4-heptafluorobutoxy)pentyl-1-oxy]benzoate, abbreviated as I.5.(HH) (S) or 3F5HPhH6 (the first notation is further used) and (S)-4'-(1-ethylhexyloxycarbonyl)biphenyl-4-yl 4-[5-(2,2,3,3,4,4,4-heptafluorobutoxy)pentyl-1-oxy] benzoate, abbreviated as II.5.(HH) (S). The molar mass of these compounds is the same, and their molecular structures are almost identical (Fig. 1). The only difference is in the chiral center, based on (S)-(+)-2-octanol and (S)-(+)-3-octanol for I.5.(HH) (S) and II.5.(HH) (S), respectively. They both exhibit the antiferroelectric smectic C_A^* phase with a high tilt angle approaching 45° [13]; they are, therefore, promising components for orthoconic LC mixtures suitable for displays [4, 5]. The previous experimental results indicate that both these compounds form a glass of a smectic phase: I.5.(HH) (S) of the hexatic smectic X_A^* phase (SmI_A^* or SmF_A^*) for cooling rates $\geq$ 5 K/min [14] and II.5.(HH) (S) of the antiferroelectric SmC_A^* phase for cooling rates $\geq$ 2 K/min [15]. The fact that these compounds can be easily supercooled is another feature that makes them good for application in LC mixtures, where the observed range of the smectic phase should be as wide as possible.

The aim of this paper is analysis of the XRD patterns of I.5.(HH) (S) and II.5.(HH) (S) collected as a function of temperature. The structural parameters of the crystal, smectic, and isotropic liquid phases are obtained and discussed in relation to the results from other experimental methods published in [14, 15]. Then, the molecular models of I.5.(HH) (S) and II.5.(HH) (S) from the same set of conformations, optimized by the DFT method, are tested to determine the tilt angle from (1). The conformations, which give the tilt angle consistent with the tilt measured by the electro-optic method [13], are supposed to be the most probable conformations exhibited by molecules in the SmC_A^* phase.

2. Experimental and computational details

The synthetic route of (S)-4'-(1-methylheptylcarbonyl)biphenyl-4-yl 4-[5-(2,2,3,3,4,4,4-heptafluorobutoxy)pentyl-1-oxy]benzoate (I.5.(HH) (S)) is described in [16, 17] and synthesis of (S)-4'-(1-ethylhexyloxycarbonyl)biphenyl-4-yl 4-[5-(2,2,3,3,4,4,4-heptafluorobutoxy)pentyl-1-oxy]benzoate (II.5.(HH) (S)) is presented in [18].

The X-ray diffraction experiment for the polycrystalline pristine samples (not melted after synthesis) was carried out with X'Pert PRO (PANalytical) diffractometer in the Bragg–Brentano geometry with the Cu K_α radiation. The diffraction patterns were collected in the 2θ = 2–30° range during heating from room temperature until the transition to isotropic liquid. The temperature was controlled using the TTK 450 (Anton Paar) stage. The XRD data analysis was performed in FullProf [19], PASCal [20, 21], and OriginPro.

The molecular modeling was performed in Gaussian 16 [22]. The conformational energy scans were carried out for isolated molecules and selected torsional angles with the semi-empirical PM7 method [23]. The lowest-energy conformations were further optimized by the DFT method (def2TZVPP basis set [24], B3LYP-D3(BJ) exchange-correlation functional [25–27]). The preparation and visualization of molecular models was done in Avogadro [28].

3. Results and discussion

3.1. Crystal unit cell

At room temperature, both compounds are in the crystal phases (Fig. 2), and the XRD patterns can be indexed in the orthorhombic and

TABLE I

Thermal expansion coefficients α_i and matrix of transition between the crystallographic directions and principal strain axes for the crystal phases of I.5.(HH) (S) and II.5.(HH) (S).

Compound	Axis	α_i ($\times 10^{-6}$) [K^{-1}]	a	b	c
I.5.(HH) (S)	x	$-231(4)$	1	0	0
	y	386(17)	0	1	0
	z	331(13)	0	0	1
	V	489(15)			
II.5.(HH) (S)	x	179(6)	0.7359	0	0.6771
	y	123(3)	0	1	0
	z	136(3)	-0.5485	0	0.8362
	V	442(4)			

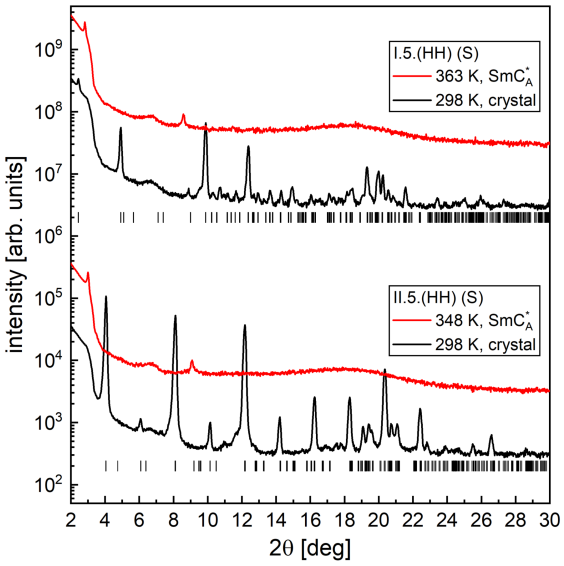

Fig. 2. X-ray diffraction patterns of I.5.(HH) (S) and II.5.(HH) (S) in their pristine crystal phases and after melting to the SmC^*_A phase. The vertical bars indicate the peak positions corresponding to the crystal unit cells mentioned in the main text. The wide maximum at $2\theta = 6$–7° is a background contribution.

monoclinic crystallographic system for I.5.(HH) (S) and II.5.(HH) (S), respectively. The unit cell sizes were determined by the Le Bail fitting method [29]. The lattice parameters in the room temperature for I.5.(HH) (S) are $a = 35.68(2)$ Å, $b = 17.23(2)$ Å, $c = 7.603(8)$ Å, $\alpha = \beta = \gamma = 90^\circ$ and for II.5.(HH) (S) are $a = 21.866(7)$ Å, $b = 4.834(6)$ Å, $c = 18.69(2)$ Å, $\beta = 92.73(9)^\circ$, $\alpha = \gamma = 90^\circ$. The parameter a for I.5.(HH) (S) is comparable with the molecule's length of 30–41 Å, based on the DFT results for various conformations. This indicates that the crystal phase of the pristine I.5.(HH) (S) sample very likely has a lamellar structure. The calculated length of the II.5.(HH) (S) molecule is 30–39 Å, which does not correspond to any lattice constant. Thus, the arrangement of molecules is likely not similar to that in the smectic phases. The differential scanning calorimetry results for pristine samples indicate that the enthalpy change at melting, which is equal to 18.0 kJ/mol for I.5.(HH) (S) [17], is much smaller than 27.8 kJ/mol for II.5.(HH) (S) [18]. This corresponds to the XRD results, which show that the lamellar crystal structure of I.5.(HH) (S) resembles more closely the smectic phase than the probably non-lamellar crystal structure of II.5.(HH) (S), therefore the enthalpy of melting is lower in the former compound.

The unit cell parameters, determined from the XRD patterns as a function of temperature (Fig. 3), were analyzed in the PASCal program, which enables the calculation of the coefficients of thermal expansion (CTEs) along the principal strain axes x, y, z [20, 21] (Table I). CTE in a given direction $i = x, y, z$ is defined as [20]

$$\alpha_i = \frac{1}{T}\left(\frac{l_i(T)}{l_i(0)} - 1\right), \tag{2}$$

where $l_i(T)$ is length (or volume, if the overall CTE is calculated) at temperature T. For I.5.(HH) (S), which crystallizes in the orthorhombic system, the principal axes overlap with the crystallographic directions a, b, c, and the transformation matrix between them is simply a unit matrix. As the b and c parameters deviate from the linear dependence above 318 K, only values from the 298–318 K range were used in calculations. The I.5.(HH) (S) compound in the crystal phase shows the positive expansion in the b and c directions, while along the a direction, CTE is negative. Another behavior is observed for the II.5.(HH) (S) crystal, which has positive CTEs along all directions. Despite significant differences in the anisotropy in thermal expansion, the volume CTE has similar values for both compounds.

3.2. Short-range order

The short-range order within the smectic layers appears in the diffraction patterns as a wide maximum with the middle at $2\theta \approx 18^\circ$. The same maximum is present after the transition to the isotropic liquid state. When plotted in the scattering vector space $q = 4\pi \sin(\theta)/\lambda$, the wide maximum has a Lorentzian shape [30, 31]

$$I(q) = \frac{I_0}{1 + \xi^2 (q - q_0)^2}, \tag{3}$$

where I_0 is the maximum height, q_0 is the maximum position, and ξ is the correlation length. The distance $w = q_0/\pi$, which corresponds approximately to the molecular width, is determined with an accuracy better than 0.01 Å (Fig. 4) and is within the

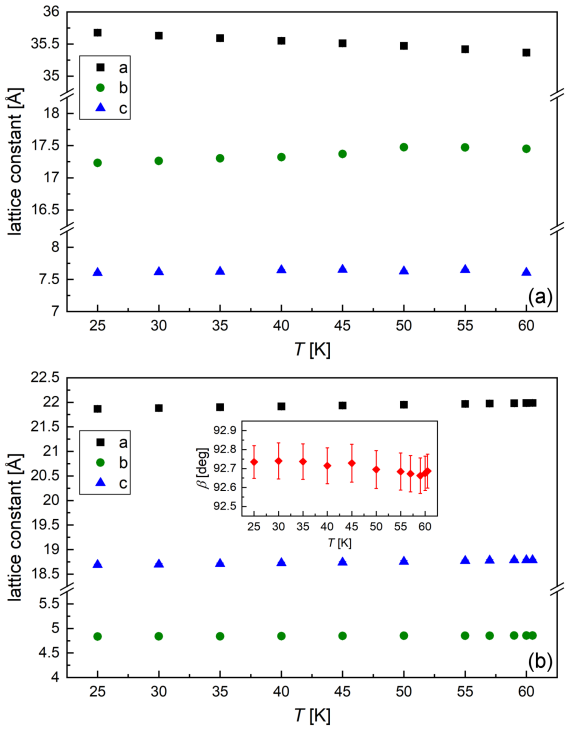

Fig. 3. Unit cell parameters for the crystal phases of I.5.(HH) (S) (a) and II.5.(HH) (S) (b).

4.76–4.99 Å range for I.5.(HH) (S) and 4.84–5.06 Å for II.5.(HH) (S). It is in agreement with slightly wider II.5.(HH) (S) molecules, due to the structure of their chiral center. Note that the presented w values are mean distances for each temperature, while the distribution of intramolecular distances is quite wide, and they may differ even by 0.5 Å between particular molecules. The mean w distance does not change significantly after the transition to isotropic liquid. The correlation length of the short-range order, determined with the accuracy of ca. 0.1–0.2 Å, decreases upon heating in the smectic phases and has an approximately constant value in isotropic liquid. It takes larger values for I.5.(HH) (S) than for II.5.(HH) (S), both in the smectic phases and isotropic liquid phase. Just above the Cr $\rightarrow$ SmC$^*_A$ transition temperature, at 341–348 K, the ξ value is equal to 6.7–7.1 Å for I.5.(HH) (S), while for II.5.(HH) (S) at lower temperatures 334.5–335.5 K, ξ equals 5.7–5.8 Å. A larger correlation length for I.5.(HH) (S) corresponds to the occurrence of the monotropic hexatic smectic phase formed by this compound upon overcooling [14], which was not observed for II.5.(HH) (S) [15]. The short-range correlations include only the nearest neighbors, as the ξ values are in the same order as the w distance. Correlation lengths obtained for other compounds in the smectic A or C phases are comparable with the results for I.5.(HH) (S) and II.5.(HH) (S) for some cases [31–33], but they can also be larger, above 10 Å [34, 35].

3.3. Smectic layer order

The lamellar order is present in the smectic phases, which corresponds to the low-angle sharp diffraction peaks. For the investigated compounds, the 1st and 3rd order peaks are visible, and the layer spacing (Fig. 5) was determined from the position of both of them using the Bragg equation

$$n\lambda = 2d\sin(\theta), \tag{4}$$

where n is the diffraction order, λ is the X-ray wavelength, d is the layer spacing, and θ is the peak position [36]. The layer spacing in the smectic phases of I.5.(HH) (S) is 1.8–2.1 Å larger than that of II.5.(HH) (S), which is caused by a longer chiral terminal chain of I.5.(HH) (S), as the tilt angle in both compounds deep in the SmC$^*_A$ phase is similar, i.e., 44.5° for I.5.(HH) (S) and 43° for II.5.(HH) (S) [13]. The SmC$^*_A$ $\rightarrow$ SmC* transition in I.5.HH (S) is only very weakly visible in the $d(T)$ plot as a discontinuous increase by 0.3 Å. For II.5.(HH) (S), no significant increase in d indicates the SmC$^*_A$ $\rightarrow$ SmA* transition. The previous results from other experimental methods [15] show that it is troublesome to detect the SmA* phase of this compound on heating.

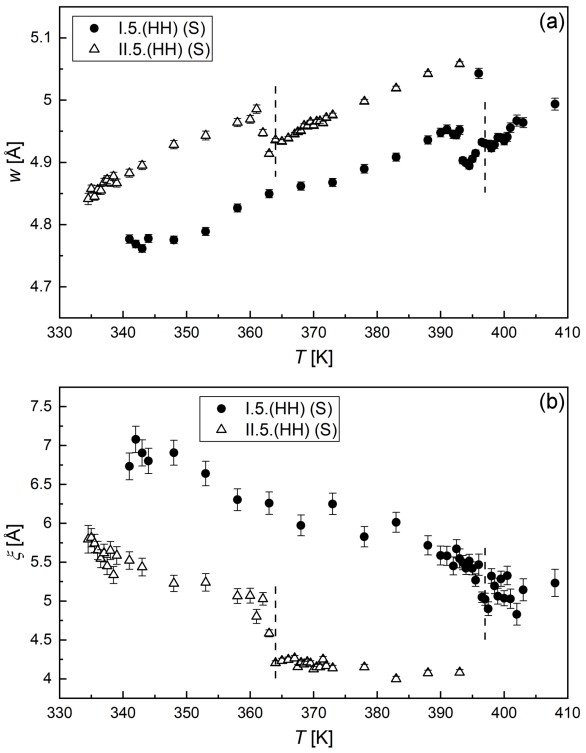

Fig. 4. Mean distance between molecules (a) and correlation length of the short-range order (b) determined from the XRD patterns. The vertical dashed lines indicate the smectic $\rightarrow$ isotropic liquid transition temperature for each compound.

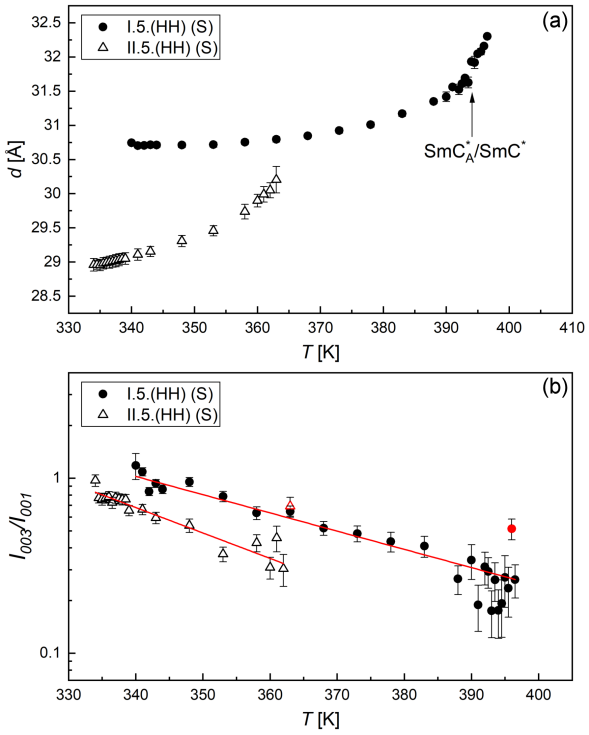

Fig. 5. Smectic layer spacing (a) and the ratio of the 1st and 3rd order peak from the lamellar order (b) determined from the XRD patterns. The Lorentz-polarization factor corrected the intensities in (b). Two outlier points in (b) close to the isotropization temperature were excluded from the linear fit.

The intensities of the 1st and 3rd order peaks are proportional to the τ_1 and τ_3 order parameters, respectively, describing the lamellar order. For the simplest, sinusoidal density wave, $1 > \tau_1 > 0$ and $\tau_m = 0$, where $m > 1$ [37]. The ratio of intensities of the 1st and 3rd order peak I_{003}/I_{001}, corrected by the Lorentz-polarization factor [38], is larger for I.5.(HH) (S) than for II.5.(HH) (S), which means that in the former compounds, there is a larger deviation from the sinusoidal density wave. The I_{003}/I_{001} ratio for both compounds increases with decreasing temperature in an exponential manner, which is visible as a linear dependence when I_{003}/I_{001} is plotted in the logarithmic scale (Fig. 5b); only the points close to the transition to the isotropic liquid show some deviations from this dependence.

3.4. Tilt angle

The conformational energy scans for a few torsional angles in the I.5.(HH) (S) and II.5.(HH) (S) molecules were previously presented in [14, 15] and were used for the interpretation of the dielectric relaxation processes. New conformations

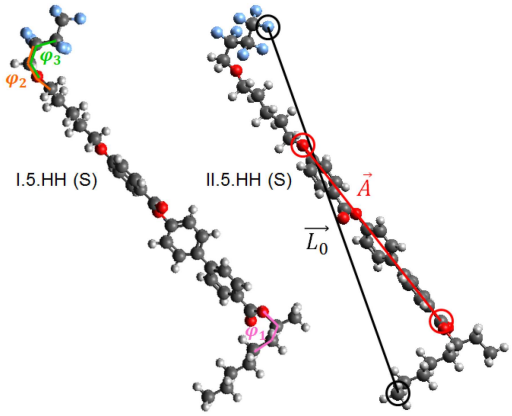

Fig. 6. Molecular model optimized with the DFT method ($\varphi_1 \approx 62$–$63.5°$, $\varphi_2 \approx 110°$, $\varphi_3 \approx 295°$). For I.5.(HH) (S), the φ_1, φ_2 and φ_3 angles are indicated. For II.5.(HH) (S), the $\boldsymbol{L_0}$ and $\boldsymbol{A}$ vectors are defined. The molecular length is obtained as $L = L_0 + 3.22$ Å, and the shape parameter $\delta\Theta$ is equal to an angle between $\boldsymbol{L_0}$ and $\boldsymbol{A}$.

were included to determine the tilt angle from the XRD results in this study. The molecular models from [14, 15] were used as the starting point for new calculations. The semi-empirical PM7 method is useful for performing quick scans of the conformational energy as a function of a given torsional angle, because the calculation for an isolated molecule consisting of 91 atoms, as it is for both considered compounds, lasts less than one minute. The amount of possible molecular conformations is large. Therefore, only selected torsional angles can be investigated in a reasonable time. These torsional angles, indicated in Fig. 6, are the C–C–C*–O angle φ_1 in the chiral center, as well as the C–O–C–C angle φ_2 and O–C–C–C angle φ_3 in the fluorinated part of the achiral chain. They were chosen because each of them significantly influences the length and shape of molecules. The PM7 scans for φ_1 and φ_3 show three local minima in energy, while for φ_2 there are two local minima (Fig. 7). Only the φ_1 scans differ slightly between I.5.(HH) (S) and II.5.(HH) (S), while the φ_2 and φ_3 scans for both compounds overlap, as these angles are far from the chiral center. In the next step, the DFT calculations, each lasting up to 12 h, were performed for conformations corresponding to the local minima in energy, without any constraints in the torsional angles. The DFT method reveals a third local minimum in energy for φ_2, and in some cases, the φ values in the optimized models differ slightly from the results of the simpler PM7 method. For each considered torsional angle, there are local minima in energy corresponding to an antiperiplanar conformation ($\varphi \approx 180°$) and two *gauche* conformations. Eventually, 27 molecular models with various values of φ_1, φ_2, and φ_3 were optimized for each compound (Table II).

TABLE II

Tilt angle Θ in the SmC^*_A phase of I.5.(HH) (S) and II.5.(HH) (S) obtained from the experimental smectic layer spacing at 340 K and 334 K, respectively, and molecular models optimized by the DFT method. For each conformation, the relative energy ΔE is given together with the values of torsional angles ϕ_1, ϕ_2, ϕ_3. The **bold** font indicates results that are in agreement with the 2° error with the experimental tilt angle [13] at corresponding temperatures, namely 44.5° for I.5.(HH) (S) and 42° for II.5.(HH) (S).

I.5.(HH) (S)					II.5.(HH) (S)				
ΔE [kJ/mol]	φ_1 [deg]	φ_2 [deg]	φ_3 [deg]	Θ [deg]	ΔE [kJ/mol]	φ_1 [deg]	φ_2 [deg]	φ_3 [deg]	Θ [deg]
0.02	62.3	78.7	50.3	**46.2(1)**	0	63.5	78.6	50.2	45.9(4)
2.81	62.4	88.6	175.6	**44.5(1)**	2.82	63.3	88.4	175.2	**41.7(3)**
4.23	62.3	109.7	294.7	**42.8(2)**	4.27	63.5	109.6	294.6	**41.2(5)**
1.70	62.4	181.3	58.5	34.4(1)	1.68	63.4	181.2	58.4	45.8(3)
3.95	62.4	180.0	180.1	**42.9(1)**	3.95	63.5	180.1	179.9	44.6(3)
1.67	62.4	178.8	301.4	**46.2(1)**	1.68	63.4	179.0	301.5	50.3(3)
4.24	62.2	250.5	65.6	–	4.26	63.4	250.6	65.4	24.9(7)
2.83	62.4	271.5	184.7	35.9(1)	2.84	63.4	269.8	183.4	35.4(3)
0	62.2	281.3	309.9	15.9(3)	0.04	63.5	281.5	309.8	33.9(5)
1.45	174.4	78.8	50.5	51.2(1)	9.99	178.6	78.7	50.4	53.1(3)
4.23	174.25	90.1	176.8	50.3(1)	12.79	178.5	89.7	176.2	51.7(3)
5.69	174.4	109.9	294.6	49.8(1)	14.24	178.7	109.9	294.5	51.7(3)
3.12	174.3	181.0	58.5	**43.7(1)**	11.66	178.7	181.3	58.5	45.4(3)
5.38	174.3	180.2	180.0	47.8(1)	13.93	178.6	180.3	180.1	49.2(2)
3.11	174.2	178.5	301.6	50.8(1)	11.68	178.7	180.5	301.5	52.5(3)
5.67	174.3	250.4	65.5	32.2(1)	14.24	178.8	250.3	65.6	33.0(3)
4.24	174.4	271.0	184.4	**44.6(1)**	12.80	178.7	271.6	184.8	45.7(3)
1.43	174.3	281.2	309.8	34.8(1)	10.00	178.8	281.2	309.8	36.3(3)
1.90	300.8	78.7	50.0	**43.0(2)**	1.86	297.5	78.7	50.0	49.0(4)
4.72	300.9	89.0	175.8	40.0(1)	4.67	297.5	87.9	174.9	44.9(3)
6.15	300.6	109.4	294.5	35.8(2)	6.14	297.5	109.6	294.6	45.0(4)
3.58	300.9	181.1	58.5	38.4(1)	3.55	297.5	181.3	58.4	**42.9(3)**
5.85	300.8	180.3	180.1	41.1(1)	5.85	297.5	179.8	179.9	45.4(3)
3.58	300.8	178.9	301.5	46.6(1)	3.55	297.6	178.8	301.5	50.6(3)
6.16	300.8	250.7	65.4	–	6.13	297.5	250.7	65.4	20.0(7)
4.74	301.0	271.5	184.7	31.3(1)	4.71	297.5	270.4	183.7	37.2(3)
1.92	300.8	281.4	309.7	18.3(3)	1.89	297.6	281.3	309.7	30.0(5)

The tilt angle Θ was calculated using formula (1). The smectic layer spacing determined just above the melting of the crystal phase, $d = 30.75(3)$ Å for I.5.(HH) (S) and 29.0(1) Å for II.5.(HH) (S), was inserted in this formula. The molecular length L was defined as the distance between the terminal C atom from the chiral chain and the terminal F atom from the achiral chain, plus the non-bonded C–F distance 3.22 Å [39]. For the sake of unambiguity of L, the same F atom, which follows the positions of the C atoms in the achiral chain, was selected for all conformations. There are various approaches to calculate the shape parameter $\delta\Theta$ [8]. In this work, $\delta\Theta$ was defined simply as an angle between the C–F vector related to the molecular length and the C–O vector, where C is located in the COO group between the biphenyl ring and the chiral center, and O is adjacent to the benzene ring (see Fig. 6). The final values of Θ obtained from the XRD and DFT results are presented in Table II. The uncertainties in Θ given in parentheses are related to uncertainties in d, which do not exceed 1°. However, for practical purposes, an agreement within the ±2 error with experimental Θ from [13] is satisfactory, and the bold font in Table II denotes such values. One can see that for both compounds, a good agreement is obtained for conformations where $\varphi_1 \approx 62$–$63.5°$ and $\varphi_2 \approx 89°$, $\varphi_3 \approx 175$–$176°$ or $\varphi_2 \approx 110°$, $\varphi_3 \approx 295°$. Thus, these conformations, among the considered ones, are most likely exhibited by the real molecules in the SmC^*_A phase.

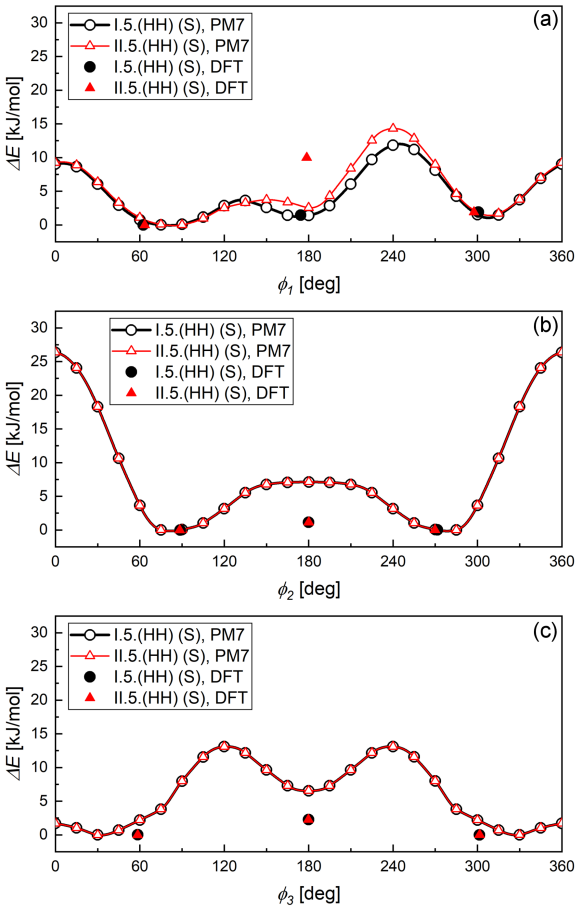

Fig. 7. Conformational energy of I.5.(HH) (S) and II.5.(HH) (S) molecules as a function of torsional angles, defined in the main text, calculated with the PM7 and DFT methods.

4. Conclusions

The structural parameters of I.5.(HH) (S) and II.5.(HH) (S), with chiral centers based on (S)-(+)-2-octanol and (S)-(+)-3-octanol, in the crystal and smectic phases were compared using the X-ray diffraction patterns registered as a function of temperature. The main conclusions are as follows:

- In the pristine samples, I.5.(HH) (S) crystallizes in the orthorhombic system, while II.5.(HH) (S) crystallizes in the monoclinic system. I.5.(HH) (S) exhibits the strong anisotropy of CET, which is negative along the *a*-axis and positive along the *b*- and *c*-axes. For II.5.(HH), CETs are positive in all directions.
- The average distance between molecules is smaller and the correlation length describing the short-range order within the smectic layers is larger for I.5.(HH) (S) than for II.5.(HH) (S).
- The smectic layer spacing and deviation from the sinusoidal density wave is larger for I.5.(HH) (S) than for II.5.(HH) (S). In both compounds, the ratio of the 3rd and 1st diffraction peaks decreases exponentially with increasing temperature.
- Among the set of 27 conformations obtained by DFT calculations, the most probable are these with $\varphi_1 \approx 62$–$63°$ and $\varphi_2 \approx 89°$, $\varphi_3 \approx 175$–$176°$ or $\varphi_2 \approx 110°$, $\varphi_3 \approx 295°$, as they lead to good agreement with the experimental tilt angle (measured by the electro-optic method in [13]) for both compounds. Further XRD experiments will show if the conformations that are considered most probable for I.5.(HH) (S) and II.5.(HH) (S) agree with the optical tilt angle for similar compounds.

Acknowledgments

We gratefully acknowledge Poland's high-performance infrastructure PLGrid Academic Computer Centre Cyfronet AGH for providing computer facilities and support within computational grant no. plgmolkryst-8.

References

[1] G. Vertogen, W.H. de Jeu, *Thermotropic Liquid Crystals, Fundamentals*, Springer-Verlag, Berlin 1988.

[2] J. Als-Nielsen, J.D. Litster, R.J. Birgeneau, M. Kaplan, C.R. Safinya, A. Lindegaard-Andersen, S. Mathiesen, *Phys. Rev. B* **22**, 312 (1980).

[3] J.P.F. Lagerwall, F. Giesselmann, *ChemPhysChem* **7**, 20 (2006).

[4] K. D'havé, P. Rudquist, S.T. Lagerwall, H. Pauwels, W. Drzewiński, R. Dąbrowski, *Appl. Phys. Lett.* **76**, 3528 (2000).

[5] R. Dąbrowski, J. Gąsowska, J. Otón, W. Piecek, J. Przedmojski, M. Tykarska, *Displays* **25**, 9 (2004).

[6] J.T. Mills, H.F. Gleeson, J.W. Goodby, M. Hird, A. Seed, P. Styring, *J. Mater. Chem.* **8**, 2385 (1998).

[7] W. Piecek, Z. Raszewski, P. Perkowski, J. Przedmojski, J. Kędzierski, W. Drzewiński, R. Dąbrowski, J. Zieliński, *Ferroelectrics* **310**, 125 (2004).

[8] A. Deptuch, T. Jaworska-Gołąb, M. Dziurka, J. Hooper, M. Srebro-Hooper, M. Urbańska, M. Tykarska, M. Marzec, *Phys. Rev. E* **107**, 034703 (2023).

[9] W. Tomczyk, M. Marzec, E. Juszyńska, R. Dąbrowski, D. Ziobro, S. Wróbel, M. Massalska-Arodź, *Acta Phys. Pol. A* **124**, 949 (2013).

[10] A. Drzewicz, E. Juszyńska-Gałązka, W. Zając, M. Piwowarczyk, W. Drzewiński, *J. Mol. Liq.* **319**, 114153 (2020).

[11] K. Drużbicki, E. Mikuli, A. Kocot, M.D. Ossowska-Chruściel, J. Chruściel, S. Zalewski, *J. Phys. Chem. A* **116**, 7809 (2012).

[12] P. Perkowski, Z. Raszewski, J. Kędzierski, J. Rutkowska, W. Piecek, J. Zieliński, S. Kłosowicz, *Ferroelectrics* **276**, 279 (2002).

[13] M. Urbańska, P. Morawiak, M. Senderek, *J. Mol. Liq.* **328**, 115378 (2021).

[14] A. Deptuch, M. Jasiurkowska-Delaporte, W. Zając, E. Juszyńska-Gałązka, A. Drzewicz, M. Urbańska, *Phys. Chem. Chem. Phys.* **23**, 19795 (2021).

[15] A. Deptuch, A. Lelito, E. Juszyńska-Gałązka, M. Jasiurkowska-Delaporte, M. Urbańska, *Phys. Chem. Chem. Phys.* **25**, 12379 (2023).

[16] M. Żurowska, R. Dąbrowski, J. Dziaduszek, K. Czupryński, K. Skrzypek, M. Filipowicz, *Mol. Cryst. Liq. Cryst.* **495**, 145/[497] (2008).

[17] M. Żurowska, R. Dąbrowski, J. Dziaduszek et al., *J. Mater. Chem.* **21**, 2144 (2011).

[18] M. Żurowska, M. Filipowicz, M. Czerwiński, M. Szala, *Liq. Cryst.* **46**, 299 (2019).

[19] J. Rodríguez-Carvajal, *Phys. B Condens. Matter* **192**, 55 (1993).

[20] M.J. Cliffe, A.L. Goodwin, *J. Appl. Cryst.* **45**, 1321 (2012).

[21] M. Lertkiattrakul, M.L. Ewans, M.J. Cliffe, *J. Open Source Softw.* **8**, 5556 (2023).

[22] M.J. Frisch, G.W. Trucks, H.B. Schlegel et al., Gaussian 16, Revision C.01, Gaussian Inc., Wallingford (CT) 2019.

[23] J.J.P. Stewart, *J. Mol. Model.* **19**, 1 (2013).

[24] F. Weigend, R. Ahlrichs, *Phys. Chem. Chem. Phys.* **7**, 3297 (2005).

[25] C. Lee, W. Yang, R.G. Parr, *Phys. Rev. B* **37**, 785 (1988).

[26] A.D. Becke, *J. Chem. Phys.* **98**, 5648 (1993).

[27] S. Grimme, S. Ehrlich, L. Goerigk, *J. Comput. Chem.* **32**, 1456 (2011).

[28] M.D. Hanwell, D.E. Curtis, D.C. Lonie, T. Vandermeersch, E. Zurek, G.R. Hutchison, *J. Cheminform.* **4**, 17 (2012).

[29] A. Le Bail, H. Duroy, J.L. Fourquet, *Mater. Res. Bull.* **23**, 447 (1988).

[30] J. Budai, R. Pindak, S.C. Davey, J.W. Goodby, *J. Phys. Lett.* **45**, 1053 (1984).

[31] J. Yu, Z. Chen, R. Teerakapibal, C. Benmore, R. Richert, L. Yu, *J. Chem. Phys.* **156**, 084504 (2022).

[32] W. Tomczyk, M. Marzec, E. Juszyńska-Gałązka, D. Węgłowska, *J. Mol. Struct.* **1130**, 503 (2017).

[33] A. Różycka, A. Deptuch, T. Jaworska-Gołąb, D. Węgłowska, M. Marzec, *Phase Trans.* **91**, 159 (2018).

[34] K. El Guermai, M. Ayadi, K. El Boussiri, *Acta Phys. Pol. A* **94**, 779 (1998).

[35] B.M. Ocko, A.R. Kortan, R.J. Birgeneau, J.W. Goodby, *J. Phys.* **45**, 113 (1984).

[36] W. Massa, *Crystal Structure Determination*, Springer-Verlag, Berlin 2000.

[37] Y. Takanishi, A. Ikeda, H. Takezoe, A. Fukuda, *Phys. Rev. E* **51**, 400 (1995).

[38] B.B. He, in: C.J. Gilmore, J.A. Kaduk, H. Schenk, *International Tables for Crystallography*, Vol. B, 2019, p. 130.

[39] R.S. Rowland, R. Taylor, *J. Phys. Chem.* **100**, 7384 (1996).

Stability of Optical Solitons in Parity–Time-Symmetric Potentials with Competition Nonlinearity

C. Huang*

College of Physics and Materials Science, Tianjin Normal University, 393 Bin Shui West Road, Xi Qing District, Tianjin 300387, China

Received: 09.01.2024 & Accepted: 12.04.2024

Doi: 10.12693/APhysPolA.146.87 *e-mail: chunfuhuang@126.com

This study investigates the existence, stability, and propagation of fundamental, dipole, and tripole modes in parity–time symmetric potentials with competing cubic and quintic nonlinearities. We discuss such parity–time solitons in the presence of a focusing quintic nonlinearity and a defocusing cubic nonlinearity. Assuming a fixed quintic nonlinearity coefficient σ_2 of 1, these solitons can exist and remain stable within a suitable power range. Fundamental solitons can remain stable even for lower values of σ_1, while dipole and tripole solitons may only be stable for larger values of σ_1. By employing appropriate parameters, a significant proportion of solitons can be stabilized. The stability and propagation of the solitons are demonstrated through linear stability analysis and direct numerical simulations.

topics: optical solitons, parity–time (PT) symmetry, stability, cubic and quintic nonlinearity

1. Introduction

Non-Hermitian Hamiltonians with parity–time (PT) symmetry have entirely real eigenvalue spectra, given that the complex potential meets the necessary condition, i.e., $V^*_{PT}(x) = V^*_{PT}(-x)$ [1–5]. The real and imaginary parts of such potentials must display symmetry and antisymmetry with respect to position. Spatial solitons in these PT potentials have been extensively studied in recent years using various nonlinear media, including Kerr media [3–9], saturable nonlinear media [10–12], and non-local media [13–17], among others [18–24]. In addition, spatial solitons have been excited in various PT-symmetric potentials, including the Scarff-II potential, optical lattice potential, harmonic-Gaussian potential, and super-Gaussian potential. Properties such as stability, symmetry breaking, and dynamic evolution have been widely discussed. In recent years, various types of optical solitons have been extensively studied, including bright solitons, gap solitons, dark solitons, vortices, and vector solitons. These solitons are supported by complex PT-symmetric potentials. It is widely accepted that linear PT-symmetric systems have a critical property, namely the existence of a threshold value for the strength of the imaginary component of a complex potential, known as the PT-symmetry breaking point. Once the threshold is surpassed, the spectrum shifts from real-valued to complex-valued. Article [25] provides a comprehensive review of nonlinear waves in PT-symmetric physical systems. In addition to Kerr or cubic nonlinearity, beam propagation has also been studied in media with higher-order nonlinearity. The presence of such nonlinearity significantly modifies beam propagation and can lead to completely new phenomena. Beam stability is achieved with higher-order nonlinearity. The inclusion of the quintic nonlinearity results in the formation of a stable composite soliton, which is not observed in Kerr media. The variational method is used to examine the generation and nonlinear dynamics of multi-dimensional optical dissipative solitonic pulses with the complex cubic–quintic Ginzburg–Landau equation [26]. In physical realizations, the quintic nonlinearity arises from three-body interactions in a dense Bose–Einstein condensate. Observations of cubic–quintic optical nonlinearity have been reported in the crystal, chalcogenide glasses, and ferroelectric films [27–30]. Recent studies have investigated the stability and evolution of solitons in media with competing cubic and quintic nonlinearities [31–37]. This article discusses multipole solitons in PT-symmetric potentials with focusing cubic and de-focusing quintic media [31]. It investigates the fundamental solitons in the cubic–quintic nonlinear Schrödinger equation with PT-symmetric potentials [32]. Additionally, it explores spatial solitons in non-parity–time-symmetric complex potentials with de-focusing

cubic and focusing quintic media [33]. This article analyses stable solitons in the one- and two-dimensional generalized cubic–quintic nonlinear Schrödinger equation with fourth-order diffraction and PT-symmetric potentials [34]. It also studies one-dimensional gap solitons in quintic and cubic–quintic fractional nonlinear Schrödinger equations with a periodically modulated linear potential [35]. Additionally, it presents families of fundamental and multipole solitons in a cubic–quintic nonlinear lattice in fractional dimension [36]. This study examines gap solitons in parity–time-symmetric optical lattices with competing cubic and quintic nonlinearities [37]. The results of [37] indicate that all dipole solitons are unstable, and only a small portion of fundamental solitons are stable when the strength of the focusing quintic nonlinearity is fixed.

After comparing the above-mentioned articles (e.g., [31–37]), we found that most of them have studied the ground state and multipole solitons with focusing cubic and defocusing quintic nonlinearity. However, there are few studies on defocusing cubic and focusing quintic nonlinearity. In particular, there has been relatively little exploration of multipole solitons in PT potentials exhibiting both focusing quintic and defocusing cubic nonlinearity. This study discusses one-dimensional spatial optical solitons in PT single potentials with focusing quintic and defocusing cubic nonlinearity. The model discussed in [31–37], i.e., one-dimensional nonlinear Schrödinger equation, is used to explore multipole solitons in PT single potentials. In this paper, we will consider a complex single potential with real part $V(X) = V_0 \operatorname{sech}^2(X/X_0)$ and imaginary part $W(X) = W_0 \operatorname{sech}(X/X_0) \tanh(X/X_0)$. When V_0, X_0, W_0 are changed, the profile of the real and imaginary components will be modulated. The Schrödinger equation can describe the propagation of a beam in nonlinear media. The nonlinearity in this article is due to cubic and quintic nonlinearities. The competing effects between these two nonlinearities play a significant role in the existence and stability of solitons. The focusing quintic nonlinearity coefficients (σ_2) are fixed at 1, while the coefficients of the cubic nonlinearity (σ_1) are varied from -1 to 0. The results indicate that solitons can exist and be stable within a suitable power range. Fundamental solitons can remain stable even for lower values of σ_1, while dipole and tripole solitons may only be stable for larger values of σ_1. However, it is important to note that these solitons are only stable within a small range of existence when appropriate parameters are employed. The stability of stationary solutions is analysed through linear stability analysis, and their evolution is verified using the beam propagation method.

The paper is organized as follows: In Sect. 2, we present the model and the method used for the linear stability analysis. In Sect. 3, we present a summary of extensive numerical results that outline the stability domains for the fundamental, dipole-, and tripole-bound states. These results are based on the computation of eigenvalues for small perturbations and are corroborated by direct simulations of perturbed propagation dynamics of the solitons. Finally, in Sect. 4, we conclude the results.

2. Theoretical model

This study examines the propagation of one-dimensional spatial optical solitons in PT-symmetric single potentials with competing cubic–quintic nonlinearities. The mathematical model used is the one-dimensional nonlinear Schrödinger equation. Optical waveguides with balanced gain and loss induce linear potentials, which aids in stabilizing various types of self-trapped modes. The propagation of the slowly varying beam envelope $\psi(X,Z)$ can be described by the normalized nonlinear Schrödinger equation, which is also discussed in [31–37],

$$\mathrm{i}\frac{\partial\psi(X,Z)}{\partial Z} + \frac{\partial^2\psi(X,Z)}{\partial X^2} + \sigma_1|\psi|^2\psi(X,Z) + \sigma_2|\psi|^4\psi(X,Z) + V_{PT}\psi(X,Z) = 0, \tag{1}$$

where X and Z are the transverse coordinate and scaled propagation distance, respectively; $\psi(X,Z)$ corresponds to the slowly varying amplitude of the light field; σ_1,σ_2 are the coefficients of the cubic and quintic nonlinearity, respectively; and $V_{PT} = V(X) + \mathrm{i}W(X)$ is the PT-symmetric potential. In the case of PT-symmetry, the potential satisfies the conditions $V(X) = V(-X)$ and $W(-X) = -W(-X)$. Here, the function $V(X)$ describes the real refractive index and $W(X)$ represents the gain-or-loss distribution of the potential.

Now we consider the solution of the form $\psi(X,Z) = \phi(X)\exp(\mathrm{i}\mu Z)$, where μ is a real propagation constant. Then we can obtain the following equation

$$\frac{\partial^2\phi}{\partial X^2} + \sigma_1|\phi|^2\phi + \sigma_2|\phi|^4\phi + V_{PT}\phi = \mu\phi. \tag{2}$$

The modified squared operator method [38] can be used to obtain a localized solution for $\phi(X)$. The stability of this solution was investigated using the Fourier collocation method [39]. The solution of (2) is given by small perturbations $f(X)$, $g(X)$, and is taken to be of the form [31–37]

$$\psi(X,Z) = \phi(X)\exp(\mathrm{i}\mu Z) + \varepsilon\left[f(X,Z)\mathrm{e}^{\lambda Z} + g^*(X,Z)\mathrm{e}^{-\lambda^* Z}\right]\exp(\mathrm{i}\mu Z). \tag{3}$$

Now substituting the expression in (1) and linearising, one gets the following coupled set of linear eigenvalue equations

$$\hat{L}\begin{Bmatrix} f \\ g \end{Bmatrix} = \lambda\begin{Bmatrix} f \\ g \end{Bmatrix}, \tag{4}$$

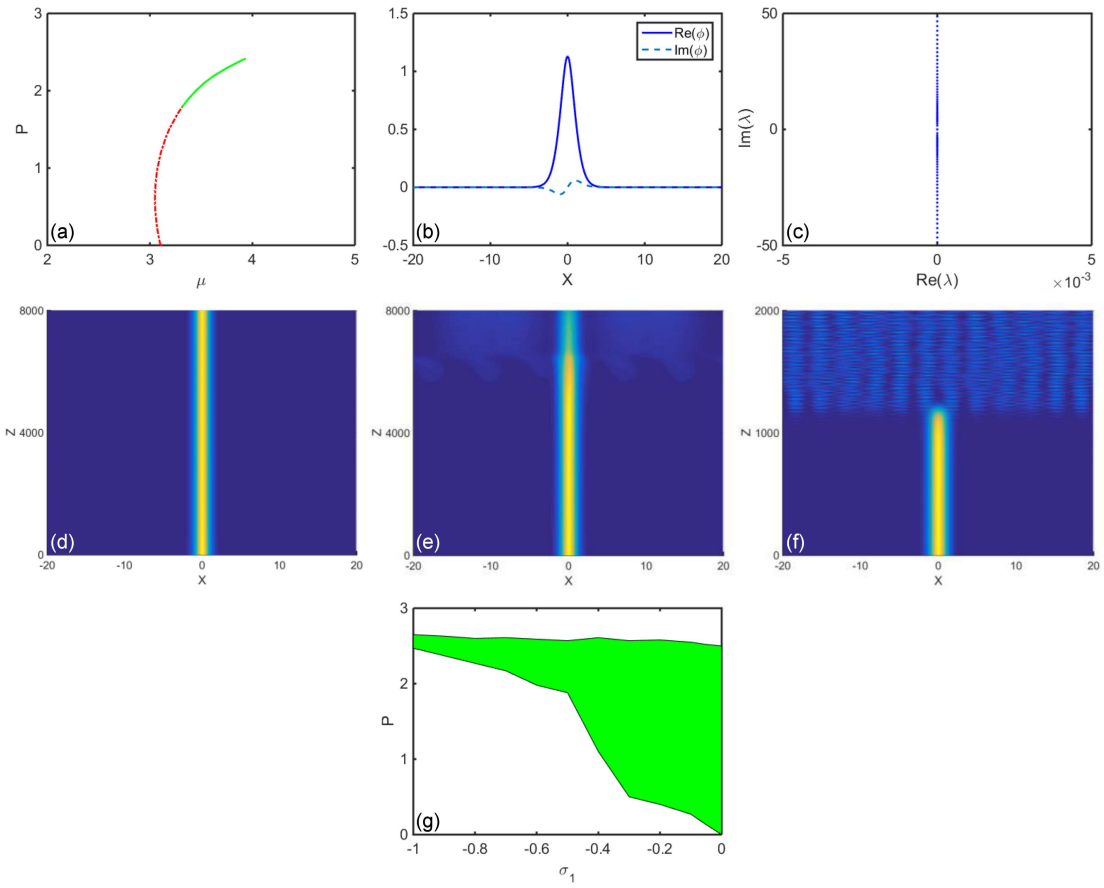

Fig. 1. (a) The dependence of the power P on the propagation constant μ. (b) The solid and dashed curves are, respectively, for real and imaginary parts of fundamental solutions when $P = 2.1$ at $\sigma_1 = -0.5$. (c) Linear stability eigenvalues when $P = 2.1$ at $\sigma_1 = -0.5$. (d, e) Stable or unstable propagations of fundamental modes when $P = 2.1$ and $P = 1.7$ at $\sigma_1 = -0.5$, respectively. (f) Unstable propagation of fundamental soliton for the lower value of σ_1, where $\sigma_1 = -1$, $P = 1.7$. (g) Stable area in green with different values of σ_1. The other parameters are chosen as $V_0 = 4$, $X_0 = 2$, $W_0 = 0.5$.

where

$$\hat{L} = \begin{Bmatrix} \hat{L}_1 & \hat{L}_2 \\ -\hat{L}_2^* & -\hat{L}_1^* \end{Bmatrix}, \tag{5}$$

while $\hat{L}_1 = \partial_{XX} + 2\sigma_1 |\phi|^2 + 3\sigma_2 |\phi|^4 + V_{PT} - \mu$, and $\hat{L}_2 = \sigma_1\phi^2 + 2\sigma_2\phi^3\phi^*$. The symbol "$*$" represents a complex conjugation. The perturbed solution will grow exponentially with Z, resulting in an unstable localized mode if real$(\lambda) \neq 0$. On the other hand, the localized modes are completely stable only when real$(\lambda) = 0$ for every λ (i.e., the system possesses solely imaginary eigenvalues).

3. Stability and evolution of solitons

This discussion concerns the solitons under the focusing quintic nonlinearity and various cubic nonlinearities in the presence of a PT potential. Specifically, let us consider a PT potential with the real part $V(X) = V_0 \mathrm{sech}^2(X/X_0)$ and imaginary part $W(X) = W_0 \mathrm{sech}(X/X_0)\tanh(X/X_0)$. When $X_0 = 1$, the PT potential is the complex Scarf II potential, considered in [1–5]. The profile of the real and imaginary components can be modulated by changing the value of X_0. The same applies to V_0 and W_0. Additionally, the values of σ_1 and σ_2 vary to form these solitons. The stability and propagation properties of the solitons are then described in detail.

Firstly, we will discuss the fundamental solitons. The properties of fundamental solitons are depicted in Fig. 1. The focusing quintic nonlinearity has a fixed coefficient of $\sigma_2 = 1$ throughout this paper, while the coefficient of the cubic nonlinearity σ_1 is varied and ranges from -1 to 0. To maintain generality, let $\sigma_1 = -0.5$, which makes the quintic nonlinearity focusing and the cubic nonlinearity defocusing. The parameters $V_0 = 4$, $X_0 = 2$ and $W_0 = 0.5$ are chosen. The dependence of the propagation constant μ on the power P (i.e., $P = \int_{-\infty}^{\infty} \mathrm{d}x\ |\phi|^2$) is shown in Fig. 1a. This fundamental soliton family exists in the domain where $3.10 \leq \mu \leq 3.92$, while the solitons are stable within the area where $3.32 \leq \mu \leq 3.92$. The stable area is plotted with

a green solid curve. The curve meets either the Vakhitov–Kolokolov (VK) [40, 41] or anti-VK [42] criteria, which serve as necessary conditions for the solitons' stability created by any defocusing or focusing nonlinearity. Solitons exist within a stable range of power, as shown by the curve. This range is bounded by minimum and maximum values, i.e., $P_{\min} \leq P \leq P_{\max}$.

Figure 1b presents the soliton profile, where the solid and dashed curves correspond to the real parts and imaginary sections of fundamental solutions at $P = 2.1$, respectively. It is evident that the solitons with a power of $P = 2.1$ are within the stable area. Figure 1c shows the linear-stability spectrum of this stable soliton where the real parts of all eigenvalues are zero when $P = 2.1$. The numerical study examines the nonlinear evolution of stable and unstable PT solitons under perturbation. Figure 1d, e shows the stable and unstable propagation of soliton mode propagation perturbed with random noise added at a level of 5% of the soliton amplitude at (d) $P = 2.1$ and (e) $P = 1.7$. In the stable case shown in Fig. 1d, the soliton intensity remains unchanged during evolution. In the unstable case depicted in Fig. 1e, the soliton intensity experiences a decrease after stable propagation for a certain distance. It should be noted that the largest real part of the corresponding eigenvalue is very small, with $\max(\mathrm{Re}(\lambda))$ being 0.0011 when $P = 1.7$. Hence, a weak instability corresponding to a very small growth rate is observed.

Specifically, for soliton families to exist under a particular power P, the cubic nonlinearity strength σ_1 must not go beyond a threshold of $\sigma_{\min} \leq \sigma_1 \leq 0$. The fundamental solitons are linearly stable only within a specific portion of their existence region. Numerical simulations indicate that power attains a maximum and a minimum value when σ_1 is between -1 and 0. No fundamental solitons exist when power exceeds the maximum. While if the power is less than the minimum, the fundamental soliton can exist for any value of σ_1 between -1 and 0. For instance, when $P = 2.1$, such fundamental solitons can exist if σ_1 is lower than the threshold, i.e., for $-1 \leq \sigma_1 \leq 0$, these solitons remain stable within the region of $-0.63 \leq \sigma_1 \leq 0$. Numerical calculations indicate that fundamental solitons do not exist when $P > 2.96$, while all fundamental solitons can exist for any value of σ_1 from -1 to 0 when $P < 1.95$. It is important to note that the stability and propagation properties of the solitons are highly sensitive to the values of σ_1. Generally, when σ_1 is increased, $P_{\min}$ decreases more than $P_{\max}$, resulting in an expansion of the stable existence area. Conversely, when σ_1 is decreased, $P_{\min}$ increases more than $P_{\max}$, leading to a shrinkage of the stable existence area. This implies that the stability region is narrower for lower values of σ_1 and wider for larger values of σ_1. Thus, the instability can be increased for lower values of σ_1. Figure 1f illustrates the unstable propagation of the fundamental soliton with $\sigma_1 = -1$ and $P = 1.7$. Evidently, the soliton intensity experiences a sudden decrease after stable propagation for a certain distance. Higher instability leads to shorter distances.

To analyse the stable properties of these solitons, we plotted the stable area for the fundamental solitons with varying values of σ_1. Figure 1g displays the stable area in green. Figure 1g illustrates that fundamental solitons can remain stable even for lower values of σ_1. It is evident that the solitons shown in Fig. 1e, f are not within the stable region. Furthermore, we aim to elucidate the effect of the potential's form on the stability regions of solitons and their impact on the spatial shape of nonlinear modes, as well as the influence of competing nonlinearities. The purpose of this investigation is to examine the role of the PT-symmetric potential on the nonlinear mode characteristics. To achieve this, we perform calculations using different values of the parameters. In general, we observe that the amplitude of the real parts of the fundamental solutions increases with an increase in V_0, however, it decreases with an increase in W_0 and X_0 at a particular power. Conversely, the amplitude of the imaginary part exhibits the opposite behaviour. In general, the stability regions of solitons will be enlarged for higher values of V_0 and lower values of W_0. Most importantly, the power P of the stable soliton decreases with the decrease in X_0, and the stable region of solitons expands. For instance, when $X_0 = 1.5$, the solitons are stable within the area where $0.55 \leq P \leq 2.15$, given the parameters $V_0 = 4$, $W_0 = 0.5$, $\sigma_1 = -0.5$. There are additional stable solitons for various values of σ_1 ranging from -1 to 0, and the stable region has expanded. Under the same conditions, the solitons are more stable for lower values of X_0.

Next, we will explore the dipole instances, as depicted in Fig. 2, which illustrates typical images of dipole solitons. For the value of σ_1, we chose -0.2, while other parameters were selected as follows $V_0 = 4$, $X_0 = 2$, $W_0 = 0.5$. The power curve of the dipole solitons is presented in Fig. 2a, revealing a clear pattern of increase in power of the dipole solitons with the propagation constant μ. Dipole soliton exists in the domain where $0 \leq P \leq 4.70$, and the solitons are stable within the area where $0.50 \leq P \leq 1.54$. The dipole soliton exists within a specific domain, and it stabilizes within a defined zone, as demonstrated by the solid green curve. The solid and dashed curves in Fig. 2b display, respectively, the real and imaginary components of dipole solutions at power level $P = 1$. Additionally, Fig. 2c exhibits the linear stability spectrum of the stable soliton where the real portions of all eigenvalues are zero. It is evident that the dipole solitons with power $P = 1$ exist within the stable region. Furthermore, we have conducted a numerical analysis of the nonlinear evolution of both stable and unstable dipole solitons under perturbation. In Fig. 2d and Fig. 2e, the stable and unstable propagations of dipole solitons are shown

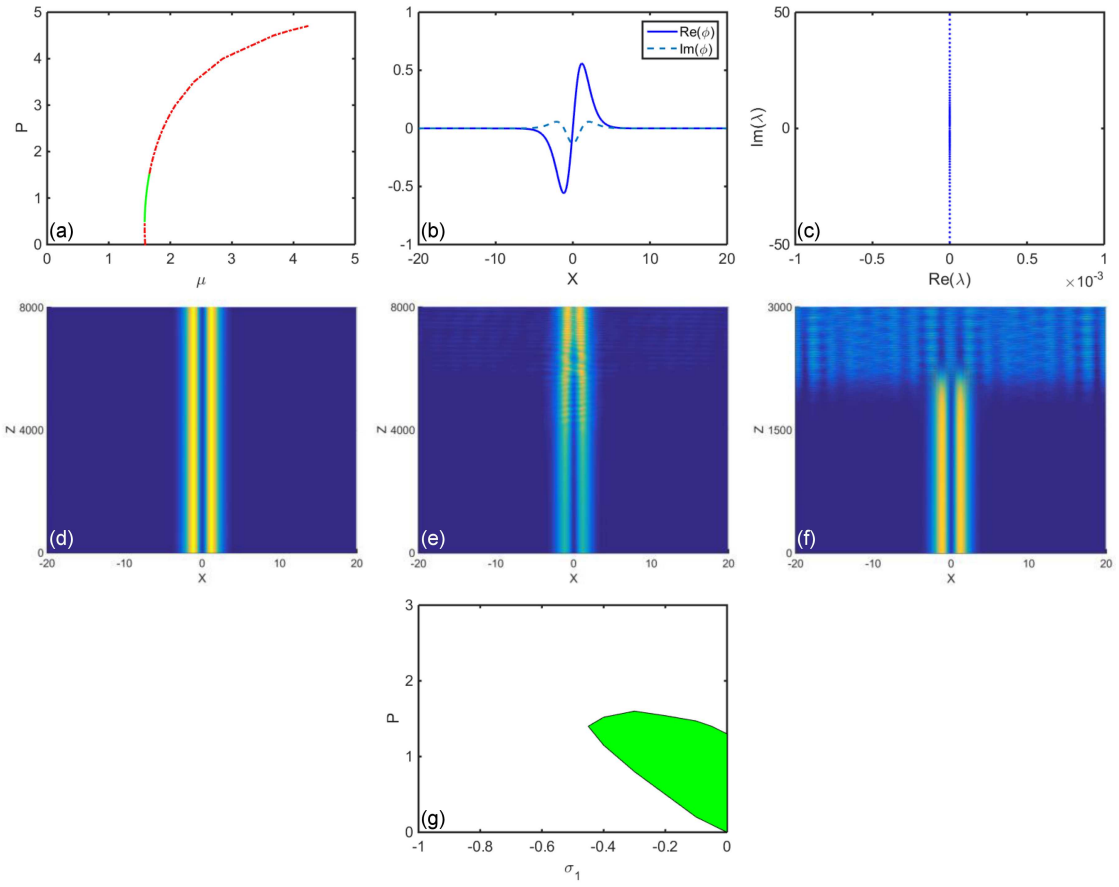

Fig. 2. (a) The dependence of the propagation constant μ on the power P. (b) The solid and dashed curves are for real and imaginary parts of dipole solutions when, respectively, $P = 1$ at $\sigma_1 = -0.2$. (c) Linear stability eigenvalues when $P = 1$ at $\sigma_1 = -0.2$. (d, e) Stable or unstable propagations of nonlinear dipole modes when $P = 1$ and $P = 1.8$ at $\sigma_1 = -0.2$, respectively. (f) Unstable propagation of dipole soliton when $P = 1$ at $\sigma_1 = -0.5$. (g) Stable area in green with different values of σ_1. The parameters are chosen as $V_0 = 4$, $X_0 = 2$, $W_0 = 0.5$.

at $P = 1$ and $P = 1.8$, respectively. Figure 2d demonstrates the robustness of dipole solitons as their intensity remains unchanged during evolution. However, in the unstable case shown in Fig. 2e, the soliton intensity decreases after stable propagation over a certain distance. The maximum real part of the corresponding eigenvalue is extremely small, with $\max(\mathrm{Re}(\lambda))$ being 0.0025 at $P = 1.8$. Such a weak instability is indicative of a very small growth rate. The effect of competing cubic and quintic nonlinearities varies depending on the value of σ_1. In general, it is easy to generate dipole solitons for any value of σ_1 ranging from -1 to 0 for a specific power P. However, the stable region is narrow in a specific section of their existence area. For instance, when given $P = 1$, in order for these dipole solitons to exist and remain stable, σ_1 should be within the range of $-0.35 \leq \sigma_1 \leq 0$. Dipole solitons become unstable when $\sigma_1 < -0.35$. We vary σ_1 over the range of -1 to 0, observing the typical unstable propagation of the dipole soliton for lower values of σ_1. Figure 2f illustrates this phenomenon with $\sigma_1 = -0.5$ and $P = 1$. It is evident that the soliton intensity undergoes changes during its propagation. In general, dipole solitons tend to be unstable for lower values of σ_1 but are relatively stable for larger values. This can be observed by comparing Fig. 2d and Fig. 2f.

In summary, Fig. 2g displays the stable area in green for these dipole solitons with varying values of σ_1. Figure 2g shows that dipole solitons may only be stable for larger values of σ_1. It is clear that the dipole solitons in Fig. 2e, f are not within the stable area. In this study, we investigate the impact of competing nonlinearities on the stability of solitons, as well as the influence of the PT-symmetric potential on the nonlinear mode characteristics. The amplitude of the real parts of the dipole soliton solutions generally increases with an increase in V_0 but decreases with an increase in W_0 and X_0 at a particular power. Conversely, the amplitude of the imaginary part exhibits the opposite behaviour. In general, the power decreases as X_0 decreases under the same conditions. The stability regions of solitons will be enlarged for higher values of V_0 and lower values of W_0, while they will shrink with the

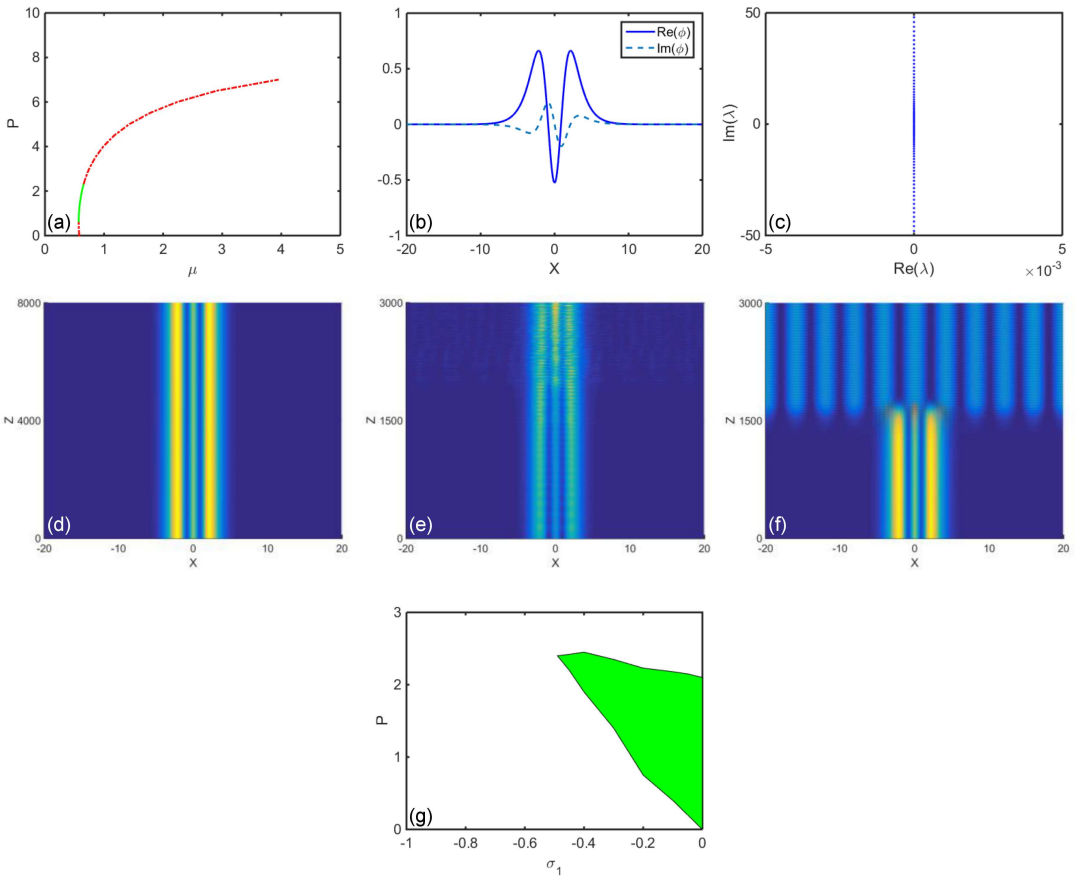

Fig. 3. (a) The dependence of the power P on the propagation constant μ. (b) The solid and dashed curves are for, respectively, the real and imaginary parts of tripole solutions when $P = 2$ at $\sigma_1 = -0.2$. (c) Linear stability eigenvalues when $P = 2$ at $\sigma_1 = -0.2$. (d, e) Stable or unstable propagations of nonlinear tripole modes when, respectively, $P = 2$ and $P = 2.6$ at $\sigma_1 = -0.2$. (f) Unstable propagation of tripole soliton when $P = 2$ at $\sigma_1 = -0.5$. (g) Stable area in green with different values of σ_1. The parameters are chosen as $V_0 = 4$, $X_0 = 2$, $W_0 = 0.5$.

decrease in X_0. For example, when $X_0 = 1$, there are no stable dipole solitons when $\sigma_1 \leq -0.38$, given the parameters $V_0 = 4$ and $W_0 = 0.5$. Generally, the stability region is narrower for lower values of σ_1 and wider for larger values of σ_1. Thus, the instability can be increased for lower values of σ_1. It should be noted that all solitons are affected by random noise, which is added at a level of 5% of the soliton amplitude at the input.

Finally, we will now consider the tripole cases. Figure 3 displays typical images of tripole solitons. Here, σ_1 is set to -0.2, while the other parameters are as follows: $V_0 = 4$, $X_0 = 2$, $W_0 = 0.5$. In Fig. 3a, we can observe the power curve of the tripole solitons. The tripole soliton family exists within the domain $0 \leq P \leq 7.0$, while the solitons are stable within the area $0.78 \leq P \leq 2.23$. The stable area is displayed as a green solid curve. Figure 3b shows the real (solid curves) and imaginary (dashed curves) parts of tripole solutions when $P = 2$. Figure 3c shows the linear-stability spectrum of the stable soliton, where the real parts of all eigenvalues are zero when $P = 2$. The stable region consists of tripole solitons with power $P = 2$. To confirm the findings of the linear stability analysis, we numerically simulated equation (1) to propagate the stationary solution. We perturbed tripole solitons with a 5% random noise and summarized the subsequent soliton evolutions in Fig. 3d, e. The results show that the intensity of the stable soliton mode propagation remains constant, while in the unstable case, it decreases. The power value of $P = 2$ in Fig. 3d falls within the stable region. However, the power value of $P = 2.6$ in Fig. 3e does not fall within the stable region. In the unstable case, the maximum real part of the corresponding eigenvalue is very small, with a maximum of $\mathrm{Re}(\lambda) = 0.0034$ when $P = 2.6$. Therefore, the growth rate is low for weak instability. When considering a particular power P, it is possible to form tripole solitons for any value of σ_1 from -1 to 0. However, their existence is limited to a narrow stable region. The competition between cubic and quintic nonlinearities changes as σ_1 varies from -1 to 0. For example, tripole solitons remain stable when $P = 2$ and σ_1 varies between -0.41 and 0, but they become

unstable when σ_1 decreases. Figure 3f displays the typical unstable propagation of a tripole soliton for a lower value of σ_1, where $\sigma_1 = -0.5$, $P = 2$. Upon comparison with Fig. 3d, f, it becomes clear that the tripole soliton can indeed be stable for a larger value of σ_1. However, for a lower value of σ_1, it becomes difficult for the tripole soliton to remain stable.

To summarise, Fig. 3g displays the stable area in green for tripole solitons with varying values of σ_1. Figure 3g shows that tripole solitons may only be stable for larger values of σ_1. It is evident that the tripole solitons illustrated in Fig. 3e, f are outside the stable region. In this study, we also investigate the impact of the PT-symmetric potential on the nonlinear mode characteristics and stability properties. Our findings indicate that, in general, the amplitude of the real parts of the tripole soliton solutions increases with an increase in V_0 but decreases with an increase in W_0 and X_0 at a particular power. Conversely, the amplitude of the imaginary part exhibits the opposite behaviour. Under the same conditions, the stability regions of solitons will be enlarged for higher values of V_0 and lower values of W_0. It is difficult to form stable solitons for very low values of X_0. Generally, the power of stable solitons decreases as X_0 increases. Tripole solitons exist when the power exceeds the minimum and is less than the maximum at a certain σ_1. The stability region is narrower for lower values of σ_1 and wider for larger values of σ_1.

Furthermore, we conducted numerous numerical simulations with alternative parameters, which yielded comparable findings. Solitons are able to exist, remain stable within a suitable power range, and sustain stability for a larger value of σ_1. A considerable proportion of solitons can be stabilized by employing appropriate parameters.

4. Conclusions

In conclusion, this study examines the existence, stability, and propagation of fundamental, dipole, and tripole modes in PT potentials with competing cubic and quintic nonlinearity. The case of PT solitons under focusing quintic nonlinearity and various defocusing cubic nonlinearity is discussed. The competing effect between cubic and quintic nonlinearities plays a significant role in the existence and stability of both fundamental and multi-pole PT solitons. The focusing quintic nonlinearity coefficients (σ_2) are fixed at 1, while the coefficients of the cubic nonlinearity (σ_1) are varied from -1 to 0. The results indicate that solitons can exist and be stable within a suitable power range, with greater stability observed for larger values of σ_1. Fundamental solitons can remain stable even for lower values of σ_1, while dipole and tripole solitons may only be stable for larger values of σ_1. These solitons may be stable within a small range of existence by employing appropriate parameters. Linear stability analysis was conducted to investigate the stability of these stationary solutions. Additionally, direct numerical simulations were used to explore the propagation of these solutions.

References

[1] C.M. Bender, S. Boettcher, *Phys. Rev. Lett.* **80**, 5243 (1998).

[2] C.M. Bender, *Rep. Prog. Phys.* **70**, 947 (2007).

[3] Z.H. Musslimani, K.G. Makris, R. El-Ganainy, D.N. Christodoulides, *Phys. Rev. Lett.* **100**, 030402 (2008).

[4] K.G. Makris, R. El-Ganainy, D.N. Christodoulides, Z.H. Musslimani, *Phys. Rev. Lett.* **100**, 103904 (2008).

[5] Z.H. Musslimani, K.G. Makris, R. El-Ganainy, D.N. Christodoulides, *J. Phys. A Math. Theor.* **41**, 244019 (2008).

[6] C. Huang, J. Zeng, *Opt. Laser Technol.* **88**, 104 (2017).

[7] X. Li, L. Wang, Z. Zhou, Y. Chen, Z. Yan, *Nonlinear Dyn.* **108**, 4045 (2022).

[8] N. Ghosh, A. Das, D. Nath, *Nonlinear Dyn.* **111**, 1589 (2023).

[9] L. Dong, L. Gu, D. Guo, *Phys. Rev. A* **91**, 053827 (2015).

[10] P. Li, C. Dai, R. Li, Y. Gao, *Opt. Exp.* **26**, 6949 (2018).

[11] T.D. Haji, T.M. Solaimani, M. Ghalandari, B. Babayar-Razlighi, *Phys. Scr.* **96**, 125531 (2021).

[12] X. Zhu, W. Che, Z. Wu, J. Xie, Y. He, *J. Opt.* **22**, 035503 (2020).

[13] X. Zhu, X. Peng, Y. Qiu, H. Wang, Y. He, *New. J. Phys.* **22**, 033035 (2020).

[14] Z. Shi, H. Li, X. Zhu, X. Jiang, *Europhys. Lett.* **98**, 64006 (2012).

[15] J. Huang, Y. Weng, H. Wang, *Opt. Exp.* **26**, 11667 (2018).

[16] J. Yang, *Phys. Rev. E* **98**, 042202 (2018).

[17] P.J. Chen, H. Wang, *Opt. Exp.* **31**, 30529 (2023).

[18] L. Qin, C. Hang, Z.Y. Shi et al., *Opt. Exp.* **31**, 11116 (2023).

[19] S. Bhatia, A. Goyal, S. Jana, C.N. Kumar, *Phys. Lett. A* **469**, 128751 (2023).

[20] W.B. Bo, R.R. Wang, W. Liu, Y.Y. Wang, *Chaos* **32**, 093104 (2022).

[21] M. Bagci, *Phys. Rev. A* **103**, 023530 (2021).

[22] E. Luz, V. Lutsky, E. Granot, B.A. Malomed, *Sci. Rep.* **9**, 4483 (2019).

[23] M. Ögren, F.K. Abdullaev, V.V. Konotop, *Opt. Lett.* **42**, 4079 (2017).

[24] Y. Zhong, H. Triki, Q. Zhou, *Nonlinear Dyn.* **112**, 1349 (2024).

[25] B.A. Malomed, D. Mihalache, *Rom. J. Phys.* **64**, 106 (2019).

[26] V. Skarka, N.B. Aleksic, *Acta Phys. Pol. A* **112**, 791 (2007).

[27] C. Zhan, D. Zhang, D. Zhu et al., *J. Opt. Soc. Am. B* **19**, 369 (2002).

[28] E.L. Falcao-Filho, C.B. de Araujo, J.J. Rodrigues Jr., *J. Opt. Soc. Am. B* **24**, 2948 (2007).

[29] K. Ogusu, J. Yamasaki, S. Maeda, M. Kitao, M. Minakata, *Opt. Lett.* **29**, 265 (2004).

[30] B. Gu, Y. Wang, W. Ji, J. Wang, *Appl. Phys. Lett.* **95**, 041114 (2009).

[31] P. Li, L. Li, D. Mihalache, *Rom. Rep. Phys.* **70**, 408 (2018).

[32] G. İzzet, A. Nalan, B. İlkay, *Opt. Commun.* **354**, 277 (2015).

[33] X. Zhu, Z. Cai, J. Liu, S. Liao, Y. He, *Nonlinear Dyn.* **108**, 2563 (2022).

[34] N.T. Nkouessi, G.C. Tiofack Latchio, A. Mohamadou, *Eur. Phys. J. D* **74**, 32 (2020).

[35] L. Zeng, J. Zeng, *Nonlinear Dyn.* **98**, 985 (2019).

[36] L. Zeng, D. Mihalache, B.A. Malomed, X. Lu, Y. Cai, Q. Zhu, J. Li, *Chaos Solitons Fract.* **144**, 110589 (2021).

[37] L. Ge, M. Shen, T. Zang, C. Ma, L. Dai, *Phys. Rev. E* **91**, 023203 (2015).

[38] J. Yang, T.I. Lakoba, *Stud. Appl. Math.* **118**, 153 (2007).

[39] J. Yang, *J. Comput. Phys.* **227**, 6862 (2008).

[40] N. Vakhitov, A. Kolokolov, *Radiophys. Quantum Electron.* **16**, 783 (1973).

[41] L. Berge, *Phys. Rep.* **303**, 259 (1998).

[42] H. Sakaguchi, B.A. Malomed, *Phys. Rev. A* **81**, 013624 (2010).

Correlated and Uncorrelated Debye–Waller Factors and Correlation Function in Atomic Vibrations Including Many-Body Effects

N. Van Hung* and N. Cong Toan

Department of Physics, VNU University of Science, 334 Nguyen Trai, Thanh Xuan, Hanoi, Vietnam

Received: 10.02.2024 & Accepted: 09.05.2024

Doi: 10.12693/APhysPolA.146.95 *e-mail: hungnv@vnu.edu.vn

Correlated and uncorrelated Debye–Waller factors and correlation function in atomic vibrations described by mean square relative displacement, mean square displacement, and displacement–displacement correlation function, respectively, have been studied based on correlated and uncorrelated Einstein models, including many-body effects. The impact of many-body effects in the derived analytical expressions of the above-considered quantities is realized by using the effective potentials of the derived Einstein models, which take into account the contributions of all nearest neighbors of vibrating atoms. The Morse potential is used to describe the single-pair atomic interactions. The difference between the correlated Debye–Waller factor and the uncorrelated one is considered to be the source of the correlation effect described by the correlation function, which is temperature- and crystal-type-dependent. The larger such difference is, the stronger the correlation effect it generates. The numerical results for the Cu crystal agree with experimental results and with those calculated using other theories.

topics: correlated and uncorrelated Debye–Waller factors, correlation function, correlated and uncorrelated Einstein models, effective potentials and many-body effects

1. Introduction

Thermal atomic vibrations and disorders in extended X-ray absorption fine structure (EXAFS) spectroscopy and other related spectroscopy give rise to Debye–Waller factors (DWFs) [1–26]. These factors used in EXAFS and related spectra depend on the temperature T as $e^{-W(T)}$ and on the wave number k (or energy). For EXAFS spectroscopy, $W(T) \approx 2k^2\sigma^2(T)$, where $\sigma^2(T)$ is the mean square relative displacement (MSRD) of bond between absorber and backscatter atoms. The EXAFS DWF is analogous to factor found in X-ray and neutron diffraction or the Mössbauer effect, where $W(T) = \frac{1}{2}k^2u^2(T)$. The difference is that the EXAFS DWF refers to correlated averages over relative displacements, as is the case of the MSRD $\sigma^2(T)$, while in X-ray absorption or neutron diffraction, $u^2(T)$ refers to the mean square displacement (MSD) of a given atom. Unfortunately, the MSRD or correlated DWF $\sigma^2(T)$ and the MSD or uncorrelated DWF $u^2(T)$ are closely related with one another and from them, the displacement–displacement correlation function (DCF) or correlation function $C_R(T)$ describing the correlation effects is generated. Accurate DWFs and other related functions such as $u^2(T)$ and $C_R(T)$ are crucial to quantitative treatment of the X-ray absorption spectra and different effects in EXAFS theory.

Many efforts have been made to derive procedures for studying DWFs of materials. Satisfactory procedures are those of classical methods [2–6], which have the advantages of simplicity and work very well at high temperatures, except for limitations at low temperatures due to the absence of zero-point vibration. Importantly, the derived procedures include also quantum methods, which have the advantages of working at both low and high temperatures. These include, for example, the effective anharmonic single-particle potential method [7], the single bond correlated Einstein model [8], the path integral effective potential [9], the full lattice dynamical (FLD) approach [10, 11], the local force constant theory [12], the dynamic matrix calculation [13], the path-integral Monte Carlo calculation [14], the anharmonic correlated Einstein model (ACEM) [15], the anharmonic correlated Debye model [16], and many others. The efforts undertaken have proven to make significant contributions to materials research, for example [17–24]. Here, ACEM is successfully applied in the development of several methods such as: EXAFS theory including anharmonic contributions [17], method for studying EXAFS of doping

materials compared to Mössbauer studies [18], pressure effects in EXAFS [19], thermodynamic properties of isotopes [20] and of semiconductors [21]. Moreover, based on DWFs, the effective methods have been derived for studying strong anharmonicity in tin monosulfide evidenced by local distortion, high-energy optic phonons [22], melting curve, eutectic point, Lindemann's melting temperature of close-packed hexagonal (hcp) binary alloys [23], and a semi-classical ACEM for hcp crystals [24]. Unfortunately, there are still few works [25, 26] concerning the uncorrelated DWF $u^2(T)$ and the DCF or correlation function $C_R(T)$ describing the correlation effects in atomic vibrations.

The purpose of this work is to derive the method enabling the calculation and analysis of correlated and uncorrelated DWFs and then correlation function in atomic vibrations (i.e., σ^2, u^2, and C_R, described, respectively, by MSRD, MSD, and DCF), including many-body effects. In Sect. 2 the analytical expressions have been derived for the correlated DWF $\sigma^2(T)$ based on the correlated Einstein model (CEM) using a correlated atomic vibration (CAV) and for the uncorrelated DWF $u^2(T)$ based on the uncorrelated Einstein model (UCEM) using a single atomic vibration (SAV). The correlation function $C_R(T)$ is generated from the difference between the derived $\sigma^2(T)$ and $u^2(T)$. The many-body effects given in the derived analytical expressions of $\sigma^2(T)$, $u^2(T)$ and $C_R(T)$ are obtained based on the CEM and UCEM effective potentials, which include contributions of all nearest neighbors of the absorber and backscatter atoms in the case of CEM and of a single atom in the case of UCEM. The created method leads to the simplification of the operation of a many-body system in the EXAFS theory to a useful one, which is a one-dimensional model. The Morse potential is assumed to describe the single-pair atomic interactions. The numerical results for Cu (Sect. 3), i.e., for one of the intensively studied crystals, are compared with: (i) experimental values taken from the measured Morse parameters (MMP) [27], (ii) measured values [7, 27–29] for $\sigma^2(T)$, and also (iii) with values calculated using other theories [25, 26] for the ratio C_R/u^2, which in fact show good agreement. Conclusions on the obtained results are presented in Sect. 4.

2. Correlated and uncorrelated DWFs and correlation function based on CEM and UCEM

2.1. Relation of correlation function with correlated and uncorrelated DWFs

The definition of MSRD or correlated DWF $\sigma^2(T)$ implies its close relation with the MSD or uncorrelated DWF u^2(T) and the DCF or correlation function C_R(T). It can be written as

$$\sigma^2(T) = \left\langle \left[\hat{\boldsymbol{R}}^0 \cdot (\boldsymbol{u}_i - \boldsymbol{u}_0)\right]^2 \right\rangle = 2u^2(T) - C_R(T), \tag{1}$$

where $\boldsymbol{u}_i - \boldsymbol{u}_0$ included in the first equation of (1) contains the atomic displacements of the i-th and 0-th sites defined by their displacements from those of the equilibrium positions, $\hat{\boldsymbol{R}}^0$ is the unit vector pointing from the 0-th site towards the i-th site, and the bracket $\langle \ldots \rangle$ denotes the thermal average.

Moreover, in the second equation of (1), the uncorrelated DWF or MSD u^2(T) has been defined as

$$u^2(T) = \left\langle \left(\boldsymbol{u}_0 \cdot \hat{\boldsymbol{R}}^0\right)^2 \right\rangle = \left\langle \left(\boldsymbol{u}_i \cdot \hat{\boldsymbol{R}}^0\right)^2 \right\rangle, \tag{2}$$

and then the DCF of correlation function C_R(T) had to take the form

$$C_R(T) = 2\left\langle \left(\boldsymbol{u}_0 \cdot \hat{\boldsymbol{R}}^0\right)\left(\boldsymbol{u}_i \cdot \hat{\boldsymbol{R}}^0\right) \right\rangle = 2u^2(T) - \sigma^2(T), \tag{3}$$

which is apparently obtained by the difference between the correlated and uncorrelated DWFs.

2.2. Effective potentials of CEM and UCEM

In order to specify the thermodynamic parameters, it is necessary to determine the local force constants [7–21]. The effective potential applied in the present theory can be expressed as a function of the displacement $x = r - r_0$ along the direction $\hat{\boldsymbol{R}}^0$, with r and r_0 being the instantaneous and equilibrium distances between the absorber and backscatter atoms. Thus, the expressions of the potencial for the CEM using CAV ($V_{\rm eff}^C(x)$) and for the UCEM using SAV ($V_{\rm eff}^S(x)$) have the following forms

$$V_{\rm eff}^{C(S)}(x) \approx \frac{1}{2} k_{\rm eff}^{C(S)} x^2, \tag{4}$$

where the difference of the mentioned potentials is caused by the difference between their effective local force constants $k_{\rm eff}^C$ for the CAV model and $k_{\rm eff}^S$ for the SAV model, used in the present theory.

Note that since atomic correlations do not involve anharmonic contribution, the effective interatomic interaction potential given by (4) only includes harmonic terms.

The values of $k_{\rm eff}^C$ for the atomic correlated effective potential can be obtained by comparing the potential $V_{\rm eff}^C(x)$ of (4) to that defined for a single bond pair in the center-of-mass frame [14] of the absorber with mass M_1 and the backscatter atoms with mass M_2. Therefore, we have

$$V_{\rm eff}^C(x) = V(x) + \sum_{j \neq i} V\left(\frac{\mu}{M_i} x\, \hat{\boldsymbol{R}}_{12} \cdot \hat{\boldsymbol{R}}_{ij}\right) = V(x) + 2V\left(-\frac{x}{2}\right) + 8V\left(-\frac{x}{4}\right) + 8V\left(\frac{x}{4}\right), \tag{5}$$

where the first term on the right concerns only absorber and backscatter atoms, the second one,

containing the sum i over absorber ($i = 1$) and backscatter ($i = 2$) and the sum j over their remaining nearest neighbors, describes the lattice contributions or many-body effect to the pair interaction and depends on crystal structure type. Here, $\hat{\boldsymbol{R}}$ is the bond unit vector. The second equation of (5) is for the monatomic face-centered cubic (fcc) crystals, in which the reduced mass $\mu = M_1M_2/(M_1 + M_2)$ is replaced by $M/2$ because $M = M_1 = M_2$ stands for the atomic mass.

The values of $k^S_{\rm eff}$ are obtained by using the potential $V^S_{\rm eff}(x)$ of (4) and a method [30] for the single-atom effective potential, which takes into account only the influence of N nearest atomic neighbors of the central atom as

$$V^S_{\rm eff}(x) = \sum_{j=1}^{N} V\left(x\hat{\boldsymbol{R}}^0 \cdot \hat{\boldsymbol{R}}_j\right) = V(x) + V(-x) + 4V\left(\frac{x}{2}\right) + 4V\left(-\frac{x}{2}\right), \tag{6}$$

where $\hat{\boldsymbol{R}}_j$ are the unit vectors of the nearest neighboring atoms with respect to the equilibrium position of the central atom. The second equation of (6) is for monatomic fcc crystals.

The advantage of applying the effective potentials given by (5) for CEM and (6) for UCEM in the present theory is the possibility of taking into account many-body effects or lattice contributions. This is achieved by including the contributions of all nearest neighbors of the absorber and backscatter atoms for the CEM and of a single atom for the UCEM, where these derived effective potentials are presented as one-dimensional. In this manner, a complicated task of many-body system in EXAFS theory is simplified to one-dimensional model.

To describe a single-pair atomic interaction, we use the Morse potential expanded up to second order (harmonic term) around its minimum

$$V(x) = D\left(\mathrm{e}^{-2\alpha x} - 2\mathrm{e}^{-\alpha x}\right) \approx D\left(-1 + \alpha^2 x^2\right), \tag{7}$$

where α describes the width of the potential, and D is the dissociation energy.

Based on the atomic structure of the fcc crystal, the effective local force constants $k^C_{\rm eff}$ of CEM and $k^S_{\rm eff}$ of UCEM, given indirectly by the Morse potential parameters in (4), could be written here as

$$k^C_{\rm eff} = 5D\alpha^2, \qquad k^S_{\rm eff} = 8D\alpha^2. \tag{8}$$

Note that the significant difference between the above $k^S_{\rm eff}$ and $k^C_{\rm eff}$ will lead to a difference of the EXAFS quantities obtained from CEM and UCEM.

2.3. Analytical expressions of correlated and uncorrelated DWFs as well as correlation function

Based on CEM, the analytical expression of the temperature-dependent correlated DWF or MSRD $\sigma^2(T)$ using CAV has been derived and given by

$$\sigma^2(T) \cong \langle x^2 \rangle = \sigma_0^2 \frac{1+z}{1-z}, \qquad \sigma_0^2 = \frac{\hbar\omega^C_E}{k^C_{\rm eff}}, \tag{9}$$

$$z = \exp\left(-\frac{\theta^C_E}{T}\right), \qquad \theta^C_E = \frac{\hbar\omega^C_E}{k_{\rm B}}, \qquad \omega^C_E = \sqrt{\frac{k^C_{\rm eff}}{\mu}}, \tag{10}$$

where μ is the reduced mass of correlated vibrating atoms and $k_{\rm B}$ is the Boltzmann constant.

Similarly, based on UCEM, the analytical expression of the temperature-dependent uncorrelated DWF or MSD u^2(T) using SAV has been derived and given in the form

$$u^2(T) = u_0^2 \frac{1+z_1}{1-z_1}, \qquad u_0^2 = \frac{\hbar\omega^S_E}{k^S_{\rm eff}}, \tag{11}$$

$$z_1 = \exp\left(\frac{-\theta^S_E}{T}\right), \qquad \theta^S_E = \frac{\hbar\omega^S_E}{k_{\rm B}}, \qquad \omega^S_E = \sqrt{\frac{k^S_{\rm eff}}{M}}, \tag{12}$$

where M is the mass of a composite atom.

In the above analytical expressions, the CEM frequencies and temperatures are given by, respectively,

$$\omega^C_E = \sqrt{\frac{k^C_{\rm eff}}{\mu}} \qquad \text{and} \qquad \theta^C_E = \frac{\hbar\omega^C_E}{k_{\rm B}}, \tag{13}$$

and the UCEM frequencies and temperatures are given by, respectively,

$$\omega^S_E = \sqrt{\frac{k^S_{\rm eff}}{M}} \qquad \text{and} \qquad \theta^S_E = \frac{\hbar\omega^S_E}{k_{\rm B}}. \tag{14}$$

Consequently, the correlation function $C_R(T)$ describing the correlation effect is calculated using (3) based on the above expressions for the uncorrelated DWF $u^2(T)$ and correlated DWF $\sigma^2(T)$. The derived correlation function has the form

$$C_R(T) = 2u_0^2 \frac{1+z_1}{1-z_1} - \sigma_0^2 \frac{1+z}{1-z}, \tag{15}$$

where σ_0^2, z and u_0^2, z_1 are defined in (9)–(10) and (11)–(12), respectively.

Hence, the correlation function $C_R(T)$ describing the correlation effects of atomic vibrations in the materials results from the difference between the correlated DWF $\sigma^2(T)$ and the uncorrelated DWF $u^2(T)$. It has the same unit as DWF, behaving as a thermodynamic parameter. Actually, the reason causing this correlation effect can be attributed to the difference between the local force constants $k^C_{\rm eff}$ and $k^S_{\rm eff}$, as well as the difference between the reduced mass μ in CEM using CAV and the mass M of a composite atom in UCEM using SAV. This property will be discussed in detail through the numerical results presented in Sect. 3 for Cu as a fcc crystal.

Note that the functions $\sigma^2(T)$, u^2(T), and C_R(T) obtained above include many-body effects or lattice contributions because they contain the effective local force constants $k^C_{\rm eff}$ and $k^S_{\rm eff}$ describing the correlated and uncorrelated DWFs which actually include many-body effects.

3. Numerical results and discussions

Now, the expressions derived in the previous sections are applied to the numerical calculations for Cu in the fcc phase. Using the Morse potential parameters of Cu [31], i.e., $D = 0.3429$ eV, $\alpha = 1.3588$ Å^{-1}, and its measured Morse parameters, i.e., (MMP) [27] $D = 0.33$ eV, $\alpha = 1.38$ Å^{-1}, the effective local force constants $k^C_{\rm eff}$, $k^S_{\rm eff}$, as well as the correlated Einstein frequencies ω^C_E and temperature θ^C_E, and the uncorrelated Einstein frequency ω^S_E and temperature θ^S_E with respect to CAV in CEM and to SAV in UCEM, respectively, have been calculated. Some of the results are included in Table I.

The calculated results for the above-considered quantities of Cu written in Table I show the significant differences between the CAV model (with upper index "C") and the SAV model (with upper index "S"). The effective local force constant for the SAV model ($k^S_{\rm eff}$) is much larger than the one ($k^C_{\rm eff}$) for the CAV model. The reasons for this difference can be attributed to the difference in the number and mass of vibrating particles, because in the CAV model, there is only half of them compared to the SAV model. Actually, in the center-of-mass frame of single bond pair for the CAV model, the crystal behaves as it consists of quasi-atoms having a reduced mass that equals only half the composite mass of the atom, as shown in (5), and their number is only half the atomic number for the SAV model, because each quasi-atom is constructed from a pair of composite atoms. This difference also leads to the result, in which the values of correlated Einstein frequency ω^C_E and temperature θ^C_E obtained from the CAV model are larger than, respectively, ω^S_E and θ^S_E, obtained from the SAV model (Table I). Here, the value of $\theta^C_E = 234$ K calculated using the present theory (Table I) is close to the experimental result of 232 K [3, 29].

Figure 1 illustrates the effective potentials $V^{C(S)}_{\rm eff}(x)$ of Cu calculated using the present theory for the CAV and SAV models, which agree well with the experimental values (Exper.) obtained from MMPs [27]. Here, the SAV potential $V^S_{\rm eff}(x)$ is bigger than the CAV potential $V^C_{\rm eff}(x)$ because the effective local force constant for the SAV model ($k^S_{\rm eff}$) is larger than the one ($k^C_{\rm eff}$) for the CAV model (Table I). This means that the atomic interaction described by the SAV model or the CEM is stronger than the one for the CAV model or the UCEM. This discrepancy also leads to the difference between other quantities such as ω^C_E, θ^C_E (calculated using CEM) and ω^S_E, θ^S_E (calculated using UCEM), written in Table I. Such properties can be understood because the number and the mass of atoms in the SAV model are larger than those of the quasi-atoms in the CAV model.

Figure 2 illustrates the temperature dependence of the Debye–Waller factors: correlated DWF or MSRD $\sigma^2(T)$, uncorrelated DWF or MSD $u^2(T)$,

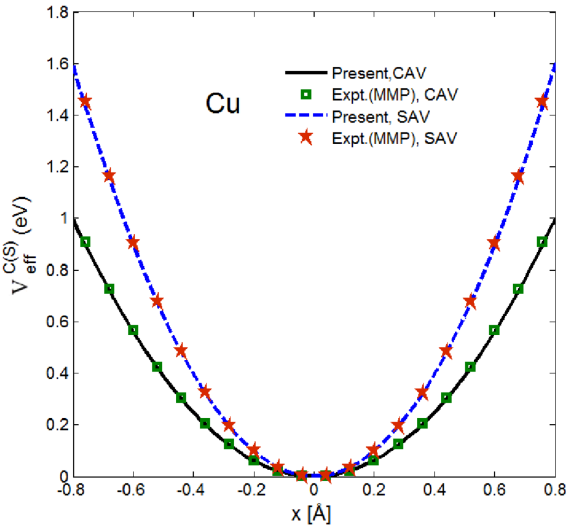

Fig. 1. Effective potentials $V^{C(S)}_{\rm eff}(x)$ of Cu, calculated using the present theory for CAV in CEM and for SAV in UCEM, and compared to the experimental values (Exper.) [27].

TABLE I

The values of $k^C_{\rm eff}$, $k^S_{\rm eff}$, ω^C_E, θ^C_E, ω^S_E, θ^S_E for Cu, calculated using the present theory and compared to the experimental values (Exper.) obtained from the MMPs [26].

Quantities	Present	Exper. [26]
$k^C_{\rm eff}$ [N/m]	49.7867	50.3450
$k^S_{\rm eff}$ [N/m]	79.6587	80.5520
ω^C_E ($\times 10^{13}$) [Hz]	3.0628	3.0799
ω^S_E ($\times 10^{13}$) [Hz]	2.7394	2.7547
θ^C_E [K]	233.9531	235.2611
θ^S_E [K]	209.2540	210.4239

and correlation function DCF $C_R(T)$ obtained from the difference, and also $\sigma^2(T)$ and $u^2(T)$ of Cu calculated using the present theory. They are all linear with T at high temperatures, beginning from the Einstein temperature where the classical limit applies, and they contain zero-point energy contributions at low temperatures, which is a quantum effect. Here, the calculated results of $\sigma^2(T)$, $u^2(T)$, $C_R(T)$ agree well with experimental values (Exper.) obtained from MMPs [26] and with the measured values for $\sigma^2(T)$, labeled as Exper. (1) [28], Exper. (2) [29], Exper. (3) [27], Exper. (4) [7]. Moreover, the values of $\sigma^2(T)$ are greater than those of $u^2(T)$, and that makes the damping factor in the EXAFS and other related spectroscopy for the SAV model greater than for the CAV model.

Note that the difference between the obtained correlated DWF $\sigma^2(T)$ and the uncorrelated one $u^2(T)$ of Cu, shown in Fig. 2, is the source causing the correlation effect described by $C_R(T)$. Hence,

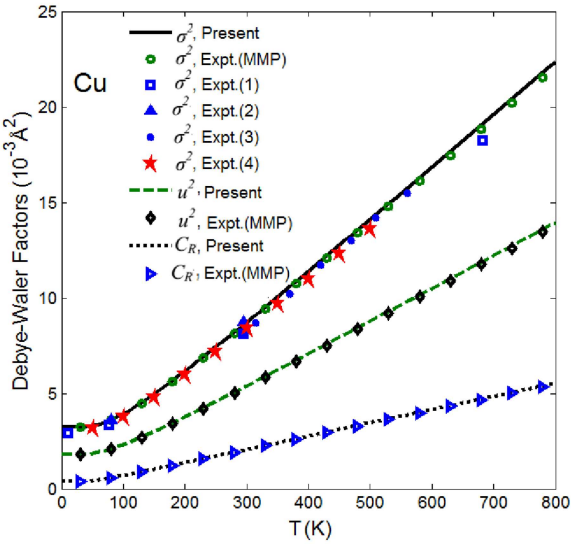

Fig. 2. Temperature dependence of correlated DWF $\sigma^2(T)$, uncorrelated DWF $u^2(T)$,and correlation function $C_R(T)$ of Cu, calculated using the present theory. The results are compared to the experimental values (Exper. (MMP)) obtained from MMPs [26] and the measured values for $\sigma^2(T)$: Exper. (1) [28], Exper. (2) [29], Exper. (3) [27], Exper. (4) [7], at different temperatures.

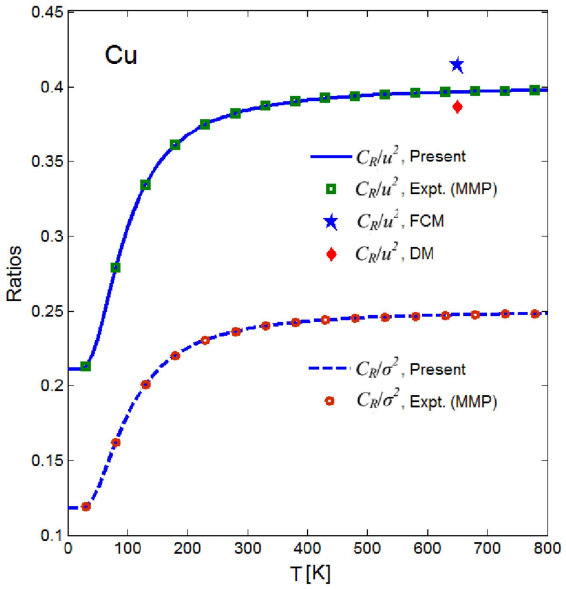

Fig. 3. Temperature dependence of the ratios C_R/u^2 and C_R/σ^2 of Cu, calculated using the present theory. The results are compared to experimental values (Exper. (MMP)) obtained from MMPs [27], as well as to the results calculated using the force constant model (FCM) [25] and Debye model (DM) [26] for the ratio C_R/u^2.

the correlation effect of Cu clearly depends on this difference appearing in different crystals. Figure 2 also shows that the larger difference between $\sigma^2(T)$ and $u^2(T)$ generates stronger correlation effect than the lesser one. Here, the correlation function $C_R(T)$ (Fig. 2) at high temperatures is stronger than at low temperatures. Moreover, the correlation effect has resulted only from the effective local force constants of the harmonic interatomic interaction potential, which clearly proves that it is a harmonic effect.

The ratio C_R/u^2 is often considered in studying EXAFS correlation effects [25, 26]. Figure 3 illustrates temperature dependence of the ratios C_R/u^2 and C_R/σ^2 of Cu, calculated using the present theory. These results show percentages of the correlation effects contributing to the thermodynamic properties of fcc crystals, e.g., to MSD or uncorrelated DWF and to MSRD or correlated DWF, respectively. They are constant at high temperatures, beginning from the Einstein temperature. This indicates that at these high temperatures, the temperature dependence of $\sigma^2(T)$, $u^2(T)$, and $C_R(T)$ of Cu is similar. The result for C_R/u^2, calculated using the present theory, is found to be in reasonable agreement with those calculated using the force constant model (FCM) $C_R/u^2 = 0.415$ [25] and the Debye model (DM) $C_R/u^2 = 0.387$ [26]. Moreover, the ratio C_R/u^2 presented in Fig. 3 is greater than C_R/σ^2. This shows that the correlation effect compared to MSD or uncorrelated DWF is larger than the one compared to MSRD or correlated DWF.

4. Conclusions

In this work, a method has been derived, enabling the calculation and analysis of the temperature-dependent correlated DWF $\sigma^2(T)$, uncorrelated $u^2(T)$, and the correlation function $C_R(T)$ in atomic vibrations of materials based on CEM and UCEM, including many-body effects.

The many-body effects shown in the derived analytical expressions of the correlated DWF $\sigma^2(T)$, uncorrelated DWF $u^2(T)$, and correlation function $C_R(T)$ have been achieved by using CEM and UCEM, i.e., models including the contributions of all nearest neighbors of the absorber and backscatter atoms (for CEM) and a single atom (for UCEM), as well as formulate their effective potentials in the useful form of one-dimensional model.

The present theory has significantly simplified a complicated many-body system task into a one-dimensional model, as well as provided a method for determining the uncorrelated DWF or MSD and correlation function that is simpler than those using X-ray absorption or neutron diffraction and other theories.

The correlation effect has been described based on only the effective local force constants of the harmonic effective potentials obtained by the CAV model used in CEM and the SAV model used in UCEM, which clearly proves that it is a harmonic effect.

The difference between the correlated DWF determined by CEM and the uncorrelated DWF determined by UCEM is considered to be the source causing the correlation effect. It has the same dimension as DWF, and is temperature and crystal types dependent. The larger this difference is, the stronger correlation effect it generates.

The reasons for the difference in the thermodynamic properties of crystals described by the correlated DWF $\sigma^2(T)$ for the CAV model used in CEM and by the uncorrelated DWF u^2(T) for the SAV model used in UCEM are attributed to the difference in their effective local force constants caused by the difference in the number and the mass of vibrating atoms between these models, where for the SAV model they are double compared to those for the CAV model.

The ratios C_R/u^2 and C_R/σ^2 provide percentages of the correlation effects contributing to the thermodynamic properties of crystals described by the functions $u^2(T)$ and $\sigma^2(T)$, respectively. Their constant values at high temperatures indicate the similarity in temperature dependence of the considered values, e.g., the correlated DWF $\sigma^2(T)$, the uncorrelated DWF $u^2(T)$, and the correlation function $C_R(T)$, at these high temperatures.

The present theory avoids the intensive FLD calculations required by a many-body system task, yet it provides a good agreement of the calculated results of $\sigma^2(T)$, $u^2(T)$, and $C_R(T)$ of Cu with the experimental ones obtained from the MMPs, the measured values for $\sigma^2(T)$, as well as values calculated using FCM and DM for C_R/u^2 of Cu. This illustrates the simplicity, advantages, and efficiency of the present theory in EXAFS data analysis, especially in studying the correlated DWF $\sigma^2(T)$, the uncorrelated DWF u^2(T), and the correlation function C_R(T) in EXAFS theory.

This theory can also be applied to the study of the considered quantities of other fcc crystals that were not considered in this work, and it can also be generalized to research these values of other crystal structures based on the calculation of the CAV and SAV local force constants of these materials.

Acknowledgments

The authors thank J.J. Rehr and P. Fornasini for their useful comments and suggestions.

References

[1] E.D. Crozier, J.J. Rehr, R. Ingalls, in: *X-ray Absorption: Principles, Applications, Techniques of EXAFS, SEXAFS and XANES*, Wiley, New York 1988, Ch. 9, p. 373.

[2] E.A. Stern, P. Livins, Zhe Zhang, *Phys. Rev. B* **43**, 8850 (1991).

[3] L. Tröger, T. Yokoyama, D. Arvanitis, T. Lederer, M. Tischer, K. Baberschke, *Phys. Rev. B* **49**, 888 (1994).

[4] N.V. Hung, R. Frahm, *Physica B* **208–209**, 97 (1995).

[5] N.V. Hung, R. Frahm, H. Kamitsubo, *J. Phys. Soc. Jpn.* **65**, 3571 (1996).

[6] N.V. Hung, *J. Phys. IV France* **7**, C2-279 (1997).

[7] J.M. Tranquada, R. Ingalls, *Phys. Rev. B* **28**, 3520 (1983).

[8] A.I. Frenkel, J.J. Rehr, *Phys. Rev. B* **48**, 585 (1993).

[9] T. Yokoyama, *Phys. Rev. B* **57**, 3423 (1998).

[10] T. Miyanaga, T. Fujikawa, *J. Phys. Soc. Jpn.* **63**, 1036 (1994).

[11] T. Miyanaga, T. Fujikawa, *J. Phys. Soc. Jpn.* **63**, 3683 (1994).

[12] A.V. Poiarkova, J.J. Rehr, *Phys. Rev. B* **59**, 948 (1999).

[13] F.D. Vila, J.J. Rehr, H.H. Rossner, H.J. Krappe, *Phys. Rev. B* **76**, 014301 (2007).

[14] S. a Beccara, G. Dalba, P. Fornasini, R. Grisenti, F. Pederiva, A. Samson, *Phys. Rev. B* **68**, 140301(R) (2003).

[15] N.V. Hung, J.J. Rehr, *Phys. Rev. B* **56**, 43 (1997).

[16] N.V. Hung, N.B. Trung, B. Kirchner, *Phys. B* **405**, 2519 (2010).

[17] N.V. Hung, N.B. Duc, R.R. Frahm, *J. Phys. Soc. Jpn.* **72**, 1254 (2003).

[18] M. Daniel, D.M. Pease, N. Van Hung, J.I. Budnick, *Phys. Rev. B* **69**, 134414 (2004).

[19] N.V. Hung, *J. Phys. Soc. Jpn.* **83**, 024802 (2014).

[20] N.V. Hung, N.B. Duc, D.Q. Vuong, T.S. Tien, N.C. Toan, *Radiat. Phys. Chem.* **80**, 109263 (2020).

[21] N.V. Hung, C.S. Thang, N.C. Toan, H.K. Hieu, *Vacuum* **101**, 63 (2014).

[22] P. Wu, K. Xia, K. Peng et al., *Phys. Rev. B* **103**, 195204 (2021).

[23] N.C. Toan, D.Q. Vuong, N.V. Hung, *Acta Phys. Pol. A* **140**, 27 (2021).

[24] N.C. Toan, N.V. Hung, *Acta Phys. Pol. A* **144**, 38 (2023).

[25] R.M. Niclow, G. Gilat, H.G. Smith, R.J. Raubenheimer, M.K. Wikinson, *Phys. Rev.* **164**, 922 (1967).

[26] G. Beni, P.M. Platzman, *Phys. Rev. B* **14**, 1514 (1976).

[27] I.V. Pirog, T.I. Nedoseikina, A.I. Zarubin, A.T. Shuvaev, *J. Phys. Condens. Matter* **14**, 1825 (2002).

[28] R.B. Greegor, F.W. Lytle, *Phys. Rev. B* **20**, 4908 (1979).

[29] T. Yokoyama, T. Sasukawa, T. Ohta, *Jpn. J. Appl. Phys.* **28**, 1905 (1989).

[30] B.T.M. Willis, A.W. Pryor *Thermal Vibrations in Crystallography*, Cambridge University Press, Cambridge, 1975.

[31] L.A. Girifalco, W.G. Weizer, *Phys. Rev.* **114**, 687 (1959).

New Insights on Critical Transitions of Single-Neuron Dynamics

H. He[a,b], K. Zhang[a], H. Yan[c] and J. Wang[a,b,d,*]

[a] *State Key Laboratory of Electroanalytical Chemistry, Changchun Institute of Applied Chemistry, Chinese Academy of Sciences, Changchun, Jilin 130022, China*
[b] *School of Applied Chemistry and Engineering, University of Science and Technology of China, Hefei, Anhui 230026, China*
[c] *Center for Theoretical Interdisciplinary Sciences, Wenzhou Institute, University of Chinese Academy of Sciences, Wenzhou, Zhejiang 325001, China*
[d] *Department of Chemistry and of Physics and Astronomy, State University of New York at Stony Brook, Stony Brook, New York 11794-3400, United States*

Received: 11.02.2024 & Accepted: 15.05.2024

Doi: 10.12693/APhysPolA.146.102 *e-mail: john.hammersley@gmail.com

Many theoretical models depicting excitable cells stem from the Hodgkin–Huxley model. Over the past few decades, quantitative studies on its electrophysiology and nonlinear dynamics have yielded considerable progress. In this study, we employ a landscape and flux theory to statistically explore the global dynamic characteristics of the classical Hodgkin–Huxley neuron. We quantify the underlying landscape and flux to address global stability. Our results provide an intuitive understanding of a global picture of the dynamic system. By quantifying the average curl flux, we reveal that it serves as the dynamical origin for the emergence of a new state and a dynamical indicator for bifurcation. In addition, we quantitatively calculate the entropy production, identifying it as an essential thermodynamic indicator for bifurcation. The time asymmetry of the cross-correlations can be directly computed from existing experimental time series, offering a practical indicator for bifurcation analysis. This paper presents our findings and their implications for a better understanding of the behavior of excitable cells.

topics: non-equilibrium Hodgkin–Huxley (HH) neuron dynamics, landscape, curl flux, critical transition

1. Introduction

The pioneering work of Hodgkin and Huxley laid the foundation for unraveling the mysteries of neuron excitability, providing a fundamental theoretical framework for investigating the electrical properties of neurons [1–6]. Since then, research in this field has expanded to explore the intricacies of neuron behavior and the mechanisms underlying neuronal activity. One aspect of this research was the investigation of local bistability, which has been extensively studied through the combined use of numerical calculations and bifurcation theory. Specifically, the condition that the direct current (DC) I is the only bifurcation parameter has been explored in detail [7, 8]. In addition, the introduction of the effective calcium concentration to modify the deterministic equations allowed the exploration of bifurcation diagrams in the $[k^+]$–V plane ($[k^+]$ representing both extracellular and intracellular potassium concentration [9]). Recent research has focused on the study of a two-bifurcation-parameter system [10], as well as the exploration of multiparameter bifurcation [11]. Of particular interest is the coexistence of stable quiescence and stable limit cycles localized in specific ranges of bifurcation parameters, which has led to the use of statistical methods to describe the nonlinear dynamics of Hodgkin–Huxley neurons [12, 13]. Overall, the work of Hodgkin and Huxley has paved the way for continued investigation into the complex dynamics of neurons and their underlying mechanisms [14]. Besides, the Hodgkin–Huxley (HH) model describes neurons that exhibit local bistability and undergo a subcritical Hopf bifurcation, which provides the possibility of state transitions and forms the basis for the dynamical mechanism of

bursting oscillations in neurons. One way to achieve this is by adding stochastic noise [15–18]. Biological neurons are constantly exposed to various types of noise in their environment, and considering the stochastic oscillations is necessary when studying their dynamical mechanisms. Although stochastic dynamics in the HH-model neurons have been partially studied, quantifying and understanding the physical mechanism of their global behavior to reveal the underlying phase transition mechanisms remains challenging.

In this work, we investigate the local bistable properties of the original four-dimensional Hodgkin–Huxley equations under the influence of noise. Additionally, we apply the recently developed theory of landscape and flux to reveal its stochastic dynamical mechanisms [19–21]. Given that the Hodgkin–Huxley neuron model is subject to noise, the prediction of neuron trajectories becomes partially infeasible. In such scenarios, it becomes more meaningful to quantitatively assess the statistical distribution of individual neuron states at different times and to characterize the overall distribution within the whole state space. The landscape–flux framework has been employed in non-equilibrium systems, offering valuable insights into associated behaviors [22–29]. This framework has proven to be a useful tool for gaining a deeper understanding of the dynamics and behavior of such systems. However, only a limited number of studies have used this theory to investigate the nonlinear dynamical mechanisms of individual HH neurons. Therefore, we explore state transitions using the topographical structure of the potential landscape and quantify the probabilistic flux and entropy production in the state space. By examining their relationship with the bifurcation parameters of the system, we analyze their roles and contributions in state transitions and the emergence of new states. We found that average flux and entropy production rate can serve as indicators of bifurcation. We also calculate differences in cross-correlation functions forward-in-time and backward-in-time and discuss the observed behaviors and the degree of time-reversal symmetry breaking. This provides a practical indicator for bifurcation that can be directly extracted from experimental time series. Moreover, we analyze the behavior of the critical slowing down in bifurcation by investigating the characteristic decay time of autocorrelation functions and its correlation near the bifurcation. By conducting these explorations, we enhance our comprehension of the nonlinear dynamical mechanisms exhibited by HH neuron models in the presence of noise, facilitating quantitative analysis. This research has substantial implications for illuminating the behavior of individual neurons and the overall functionality of the nervous system. Drawing upon the intricate landscape structure of its diverse states, we present a fresh perspective on this fundamental aspect of neuronal excitability.

2. Methods

2.1. Stochastic Hodgkin–Huxley equations

The Hodgkin–Huxley (HH) model has made substantial contributions to the understanding of neuronal electrophysiology, providing a foundational framework for studying the electrical properties of neurons. This model is characterized by a system of four nonlinear ordinary differential equations (ODEs). In the real world, neurons are constantly influenced by noise, including external noise (such as interference signals from the stimulus current) and internal noise (such as stochasticity in ion channels). These noises affect the activity of neurons, introducing randomness and uncertainty into the neuronal system. When investigating neuronal behavior and information processing, it is crucial to take these noise factors into account. Many previous studies introduced current noise and subunit noise to an HH neuron [30–32]. Due to ease of implementation and computational efficiency, current noise and subunit noise have become widely adopted as approximations for modeling stochastic HH dynamics. In our study, we incorporated these two types of noise into the statistical HH model, which is mathematically represented by a system of four stochastic nonlinear equations

$$\begin{aligned}
C_m\frac{\mathrm{d}V}{\mathrm{d}t} &= -\overline{g_{\mathrm{K}}}\,n^4(V-V_{\mathrm{K}}) - \overline{g_{\mathrm{Na}}}\,m^3h\,(V-V_{\mathrm{Na}})\\
&\quad -g_L(V-V_L) + I + \Gamma_1(\boldsymbol{x},t),\\
\frac{\mathrm{d}m}{\mathrm{d}t} &= \alpha_m(V)(1-m) - \beta_m(V)m + \Gamma_2(\boldsymbol{x},t),\\
\frac{\mathrm{d}h}{\mathrm{d}t} &= \alpha_h(V)(1-h) - \beta_h(V)h + \Gamma_3(\boldsymbol{x},t),\\
\frac{\mathrm{d}n}{\mathrm{d}t} &= \alpha_n(V)(1-n) - \beta_n(V)n + \Gamma_4(\boldsymbol{x},t).
\end{aligned} \tag{1}$$

Here, $\Gamma_1(\boldsymbol{x},t) = A_V\Gamma(\boldsymbol{x},t)$, $\Gamma_2(\boldsymbol{x},t) = A_m\Gamma(\boldsymbol{x},t)$, $\Gamma_3(\boldsymbol{x},t) = A_h\Gamma(\boldsymbol{x},t)$, $\Gamma_4(\boldsymbol{x},t) = A_n\Gamma(\boldsymbol{x},t)$, $\boldsymbol{A}_{\boldsymbol{\Gamma}(\boldsymbol{x},t)} = [A_V, A_m, A_h, A_n]$ is the scaling factors matrix of Gaussian white noise, while Γ represents Gaussian white noise, which is a type of stochastic force. In this article, we transformed the third equation of (1) by multiplying both sides of it by 100, obtaining the final form $\frac{\mathrm{d}h1}{\mathrm{d}t} = \alpha_h(V)(100-h1) - \beta_h(V)h1 + \Gamma_3(\boldsymbol{x},t)$ (where $h1 = 100h$). In (1), V is the membrane potential, and I is defined as $I = I_{\mathrm{stim}}/A$, denoting the stimulus current applied per unit area of the cell membrane. The scaling factor for potassium ion conductance, measured in $\mathrm{mS/cm^2}$, is $\overline{g_{\mathrm{K}}}$. The variable n is designated as the activation variable for potassium ($\mathrm{K^+}$) channels, ranging from 0 to 1. This reflects the probability of each subunit in the channel being open. The model assumes that a potassium channel consists of four cooperative subunits, fully open only when all are activated. This assumption is an effective

simplification that proves to be very effective in many scenarios. The equilibrium potential of potassium ions is represented by V_{K}. Then, the term $\overline{g_{\mathrm{K}}}\, n^4(V-V_{\mathrm{K}})$ naturally depicts the current across the cell membrane caused by potassium ions. Accordingly, $\overline{g_{\mathrm{Na}}}$ is the scaling factor for sodium ion conductance. The gating variables m and h are dimensionless and represent the activation variable and the inactivation variable for sodium channels, respectively. They also range from 0 to 1 and jointly represent the opening and inactivation of sodium channels, a concept validated by further research. The equilibrium potential of sodium ions is represented by V_{Na}, and $\overline{g_{\mathrm{Na}}}\, m^3h(V-V_{\mathrm{Na}})$ is the component of the current across the cell membrane caused by sodium ions. Moreover, the term $g_L(V-V_L)$ denotes additional factors influencing the generation of positive or negative currents across the cell membrane, where g_L is the leak conductance — a constant signifying the total conductance of other ions across the membrane, and V_L is the equilibrium potential for the leak current, generally approximating the resting membrane potential. The capacitance of the neuronal membrane is represented by C_m.

In the above system of nonlinear ODEs, the quantitative description of α_x and β_x, where x can represent m, h, or n, takes the form

$$\begin{aligned}
\alpha_m &= \frac{\overline{\alpha_m}\,(V-vm)}{1-\mathrm{e}^{-(V-vm)/K_{\alpha m}}},\\
\beta_m &= \overline{\beta_m}\,\mathrm{e}^{-V/K_{\beta m}},\\
\alpha_h &= \overline{\alpha_h}\,\mathrm{e}^{-V/K_{\alpha h}},\\
\beta_h &= \frac{\overline{\beta_h}}{1+\mathrm{e}^{-(V-vh)/K_{\beta h}}},\\
\alpha_n &= \frac{\overline{\alpha_n}\,(V-vn)}{1-\mathrm{e}^{-(V-vn)/K_{\alpha n}}}, \beta_n = \overline{\beta_n}\,\mathrm{e}^{-V/K_{\beta n}}.
\end{aligned} \tag{2}$$

In (1)–(2), α_m and β_m represent the rates at which activation of molecules opens or closes sodium ion channels, respectively. The scaling factors for these rates are denoted as $\overline{\alpha_m}$ and $\overline{\beta_m}$. The equilibrium potentials for activation and inactivation processes in sodium channels are represented by vm and vh, respectively. Similarly, α_h and β_h denote the rates at which inactivating molecules switch between open and closed states in sodium channels, with associated constants $\overline{\alpha_h}$ and $\overline{\beta_h}$. For potassium ion channels, α_n and β_n describe the rates of subunit gate transitions, with vn indicating their equilibrium potential. The constants related to these rates and transitions in both sodium and potassium channels are $K_{\alpha m}$, $K_{\beta m}$, $K_{\alpha h}$, $K_{\beta h}$, $K_{\alpha n}$, and $K_{\beta n}$. These parameters collectively define the gating kinetics of the ion channels in the model.

Focusing on the sodium and potassium ion channel dynamics in neurons, the HH model accurately simulates Na^+ and K^+ ion flows during action potentials and response to stimulus variations, elucidating action potential frequency modulation. The HH model quantitatively explains action potential generation and phenomena such as refractory periods and anode break effects. Although the HH model provides an idealized representation of neuronal electrophysiological activity, and HH-like models based on ion channels can capture various aspects of neuronal characteristics, it is evident that each neural system operates as a non-equilibrium system that is constantly influenced by input and stochastic disturbances. These random noise sources, originating from the environment and inherent system dynamics, play a crucial role in neurophysiology [33, 34]. Therefore, analyzing stochastic dynamic phenomena in neuronal models holds the utmost significance. In our investigation, we augment the original system of nonlinear ODEs by adding Gaussian white noise terms, resulting in a series of Langevin equations (LEs) [15].

2.2. Landscape and flux theory

When a biological system is functioning, it is inevitably subjected to intrinsic noise, which is inherent to any system operating above absolute zero temperature. There are also external fluctuations arising from the environment. To simplify our analysis, we use Gaussian white noise as a means of simulating environmental effects. Consequently, the inclusion of noise modifies the dynamics described by $\frac{\mathrm{d}\boldsymbol{x}}{\mathrm{d}t} = \boldsymbol{F}(\boldsymbol{x}) + \Gamma(\boldsymbol{x},t)$, where $\Gamma(\boldsymbol{x},t)$ is Gaussian white noise. Here, $\boldsymbol{F}(\boldsymbol{x})$ represents the driving force of the system, which corresponds to the deterministic HH equations described in (9) in the Appendix. The vector variable $\boldsymbol{x}$ represents the state of the studied neuron in the phase space, specifically characterized by (V, m, h, n). The amplitude of the noise can be determined by $\langle\Gamma(\boldsymbol{x},t)\Gamma(\boldsymbol{x},t')\rangle = 2D(\boldsymbol{x})\,\delta(t-t') = 2\mathcal{D}\,G(\boldsymbol{x})\,\delta(t-t')$, where $\mathcal{D}$ is the intensity of the noise and $G(\boldsymbol{x})$ is a diffusion matrix. Deterministic dynamical equations change into a series of nonlinear Langevin equations. Correspondingly, the main characteristics we explore will be investigated using non-equilibrium statistical concepts and methods, rather than chasing stochastic trajectories that stem from diverse initial conditions. The Langevin equation (LE) investigates the statistical characteristics of the system's trajectories. We can equivalently transform it to the probability distribution of the entire state space at a given time. It allows us to study the Fokker–Planck diffusion equations that can be deduced from LEs to explore such open systems [22, 35, 36], namely

$$\begin{aligned}
\frac{\partial P(\boldsymbol{x},t)}{\partial t} &= -\sum\nolimits_i \frac{\partial[F_i(\boldsymbol{x})P(\boldsymbol{x},t)]}{\partial x_i}\\
&\quad + \sum\nolimits_i \sum\nolimits_j \frac{\partial^2[D_{ij}(\boldsymbol{x})P(\boldsymbol{x},t)]}{\partial x_i \partial x_j}.
\end{aligned} \tag{3}$$

Here, $D_{ij}(\boldsymbol{x}) = \mathcal{D}\,G_{ij}(\boldsymbol{x})$. The detailed derivation is provided in the Appendix. It is noteworthy that, due to the application of additive and

isotropic Gaussian white noise, for the sake of theoretical convenience, we consider the diffusion matrix $G(\boldsymbol{x})$ to be an identity matrix. By imposing appropriate natural boundary conditions and ensuring sufficient decay in the outer region, we can explore the asymptotic behavior of the Fokker–Planck equation and derive the corresponding steady-state probability distribution. We use P_{ss} to represent the aforementioned steady-state probability distribution (small "ss" denotes statistical steady states). Now, we define a probabilistic flux $\boldsymbol{J}$ that satisfies $\boldsymbol{J} = \boldsymbol{F}P - \nabla \cdot (\mathcal{D}GP)$. Combining this with (3), we obtain the probability conservation form of the Fokker–Planck equation $\frac{\partial P(\boldsymbol{x},t)}{\partial t} + \nabla \cdot \boldsymbol{J}(\boldsymbol{x},t) = 0$. When the system reaches a steady state after a sufficiently long time under appropriate boundary conditions, the probability density no longer changes with time. Then, we can easily infer that the divergence of the probabilistic flux vanishes, i.e., $\nabla \cdot \boldsymbol{J}_{ss} = 0$. Since we apply additive Gaussian white noise to the system to explore its global stability, the diffusion matrix D is a constant matrix, indicating that the divergence of D is zero ($\nabla \cdot D(\boldsymbol{x}) = 0$). We can then deduce the driving force of the system accordingly as

$$\boldsymbol{F} = \frac{\boldsymbol{J_{ss}} + \mathcal{D}(\nabla P_{ss})}{P_{ss}} = \frac{\boldsymbol{J}_{ss}}{P_{ss}} - \mathcal{D}\,\nabla U, \tag{4}$$

where ∇U represents the gradient of the potential function U associated with the system. By analogy to the Boltzmann law in equilibrium systems, we define the population probability potential U as

$$U = -\ln\left(P_{ss}\right). \tag{5}$$

The newly defined non-equilibrium potential U reflecting the weight of the states offers a clear physical interpretation and enables the evaluation of global stability and behavioral characteristics. The landscape, which corresponds to the three-dimensional (3D) topographical structure of U, plays a crucial role in landscape and flux theory. The presence of basins and barriers within this landscape allows for a comprehensive depiction of global stability and the probability distribution of all states. Based on the deductions mentioned earlier, we successfully decompose the system's driving force into two components. According to (4), the first component is associated with the steady-state probabilistic flux $\boldsymbol{J}_{ss}$ and the density of the probability distribution P_{ss}, while the second component is related to the gradient of the potential landscape U. In a steady state, the probabilistic flux has zero divergences, indicating two representing scenarios: (i) when the net input or output is zero, the system maintains detailed balance, and (ii) when the flux is non-zero, but with zero divergences, the system experiences a non-equilibrium state with broken detailed balance. Non-zero, divergence-free flux is a hallmark of non-equilibrium systems [20]. It can be viewed as a rotational and curl flux. The dynamics of non-equilibrium systems are co-determined by both the non-equilibrium potential and the curl flux, resembling the motion of electrons in an electric field (characterized by the potential gradient) and a magnetic field (reflected by the curl flux).

2.3. Non-equilibrium thermodynamics, average probability flux, and dissipative-dependent EPR

For non-equilibrium systems, an intriguing question is the specific degree of departure from equilibrium. This can be characterized using several specific quantities. As discussed earlier, non-zero yet divergence-free rotational flux serves as a distinctive signature of non-equilibrium systems, and substantial evidence suggests its intimate correlation with the existence of non-equilibrium energy pumps. This flux plays a pivotal role in maintaining the stability of the limit cycle oscillations within non-equilibrium systems [19–26, 37]. Inspired by this, we can define an average probabilistic flux $J_{av} = \frac{\int \mathrm{d}\boldsymbol{x}\,|\boldsymbol{J}_{ss}|}{\int \mathrm{d}\boldsymbol{x}}$ to quantify the global non-equilibrium extent of a system. Moreover, in non-equilibrium systems, energy consumption and dissipation are inevitable. The energy dissipation, which is associated with the entropy production rate in the steady state of the non-equilibrium system, serves as a global physical characteristic for measuring the system's departure from equilibrium. For non-equilibrium systems, the change in entropy over time can be divided into two parts, i.e.,

$$\frac{\mathrm{d}S}{\mathrm{d}t} = -\frac{\mathrm{d}}{\mathrm{d}t}\int \mathrm{d}\boldsymbol{x}\; P(\boldsymbol{x},t)\ln\big(P(\boldsymbol{x},t)\big) = \int \frac{\mathrm{d}\boldsymbol{x}\;(\boldsymbol{J}\cdot(\mathcal{D}G)^{-1}\cdot\boldsymbol{J})}{P} - \int \mathrm{d}\boldsymbol{x}\,(\boldsymbol{J}\cdot(\mathcal{D}G)^{-1}\cdot\boldsymbol{F}_{eff}) = S'_t - S'_e, \tag{6}$$

where the entropy production rate (EPR) $S'_t = \int \mathrm{d}\boldsymbol{x}\;\frac{(\boldsymbol{J}\cdot(\mathcal{D}G)^{-1}\cdot\boldsymbol{J})}{P}$ is non-negative. It represents the total entropy change in the system and its surroundings and always obeys the second law of thermodynamics. On the other hand, the heat dissipation rate or the entropy flow rate $S'_e = \int \mathrm{d}\boldsymbol{x}\;(\boldsymbol{J}\cdot(\mathcal{D}G)^{-1}\cdot(\boldsymbol{F} - \mathcal{D}\nabla\cdot G))$ can be positive or negative, taking into account the energy and information flow between the system and its environment, leading to an increase or decrease in the system's entropy, respectively. Hence, the entropy of a non-equilibrium system does not necessarily always increase or maximize, while the total entropy production is always positive. We define the effective force $\boldsymbol{F}_{eff}$ as $\boldsymbol{F}_{eff} = \boldsymbol{F} - \mathcal{D}\nabla\cdot G$ [20–22, 25, 38].

2.4. Time irreversibility of the cross-correlation function and critical slowing down

The average difference between the forward-in-time and backward-in-time cross-correlation of two random sequences enables us to evaluate the extent

of detailed balance breaking and quantify the time irreversibility of a non-equilibrium system [26, 37]. It can be calculated as

$$\Delta CC = \sqrt{\frac{1}{t_f}\int_0^{t_f} \mathrm{d}\tau \left(C_{XY}(\tau) - C_{YX}(\tau)\right)^2}, \quad (7)$$

where $C_{XY}(\tau)$ and $C_{YX}(\tau)$ present the forward-in-time cross-correlation function and backward-in-time cross-correlation function, respectively. Here, $C_{XY}(\tau) = \langle X(0)Y(\tau)\rangle = \sum X^i Y^j P_i^{ss} P_{ij}(\tau)$ (i, j are used to denote different states); P_i^{ss} is the value of steady-state probability at state i; $P_{ij}(\tau)$ represents the probability of the system transitioning from state i to state j within a time interval τ. Additionally, $C_{XY}(\tau) - C_{YX}(\tau) = X^A Y^B (P_A^{ss} P_{AB}(\tau) - P_B^{ss} P_{BA}(\tau)) = X^A Y^B J_{AB}^{ss} \tau$, (when τ is small) [24, 26, 35]. Evidently, the disparity between the forward-in-time and backward-in-time cross-correlation functions is intricately linked to the level of the steady-state probabilistic flux or the degree of detailed balance breaking.

Neurons can demonstrate abrupt transitions or systemic shifts, such as the shift from a resting state to the firing of an action potential. This occurrence is commonly referred to as a critical transition. As the system approaches a critical transition point, the internal dynamics would undergo a state transition. During this phase, alterations in the autocorrelation function often reveal notable features, such as increased and prolonged temporal correlations. This insight encourages the use of the autocorrelation function analysis, offering clues into the internal dynamics as the system approaches a critical state. This approach serves as a quantitative measure of the critical slowing down behavior.

3. Results and discussion

3.1. Linear stability analysis of the Hodgkin–Huxley model

To investigate the different states of a single neuron, we start with linear stability analysis and use MATLAB to find numerical solutions. This analysis helps us predict the long-term behavior and stability of the system under different parameter conditions. Explanations and default values of constants in the HH equations, unless otherwise specified, are provided in Table I [5, 39].

Linear stability analysis is a method used to study the stability of deterministic dynamic systems described by differential or difference equations. Numerous researchers have extensively explored the linear stability analysis of the HH model [7, 40]. Here, we summarize the key findings of the linear stability analysis of the HH model.

The basic steps involve finding equilibrium points, linearizing dynamic equations, calculating the Jacobian matrix, and determining eigenvalues to assess stability. The Jacobi matrix is a matrix of partial derivatives that describes the linearized dynamics of the model around an equilibrium point. During linear stability analysis, the stability of the equilibrium points is determined by examining the real and imaginary eigenvalue parts of that the Jacobi matrix. If all eigenvalues have negative real parts, the equilibrium point is stable. If one or more eigenvalues have positive real parts, the equilibrium point is unstable. If there are eigenvalues with zero real parts and non-zero imaginary parts, further analysis may be required. Such equilibrium points are considered non-hyperbolic, and the geometric structure near these points may change. This behavior is known as a bifurcation at non-hyperbolic point. The Jacobian matrix of the HH model (see (10) and (11) in Appendix) can be represented as

$$\mathcal{J}_{\mathrm{Jacobi}} = \begin{bmatrix} \frac{\partial f_1}{\partial V} & \frac{\partial f_1}{\partial m} & \frac{\partial f_1}{\partial h} & \frac{\partial f_1}{\partial n} \\ \lambda_m m'_\infty & -\lambda_m & 0 & 0 \\ \lambda_h h'_\infty & 0 & -\lambda_h & 0 \\ \lambda_n n'_\infty & 0 & 0 & -\lambda_n \end{bmatrix}, \quad (8)$$

where $\lambda_x = \alpha_x(V) + \beta_x(V)$ and $x_\infty = \frac{\alpha_x(V)}{\alpha_x(V)+\beta_x(V)}$. Here, x can be replaced with m, h, n. The detailed derivation can be found in the Appendix. In Table II, we present the eigenvalues denoted as λ_i for $i = 1, 2, 3, 4$. To investigate the stability of the system, we apply the linear stability analysis method. This analysis identifies critical points where the stability of the system exhibits a qualitative change, known as a bifurcation. We can determine the system's stability under different conditions by examining the signs of the corresponding eigenvalues λ. It is observed that when $I < 9.7796$ μA/cm^2 and $I > 154.5266$ μA/cm^2, the states of the system are stable. In other words, the system will remain in its steady state under these specific current conditions.

To gain a comprehensive understanding of the dynamic behavior and stability of the HH model, and to visually illustrate the formation and evolution of attractors, we employed the MatCont software to generate a bifurcation diagram with the parameter I as the bifurcation parameter.

Figure 1a presents a bifurcation diagram with I as the bifurcation parameter, ranging from $I = -18$ μA/cm^2 to $I = 200$ μA/cm^2. Solid gray lines represent stable steady states, corresponding to stable resting states of neurons in physiology, denoted as SRS, while dashed gray lines represent unstable steady states, denoted as URS. As I increases, a subcritical Hopf bifurcation, denoted as H1, occurs. Stable limit cycle oscillations are shown by the maximum (solid orange line) and minimum (solid yellow line) V values, labeled as SLC. Unstable limit cycle oscillations are also shown by the maximum (scattered orange dots) and minimum (scattered yellow dots) V values, labeled as ULC. The second Hopf bifurcation point is marked as H2. This visualization effectively elucidates the system's dynamic

TABLE I

Explanations and default values of parameters.

Parameters	Explanation	Default values
C_m	neuronal membrane capacitance	1.0 μF/cm^2
g_{Na}	sodium conductance	120 mS/cm^2
g_K	potassium conductance	36 mS/cm^2
g_L	leak conductance	0.3 mS/cm^2
V_{Na}	equilibrium potential of sodium ions	115 mV
V_K	equilibrium potential of potassium ions	-12 mV
V_L	reversal potential for the leak current	10.599 mV
$\overline{\alpha_m}$	constant related to the transfer rate of activating molecules (closed $\rightarrow$ open), denoted as α_m	0.1 ms^{-1}
$\overline{\beta_m}$	constant related to the transfer rate of activating molecules (open $\rightarrow$ closed), denoted as β_m	4.0 ms^{-1}
vm	equilibrium potential of activating molecules	25.0 mV
$K_{\alpha m}$	dimensionless constant related to α_m	10.0
$K_{\beta m}$	dimensionless constant related to β_m	8.0
$\overline{\alpha_h}$	constant related to the transfer rate of inactivating molecules (open $\rightarrow$ closed), denoted as α_h	0.07 ms^{-1}
$\overline{\beta_h}$	constant related to the transfer rate of inactivating molecules (closed $\rightarrow$ open), denoted as β_h	1.0ms^{-1}
vh	equilibrium potential of inactivating molecules	30.0 mV
$K_{\alpha h}$	dimensionless constant related to α_h	20.0
$K_{\beta h}$	dimensionless constant related to β_h	10.0
$\overline{\alpha_n}$	constant related to the transfer rate of each subunit gate (closed $\rightarrow$ open), denoted as α_n	0.01 ms^{-1}
$\overline{\beta_n}$	constant related to the transfer rate of each subunit gate (open $\rightarrow$ closed), denoted as β_n	0.125 ms^{-1}
vn	equilibrium potential of each subunit gate	10.0 mV
$K_{\alpha n}$	dimensionless constant related to α_n	10.0
$K_{\beta n}$	dimensionless constant related to β_n	80.0

TABLE II

Numerical results for stability analysis.

I	V_0	m_0	h_0	n_0	λ_1	λ_2	λ_3	λ_4
0.0000	0.0000	0.0529	0.5961	0.3177	-4.6753	$-0.20+0.38$i	$-0.20-0.38$i	-0.1207
5.0000	3.2667	0.0772	0.4794	0.3687	-4.5975	$-0.10+0.52$i	$-0.10-0.52$i	-0.1292
9.7796	5.3459	0.0973	0.4062	0.4018	-4.7643	0.5862i	-0.5862i	-0.1385
120.0000	19.8776	0.3661	0.0886	0.6175	-8.7149	$0.15+0.97$i	$0.15-0.97$i	-0.2810
154.0000	21.9132	0.4189	0.0706	0.6429	-9.4024	$0.0024+1.0618$i	$0.0024-1.0618$i	-0.3104
154.5266	21.9419	0.4197	0.0704	0.6432	-9.4121	1.0629i	-1.0629i	-0.3109
155.0000	21.9677	0.4204	0.0702	0.6436	-9.4208	$0.0021+1.0640$i	$0.0021-1.0640$i	-0.3113
180.0000	23.2537	0.4544	0.0609	0.6588	-9.8554	$-0.11+1.11$i	$-0.11-1.11$i	-0.3310

behavior as the parameter I varies, including the presence of stable and unstable periodic solutions and their relationship to stable and unstable steady states.

At the top corner of panel (a), the nested inset plot depicts the phase states of the system for different bifurcation parameter ranges. The dark blue vertical line marks the boundary between stable steady states and stable limit cycles, labeled I_0. The purple vertical line represents the I value of H1, denoted as I1, while the red vertical line, marked as I2, indicates the boundary between stable limit cycles and stable resting states at H2. Through calculation, we obtain $I_0 = 6.2645$ μA/cm^2, $I_1 = 9.7796$ μA/cm^2, and $I_2 = 154.5266$ μA/cm^2. These three vertical dividing lines delineate distinct states within the system. In Fig. 1a, B represents the bistable region of the classical HH model,

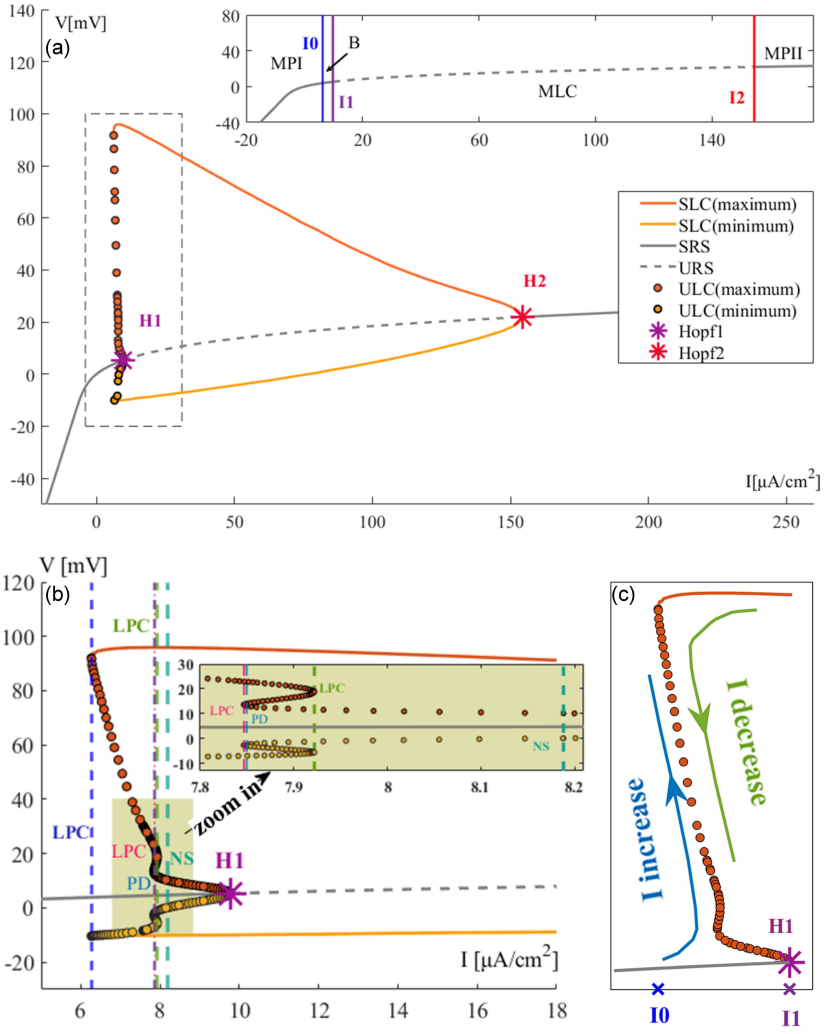

Fig. 1. Deterministic bifurcation diagram. (a) Overall bifurcation diagram with I as the bifurcation parameter. The solid orange line shows the maximum V value within the stable limit cycle (SLC), while the solid yellow line shows the minimum V value within SLC. The solid gray line represents a stable resting state, denoted as SRS. The dashed gray line represents an unstable resting state, denoted as URS. The scattered orange dots denote the maximum value of V within the unstable limit cycle (ULC), while the scattered yellow points represent the minimum value of V within ULC. Here, H1 is the first Hopf bifurcation point and H2 is the second Hopf bifurcation point. The axes embedded above are a simplified diagram of the overall bifurcation plot. The dark blue vertical line is marked as I_0, the purple vertical line is marked as I_1, and the red vertical line is marked as I_2. MPI signifies the region $I < I_0$, where neurons are in a stable resting state, while MPII represents the stable resting state when $I > I_2$. The region between I_0 and I_1 is denoted as B, indicating the bistable region where neurons oscillate between SRS and SLC. MLC denotes the parameters region that the system undergoes a mono-stable limit cycle, which is between I_1 and I_2. (b) Local dynamical bifurcation detail illustration of the bistable region in the HH model. The dark blue vertical dashed line indicates the limit point bifurcation of cycles (LPC) at the boundary, where one stable limit cycle and one unstable limit cycle merge into a single limit cycle. The coordinate area inserted in the upper right corner is an enlarged illustration of the yellow rectangular area to the right of the dark blue LPC. It includes a pink vertical dashed line indicating LPC at the boundary, where two unstable limit cycles merge into one unstable limit cycle, while the blue vertical dashed line represents the period-doubling bifurcation, labeled PD. The green vertical dashed line marks another occurrence of LPC. The fluorescent green vertical dashed line represents the Neimark–Sacker (NS) bifurcation. (c) Dynamical evolution diagram of the HH neuron near H1 without noise. The blue solid line with arrows indicates the evolution direction of the dynamic state near H1 as I gradually increases, while the green solid line with arrows represents the dynamic evolution path as I gradually decreases. The solid gray line represents a stable resting state. The scattered orange dots show the maximum value of V during oscillations of ULC, providing a simplified representation of different ULC. The solid orange line represents the maximum value of V during stable limit cycle oscillations, providing a simplified representation of different SLC. The relative positions of I_0 and I_1 are marked with dark blue and purple crosses, respectively.

and MLC signifies a singular stable limit cycle region. Additionally, we denote the region $I < I_0$ as MPI and the region $I > I_2$ as MPII, corresponding to regions of stable resting states.

Figure 1b provides an enlarged view of the dashed rectangular region in panel (a), including a further magnified illustration that illustrates multiple bifurcations from stable resting states to stable limit cycles. Discrete orange and yellow dots represent, respectively, the maxima and minima of the unstable limit cycles, while vertical dashed lines mark the locations of bifurcations. The limit point bifurcation is a critical phenomenon in nonlinear dynamical systems. It involves the transition of equilibrium or periodic solutions (limit cycles) from stable to unstable states, or vice versa. This process can give rise to new stable solutions or the disappearance of existing ones. The term "limit point bifurcation of cycles" (LPC) specifically denotes this behavior in the context of periodic solutions (limit cycles). The emergence of LPC indicates a change in the characteristics or numbers of limit cycles. In panel (b), LPC at $I = I_0 = 6.2645\ \mu\text{A/cm}^2$ (dark blue vertical dashed line) indicates the merging of the stable limit cycle and the unstable limit cycle into a single limit cycle. LPC at $I = 7.9220\ \mu\text{A/cm}^2$ (green vertical dashed line) represents the merging of a unstable limit cycle with a relatively large amplitude with another an unstable limit cycle with relatively small amplitude into an unstable limit cycle with an amplitude between the two. LPC at $I = 7.8465\ \mu\text{A/cm}^2$ (pink vertical dashed line) is similar to LPC at green vertical dashed line, indicating the merging of two unstable limit cycles into one unstable limit cycle. For simplification, we will refer to LPCs occurring at different currents by their colors. For example, LPC corresponding to a dark blue vertical dashed line is simplified as a dark blue LPC. PD denotes the period doubling (flip) bifurcation, happening at $I = 7.8495\ \mu\text{A/cm}^2$ (blue vertical dashed line). When switching from the PD point to another branch, the period of the unstable limit cycle undergoes a sudden doubling. And NS, i.e., the Neimark–Sacker (secondary Hopf) bifurcation, occurs at $I = 8.1882\ \mu\text{A/cm}^2$ (mint green vertical dashed line) [41, 42]. In the upper right corner of panel (b), the inserted subplot provides an enlarged illustration of the yellow rectangular area to the right of the dark blue LPC. This is to get a clearer representation of the detailed dynamics within the interval $7.8 < I < 8.21\ \mu\text{A/cm}^2$ and to offer a clearer distinction of bifurcation positions in this range.

Dynamical evolution trends near H1 are depicted in panel (c). The solid gray line represents the stable resting state. The scattered orange dots represent the maximum values of V during the oscillations of the unstable limit cycles, providing a simplified representation of the different unstable limit cycles. The solid orange line represents the maximum values of V during stable limit cycle oscillations, simplifying the representation of different stable limit cycles. As the bifurcation parameter I gradually increases from a value below $I_0 = 6.2645\ \mu\text{A/cm}^2$ and goes across $I_1 = 9.7796\ \mu\text{A/cm}^2$ (corresponding to the first Hopf bifurcation point H1), the system evolves overall along the direction of the blue arrow, switches from the stable resting state represented by the solid gray line to H1, and then to the unstable limit cycle indicated by the scattered orange dots, and ultimately reaches the stable limit cycle represented by the solid orange line. In this process, the Hodgkin–Huxley neuron undergoes a sequence of bifurcations: from a stable resting state to H1, further to NS (where $I = 8.1882\ \mu\text{A/cm}^2$), then to the pink LPC, followed by PD (where $I = 7.8495\ \mu\text{A/cm}^2$), and then to the green LPC, further reaching the dark blue LPC, and eventually entering the stable limit cycle oscillations. The HH neuron will evolve in the direction of the green arrow in Fig. 1c, sequentially undergoing processes starting from the stable limit cycle represented by the solid orange line, to the unstable limit cycle represented by the scattered orange dots, and eventually reaching the stable resting state represented by the solid gray line. During this whole process, a series of bifurcations will take place (see Fig. 1b): the system first reaches the dark blue LPC, through PD to the green LPC, then to the pink LPC, further to NS, and it eventually reaches a stable resting state. This explains why, without noise, the system only reaches limit cycles after passing H1 by gradually increasing the current I. When $I_0 < I < I_1$ is fulfilled, a coexistence of SRS and SLC emerges, involving: a large amplitude stable limit cycle, one to three small-amplitude unstable limit cycles, and a stable resting state. Particularly, in the region between pink LPC and the green LPC, where multiple unstable limit cycles appear, we designate it as the w interval. The complex dynamics within this interval are key features that distinguish the classic HH model from a series of simplified HH models, such as the Morris–Lecar (ML) model [7]. Eventually, the unstable limit cycle disappears at I_1. At the endpoint zone MPII, a single steady-state solution exists. This result demonstrates that when the stimulus current is too high, the cell becomes inactive or dies, illustrating the importance of parameter regulation for cellular dynamics. The discussions presented above are conducted under the conditions of deterministic equations.

3.2. Landscape and flux of a Hodgkin–Huxley neuron

We now explore the application of the landscape–flux approach to neuronal dynamics by investigating the HH model with Gaussian white noise (see (1)). When we apply Gaussian white noise

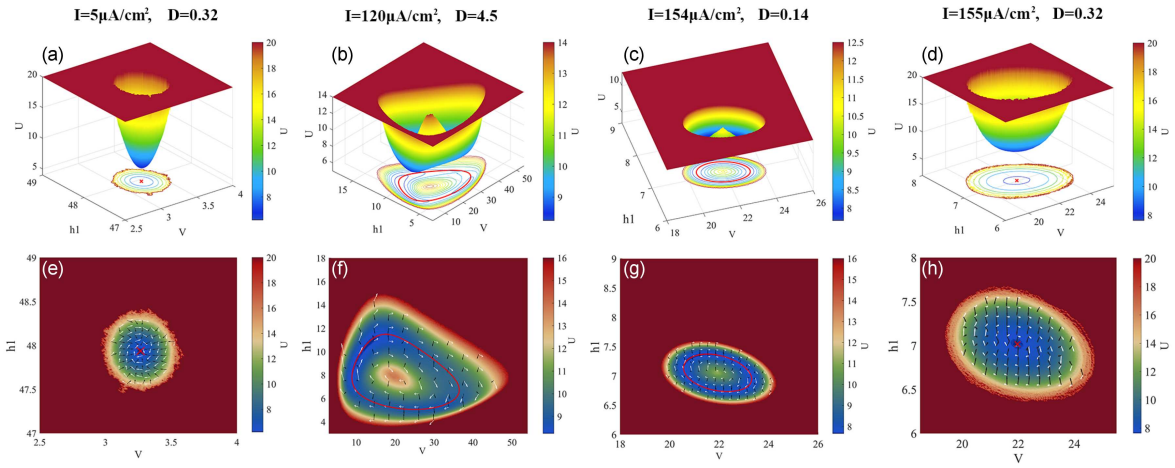

Fig. 2. The underlying potential landscapes and patterns of curl flux distribution evolve as the bifurcation parameter I increases under varying intensities of Gaussian white noise. Values of stimulus current I and noise intensity $\mathcal{D}$ are shown at the top of each panel. Panels (a)–(d) show 3D landscapes under different stimulus currents and fluctuation strengths. Panels (e)–(h) show 2D dimensional contour plots of the landscapes and steady-state fluxes under different stimulus currents and fluctuation strengths. In panels (a) and (d), the red "cross" indicates the single stable attractor corresponding to the deterministic equations. In panels (b) and (c), the red circles represent the stable limit cycles of the deterministic equations under the condition of a given stimulus current and noise intensity. Panels (e)–(h) illustrate the distribution of non-equilibrium driving forces under the conditions corresponding to the top ones. The white arrows represent the steady-state probabilistic curl flux, while the black arrows depict the landscape gradient distribution.

simultaneously in each dimension, then we use a one-dimensional array $\boldsymbol{A_I} = [A_V, A_m, A_h, A_n]$ to scale the magnification of the same noise intensity in different dimensions. We establish the corresponding probabilistic diffusion equation to obtain statistically steady-state probability distributions in the state space of the system. As the HH model is inherently four-dimensional, directly visualizing its potential landscape poses challenges. Thus, we focus on two key variables in the model, namely V and $h1$, while integrating the remaining variables to depict the comprehensive features of a single neuron on a global scale.

Figure 2 shows the three-dimensional and two-dimensional (2D) potential landscape, as well as the driving forces' distribution of the HH neuron for different values of the bifurcation parameter I, with the dimension noise amplification matrix set to $\boldsymbol{A_I} = [1.0, 0.0001, 1.0, 0.0001]$. Notably, for computational convenience, we have introduced the variable $h1 = 100h$ to facilitate the depiction of the corresponding potential landscape. When $I = 5\ \mu\mathrm{A/cm}^2$ and $\mathcal{D} = 0.32$, we evenly distributed 20×23 initial points across the $(V, h1)$ plane and tracked their trajectories from $t = 0$ to $t = 108\,315\,000$. Subsequently, we collected sample points from all trajectories between $t = 2\,500\,000$ and $t = 108\,315\,000$ to compute the probability distribution P. Then, we further calculated the probability distribution P for all trajectories between $t = 3\,000\,000$ and $t = 108\,315\,000$ and compared the results of these two computations. We found that P was the same for both calculations. Therefore, we hypothesize that the system reaches a non-equilibrium steady state after $t = 3\,000\,000$ time steps. Unless stated otherwise, we collected sample points for analysis by tracking trajectories from 20×23 initial points on the $(V, h1)$ plane, starting from $t = 3\,000\,000$ onwards. As depicted in Fig. 2a, when Gaussian white noise is introduced and in the context of a long-time limit, the uniqueness of the steady-state solutions in the deterministic equation diminishes. Instead, the final distribution of the global states assumes a funnel-shaped configuration. The stable resting state solution of the deterministic equation (marked by a red cross in the figure) resides at a local minimum of U, which indicates the maximum probability within the overall state distribution. In panel (e), the corresponding driving forces of the system under the conditions outlined in panel (a) are elucidated. The black arrows signify the force arising from the negative gradient of the potential landscape, consistently propelling the system's instantaneous state towards states of higher probability. Globally, the gradient force continually attracts the system toward the lowest point of the potential landscape funnel. The white arrows symbolize the probabilistic curl flux, which can be observed rotating around the single stable attractor, attempting to perturb the instantaneous state in conjunction with the gradient force. This effectively disrupts the point attractor and holds the capacity to trigger the emergence of new states. Besides, through the combined action of probabilistic curl flux, the system is not solely dragged by the gradient force directly to the bottom of the funnel. Instead, it

spirals down towards the attractor basin. This illustrates the essential interplay between both factors in maintaining the dynamics of non-equilibrium systems.

In Fig. 2b and c, the potential landscapes associated with a singularly stable limit cycle oscillation are illustrated. The topography of these landscapes resembles a Mexican hat, with the steady-state curl flux in the ring valley prominently overshadowing the influences exerted by the steady-state non-equilibrium potential's negative gradient. This dominance of probabilistic flux plays a vital role in sustaining the stability of the periodic oscillatory behavior. In two panels (b) and (c), the red circles represent the limit cycles of stable periodic oscillations under each respective input current ($I = 120\ \mu\text{A/cm}^2$ in (b), and $I = 154\ \mu\text{A/cm}^2$ in (c)) in the absence of noise. Panels (f) and (g) depict the distributions of driving forces in non-equilibrium systems, corresponding to those illustrated in (b) and (c). In panels (f) and (g), the white arrows denote the curl flux components of the non-equilibrium driving forces, whereas black arrows represent the negative gradient part of these driving forces. The red circles in these panels also denote the limit cycles for stable periodic oscillations, specific to each input current in the noise-free setting. Notably, in the vicinity of these limit cycles, the probabilistic curl flux is observed to align parallelly. This observation provides a detailed explanation of the previously mentioned phenomenon, namely the stability of the periodic oscillations is maintained due to the steady-state curl flux within the ring valley significantly surpassing the influence of the steady-state non-equilibrium potential's negative gradient.

As the bifurcation parameter I increases, neuronal behavior switches from periodic oscillations to a non-firing state, which biologically corresponds to neuronal inactivation or even cell death. Figure 2d depicts the potential landscape topography at the electrical current $I = 155\ \mu\text{A/cm}^2$, which is just after the second Hopf bifurcation point H2, where neurons are incapable of discharging. The topography is similar to that explained in panel (a), but with a noticeably larger and broader funnel structure at the same noise intensity of $\mathcal{D} = 0.32$. It is conceivable that in a range where the current value I exceeds the second Hopf bifurcation point H2, the landscape funnel would become progressively sharper and narrower as the I values increase, for the same noise intensity. Panel (h) describes the distribution of the system's driving forces corresponding to (d). In a low-noise environment, the probabilistic flux continues to be rotational; however, the role of the negative gradient of the steady-state non-equilibrium potential grows more pronounced compared to the circulatory effect. The system state would follow a downward spiral trajectory to the lowest point of the potential landscape funnel configuration, marked by the red cross in panels (d) and (h). This point corresponds to the resting state of the neuron at the input current $I = 155\ \mu\text{A/cm}^2$ in a noise-free scenario.

3.3. A quantitative assessment of the system's stability and robustness under a noisy background

Next, we investigate the impact of noise on neurons within the MPI parameter set (i.e., in the region $I < I_0$). The noise intensity coefficients are denoted by $\boldsymbol{A_\Gamma} = [100.0, 0.0001, 0.1, 0.0001]$. When $I = -10\ \mu\text{A/cm}^2$, as depicted in Fig. 1, the deterministic HH neuron is in the MPI parameter regime and will remain in the resting state without external stimulation. We collected simulated time series data of the membrane potential V under noise intensities $\mathcal{D} = 0.45$ and $\mathcal{D} = 0.01$ at $I = -10\ \mu\text{A/cm}^2$. It was observed that noise with the intensity of $\mathcal{D} = 0.45$ could trigger action potentials in the HH neuron, while noise with an intensity of $\mathcal{D} = 0.01$ could not facilitate the generation of action potential. This indicates that sufficiently high noise intensity can help the HH neuron to depart from the resting state and fire an action potential earlier compared to the deterministic HH neuron. Subsequently, we will focus on exploring the underlying dynamics of the HH neuron at noise intensities that can facilitate action potential firing in the MPI parameter set. As an example in our investigation, we will use the noise intensity $\mathcal{D} = 0.45$ at $I = -10\ \mu\text{A/cm}^2$. Figure 3a illustrates the transition of HH neurons under the MPI parameters from a resting state to spike generation in the presence of sufficiently intense finite noise. Starting from the resting state corresponding to $I = -10\ \mu\text{A/cm}^2$, the dynamic process lasts sufficiently long. After reaching a statistically steady state, we gather all trajectories and states that occurred in the dynamic process in the sufficient time. The collection of all trajectories and states is plotted as a final two-dimensional mapping of the potential landscape. The white dashed line signifies a threshold division, where the points on the left are directly pulled back to the resting state by the system's driving force, while the points on the right complete a cycle under the driving force, indicating the generation of action potential. This illustrates the neuron's sensitivity to a threshold. This corresponds to a phenomenon commonly observed in fast-spiking cells when subjected to appropriate current stimulation, characterized by intermittent switching between low-frequency periodic firing and a resting state [43]. When noise leads the HH neurons to go beyond the threshold, the phase trajectory can follow a circular path back to the resting state under the influence of curl flux. Subsequently, the system further assesses the possibility of crossing the threshold again based on the real-time noise contributions. Another action

potential occurs when the neuron's parameters successfully go cross the threshold again. However, if the noise fails to assist the neuron in crossing the threshold, it can directly return to the resting state rather than completing a circular path. As a result, competitive dynamic emerges between the resting state and the circular limit cycle under sustained noise influence. The unpredictability of noise presents a challenge in maintaining continuous, sustained discharges, ultimately resulting in an overall low-frequency firing pattern. Hence, a competitive dynamic emerges between the resting state and the circular limit cycle under sustained noise influence.

Figure 3b illustrates the probabilistic flux distribution of the system once it reaches a statistically steady state, where the distribution aligns nearly parallel to the direction of the system's driving force $\boldsymbol{F}$. In the low noise limit, the potential function linked to the gradient part of the driving force resembles a Lyapunov function in deterministic dynamics. The points where the gradient of this potential function hits zero act as attractors in deterministic dynamics. Here, the resting state and action potential correspond to stable points and limit cycles, respectively. The gradient force guides the system's trajectories toward the bottom region of the potential function, i.e., stable points and limit cycles. The driving force linked to the probabilistic flux facilitates transitions between different states in the system. Additionally, due to sufficiently small noise, the numerical value of the gradient force is typically orders of magnitude smaller than the driving force associated with the probabilistic flux. This results in a distribution of the probabilistic flux closely resembles the overall driving force distribution of the system. The oscillation period can be approximated by the loop integral of $\boldsymbol{J}_{ss}/P_{ss}$ along the circular oscillation path [19].

It can be seen from (5) that the smaller the value of U, the greater the probability of the corresponding state. The resting state precisely sits at the lowest point of the entire potential landscape, marked as U_{rest}. The population probability potential U corresponding to the threshold can be represented using the minimum value of U on the white dashed line, labeled U_{thresh}. When a neuron transitions from the resting state to firing an action potential, it needs to jump from the lowest level to the height of U_{thresh} of the potential landscape. We use $\Delta U = U_{\text{thresh}} - U_{\text{rest}}$ to measure the barrier height between two states. Figure 4a illustrates the trend of the corresponding barrier height as the bifurcation parameter changes. When subjected to noise of the same intensity, the resulting green curve represents a fitting curve of the data points, which takes the form of $a\exp(-b\,x) + c$ (where a, b, and c are constants greater than zero). This indicates that as the stimulation current increses, the barrier height between the resting state and the firing action potential exhibits exponential reduction, making the

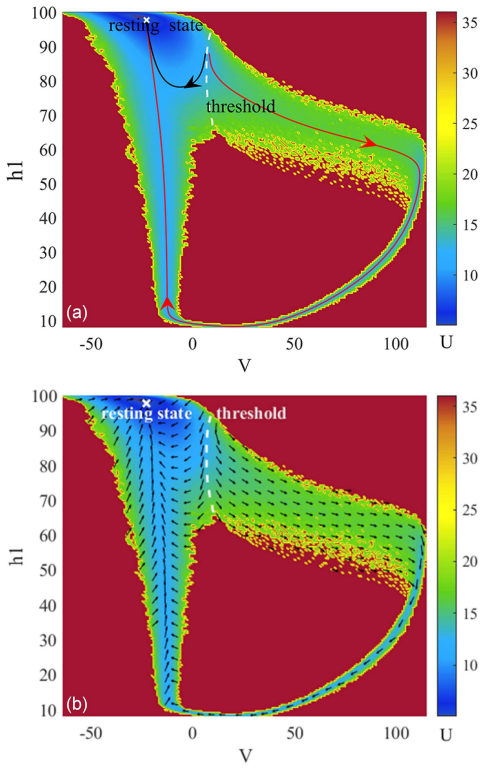

Fig. 3. The impact of noise on HH neuron dynamics. (a) HH neurons under MPI parameters compete between action potentials and subthreshold oscillations near the threshold. The white cross signifies the resting state. The black and red lines depict distinct driving force streamlines from two points near the threshold. The white dashed line separates the resting state from spikes, depicting the neuron's threshold ($I = -10\ \mu\text{A/cm}^2$, $\mathcal{D} = 0.45$). (b) The distribution of probabilistic flux throughout the entire process. The direction of the black arrows represents the direction of the system's probabilistic flux.

transition from the resting state to the action potential easier. Therefore, the barrier height between the resting state and the action potential measures the difficulty of transitioning between these two states, serving as a quantification criterion to estimate the robustness of the resting state.

Under substantial Gaussian white noise, the HH neuron departs from its deterministic resting state, overcoming the height of the potential landscape, ΔU, to reach the threshold potential for generating an action potential. This critical period, from the starting point until just beyond the threshold potential, moments before the action potential is initiated, represents the minimum duration needed for the HH neuron to escape its resting state, or represents the initial transition time from the resting state to the onset of an action potential. Concerning the potential landscape's topography, this duration signifies the time required to depart from the resting state's lowest point and reach

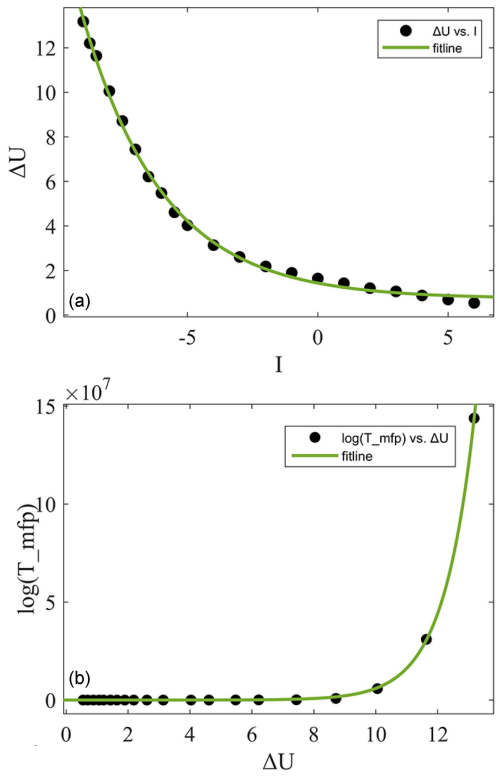

Fig. 4. Quantification of the transition difficulty of Hodgkin–Huxley neurons from the resting to the action potential state under MPI parameters. (a) Change in barrier height versus bifurcation parameter I for the resting-to-action potential transition ($\mathcal{D} = 0.245$). (b) The logarithm of the mean first pass time needed to reach the action potential from the resting state as a function of barrier height ($\mathcal{D} = 0.245$).

U_{thresh} for the first time. We refer to this duration as the "first-passage time". By recording the first passage time repeatedly and calculating the average, we will get the mean first passage time (MFPT) — denoted as Tmfp. It offers another quantification of the stability of the system. Figure 4b illustrates the natural logarithm of Tmfp vs the barrier height ΔU. Under the same noise intensity, the fitted curve exhibits an exponential trend (fitted formula $a\exp(bx)$, where both a and b are greater than 0). This indicates that as the barrier height increases, the required evolution time becomes longer, and the transition between different states becomes harder. Looking from left to right at the panel (b), the system becomes more and more stable. The quantitative fitting here shares a resemblance with the Arrhenius law observed in equilibrium systems.

For the MLC parameter set of the HH neuron, the comparative analysis between panels (b) and (c) in Fig. 2 reveals varying heights of the central island in the potential landscape, corresponding to different noise intensities and bifurcation parameters. To quantitatively determine the stability of the system's limit cycle attractor, we relied on 3D potential landscapes to establish two barrier heights, which aided us in tracing the range of the limit cycle's path distribution in the state space. One barrier is the difference in population probability potential between the highest point on the central island in a Mexican hat and the lowest point along the circular path — it is denoted as Barrier1 $= U_0 - U_{\min}$; the other is the difference between the highest point of the central island and the value of U at the maximum along the circular path, i.e., Barrier2 $= U_0 - U_{\max}$. For different bifurcation parameters under the same noise intensity, the height of the central island is correlated to the size of the corresponding red circle in the 2D phase space shown in panels (b), (c), (f) and (g) in Fig. 2. A larger circular area indicates the need for greater noise assistance or more statistical data points to reach the high points within the central island. Statistically, under the same noise intensity, it's easier to reach the central island with a smaller circular area, which naturally results in a smaller formed barrier height. Here, we study the stability of the system's limit cycle attractor under varying noise intensities applied to the same bifurcation parameter.

In Fig. 5a, the variations of two barrier heights, Barrier1 and Barrier2, vs the fluctuations of noise intensity are presented. The solid line corresponds to the difference in barrier heights along the upper boundary of the attractor of the limit cycle, labeled Barrier1. In contrast, the dashed line represents the Barrier signifying the lower boundary of the limit cycle. Both Barrier1 and Barrier2 decrease as the noise intensity scaling coefficient $\mathcal{D}$ increases. Panel (b) illustrates the relationship between the average first-passage time τ of the limit cycle attractor and barrier heights. The escape time increases with the barrier height. Thus, for the same input stimulus current, higher applied noise leads to smaller barrier heights and shorter average first-passage times from the limit cycle attractor, indicating greater instability of the limit cycle.

3.4. Entropy production, average probabilistic flux, and phase transitions

Considering the phase transition of the HH neuron with Gaussian white noise, we use the stimulus current I as a changing parameter for comparison with a deterministic bifurcation diagram. Figure 6a displays the system's EPR and the average probabilistic flux J_{av} variations with I under finite-amplitude Gaussian white noise. Here, the scales of the two y axes for flux (on the right) and EPR (on the left) are different. Before reaching the initial bifurcation point I_1, J_{av} maintains relatively low values. It undergoes an abrupt increase at I_1, marking a discontinuous phase transition.

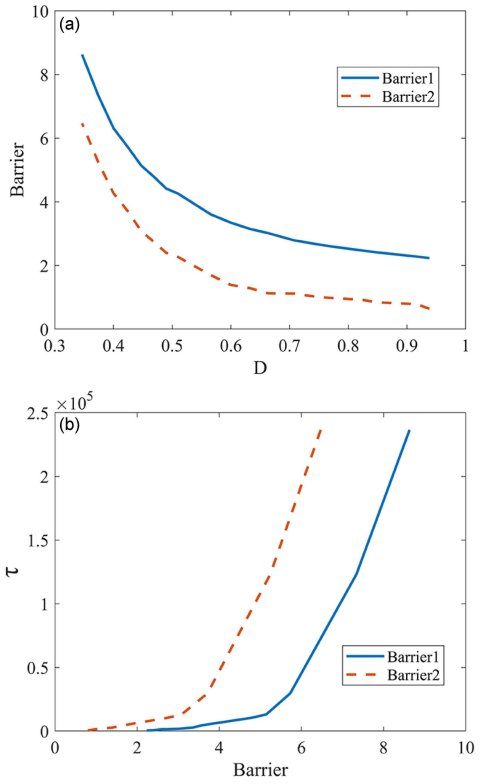

Fig. 5. Barrier heights and escape time in Hodgkin–Huxley neurons under MLC parameters. (a) Barrier heights $U_0 - U_{\min}$ and $U_0 - U_{\max}$ vs noise intensity for $I = 120\ \mu\text{A/cm}^2$. (b) Comparison of escape time with barrier heights for various noise intensities.

Subsequently, J_{av} gradually decreases to zero at I_2, indicating a continuous phase transition within the system. However, as shown in Fig. 3, under sufficient finite noise conditions, the system experiences a transition period between the resting state and action potentials before I_1, corresponding to zone B in the deterministic bifurcation diagram. This suggests that due to noise influence, the system undergoes oscillations even before I_1. Why doesn't J_{av} undergo a sudden change earlier?

We divided the entire state space into a grid of small 200×200 squares and tracked all trajectory points once the non-equilibrium steady state was reached. By calculating the average absolute values of the probabilistic flux J_{unit} for each grid and summing these values throughout the system, we obtained the total absolute values of the probabilistic flux J_{total}. Dividing this by the total number of squares in the state space, we can get the average probabilistic flux J_{av} over the entire state space. When the HH neuron is influenced by limited noise and is sufficiently distant from the Hopf bifurcation point H1 within the MPI parameter set, it will generate intermittent irregular action potentials (see Fig. 3). When the resting state coexists with periodic oscillations, reaching a non-equilibrium steady state, we partition the entire state space into two parts: the annular funnel region where the static points are situated, and the circular path formed by the limit cycle. To roughly estimate the average flux J_{av} in this bistable state, we distinquish it into $J_{av-\text{funnel}}$ in the annular funnel region and J_{av0} along the circular path. In the circular depression area where the resting state resides (we refer to Fig. 2e and h), $J_{av-\text{funnel}}$ exhibits no significant changes compared to $J_{av-I-\text{smaller}}$ observed when the periodic oscillations have not appeared. We isolated the circular path by excluding the funnel region around the resting state and computed the average probabilistic flux along this circular path using $J_{av0} = (\oint \mathrm{d}l\ J)/(\oint \mathrm{d}l)$. Subsequently, by dividing this value by the number of the spatial grid squares excluding the area around the resting state, we obtained J_{av1} for the entire state space.

Interestingly, J_{av0} exhibits a magnitude comparable to J_{av} after the phase transition (I is within the MLC range). The subsequent J_{av1}, on the contrary, is approximately four orders of magnitude smaller than J_{av}. Due to the limited noise and small stimulation current, the distribution of the resulting limit cycle in the state space is narrow. This limited spread prevents the formation of explicit central islands, as Fig. 2b and c, because trajectories corresponding to the intermediate region within the circular path cannot be reached. Although this is not a fundamental defect, the system, influenced by limited noise intensity and within a finite computational time (recorded at time $t = 108\,315\,000$), fails to reach states with a particularly small probability distribution near the vertices of the central islands. Consequently, this explains why the average probabilistic flux J_{av1} across the entire state space does not undergo an immediate abrupt change when the resting state coexists with periodic oscillations in the system. EPR also experiences a sudden change at I_1 and then gradually approaches zero at I_2. This is due to the close relationship between the calculation of EPR and the probabilistic flux.

When looking at Fig. 2e–h and Fig. 3b, the gradient part of the system's driving force continuously directs the system state towards the bottom region of the potential landscape, stabilizing point attractors and limit cycles if they exist. Meanwhile, the curl flux, because of its rotational nature, tends to destabilize point attractors. Greater curl flux may render the original state less stable and can even alter the landscape's topography, finally generating new states, leading to a phase transition (as observed in Figs. 2e, 2f, and 3b). Together, these three mentioned panels of the figures capture the different stages of the entire process. Figure 2g and h vividly illustrates the less pronounced changes in the curl flux during a continuous phase transition. Hence, the curl flux plays a dynamic role in driving phase transitions or bifurcations/catastrophes in non-equilibrium systems.

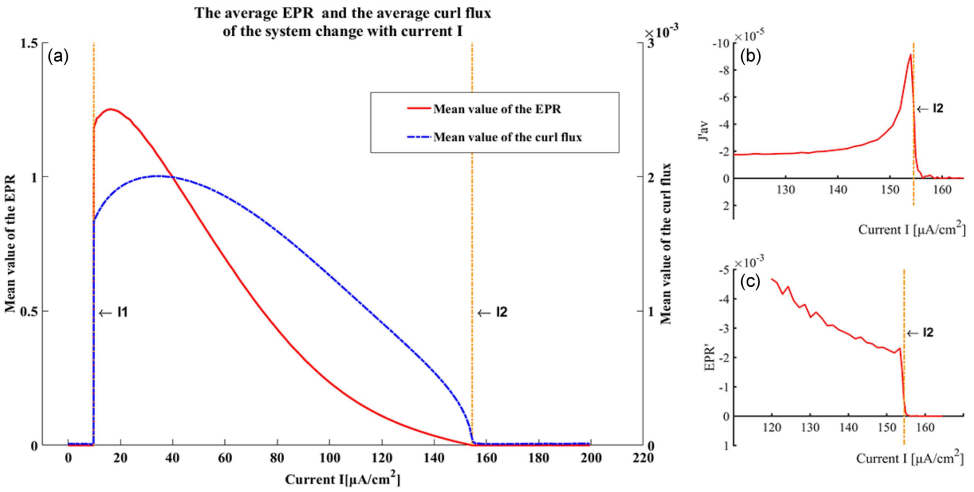

Fig. 6. EPR and the average probabilistic flux J_{av}. The solid red line represents the mean value of EPR across the entire state space. In contrast, the dashed blue line reflects the relationship between the system's average probabilistic flux J_{av} and the bifurcation parameter. The noise intensity is set at $\mathcal{D} = 0.1$. The two vertical dashed lines correspond to the two Hopf bifurcation points, I_1 and I_2, in the deterministic bifurcation diagram. (b) First derivative of the average curl flux with respect to the stimulus current. (c) First derivative of EPR with respect to stimulus current.

The entropy production rate (EPR) quantifies irreversible processes within a system, indicating its tendency to move towards higher entropy states. When a non-equilibrium system reaches a statistically steady state after a sufficiently long time, the numerical value of EPR equals the system's heat dissipation rate or entropy flow rate S'_e. This equivalency allows EPR to describe the energy transfer within the system. Within the range of $I_0 < I < I_1$, as genuine limit cycles are not formed, neurons can only physiologically engage in low-frequency discharges, and therefore, EPR undergoes a sudden change only at $I = I_1$.

As for the second Hopf bifurcation point I_2, we calculated the first derivatives of the flux and EPR around I_2, as shown in Fig. 6b and c. We found that both the first derivatives of EPR and the flux show discontinuous changes at I_2, indicating a second-order phase transition at I_2. The physical meaning of the transition is that the neuron's steady states change from stable periodic oscillation to a stable resting state as the stimulus current increases. EPR can be considered as the thermodynamic origin of bifurcation or phase transition points in a non-equilibrium system. Both J_{av} and EPR can serve as order parameters for bifurcations and phase transitions at I_1 and I_2 of the system.

3.5. Time irreversibility of the cross-correlation function and critical slowing down

For the practical side, the average flux and EPR are not always easy to quantify directly from experimental observations such as time series. However, the non-equilibrium nature can be extracted directly from the time asymmetry of the cross-correlations of the observables. If we consider a neuron operating under the influence of noise, receiving a constant stimulus current and reaching a statistically steady state as a non-equilibrium state, we can calculate the difference in two-point cross-correlation functions for the forward and reverse times. This method helps quantify the extent of detailed balance breaking and irreversibility of time within the system.

Figure 7a displays a time series plot of the neuron membrane potential V and the parameter $h1$, representing the inactivation of sodium channels. With relatively small noise applied and operated at $I = 10\ \mu\text{A/cm}^2$ within the MLC range, V and $h1$ demonstrate overall stable periodic oscillations. However, setting the diffusion coefficient matrix $\boldsymbol{A_I}$ to $[100.0, 0.0001, 0.1, 0.0001]$ results in maximal noise intensity imposed on V, leading to more pronounced jagged fluctuations between action potentials compared to those observed in $h1$. Figure 7b shows the forward-in-time and backward-in-time cross-correlation functions between V and $h1$. The black line represents the correlation function proceeding forward in time — denoted as C_{Vh1}, while the blue line corresponds to the function reverse in time — denoted as C_{h1V}. The lines exhibit an approximate phase-complementary periodic oscillation and gradually diminish in amplitude toward zero. Figure 7c illustrates the time-evolving trend of the difference between forward-in-time and backward-in-time cross-correlation functions — denoted as $C_{Vh1} - C_{h1V}$. Similarly, there are displayed periodic-like oscillations, with the amplitude gradually decreasing towards zero. It is important to

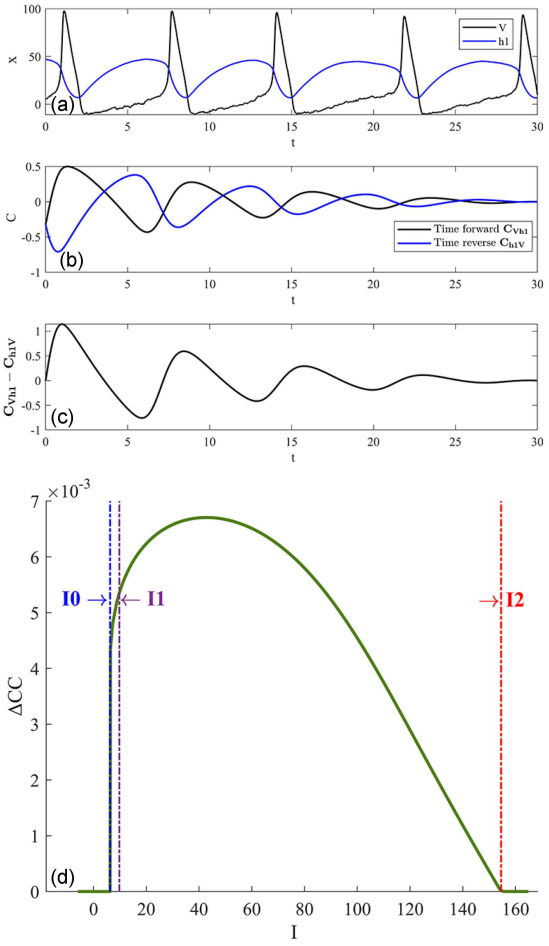

Fig. 7. Quatification of the time irreversibility and the degree of detailed balance breaking. (a) Trajectories of the membrane potential V and $h1$ (I = 10 μA/cm^2, $\mathcal{D} = 0.04$, and $h1 = 100h$). (b) Time-forward C_{Vh1} (black) and time-reverse C_{h1V} (blue) cross-correlation function between V and $h1$. Panel (c) represents the difference between forward-in-time and backward-in-time cross-correlation functions, $C_{Vh1}-C_{h1V}$, plotted vs t. (d) Illustration of the average difference of $C_{Vh1}-C_{h1V}$, denoted as ΔCC, in relation to I. The solid green line indicates the change in ΔCC vs the bifurcation parameter I. The purple vertical dashed line corresponds to the current I_1 at the first Hopf bifurcation point, H1, while the red vertical dashed line represents I_2 at the second Hopf bifurcation point, H2. The dark blue vertical dashed line corresponds to the current I_0.

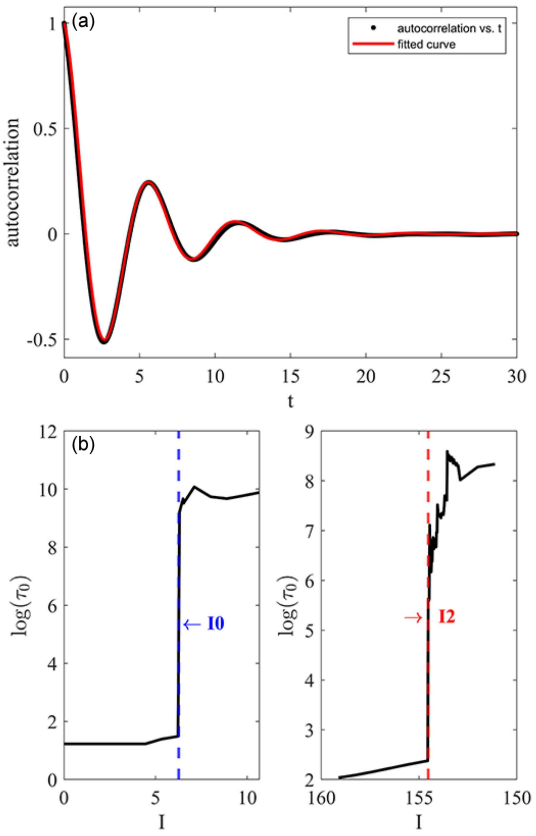

Fig. 8. The phenomenon of critical slowing down near the subcritical Hopf bifurcation point H1 in the Hodgkin–Huxley neuron. (a) The two-point autocorrelation function of $h1$ and its fitting line ($\mathcal{D}$ = 0.045 and $I = 5.4709$ μA/cm^2). (b) The natural logarithm of τ_0 vs I (black solid line). The dark blue dashed vertical line is $I_0 = 6.2645$ μA/cm^2. The red dashed vertical line is $I_2 = 154.5266$ μA/cm^2.

note that in panels (a), (b), and (c), the condition $t = 0$ does not represent the initial time of recording the trajectory. Instead, it signifies a point in time reached after the system has been running for a sufficiently long time to attain a statistically steady state.

Figure 7d displays the variation of the average difference $C_{Vh1} - C_{h1V}$, denoted as ΔCC, with respect to the bifurcation parameter I. The two dashed lines represent the stimulus currents I_1 and I_2 corresponding to the two Hopf bifurcation points. The forward-in-time and backward-in-time cross-correlation functions serve as quantifiable indicators of detailed balance breaking and time irreversibility, respectively. Their experimental application, such as in the use of fluorescence correlation spectroscopy in single-molecule enzymology [44, 45], may be a practical method for identifying potential bifurcations or non-equilibrium phase transitions in HH neurons. Comparing this with Fig. 6, ΔCC exhibits a similar overall trend to J_{av} and EPR, however, it shows an earlier significant change near I_0. This aligns with the boundary between the MPI and B regions in the deterministic bifurcation diagram (Fig. 1a), suggesting that ΔCC might be a more effective predictor of phase transitions compared to J_{av} and EPR.

For neurons capable of transitioning from a resting state to spike firing, it is theoretically possible to provide an indicator regarding the characteristics of the critical slowing down as the neuron

approaches the first Hopf bifurcation point H1 from its resting state, as well as the H2 Hopf bifurcation point from the resting state. To observe the phenomenon of the critical slowing down within a finite observation window, we require appropriate noise intensity and an observation interval sufficiently close to H1 and H2. Adjusting these factors can enhance the accuracy and visibility of observing neuronal state transitions. We set $\mathcal{D} = 0.045$ and $\boldsymbol{A_I} = [1.0, 0.0001, 1.0, 0.0001]$ for our investigation. We used MATLAB to compute and normalize $h1$'s two-point autocorrelation function. Then, we applied the "cftool" toolbox to fit the resulting curve using the function $\exp(-x/\tau_0)\cos(wx)$, $w = 2\pi T$, where τ_0 represents a coherence time for the oscillation [26, 46, 47]. Figure 8a illustrates the curve of autocorrelation function for $I = 5.4709\ \mu\mathrm{A/cm}^2$. The red line signifies the fitted curve, which displays the remarkable proximity to the original data. Through this fitting process, we determined the value of τ_0. In Fig. 8b, we plotted the natural logarithm of τ_0 vs the current I. The natural logarithm of τ_0 exhibits a dramatic change at I_0 and I_2, indicating a strong correlation between critical slowing down and Hopf bifurcation for the classical HH neuron model. Therefore, critical slowing down, average flux, EPR, and irreversible cross-correlation can provide indicators for bifurcation from the fluctuation, dynamics, thermodynamics, and time asymmetry perspectives.

4. Conclusions

In this study, we thoroughly investigated the local bistability properties of the original four-dimensional Hodgkin–Huxley equations under the influence of noise. Combined with landscape and flux theory, we conducted a comprehensive analysis of the stochastic dynamics of a single HH neuron, revealing the characteristics of potential landscapes and non-zero curl flux after it reaches a statistically steady state. We decomposed the driving force of the system into two parts: one closely related to the gradient of the probability distribution potential U, in short as the gradient force, and the other associated with the steady-state probabilistic flux $\boldsymbol{J}_{ss}$ and the steady-state probability distribution density P_{ss}. The gradient force tends to drag the real-time system state toward states with a larger probability distribution, effectively stabilizing the system state on stable attractors in non-equilibrium systems. The component associated with the steady-state probabilistic flux $\boldsymbol{J}_{ss}$, exhibiting a rotational characteristics, is dedicated to driving and sustaining periodic oscillations.

We explored how strong noise triggers oscillations prematurely, leading to a competitive coexistence between neuronal quiescence and spike discharges. Despite sufficient noise, the dominating rotational force driving the emergence and sustenance of stable oscillations dominates over the gradient force. Moreover, by evaluating the barrier height in coexistence states, we quantified the stability of the resting state and further investigated the stability of limit cycles in regions exclusively characterized by stable periodic oscillations.

Through computation of the entropy production rate (EPR) and the average probabilistic flux J_{av}, we discovered that both J_{av} and EPR serve as quantitative indicators for bifurcations or phase transitions in the HH neurons. As it is not easy to directly measure these two metrics in experiments, we further discussed the average difference between forward-in-time and backward-in-time cross-correlations and the critical slowing down, which can be directly measured in experiments. Moreover, the average difference between forward-in-time and backward-in-time cross-correlations tends to undergo a break earlier than EPR and J_{av}, marking it as an earlier warning signal for bifurcation or phase transition points. In the original HH model, there exists a subcritical Hopf bifurcation rather than a saddle-node bifurcation, and the critical slowing down is closely associated with the subcritical Hopf bifurcation.

Acknowledgments

This work was supported by the Natural Science Foundation of Jilin Province, China (Grant No. 20210101141JC). H.H. thanks for useful discussions by Xiaochen Wang, Wei Wu, Linqi Wang, Li Xu, Chong Yu, Wenbo Li, and Xuanhua Wang.

Appendix

A1. The classical Hodgkin–Huxley equations and the Jacobian matrix in their deterministic form

The deterministic Hodgkin–Huxley model can be written as

$$\begin{aligned}
C_m\frac{\mathrm{d}V}{\mathrm{d}t} &= -\overline{g_{\mathrm{K}}}n^4(V-V_{\mathrm{K}}) - \overline{g_{\mathrm{Na}}}m^3h(V-V_{\mathrm{Na}}) \\
&\quad -g_L(V-V_L) + I, \\
\frac{\mathrm{d}m}{\mathrm{d}t} &= \alpha_m(V)(1-m) - \beta_m(V)m, \\
\frac{\mathrm{d}h}{\mathrm{d}t} &= \alpha_h(V)(1-h) - \beta_h(V)h, \\
\frac{\mathrm{d}n}{\mathrm{d}t} &= \alpha_n(V)(1-n) - \beta_n(V)n.
\end{aligned} \tag{9}$$

During the linear stability analysis, stochastic forces of the system are neglected and all equations on the left-hand side are set to zero. The corresponding

expressions on the right-hand side are denoted in order as f_1, f_2, f_3, f_4. Then, the Jacobian matrix in the deterministic form is as follows

$$\mathcal{J}_{Jacobi} = \begin{bmatrix} \frac{\partial f_1}{\partial V} & \frac{\partial f_1}{\partial m} & \frac{\partial f_1}{\partial h} & \frac{\partial f_1}{\partial n} \\ \frac{\partial f_2}{\partial V} & \frac{\partial f_2}{\partial m} & \frac{\partial f_2}{\partial h} & \frac{\partial f_2}{\partial n} \\ \frac{\partial f_3}{\partial V} & \frac{\partial f_3}{\partial m} & \frac{\partial f_3}{\partial h} & \frac{\partial f_3}{\partial n} \\ \frac{\partial f_4}{\partial V} & \frac{\partial f_4}{\partial m} & \frac{\partial f_4}{\partial h} & \frac{\partial f_4}{\partial n} \end{bmatrix} \tag{10}$$

Next, let us illustrate the procedure using $\frac{\partial f_2}{\partial V}$ and $\frac{\partial f_2}{\partial m}$ as examples. The remaining terms can be derived by similar methods, i.e.,

$$\begin{aligned} \frac{\partial f_2}{\partial V} &= \frac{\partial}{\partial V}\big[\alpha_m(V)(1-m) - \beta_m(V)m\big] = \\ &\frac{\partial}{\partial V}\big[\alpha_m(V) - m\alpha_m(V) - \beta_m(V)m\big] = \\ &\dot{\alpha_m}(V) - [\dot{\alpha_m}(V)+\dot{\beta_m}(V)]m = \\ &\dot{\alpha_m}(V)[\dot{\alpha_m}(V)+\dot{\beta_m}(V)]\frac{\alpha_m(V)}{\alpha_m(V)+\beta_m(V)} = \\ &\big[\alpha_m(V)+\beta_m(V)\big]\left[\frac{\dot{\alpha_m}(V)[\alpha_m(V)+\beta_m(V)]}{[\alpha_m(V)+\beta_m(V)]^2}\right. \\ &\left.-\frac{\alpha_m(V)[\dot{\alpha_m}(V)+\dot{\beta_m}(V)]}{[\alpha_m(V)+\beta_m(V)]^2}\right] = \lambda_m \dot{m}_\infty \frac{\partial f_2}{\partial m} = \\ &-[\alpha_m(V)+\beta_m(V)] = -\lambda_m \end{aligned} \tag{11}$$

In the above equations, $\lambda_m = \alpha_m(V) + \beta_m(V)$ and $m_\infty = \frac{\alpha_m(V)}{\alpha_m(V)+\beta_m(V)}$. The same procedure can be applied to derive other elements of the Jacobian matrices.

A2. From Langevin equations (LEs) to Fokker–Planck equations

The system dynamics satisfy the following equation

$$\frac{\mathrm{d}x_i}{\mathrm{d}t} = f_i(\boldsymbol{x}, t) + \sum_{j=1}^{m} g_{ij}\Gamma_i(t). \tag{12}$$

The first two moments of the Langevin force component $\Gamma_i(t)$ are given by

$$\begin{aligned} &\langle \Gamma_i(t)\rangle = 0, \\ &\langle \Gamma_i(t_1)\Gamma_j(t_2)\rangle = 2\mathcal{D}_i\,\delta_{ij}\delta(t_1 - t_2), \end{aligned} \tag{13}$$

where $i, j = 1, 2, ..., n$. The multiplication factor g_{ij} in (12) eliminates the variations of stochastic forces to the variable $\boldsymbol{x}$. In (13), δ_{ij} satisfies

$$\delta_{ij} = \begin{cases} 1, & \text{if} i = j, \\ 0, & \text{if} i \neq j. \end{cases} \tag{14}$$

To deduce an equation satisfied by the system's distribution function $P(\boldsymbol{x}, t)$ from the Langevin equation (LE), it is essential to compute the various order transition moments $M_n(\boldsymbol{x}, t, \tau)$. As an example, we consider the one-dimensional case

$$M_n(x, t, \tau) = \langle \big(x(t+\tau) - x(t)\big)^n \rangle \quad (\tau \ll 1). \tag{15}$$

Starting from (12), the stochastic dynamics can be described by $\frac{\mathrm{d}x}{\mathrm{d}t} = f(x,t) + g(x,t)\Gamma(t)$. From here, it is easy to get

$$x(t+\tau) - x(t) = \int_t^{t+\tau} \mathrm{d}t' \,\big[f(x(t'), t') + g(x(t'), t')\Gamma(t')\big]. \tag{16}$$

Assuming that the integrands f and g can be expanded in terms of $x(t')-x(t)$, it holds

$$\begin{aligned} &f(x(t'), t') = f(x(t), t') + f'(x(t), t')(x(t') - x(t)) + \ldots \\ &g(x(t'), t') = g(x(t), t') + g'(x(t), t')(x(t') - x(t)) + \ldots \end{aligned} \tag{17}$$

Substituting the expression (17) into (16) yields

$$\begin{aligned} x(t+\tau) - x(t) = &\int_t^{t+\tau} \mathrm{d}t' \; f(x(t), t') \\ &+ \int_t^{t+\tau} \mathrm{d}t' \; f'(x(t), t')\big(x(t') - x(t)\big) + \ldots \\ &+ \int_t^{t+\tau} \mathrm{d}t' \; g(x(t), t')\Gamma(t') \\ &+ \int_t^{t+\tau} \mathrm{d}t' \; g'(x(t), t')\big(x(t') - x(t)\big)\Gamma(t') + \ldots \end{aligned} \tag{18}$$

Repeatedly using (18) for the $x(t+\tau) - x(t)$ term in the expression gives

$$\begin{aligned} x(t+\tau) - x(t) = &\int_t^{t+\tau} \mathrm{d}t' \; f(x(t), t') \\ &+ \int_t^{t+\tau} \mathrm{d}t' \; f'(x(t), t') \int_t^{t'} \mathrm{d}t'' \; h(x(t'), t'') \\ &+ \int_t^{t+\tau} \mathrm{d}t' \; f'(x(t), t') \int_t^{t'} \mathrm{d}t'' \; \mu(x(t'), t'')\Gamma(t'') \\ &+ \cdots + \int_t^{t+\tau} \mathrm{d}t' \; g'(x(t), t')\Gamma(t') \\ &+ \int_t^{t+\tau} \mathrm{d}t' \; g'(x(t), t')\Gamma(t') \int_t^{t'} \mathrm{d}t'' \; h(x(t'), t'') \\ &+ \int_t^{t+\tau} \mathrm{d}t' \, g'(x(t), t')\Gamma(t') \int_t^{t'} \mathrm{d}t'' \, \mu(x(t'), t'')\Gamma(t'') \\ &+ \ldots \end{aligned} \tag{19}$$

To understand the statistical properties of $x(t)$ and obtain higher-order correlations such as $\langle x(t_1)x(t_2)x(t_3)x(t_4)\ldots\rangle$, we make the practical assumption that the random variable $\Gamma(t)$ follows a Gaussian distribution. That means,

$$\begin{aligned} &\langle \Gamma(t_1)\Gamma(t_2)\Gamma(t_3)\ldots\Gamma(t_{2n-1})\rangle = 0, \\ &\langle \Gamma(t_1)\Gamma(t_2)\Gamma(t_3)\ldots\Gamma(t_{2n})\rangle = \\ &\quad (2\mathcal{D})^n \sum_i^n [\delta(t_{i_1} - t_{i_2})\delta(t_{i_3} - t_{i_4})\ldots\delta(t_{i_{2n-1}} - t_{i_{2n}})]. \end{aligned} \tag{20}$$

By combining the statistical properties of the Langevin force mentioned above by (13) and (20) with (19), we can calculate the higher-order transition moments (see (15)). The first-order transition moment is given by

$$M_1(x,t,\tau) = \langle x(t+\tau) - x(t) \rangle = \left[f(x,t) + \mathcal{D} g'(x,t) g(x,t) \right] \tau + \mathcal{O}(\tau^2). \tag{21}$$

Here, $O(\tau^2)$ represents the higher-order infinitesimal of τ. Similarly, one can obtain

$$M_2(x,t,\tau) = \langle [x(t+\tau) - x(t)]^2 \rangle = 2\mathcal{D} g^2(x,t)\tau + O(\tau^2), \tag{22}$$

and

$$M_n(x,t,\tau) = \langle [x(t+\tau) - x(t)]^n \rangle \leq O(\tau^2) \tag{23}$$

for $n \geq 3$. Assuming that the process under investigation is a Markov process, and using $\rho(x,t)$ to represent its distribution function and p to represent the probability of being in a certain state, the following relations are derived

$$\rho(x, t+\tau) = \int \mathrm{d}x' \; p(x, t+\tau | x', t) \rho(x', t), \tag{24}$$

$$\rho(x, t+\tau) - \rho(x,t) = \frac{\partial \rho(x,t)}{\partial t} \tau + O(\tau^2). \tag{25}$$

In $p(x, t+\tau | x', t) = \int \mathrm{d}y \; \delta(y-x) \, p(y, t+\tau | x', t)$, let expand the term $\delta(y-x)$, namely

$$\delta(y-x) = \delta(x' - x + y - x') = \sum\nolimits_{n=0}^{\infty} \frac{(y-x')^n}{n!} \left(\frac{\partial}{\partial x} \right)^n \delta(x'-x). \tag{26}$$

After substituting it into the previous integral identity (24), we get the result

$$p(x, t+\tau | x', t) = \left[1 + \sum\nolimits_{n=1}^{\infty} \frac{1}{n!} \left(-\frac{\partial}{\partial x} \right)^n M_n(x', t, \tau) \right] \delta(x'-x), \tag{27}$$

where

$$M_n(x', t, \tau) = \int \mathrm{d}y \; (y - x')^n p(y, t+\tau | x', t). \tag{28}$$

Substituting (27) into (24) and comparing with (25), one gets

$$\frac{\partial \rho(x,t)}{\partial t} = L_{KM} \; \rho(x,t), \tag{29}$$

$$L_{KM} = \sum_{n=1}^{\infty} \left(-\frac{\partial}{\partial x} \right)^n D_n(x,t), \tag{30}$$

$$D_n(x,t) = \lim_{\tau \to 0} \frac{M_n(x,t,\tau)}{n! \tau}. \tag{31}$$

Since $p(x,t|x',t)$ is the transition probability at time t' with an initial distribution satisfying $\rho(x,t) = \delta(x - x')$, this transition probability also follows

$$\frac{\partial p(x,t|x',t)}{\partial t} = L_{KM} \, p(x,t|x',t). \tag{32}$$

This is the Kramers–Moyal forward equation. Comparing the high-order moment equation M_n here with the previously defined one, it is easy to obtain

$$D_1(x,t) = f(x,t) + \mathcal{D} g'(x,t) g(x,t),$$
$$D_2(x,t) = \mathcal{D} g^2(x,t),$$
$$D_n(x,t) = 0, \quad (n \geq 3). \tag{33}$$

Thus, the Kramers–Moyal equation with truncation at the second order of partial derivatives is

$$\frac{\partial \rho(x,t)}{\partial t} = -\frac{\partial}{\partial x} \left[f(x,t) + \mathcal{D} g'(x,t) g(x,t) \right] \rho(x,t) + \mathcal{D} - \frac{\partial^2}{\partial^2 x} \left[g^2(x,t) \rho(x,t) \right]. \tag{34}$$

This is the Fokker–Planck equation for a one-dimensional variable system.

The Fokker–Planck equation corresponding to the multi-variable Langevin equations can be derived using a similar approach, i.e.,

$$\frac{\partial \rho(\boldsymbol{x},t)}{\partial t} = -\sum_i \frac{\partial}{\partial x_i} \left[D_i(\boldsymbol{x},t) \rho(\boldsymbol{x},t) \right] + \sum_i \sum_j \frac{\partial^2}{\partial x_i \partial x_j} [D_{ij}(\boldsymbol{x},t) \rho(\boldsymbol{x},t)], \tag{35}$$

$$D_i(\mathbf{x},t) = \lim_{\tau \to 0} \frac{\langle x_i(t+\tau) - x_i \rangle}{\tau} = f_i(\boldsymbol{x},t) + D \sum_k \sum_l g_{kl} \frac{\partial}{\partial x_k} g_{il}, \tag{36}$$

$$D_{ij}(\boldsymbol{x},t) = \lim_{\tau \to 0} \frac{\langle [x_i(t+\tau) - x_i][x_j(t+\tau) - x_j] \rangle}{\tau} = D \sum_k g_{ik} g j k. \tag{37}$$

References

[1] A.L. Hodgkin, A.F. Huxley, B. Katz, *J. Physiol.* **116**, 424 (1952).

[2] A.L. Hodgkin, A.F. Huxley, *J. Physiol.* **116**, 449 (1952).

[3] A.L. Hodgkin, A.F. Huxley, *J. Physiol.* **116**, 473 (1952).

[4] A.L. Hodgkin, A.F. Huxley, *J. Physiol.* **116**, 497 (1952).

[5] A.L. Hodgkin, A.F. Huxley, *J. Physiol.* **117**, 500 (1952).

[6] M. Piccolino, *Trends Neurosci.* **25**, 552 (2002).

[7] B. Hassard, *J. Theor. Biol.* **71**, 401 (1978).

[8] J. Rinzel, R.N. Miller, *Math. Biosci.* **49**, 27 (1980).

[9] K. Aihara, G. Matsumoto, *Biophys. J.* **41**, 87 (1983).

[10] J. Guckenheimer, J.S. Labouriau, *Bull. Math. Biol.* **55**, 937 (1993).

[11] H. Fukai, S. Doi, T. Nomura, S. Sato, *Biol. Cybern.* **82**, 215 (2000).

[12] P. Rowat, *Neural Comput.* **19**, 1215 (2007).

[13] I. Bashkirtseva, L. Ryashko, *Int. J. Bifurc. Chaos* **29**, 1950186 (2019).

[14] C. Meunier, I. Segev, *Trends Neurosci.* **25**, 558 (2002).

[15] J.H. Goldwyn, E. Shea-Brown, *PLoS Comput. Biol.* **7**, e1002247 (2011).

[16] E.V. Pankratova, A.V. Polovinkin, E. Mosekilde, *Eur. Phys. J. B Condens. Matter Complex Syst.* **45**, 391 (2005).

[17] T. Takahata, S. Tanabe, K. Pakdaman, *Biol. Cybern.* **86**, 403 (2002).

[18] M. Güler, *Neural Comput.* **25**, 2355 (2013).

[19] J. Wang, L. Xu, E. Wang, *Proc. Natl. Acad. Sci.* **105**, 12271 (2008).

[20] J. Wang, *Adv. Phys.* **64**, 1 (2015).

[21] X. Fang, K. Kruse, T. Lu, J. Wang, *Rev. Mod. Phys.* **91**, 045004 (2019).

[22] H. Yan, L. Zhao, L. Hu, X. Wang, E. Wang, J. Wang, *Proc. Natl. Acad. Sci.* **110**, E4185 (2013).

[23] H. Yan, K. Zhang, J. Wang, *Chinese Phys. B* **25**, 078702 (2016).

[24] C. Li, E. Wang, J. Wang, *Biophys. J.* **101**, 1335 (2011).

[25] L. Xu, D. Patterson, A.C. Staver, S.A. Levin, J. Wang, *Proc. Natl. Acad. Sci.* **118**, e2103779118 (2021).

[26] K. Zhang, J. Wang, *J. Phys. Chem. B* **122**, 5487 (2018).

[27] X. Wang, Y. Wu, L. Xu, J. Wang, *J. Chem. Phys.* **159**, 154105 (2023).

[28] H. Yan, F. Zhang, J. Wang, *Commun. Phys.* **6**, 110 (2023).

[29] L. Xu, D. Patterson, S.A. Levin, J. Wang, *Proc. Natl. Acad. Sci.* **120**, e2218663120 (2023).

[30] H.C. Tuckwell, J. Jost, *Physica A* **388**, 4115 (2009).

[31] V. Baysal, Z. Saraç, E. Yilmaz, *Nonlinear Dyn.* **97**, 1275 (2019).

[32] Q. Kang, B.-Y. Huang, M.-C. Zhou, *IEEE Trans. Cybern.* **46**, 2083 (2015).

[33] A.S. Pikovsky J. Kurths, *Phys. Rev. Lett.* **78**, 775 (1997).

[34] A.A. Faisal, L.P.J. Selen, D.M. Wolpert, *Nat. Rev. Neurosci.* **9**, 292 (2008).

[35] H. Risken, *The Fokker-Planck Equation*, Springer, Berlin 1996.

[36] W. Coffey, Y.P. Kalmykov, *The Langevin Equation: With Applications to Stochastic Problems in Physics, Chemistry and Electrical Engineering*, Vol. 27, World Scientific, 2012.

[37] L. Xu, J. Wang, *J. Phys. Chem. B* **124**, 2549 (2020).

[38] F. Zhang, L. Xu, K. Zhang, E. Wang, J. Wang, *J. Chem. Phys.* **137**, 065102 (2012).

[39] P. Dayan, L.F. Abbott, *Theoretical Neuroscience: Computational and Mathematical Modeling of Neural Systems*, MIT press, 2005.

[40] J. Wang, L. Chen, X. Fei, *Chaos, Solit. Fractals* **31**, 247 (2007).

[41] S. Wiggins, *Introduction to Applied Nonlinear Dynamical Systems and Chaos*, Springer-Verlag, 2003.

[42] R.J. Sacker, *J. Differ. Equ. Appl.* **15**, 753 (2009).

[43] T. Tateno, A. Harsch, H.P.C. Robinson, *J. Neurophysiol.* **92**, 2283 (2004).

[44] H. Qian E.L. Elson, *Proc. Natl. Acad. Sci.* **101**, 2828 (2004).

[45] Q. Liu, J. Wang, *Proc. Natl. Acad. Sci.* **117**, 923 (2020).

[46] C. Meisel, A. Klaus, C. Kuehn, D. Plenz, *PLoS Comput. Biol.* **11**, e1004097 (2015).

[47] D.A. Steyn-Ross, M.L. Steyn-Ross, M.T. Wilson, J.W. Sleigh, *Phys. Rev. E* **74**, 051920 (2006).

Subscription terms/Warunki prenumeraty — 2024

Acta Physica Polonica is issued as two separate journals, namely *A* and *B*, in Warszawa and Kraków, respectively. Each of the periodicals is published in the indicated scope and sold by its respective Publisher (see details below). A subscription order should be submitted to the relevant Publisher.

◇ The subscription price of *Acta Physica Polonica A* (*APPA*) is **450 EUR** (surface mail delivery, priority mail on demand with extra **90 EUR** postage rate).

The Publisher of *Acta Physica Polonica A*:

The Director of Institute of Physics
Polish Academy of Sciences
al. Lotników 32/46
02-668 Warsaw, Poland
e-mail: appol@ifpan.edu.pl

bank account BGK S.A. Warszawa:
PL 35 1130 1017 0013 4373 9820 0027
(int. bank code SWIFT: GOSKPLPW)

The archival *APPA* issues (if still available) can be purchased at the Editorial Board of *APPA*.

◇ Cena prenumeraty rocznej *Acta Physica Polonica A* wynosi **2100 PLN** (netto).

Prenumeratę przyjmuje Wydawca:

Dyrektor Instytutu Fizyki
Polskiej Akademii Nauk
al. Lotników 32/46
02-668 Warszawa, Polska
e-mail: appol@ifpan.edu.pl

konto bankowe BGK S.A. Warszawa:
89 1130 1017 0013 4373 9820 0025

◇ The subscription price of *Acta Physica Polonica B* can be obtained by contacting its Publisher:

Institute of Physics
Jagiellonian University
Łojasiewicza 11
30-348 Kraków, Poland
e-mail: acta.phys.pol.b@uj.edu.pl

ACTA PHYSICA POLONICA A
Volume 146 — Number 1

Special Segment

Regular Segment